A High-throughput, Combinatorial and Robotic approach to catalysis

By

KARISKA POTGIETER

Submitted in fulfilment of the requirements for the degree

PHILOSOPHIAE DOCTOR

in

CHEMISTRY

at the

UNIVERSITY OF JOHANNESBURG

February 2021

Declaration

I, Kariska Potgieter, herewith declare that this thesis titled “A High-throughput, Combinatorial and Robotic approach to catalysis“, submitted for a degree Philosophiae Doctor (PhD) in Chemistry to the University of Johannesburg, is an original report of my research, and it has been composed solely by myself and has not been submitted, in whole or in part, to this or any tertiary institution for any previous degree. All sources of information presented in this thesis have been acknowledged through complete references.

…….

Kariska Potgieter

February 2021

Acknowledgements

I want to extend my sincere and heartfelt gratitude to the following people who have supported me in my endeavour:

Foremost, to **God Almighty** for without His grace and blessings, I would not have been able to persevere through this study. I thank Him for the wisdom, strength and peace of mind during this time.

My supervisor, **Prof Reinout Meijboom** for all his support and exciting ideas for my research. Thank you for your guidance, advise and for granting me the opportunity to do a PhD with you. Thank you for believing in me and for making it possible for me to complete some of the research in England. I have learned so much from you.

My co-supervisor, **Dr Elize Smit**, thank you for always making time for me to discuss work, your guidance and advise. Because of you, I see chemistry in a different light. **Prof Frank von Delft**, for the research invitation to Diamond Light Source in the UK. This allowed me to grow as a person and in my research. **Dr Anthony Aimon**, for making me feel welcome in the group and guiding me during my research visit. Thank you for pushing me out of my comfort zone. I have learned so much from you.

I am also grateful to the Department of Chemical Sciences at the University of Johannesburg for hosting me during my studies. A special thanks to **Mrs Eureka O'Rourke** and **Mrs Nelmarie Müller** for your support and encouraging words when the days were tough. I appreciate you in my life. To Diamond Light Source and the Global Challenges Research Fund (GCRF) through Science & Technology Facilities Council (STFC), Synchrotron Techniques for African Research and Technology (START) for funding provided for my research visit. The Metacatalysis group in the Department of Chemical Sciences, for your continued support during my studies, especially **Dr Oyekunle Azeez Alimi** for your support and with the 3D printing.

Deon van der Watt, my partner, thank you for your unconditional love and for always believing in me. You showed me the light in times I couldn't find my way through the darkness. My parents, **Johan** and **Sabine Potgieter** thank you for your love, support, and opportunities you gave me. **Tannie Elsa,** for believing in me, motivating me and for all your endless love and support. My brother **Ruben Potgieter** for your love, support and inspiration. **Charmaine Jacobs**, you have inspired me so much. Thank you for your support, love and motivation. And also to **Oom Deon van der Watt**, **Rainier van der Watt** for your support and motivation. And finally, my family, for your motivation and support.

And finally, I would like to appreciate all my friends, **Frikkie Malan, Calsey Zevenster**, **Charlene Andraos**, **Nicolene Aspeling**, **Trudie de Bruyn**, **Natasha Sanabria** and **Ji-Hyang Noh**, for all your support, motivation, encouraging words and guidance during my studies. I am truly blessed with all of you, and you all mean the world to me!

“It always seems impossible until it’s done”

- Nelson Mandela -

Table of content

Chapter 1 – An Introduction to the High-throughput, Combinatorial and Robotic approach to catalysis 1

1.1 Heterogeneous catalysis 2
1.1.1 Mesoporous metal oxide (MMO) materials 3
1.1.1.1 Hard-template mesoporous metal oxide synthesis 4
1.1.1.2 Soft-template mesoporous metal oxide synthesis 5
1.1.1.3 Surfactants as structure-directing agents 6
1.1.1.4 Sol-gel chemistry 8
1.1.1.5 Evaporation-induced self-assembly 11
1.1.2 Multicomponent mesoporous metal oxide materials 12
1.1.3 Supporting nanoparticles on mesoporous metal oxides 13
1.1.4 Application of mesoporous metal oxides as catalysts in oxidation reactions 14
1.2 High-throughput approach to catalysis 17
1.2.1 High-throughput and/or combinatorial heterogeneous catalysis 19
1.2.1.1 Early approaches to high-throughput heterogeneous catalysis 19
1.2.1.2 Split-and-pool approach 20
1.2.1.3 Inkjet printing catalyst libraries 23
1.2.1.4 Deconvolution of the libraries to identify hits 27
1.2.2 High-throughput and/or combinatorial homogeneous catalysis 29
1.3 The robotics approach to high-throughput chemistry 31
1.3.1 Liquid handlers 32
1.3.1.1 Commercially available liquid handlers 32
1.3.2 Acoustic liquid handling 33
1.3.2.1 Catalytic application of acoustic liquid handlers 33

1.3.3 Open-Source liquid handling robots 34
1.3.3.1 The Opentrons 34
1.3.3.2 The EvoBot 35
1.3.3.3 Alternative custom-built liquid handler 36
1.4 Conclusion 36
1.5 References 37

Chapter 2 - A multidimensional group testing approach to Mizoroki-Heck and Suzuki C-C coupling reactions catalysed by homogeneous Pd phosphine complexes 52

2.1 Introduction 54
2.2 Experimental 58
2.2.1 Materials 58
2.2.2 Method 59
2.2.2.1 Solvent mixture 60
2.2.2.2 Phosphine ligand mixture 60
2.2.2.3 A general description of the split-and-pool deconvolution approach 60
2.2.2.4 Gas chromatography flame ionisation detector (GC-FID) analysis 65
2.3 Results and discussion 66
2.3.1 Mizoroki-Heck C-C coupling between butyl acrylate and aryl halides (PhI, PhBr, PhCl) 66
2.3.1.1 Coupling between iodobenzene (PhI) and butyl acrylate 67
2.3.1.2 Coupling between bromobenzene (PhBr) and butyl acrylate: 68
2.3.1.3 Coupling between chlorobenzene (PhCl) and butyl acrylate 69
2.3.2 Suzuki C-C coupling between phenylboronic acid and 4-bromotoluene 69
2.3.2.1 A variation in the deconvolution strategy for the Suzuki reaction 71
2.3.3 General aspects of the Mizoroki-Heck and Suzuki cross-coupling reactions 72

2.3.3.1 The role of the base 72
2.3.3.2 Role of the solvent 73
2.3.3.3 Role of the phosphine ligand 74
2.4 Conclusion 75
2.5 Acknowledgements 75
2.6 References 76

Chapter 3 - Robotics-Assisted High-throughput Catalytic Investigation of PVP Nanoparticles in the Oxidation of Morin 80

3.1 Introduction 82
3.2 Experimental 87
3.2.1 Materials 87
3.2.2 Instrumentation 87
3.2.2.1 Opentrons – liquid handling robot (pipetting robot) 87
3.2.2.2 UV/vis microplate reader 87
3.2.2.3 High-resolution transmission electron microscopy (HR-TEM) 87
3.2.2.4 Data fitting 88
3.2.3 Methods 88
3.2.3.1 Synthesis of PVP stabilised nanoparticles 88
3.2.3.2 Catalytic oxidation of morin 88
3.2.4 Plate reader 91
3.3 Results and Discussion 91
3.3.1 Synthesis of polyvinyl pyrrolidone nanoparticles (PVP NPs) 91
3.3.1.1 Transmission Electron Microscopy (TEM) imaging 92
3.3.2 Opentrons setup for the catalytic study 93
3.3.3 Catalytic oxidation of morin 94
3.3.3.1 Catalyst concentration variation 94

3.3.3.2 Morin concentration variation 95
3.3.3.3 Hydrogen peroxide concentration variation 96
3.4 Conclusion 99
3.5 Acknowledgements 99
3.6 References 99

Chapter 4 - Robotic Catalysis: A High-throughput Method for Miniature Screening of Mesoporous Metal Oxides 105

4.1 Introduction 106
4.2 Experimental 108
4.2.1 Chemicals and materials 108
4.2.2 Synthesis of mesoporous metal oxide (MMO) formulations 109
4.2.2.1 Synthesis of mesoporous cobalt oxide formulation 109
4.2.2.2 Synthesis of mesoporous manganese oxide formulation 109
4.2.3 Synthesis of polyvinyl pyrrolidone (PVP) stabilised nanoparticles (NPs) 109
4.2.3.1 Pd-PVP NPs 109
4.2.3.2 Au-PVP NPs 109
4.2.4 Customised catalyst plate/s 110
4.2.4.1 Dispensing of the catalyst formulation onto the glass plate 110
4.2.4.2 Heat treatment of the glass plate to form the catalyst plate: 110
4.2.4.3 Custom 3D printed catalyst plate: 110
4.2.5 Characterisation of bulk and miniature catalysts: 110
4.2.5.1 Surface area analysis 110
4.2.5.2 Transmission electron microscopy (TEM) imaging 111
4.2.6 Catalytic evaluation of the catalyst 111
4.2.7 Data fitting 112

4.3 Results and Discussion 112
4.3.1 Morphological comparison between the miniature and bulk catalysts 112
4.3.1.1 TEM imaging 112
4.3.2 The High-throughput catalyst screening system 114
4.3.2.1 Nano-droplet transfers to the glass plate 115
4.3.2.2 Glass as a catalyst support 115
4.3.2.3 The customised 3D printed catalyst plate 116
4.3.3 Evaluation of the catalyst plates for the oxidation of morin 117
4.4 Conclusion 122
4.5 Acknowledgements 123
4.6 References 123

Chapter 5 - The Use of Robotics and 3D Printing in Chemistry – An Open-Source Approach 130

5.1 Introduction 131
5.2 Experimental 135
5.2.1 Materials 135
5.2.1.1 EvoBot 135
5.2.1.2 3D printing 135
5.2.2 Method 136
5.2.2.1 EvoBot 136
5.2.2.2 3D printing 136
5.3 Results and discussion 136
5.3.1 Assembly of the EvoBot robot 136
5.3.2 Electronics and coding 142
5.3.3 3D printing in the laboratory 144
5.3.3.1 Custom-designed 3D printed labware 144

5.3.3.2 Open-Source 3D printed labware 145
5.4 Future work 146
5.5 Conclusions 147
5.6 Acknowledgements 148
5.7 References 148

Chapter 6 – Conclusions, Recommendations and Future work 151

Conclusions, Recommendations and Future work 152

Appendices 157

Supplementary information 157

List of Figures, Tables and Schemes

Figures

Chapter 1

Figure 1.1: Mesoporous material synthesis using the hard-template method. During the synthesis, the nanoparticles form nano-structures which are connected with short bridges as illustrated in the image. This image was adapted from Machado *et al.* [19]. 4

Figure 1.2: The soft-template method used for the synthesis of mesoporous materials. During the synthesis, the soft-template is formed by the interaction of micelles. The metal precursor then coordinates to the micelles to form the mesoporous channels or pores. Finally, the soft-template is removed at high temperatures [28]. 6

Figure 1.3: Synthesis of a mesoporous metal oxide using the sol-gel method. The first stage involves the surfactant assembly using pluronic surfactant F127 as an SDA, followed by the organisation of the inorganic precursor (metal nitrate salt) over the surfactant assembly. Essentially the metal coordinates to the surfactant to form the inorganic-organic precursor. And finally, the mesoporous metal oxide is formed when the surfactant is decomposed at high temperatures. 8

Figure 1.4: Split-and-pool approach to combinatorial library synthesis. In the first stage, the starting materials or the beads are split into equal portions. The portions are then treated with different reagents. The portions are then pooled and mixed and split again into equal portions. The new portions are then treated with different reagents. A mixture of compounds (either catalysts, reagents or products) is the result. 22

Figure 1.5: Schematic representation of a deconvolution process, where six bases (B), six solvents (S) and 20 ligands (L) are deconvoluted in a homogeneous catalytic reaction. Initially, the bases are deconvoluted, followed by the solvents then finally the ligands. A total of 19 reactions are performed to deconvolute to the best base, solvent and ligand. Conventionally 720 reactions are needed if one parameter is investigated at a time. 28

Figure 1.6: (a) Opentrons 2 (OT-2) (photo obtained from the Opentrons website) is the second version of an Open-Source liquid handling robot. (b) The transfer of reagents into a 96-well plate.(photo by K Potgieter). 34

Figure 1.7: The EvoBot liquid handling robot [170] 35

Chapter 2

Figure 2.1: Schematic representation of a generic C-C cross-coupling reaction. 57

Figure 2.2: Schematic representation of a general split-and-pool deconvolution approach. This approach was used to deconvolute six bases, six solvents, and up to 20 phosphine ligands. This multidimensional group testing strategy was used for reagent optimisation for the Heck and Suzuki cross-coupling reactions. 61

Figure 2.3: Reaction equation for the Mizoroki-Heck C-C coupling between butyl acrylate and an aryl halide. 66

Figure 2.4: Schematic representation of the deconvolution approach followed to identify the best base, solvent, and phosphine ligand in the Mizoroki-Heck C-C coupling reaction between iodobenzene and butyl acrylate. The best base, solvent, and phosphine ligand were identified as K_2CO_3, acetonitrile, and tricyclohexylphosphine. 67

Figure 2.5: Schematic representation of the deconvolution approach followed to identify the best base, solvent, and phosphine ligand in the Mizoroki-Heck C-C coupling reaction between bromobenzene and butyl acrylate. The best base, solvent, and phosphine ligand were identified as K_2CO_3, acetonitrile, and tricyclohexylphosphine. 68

Figure 2.6: Reaction equation for the Suzuki C-C coupling between phenylboronic acid and an aryl halide. 69

Figure 2.7: Schematic representation of the deconvolution approach to identify the best base, solvent, and phosphine ligand in the Suzuki C-C coupling reaction between phenylboronic acid and 4-bromotoluene. The best base, solvent, and phosphine ligand were identified as K_2CO_3, ethanol, and benzyldiphenylphosphine. 70

Figure 2.8: Schematic representation of the variation in deconvolution setup for the Suzuki reaction between phenylboronic acid and 4-bromotoluene. This was done to confirm the previous findings (section 2.3.2) determine if the same system can be identified as previously found. The best base and solvent were also found to be K_2CO_3 and ethanol. All phosphine reactions gave similar results (conversions > 90%). 71

Chapter 3

Figure 3.1: **(a)** Representation of the 96-well microtiter plate with the 12 final concentrations of each catalyst, using four replicates. Row A – D represents the four replicates used for the Pd-PVP NPs, and row E – H represents the four replicates used for the Au-PVP NPs. The columns 1 – 12 represents the concentration range of the catalysts increasing from 5 μM to 150 μM. **(b)** Final plate representation, following the addition of all the reagents by the Opentrons for the catalyst concentration variation study. This figure shows the composition of well A6 as an example. This well contains 155 μL water, 30 μL oxidant or hydrogen peroxide (0.45 mM), 30 μL dye or morin solution (50 μM) and 145 μL of PdPVP NPs. For this plate, concentrations (5 – 150 μM) and the volume of the NPs were increased from A1 – D1 to A12 – D12 for the PdPVP NPs, and from E1 – H1 to E12 – H12 for the AuPVP NPs, in a range of 10 – 300 μL. 90

Figure 3.2: Transmission electron microscopy imaging of the **(a)** Pd- and **(b)** Au-PVP NPs synthesised using the polyol method. The Pd-PVP NPs had an average size of 16.56 nm, and the Au-PVP NPs have an average size of 10.8 nm..... 92

Figure 3.3: (a) The decrease in absorbance at λ 410 nm of morin over time, using Pd-PVP NPs as a catalyst. The points correspond to the concentration of the Pd-PVP NPs. (b) The graph shows the influence of Pd-PVP NP concentration on the observed rate (k_{obs}) for the oxidation of morin at 25 °C. The concentration of morin was 50 μM and for H_2O_2 0.45 mM. Each k_{obs} value corresponds to a certain concentration of Pd-PVP NPs. The black square points represent the catalytic dynamic range, and the red circle points represent the diffusion limitation domain. 94

Figure 3.4: (a) The decrease in absorbance of morin at λ 410 nm, over 2 hrs when using Au-PVP NPs as a catalyst. (b) The graph shows the influence of Au-PVP NP concentration on the observed rate (k_{obs}) for the oxidation of morin at 25 °C, using a concentration of 50 μM for morin and 0.45 mM for H_2O_2. Each k_{obs} value corresponds to a certain concentration of Au-PVP NPs. The catalytic dynamic range is represented by the red fitted linear curve. 95

Figure 3.5: The influence of the concentration of morin on the k_{obs} using a constant concentration of **(a)** 35 μM for the Pd-PVP NPs, and **(b)** 85 μM for the Au-PVP NPs. The influence was investigated at 25 °C, 35 °C, and 45 °C. All the experiments were conducted at a constant concentration of 0.45 mM of the H_2O_2. 96

Figure 3.6: The variation of the concentration of the hydrogen peroxide from 0.67 – 20 mM, and the influence on the k_{obs}. A constant concentration of 50 μM morin was used for all experiments. The catalyst concentration was also kept constant at **(a)** 35 μM for the Pd-PVP NPs, and **(b)** 85 μM for the Au-PVP NPs. 97

Chapter 4

Figure 4.1: TEM images of **(a)** the bulk Co_3O_4-MMO sample, and for **(b)** the miniature Co_3O_4-MMO sample. Comparing the images of both samples, it can be seen that the particles size is uniform, approximately 20 nm. 113

Figure 4.2: TEM images of **(a)** the bulk Co_3O_4-MMO sample, and for **(b)** the miniature Co_3O_4-MMO sample. From these images, the pore network structures (represented by the parallel lines, and circled in white) can be seen for both the bulk and the miniature samples. 113

Figure 4.3: A comparison of **(a)** the Au/Co_3O_4-MMO, **(b)** Pd/Co_3O_4-MMO and **(c)** Co/Mn-MMO miniature catalysts using TEM. The particles sizes are comparable to the bulk sample, approximately 20 nm. The white bars represent the scale of the TEM images. 114

Figure 4.4: **(a)** The glass plate (LCP sandwich set glass plate, 1 mm thick) used as a support for the catalysts synthesis as well as evaluation of the catalysts for the oxidation of morin. The catalyst formulation (Co_3O_4 formulation) was deposited onto the glass plate using an acoustic liquid handler. The volume of the formulation was increased over the 96-well areas. A glass plate holder was designed, and 3D printed to hold the glass plate in the instrument during formulation deposition. **(b)** Catalysts after calcination at 400 °C. 115

Figure 4.5: **(a)** The 3D printed bottomless 96-well plate fixed to **(b)** the glass plate (containing the already calcined catalysts) using epoxy glue, dispensed with a Nordson EFD Pro4 glue dispensing robot. **(c)** The actual catalyst plate, with the glass plate and catalysts in individual wells. 117

Figure 4.6: The observed rate constant (k_{obs}) obtained for the best catalyst from each catalyst plate. Negative and positive controls were included for all the catalyst plates, and the average rate was calculated for each control and is represented in the figure. The rate of reaction for the bulk Co_3O_4 catalyst determined using the conventional method (CM) in a round bottom flask (RBF) for 1 hour is given. A negative control (NC), as a blank measurement, was included to show that the reaction takes place slowly in the absence of a catalyst, and a positive control (PC, 0.025 mg/mL bulk Co_3O_4 dispersed in deionised water and added to empty well in the custom catalyst plate before the analysis in the plate reader) to show that Co_3O_4 is active in the oxidation of morin. 119

Chapter 5

Figure 5.1: An example of a figure provided in the building instruction documentation of the EvoBot. The figure represents the assembly of the actuator layer (https://bitbucket.org/afaina/evobliss-hardware and https://bitbucket.org/afaina/evobliss-software). 137

Figure 5.2: The frame of the EvoBot constructed using aluminium V-slot profiles. The height controls can also be seen in the figure. 138

Figure 5.3: **(a)** Carriage plates and **(b)** electronic cover parts laser-cut from 3 mm and 1 mm aluminium sheets, respectively. 139

Figure 5.4: **(a)** Design files for the syringe module electronic cover, **(b)** the .dxf files converted to a 2D model and **(c)** extruded to a 1 mm 3D model using Onshape CAD program. 139

Figure 5.5: **(a)** Design files for the carriage plates, **(b)** the .dxf files converted to 2D models, and **(c)** extruded to a 4 mm 3D model using the Onshape CAD program. 141

Figure 5.6: **(a)** 3D printed carriage plates and **(b)** the syringe module electronic covers. The parts were 3D printed using PLA filament. 141

Figure 5.7: **(a)** PCB for the EvoBot robot and the **(b)** syringe module. 142

Figure 5.8: An example of the RAMPS and Arduino wiring diagram provided with the building instructions of the EvoBot. 143

Figure 5.9: The wiring of the EvoBot robot – **(a)** RAMPS 1.4 and the **(b)** syringe module. 143

Figure 5.10: **(a)** The CAD model of the cuvette insert or holder for the centrifuge. This was designed in Onshape and **(b)** 3D printed using PLA filament. This was designed for plastic cuvettes with a path length of 1 cm..... 144

Figure 5.11: BET tube holder for accurately weigh out samples to be analysed on the BET. 145

Figure 5.12: Oil bath test tube holders. **(a)** For larger test tubes, **(b)** for smaller test tubes, and **(c)** and **(d)** the 3D printed models of test tube holders printed with PLA filament..... 145

Figure 5.13: Labware 3D printed from open-source files obtained and downloaded from thingiverse.com. 146

Tables

Chapter 2

Table 2.1: Phosphine ligands with their respective numbering, used for the Heck and Suzuki C-C coupling deconvolution reactions..... 59

Table 2.2: Reaction numbers and reagents under investigation for the Mizoroki-Heck cross-coupling between iodobenzene (PhI) and butyl acrylate. 62

Table 2.3: Reaction numbers and reagents under investigation for the Mizoroki-Heck cross-coupling between bromobenzene (PhBr) and butyl acrylate..... 63

Table 2.4: Reaction numbers and reagents under investigation for the Suzuki cross-coupling between phenylboronic and 4-bromotoluene..... 64

Table 2.5: Reaction numbers and reagents under investigation for the Suzuki cross-coupling between phenylboronic and 4-bromotoluene using a different deconvolution approach. 65

Chapter 5

Table 5.1: List of stepper motors originally used for the EvoBot which had to be substituted with different motors due to availability in South Africa. 142

Schemes

Chapter 3

Scheme 3.1: The oxidation and over-oxidation of morin. 85

Scheme 3.2: Pseudo-first kinetic scheme of the oxidation of morin by PVP templated nanoparticles. Both the morin and hydrogen peroxide adsorbs to the surface of the particle for the reaction to take place. 85

Chapter 4

Scheme 4.1: Pseudo first-order kinetic scheme for the oxidation of morin by the mesoporous metal oxides. 118

Scheme 4.2: The schematic representation of the oxidation and over-oxidation of morin . 120

List of abbreviations

°C	Degree Celsius
3D	3-Dimensional
4-AP	4-aminophenol
4-NP	4-nitrophenol
AAO	Anodic aluminium oxides
ABS	Acrylonitrile butadiene styrene
ADE	Acoustic droplet ejection
AuNP	Gold nanoparticles
BET	Brunauer–Emmett–Teller
BOM	bill of materials
CAD	Computer-aided design
C-C	Carbon-carbon coupling
CM	Conventional method
CMC	Critical micelle concentration
CO	Carbon monoxide
DCC	Dynamic covalent chemistry
DCM	Dichloromethane
DMF	Dimethylformamide
DNA	Deoxyribonucleic acid
DOD	Drop-on-demand
EISA	Evaporation-induced self-assembly
ELISA	Enzyme-linked immunosorbent assay
ESI-MS	Electrospray ionisation mass spectrometry
EVLIT	Evolving living technologies
FOSH	Free and open-source hardware
FOSS	Free and open-source software
GC-FID	Gas chromatography flame ionisation detection
HCl	Hydrochloric acid
HPLC	High-performance liquid chromatography
HR-TEM	High-resolution transmission electron microscopy
IJP	Inkjet printing

IR	Infrared
IUPAC	International Union of Pure and Applied Chemistry
K	Kelvin
k_{obs}	observed rate
LCP	Lipidic cubic phase
LCT	Liquid crystal templating
MCM-48	Mobil Composition of Matter (mesoporous silica)
MeCN	Acetonitrile
min	Minutes
MMO	Mesoporous metal oxide
MNP	Metal nanoparticles
NC	Negative control
NEt_3	Triethylamine
nL	nanolitre
nm	nanometer
NP	nanoparticles
OCT	Optical Coherence Tomography
OT1	Opentrons 1
OT2	Opentrons 2
PC	Positive control
PCB	Printed circuit board
PCR	polymerase chain reaction
PdNP	Palladium nanoparticles
PEMFC	Polymer electrolyte membrane fuel cells
PEO	Polyethylene oxide
PETG	Polyethylene terephthalate glycol-modified
PhBr	Bromobenzene
PhCl	Chlorobenzene
PhI	Iodobenzene
PLA	polylactic acid
PMMA	poly(methyl methacrylate)
POM	polyoxymethylene
PVK	polyvinyl carbazole
PVP	Polyvinyl pyrrolidone

RBF	Round bottom flask
RNA	Ribonucleic acid
SBA-15	Santa Barbara Amorphous type material no. 15
SDA	Structure-directing agent
STEM	science, technology engineering and mathematics
TEM	Transmission electron microscopy
TOF	Turn over frequency
TOF-MS	Time-of-flight mass spectrometry
TON	Turn over number
UV/Vis	Ultraviolet-visible light

Publications, conferences and awards

Publications:

- **Kariska Potgieter**, Anthony Aimon, Elize Smit, Frank von Delft and Reinout Meijboom. *Robotic Catalysis: A High-throughput Method for Miniature Screening of Mesoporous Metal Oxides*. (Published in Chemistry Methods).
- **Kariska Potgieter**, Elize Smit and Reinout Meijboom. *A multidimensional group testing approach for the reagent optimisation of a Suzuki C-C coupling reaction*. (Manuscript under review at Catalysis Letters)
- **Kariska Potgieter** and Reinout Meijboom. Robotics-Assisted *High-throughput Catalytic Investigation of PVP Nanoparticles in the Oxidation of Morin.* (Provisionally accepted in Journal of Chemical Technology and Biotechnology).
- **Kariska Potgieter**, Matthew A. J. Nel, Andre L. Nel and Reinout Meijboom. *The Use of Robotics and 3D Printing in Chemistry – An Open-Source Approach*. (Manuscript in progress).
- Oluwatayo Racheal Onisuru, Oyekunle Azeez Alimi, **Kariska Potgieter**, and Reinout Meijboom. *Continuous Flow Catalytic Degradation of Hexacyanoferrate Ion through electron transfer induction in a 3D-Printed Flow Reactor.* (Published in Journal of Materials Engineering and Performance, paper not part of this thesis)

Conferences and awards:

- Kariska Potgieter, Anthony Aimon, Elize Smit, Frank von Delft and Reinout Meijboom. *Robotic Catalysis: A High-throughput Method for Miniature Screening of Mesoporous Metal Oxides*. **Young Spectroscopist / Mass Spectrometrist's Symposium 2019**. Johannesburg, South Africa. (Won second prize for the Northern region).
- Kariska Potgieter, Anthony Aimon, Elize Smit, Frank von Delft and Reinout Meijboom. *Robotic Catalysis: A High-throughput Method for Miniature Screening of Mesoporous Metal Oxides*. **19de jaarlikse Studentesimposium in die Natuurwetenskappe** (Won third prize of the PhD section).

- I was invited for a research visit at Diamond Light Source, Oxford, UK (March – August 2019). Research conducted was under the supervision of Prof. Frank von Delft and Dr Anthony Aimon.

Keywords

Robotic catalysis, High-throughput experimentation, Combinatorial catalysis, Deconvolution, Heterogeneous catalysis, Mesoporous Metal Oxides, nanoparticles, Oxidation of Morin, Mizorok-Heck reaction, Suzuki reaction, Open-Source, 3D printing.

Abstract

In catalysis, the traditional approach often involves the synthesis and evaluation of catalysts by using the Edisonian approach. This is time-consuming, and limitations are complex and not always given. A high-throughput and/or combinatorial approach can be used for catalyst discovery by the simultaneous synthesis and evaluation of catalysts. By using such methods, one can discover new catalysts and identify the best catalyst or reagents in a fast way. High-throughput and combinatorial approaches to catalysis were investigated.

As proof of principle, a multidimensional group testing strategy was used for the ultra-fast optimisation of reagents for C-C cross-coupling reactions. Reagents, including the bases, solvents, and phosphine ligands for the Pd-catalysed Mizoroki-Heck and Suzuki reactions, were deconvoluted to find the optimal reagent. A multidimensional group testing strategy was used by split-and-pooling the reagents, followed by the deconvolution to identify the best reagent. Six bases, six solvent, and up to twenty phosphine ligands were investigated, and the optimal reagents could be identified using a total of 19 reactions for each cross-coupling investigation. The deconvolution resulted in K_2CO_3 as the optimal base for both cross-coupling reactions. The optimal solvent was found to be acetonitrile and ethanol for the Mizoroki-Heck and Suzuki reaction, respectively. And finally, tricyclohexylphosphine and benzyldiphenylphosphine were found as the optimal ligands for these reactions, respectively. The optimal system for the Suzuki reaction was confirmed by employing a completely different deconvolution approach.

Robotics can also be applied in high-throughput experimentation. The fast and effective kinetic analysis of the catalytic oxidation of a dye was investigated by employing a robotic system. This was demonstrated for the catalytic oxidative degradation of morin by Au- and Pd-polyvinylpyrrolidone (PVP) templated nanoparticles (NPs). The system used included a commercially available, Open Source liquid handling robot, a microtiter plate, and a UV/Vis microplate reader. Palladium and gold PVP NPs were synthesised by using a polyol method, and the sizes of both the NPs were determined to be between 10 and 20 nm. The NPs were evaluated by UV/Visible light, for the oxidation of morin in a 96-well plate, using a microplate reader. The catalyst concentration variation step for both catalysts was performed in one experiment. Twelve concentrations were investigated in four replicates, simultaneously.

Therefore, in one experiment, the optimal concentration of both NPs was determined. The concentration variation steps of the morin and the hydrogen peroxide at different temperatures (25 °C, 35 °C and 45 °C) were also investigated using a similar approach (12 concentrations with four replicates). This was done to determine the effect of the concentration on the observed reaction rate (k_{obs}), for both the morin and hydrogen peroxide. This system showed that it is possible to investigate the oxidative degradation of a dye in a fast way by employing robotics and a high-throughput system.

The high-throughput screening of mesoporous metal oxides (MMO) was investigated by using a system created by robotics and 3D printing. As proof of concept, the simultaneous screening of up to 96 derivatives of Co_3O_4 MMOs (as miniature catalysts) was investigated for the degradation of morin. These included a multicomponent (Co/Mn) MMO, as well as Au- and Pd-PVP NPs immobilised on the Co_3O_4-MMO. An acoustic liquid handling robot was used to deposit nano-droplets of the MMO and NP formulations onto a glass plate. Following different heat treatments (ageing at 80 °C, drying at 150 °C, and calcination at 400 °C) the miniature MMO catalysts were formed on the glass plate. A customised 3D printed 96-well plate was fixed to the glass plate using a glue dispensing robot and epoxy glue. Four catalyst plates were investigated, including Co_3O_4-, Au/Co_3O_4-, Pd/Co_3O_4-, and Co_3O_4/MnO_x-MMO. The observed rates for each catalyst were used to identify the most active catalyst. It was shown that such a customised high-throughput system could be used to screen MMO catalysts of the oxidation of morin dye.

Open-Source hardware is the development of hardware, which is freely available. An example of Open-Source hardware is 3D printing and the EvoBot. The EvoBot is an affordable liquid handling robot which was developed for projects focussing on evolving living technologies, and it's mostly used in life sciences for basic dilutions and cell cultures. In chemistry, liquid handling robots are used for high-throughput experiments, for example, in catalyst discovery for the parallel synthesis and the screening of catalysts. The assembly of the EvoBot, as well as the issues encountered, are discussed. Moreover, the use of 3D printing to improve productivity in the laboratory is also considered.

These studies illustrate that different high-throughput approaches can be used for either reagent optimisation, catalyst screening, and discovery as well as the fast and effective kinetic analysis of the catalytic degradation of a dye. Moreover, there is no need to purchase high-end expensive

liquid handling robots. Open-Source hardware makes it possible to build laboratory equipment that is reliable and affordable.

Chapter 1

An Introduction to the Mesoporous metal oxides, and the High-throughput, Combinatorial and Robotic approach to catalysis

Chapter 1

An Introduction to Mesoporous metal oxides, and the High-throughput, Combinatorial and Robotic approach to catalysis

This literature review focuses on heterogeneous catalysis, mainly the use of mesoporous metal oxides as catalysts. The synthesis and application of these materials are discussed. Moreover, by using high-throughput and/or combinatorial methods, both heterogeneous and homogeneous catalysts can be screened in a much faster way compared to the traditional Edisonian approach. Hence, high-throughput and/or combinatorial approaches towards catalysis are discussed, focusing on robotic techniques used to achieve this.

1.1 Heterogeneous catalysis

The development of heterogeneous catalysis has become more popular due to the many advantages it offers compared to homogeneous catalysis. Homogeneous catalysis has been used extensively in research and industry due to high conversion rates since the catalysis occurs in one phase [1]. High conversion rates are obtained due to the catalyst acting as a single entity with a single active site for the reaction to take place. However, homogeneous catalysts cannot easily be recovered or recycled as compared to heterogeneous catalysts. Catalyst recyclability is an advantage of heterogeneous catalysis, where the catalysis takes place in two different phases (solid and liquid or gas). These phases consist of a solid phase representing the heterogeneous catalyst, and the liquid or gas phase containing the substrate/s. A two-phase system allows for catalyst recovery and recyclability upon completion of the reaction [1].

Moreover, homogeneous catalytic processes often produce large amounts of waste materials polluting the environment. The catalyst might also adsorb to the reactor walls, leading to contamination of future reactions taking place in the same reactors. Therefore, the use of heterogeneous catalysis has become more prevalent in recent years. To bridge the gap between these two systems, homogeneous catalysts are often immobilised onto heterogeneous supports. In this way, the newly formed catalyst exhibits unique properties of both catalysts. The efficiency of the catalyst is not compromised, and yet the catalyst can be recovered and recycled after every reaction [1–3]. Homogeneous catalysts that can be

supported include transition metal complexes, mono-and bimetallic nanoparticles [1, 3], just to mention a few. Mostly silica [2], carbon [4], clay, zeolites, metal oxides [5–7] and other solid catalysts are used as heterogeneous catalyst supports. Among these, it is believed that mesoporous metal oxide materials are the most ideal support. This is attributed to the 3D pore network, which increases the surface area and porosity of the material. The pores are mostly uniform and interconnected, creating spaces in the catalyst for reactants to adsorb, promoting the catalyst and reagent interaction [1, 8, 9].

1.1.1 Mesoporous metal oxide (MMO) materials

The history of mesoporous materials began with the discovery of zeolites. The discovery dates back to 1765, when zeolites were discovered by Cronstedt [10]. The first synthesis was attempted in 1862 by St. Claire Deville [11]. Zeolites are materials that exhibit aluminosilicate frameworks and are synthesised without the use of surfactants as structure-directing agents. The synthesis employs single molecules as templates giving rise to small pores inside the framework of these materials [12, 13]. Therefore, the term "porous" is often used to describe these materials. The most general definition of a porous material is a continuous and solid network containing voids (pores). A material is said to be porous if these voids or pores can be filled with something, for example, with a gas, a liquid or sometimes even with solids [13]. Numerous porous materials have already been described, and according to the International Union of Pure and Applied Chemistry (IUPAC), there are three types of porous materials: mesoporous, microporous and macroporous materials and they all differ in the size of the pores [13]. The name mesoporous has been adopted from the Greek prefix *meso* meaning "in-between". The IUPAC defines any porous material having pore dimensions of between micropore and macropore, as mesoporous materials [13, 14]. Mesoporous materials can also be classified as nanoporous materials, with pores that range in size of typically 1 – 100 nm.

Mesoporous silicas are probably the most popular mesoporous materials. This material was first discovered in the 1990s, and since then have been used for a large number of applications [15]. It is known that mesoporous silica is relatively easy to prepare; however, the preparation of non-silica mesostructures are a bit more challenging. This is due to the hydrolysis and condensation of non-silica precursors, which are generally more difficult to

control [16]. Even though the non-silica mesoporous materials are more difficult to synthesise, the resulting materials possess *d*-shell electrons within their nanosized walls.

Moreover, redox-active internal surfaces with pores are obtained, and the pores are connected to each other with a network. With these unique features, non-silica mesoporous materials have interesting properties and are used in numerous applications. These applications include energy conversion and storage, catalysis, sensing, adsorption, separation and magnetic devices [15]. As mentioned above, these non-silica mesoporous metal oxides (MMOs) can be synthesised using different methods such as the hard- and soft-templating methods.

1.1.1.1 Hard-template mesoporous metal oxide synthesis

The hard-templating method for the synthesis of MMOs can also be referred to as the nanocasting, exotemplating or repeated templating method. The hard-template which this method refers to is a rigid material that is used in the synthesis to cast the mesoporous materials. This material has a stable structure which will directly determine the size and morphology of the sample particle. There are numerous choices of hard-templates, which include: polymer microspheres, porous membranes, plastic foams, ion exchange resins, and porous anodic aluminium oxides (AAO) [15, 17, 18]. The hard-template materials are used as a mould to cast the other material of interest. The mould is then removed, and only the material of interest remains (**Figure 1.1**).

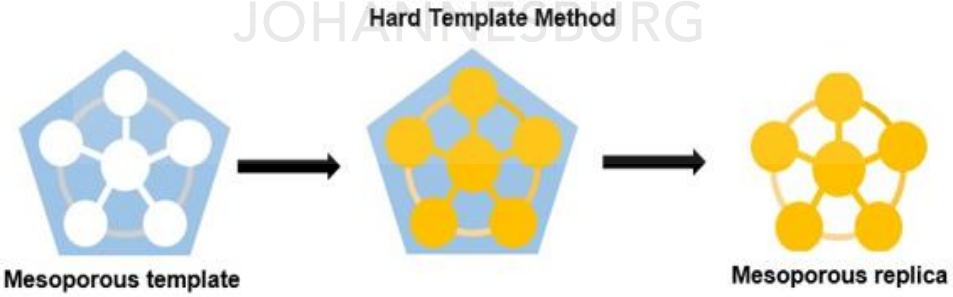

Figure 1.1: Mesoporous material synthesis using the hard-template method. During the synthesis, the nanoparticles form nano-structures which are connected with short bridges as illustrated in the image. This image was adapted from Machado *et al.* [19].

Often AAO and mesoporous silica (MCM-48), which is an abbreviation for Mobil Composition of Matter, are used as hard templates [15, 20]. The material SBA-15 (Santa Barbara Amorphous type material no. 15) is another popular mould used for the hard-

templating synthesis of mesoporous materials. The first step involves the infiltration of the silica mesopores with a precursor solution. The precursor solution is then converted to a solid by reduction or decomposition inside the pores. Finally, the silica template is removed with aqueous NaOH or HF [15]. The mesoporous silica that is used as the hard-template can give rise to materials having various shapes, pores as well as sizes. Hard-template moulds which are generally used included; MCM-41 [21], MCM-48 [20, 22], SBA-15 [23] and KIT-6 [24, 25].

The first highly ordered crystalline porous transition metal oxide that was synthesised using the hard-template method was reported in 2003 [26]. An amine functionalised SBA-15 was used as a template, and $K_2Cr_2O_7$ was used as the metal precursor to synthesise mesoporous single-crystalline Cr_2O_3, with nanowire arrays connected by short bridges [15, 26].

1.1.1.2 Soft-template mesoporous metal oxide synthesis

The synthesis of a hard-template can sometimes be disadvantageous, and, the specificity of the hard-template can pose some issues during the synthesis. A complementary hard-template is needed to synthesise a specific mesoporous material with a specific shape and size, and there are not as many hard templates available compared to soft templates [27]. However, this can also be an advantage, using a hard template, one can synthesise a product with a specific size and shape that corresponds to the hard template. Moreover, the shape and size of the resulting material are not variable. Therefore, to overcome some of these disadvantages, the soft-template method has been widely used [28].

In contrast to the hard-template method, the soft-template method does not consist of a fixed, rigid structure that is responsible for the formation of the pores. The soft-template method relies on the polymerisation of surfactant molecules [29]. This method was first used in 1994 by Stucky and co-workers [30], for the synthesis of WO_3, Nb_2O_5 and Fe_2O_3 materials. In this method, the structure is formed utilizing inter- or intramolecular interactions such as hydrogen bonding, chemical bonding and/or electrostatic forces. Due to these interactions, aggregates form, which ultimately creates the template (**Figure 1.2**). Inorganic species or a metal precursor are then deposited on the surface or into the interior of the templates. The deposition is done using different strategies which include electrochemical methods, precipitation, or other synthetic methods. This leads to the formation of particles that exhibit

many different shapes and sizes. The soft-templates include, for example, surfactants, polymers and biopolymers [17].

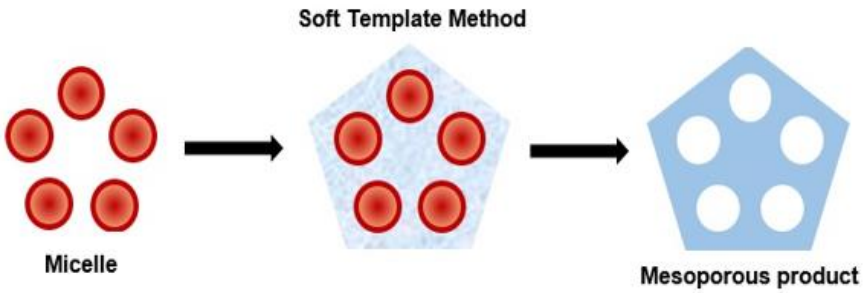

Figure 1.2: The soft-template method used for the synthesis of mesoporous materials. During the synthesis, the soft-template is formed by the interaction of micelles. The metal precursor then coordinates to the micelles to form the mesoporous channels or pores. Finally, the soft-template is removed at high temperatures [28].

Surfactants include amphiphilic molecules, ionic and non-ionic surfactants. Amphiphilic molecules are often used since they can easily form ordered molecules in solution, which includes liquid crystals, vesicles, micelles, microemulsions and self-assembled films [17, 31]. The interaction between the liquid crystal phase of a surfactant and organic-inorganic interface plays a role in the morphology of the mesoporous material. It is said that the surfactant being used is the structure-directing agent [32, 33]. Liquid crystal phases that form in solution when surfactants are present can give rise to different structures such as lamellar phase, cubic phase, as well as hexagonal phases [13, 17]. The pH of the solution plays a pivotal role in the interaction between the organic and inorganic interface. In a strong acidic environment, interactions will consist of weak hydrogen bonds; however, in a strong basic environment, electrostatic attraction forces are present [17]. Following the synthesis of the mesoporous materials, the soft-template (often surfactants or block copolymers) are decomposed by high temperatures (**Figure 1.2**). This enables various phases of mesoporous material to be formed, with ordered or disordered pores [28].

1.1.1.3 Surfactants as structure-directing agents

In the synthesis of mesoporous metal oxide materials, the organic surfactant, also known as a structure-directing agent (SDA), plays a crucial role in the structure formation. Various types of molecules can be used as SDA's. Surfactants, for example, can be used as an SDA, due to its unique property of having the coexistence of a chemically bonded hydrophobic (non-polar) hydrocarbon tail and a hydrophilic (polar) head. When these molecules are dissolved in

a solvent, small aggregates form and assemble into micelles [13]. Moreover, when using an aqueous media or polar solvents, the polar heads of the molecule interacts with the solvent. This allows for the surfactant to form micelles, with the non-polar tails in the core of the micelles, and the polar head on the periphery, interacting with the polar environment [13].

The distribution of the surfactant molecules present on the surface of the solvent or as micelles in the bulk of the solvent, strongly depend on the amount of surfactant being used. At low concentrations, the surfactant will favour the surface of the solvent; however, as the concentration increases, the surfactant starts to arrange into micelles in the bulk of the solvent. The concentration where micelles start to form is known as the critical micelle concentration (CMC), and when the concentration surpasses the CMC, self-assembly of micelles occurs to form 3D spherical or 2D rod-like shapes. These shapes ultimately act as the SDA to generate the pore shape and sizes [13].

There are three steps involved in the formation of mesoporous materials. The first step is the surfactant self-assembly, followed by the organisation of the inorganic precursor over the surfactant assembled structure. This forms a stable inorganic-organic hybrid. The final step is the decomposition of the surfactant by heat treatment of the material. During this process, the MMO is formed [13]. This is illustrated in **Figure 1.3**. This method is also referred to as the sol-gel method and has been extensively used for the synthesis of various types of MMOs. These include mesoporous gold-silica nanocomposites [34], single- and multi-component mesostructured metal oxides [35, 36], and iron(III)oxide monoliths using Fe(III) salts [37]. Sol-gel processes have the advantage of producing a solid-state material from a chemically homogeneous precursor. Furthermore, this process enables greater control over particle morphology and size [38].

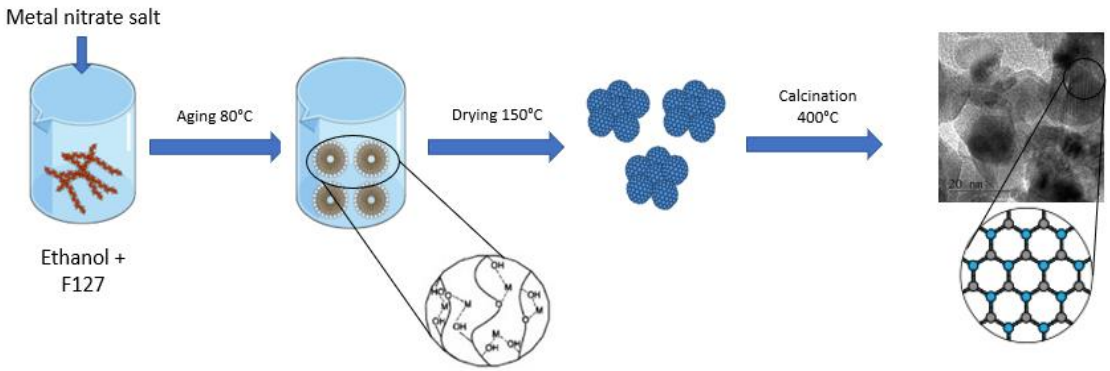

Figure 1.3: Synthesis of a mesoporous metal oxide using the sol-gel method. The first stage involves the surfactant assembly using pluronic surfactant F127 as an SDA, followed by the organisation of the inorganic precursor (metal nitrate salt) over the surfactant assembly. Essentially the metal coordinates to the surfactant to form the inorganic-organic precursor. And finally, the mesoporous metal oxide is formed when the surfactant is decomposed at high temperatures.

1.1.1.4 Sol-gel chemistry

Sol-gel chemistry refers to a process where an inorganic polymer or ceramics is formed from a solution, through the transformation of a liquid precursor to a so-called "sol". Following the formation of the sol, the structured network is generated, which is referred to as the "gel". This method involves two phases. These phases are known as the solution (sol) and gelation (gel) phases. A sol is referred to as a colloidal suspension of solid particles. In contrast, the gel is an interconnected network of solid-phase particles that form an entity through a secondary phase, usually the liquid phase [39]. The sol-gel process has numerous advantages which include high yields, low-temperature preparations (often referred to as soft chemistry), and most importantly low production costs. This process results in unique features such as the possibility to control the physico-chemical properties of the end product through several parameters [39].

There are two types of sol-gel methods, namely non-hydrolytic and hydrolytic methods. The non-hydrolytic method is named accordingly since water is not generated during the synthesis. There have been many syntheses of oxides involving precursors such as chlorides, alkoxides, acetylacetonates as complexing agents, with oxygen donors such as alkoxides, ethers, alcohols, aldehydes and ketones [40]. The hydrolytic synthesis of MMOs will be the focus of this discussion. Compared to the non-hydrolytic method, the hydrolytic sol-gel

process involves the *in-situ* generation of water, through the hydrolysis and condensation of metal alkoxide precursors. Moreover, metal acetylacetone can also be used [41]. The sol can also be referred to as a colloidal suspension [38], and the gel, on the other hand, is simply a non-fluid 3D network that extends through a fluid phase. The gels can be grouped into four types; ordered lamellar gels, covalent polymer networks, a network of physically aggregated polymers and also disordered particulate gels [38].

There are five major steps involved in the sol-gel synthesis of MMO materials. (1) The first step involves the synthesis of the "sol" utilising the hydrolysis and partial condensation of alkoxides. (2) Thereafter the "gel" forms via polycondensation to form the metal-oxo-metal or metal-hydroxy-metal bonds. (3) During the ageing stage, condensation continues within the gel networks, which sometimes causes it to shrink and hence the solvent is expelled. (4) When drying the sample, a dense "xerogel" is formed via a collapse of the porous network [39]. (5) Finally, during the calcination stage which degrades the surface, M-OH bonds are degraded forming the MMO. Different parameters can easily control these stages. These parameters include: (1) the concentration and type of precursor; (2) the nature of the solvent; (3) the pH of the solution; (4) additives including catalysts, surfactants, and/or other structure-directing agents; (5) pre-and post-heat treatments of the materials and (6) the ageing time [39].

There are a few key processes to consider during the sol-gel process. During the gelation step, where hydrolysis takes place, a nucleophilic substitution reaction is hypothesised. This results in the replacement of an alkoxy group of the metal precursor, with a hydroxyl group. The most common precursor used in the sol-gel process is an alkoxyl metal, $M_x(OR)_y$, precursor. The nucleophilic addition of water is then followed by a proton transfer which ultimately results in the OH group becoming a better leaving group. During the hydrolysis stage, a polycondensation reaction occurs simultaneously. This allows for the following reactions to occur; the hydrolysed alkoxide molecule can either react with another OH group, eliminating water, or react with an alkoxy group resulting in an alcohol molecule [39]. During the hydrolysis and polycondensation processes, small clusters form that bind to each other to form a single 3D polymeric network, which is referred to as the gel.

The resulting gel is then subjected to a few heat treatments, where it is aged, dried and ultimately calcined to obtain the required metal oxide material. During the drying stage at

approximately 100 °C, the water and the most common solvent used, alcohol, is desorbed. This results in the formation of a primitive porous backbone. The product of the uncontrolled drying stage is called a xerogel, and if a structure-directing agent is not present, a disordered porous network will be the result [39].

Originally, early transition metals such as titanium (Ti) and zirconium (Zr) and *p*-block metals such as aluminium (Al) and silicon (Si) were used to form alkoxides. However, a larger number of alkoxides can be obtained by the anodic dissolution of the metal precursor in alcohol. This is an electrochemical process where metal dissolves from the anode into the bulk electrolyte solution. Gases are also released from the cathode during this reaction [42]. It is therefore important to use alcohol in the solvent system for the synthesis of the sol-gel intermediate, and ultimately the catalyst [38]. As mentioned above, many factors may influence the sol-gel synthesis. Another example is the electronegativity difference between the oxygen and the metal, which might affect the ionic character of the M-O bond.

A very important factor to consider when using the sol-gel synthesis is the heat treatment of the sol or gel. The rate of evaporation during gel formation can have an impact on the structure. Not only this, further heat treating the material when removing the surface hydroxyl groups to form a crystalline product, may also have an influence [38]. When the gel is formed, and the solvent has to be removed to produce the network, a few factors have to be considered. When the movement of the solvent through the gel results in capillary forces, it might cause the network to collapse. This can be overcome by ageing the materials for a long time before drying takes place. Furthermore, some densification is possible due to the expulsion of the sol from within the gel. This uncontrolled drying forms xerogels which often contains large amounts of small pores, resulting in a larger surface area. Moreover, the presence of a structure-directing agent is necessary to avoid disordered pores [38]. One of the most used methods for templating sol-gel materials is the use of the evaporation-induced self-assembly (EISA) method.

The EISA method can be used to introduce ordered mesoporosity into bulk or thin-film metal oxide materials. This method involves a mixture of water, ethanol and a metal alkoxide, metal chloride or metal nitrates with a structure-directing agent such as a block copolymer. As compared to simple sol-gel condensation, the EISA method relies on slow evaporation of the solvent to form a mesophase. The inorganic precursor accumulates around the formed

liquid-crystal template, and this results in a well-ordered mesostructure in the resulting metal oxide [38].

1.1.1.5 Evaporation-induced self-assembly

The evaporation-induced self-assembly (EISA) method can be used to prepare thin films that have many applications in molecule detection, separation, environmental sciences, medicine, catalysis, optics, *etc*. There are a few parameters that may influence the self-assembly process. They can be divided into two categories; the chemical parameters which influence the quantities of surfactant and inorganic precursors and the sol-gel hydrolysis condensation reactions [43]. Then secondly, the processing conditions that influence the diffusion of volatile ethanol, water and hydrochloric acid (HCl) molecules, or to form the thin film.

To form reproducible mesoporous organised thin films which are always homogeneous and transparent, there are three main factors to consider. Firstly, it is a prerequisite that the solvent wets the substrate completely and that it is volatile enough. Secondly, the nanostructures that formed have pore and wall dimensions in the range of 1 – 10 nm. It is therefore important to ensure that the dimensions of the inorganic entities that stabilise the solution not exceed an order of magnitude of the dimensions of the pores and walls. Also, the organisation is governed by the interaction between the surfactant head groups and the inorganic precursors [44]. Another factor is that the nature and density of the chemical group present at the surface of the inorganic precursor must be known and be controlled. The last factor to consider is the relative amounts of organic and inorganic components. It must be fixed to ensure that the networks remain stable in the intermediate hybrid state as well as after the removal of the template [43, 45].

Two main methods have been proposed to describe the hybrid nano-organisation when using ionic surfactants. There is the liquid crystal templating (LCT) mechanism, where the inorganic precursors condense around a stabilised surface mesophase. Secondly, there is the cooperative self-assembly (CSA) mechanism where the surfactant and the inorganic precursor combine in the first stage to form a hybrid intermediate entity which behaves as individual surfactant species or building blocks of the hybrid structure [43].

The mesostructured metal oxide phases that exist in these materials strongly depend on a few factors. These include: 1) the degree of charge-matching at the organic-inorganic interface; 2)

the interaction of metal precursor with the organic surfactant heads; 3) the flexibility of the metal-oxygen-metal bond angles; 4) and the occurrence of redox reactions in the walls of the oxide [45].

1.1.2 Multicomponent mesoporous metal oxide materials

The most commonly used MMOs only contain one metal. These include materials such as TiO_2, ZrO_2, CeO_2, and Co_3O_4 *etc*. However, mixed metal oxide materials have also been reported. For example, Mo-V-Sb-Nb oxides are reactive and selective for the oxidation of propane to acrylic acid, it is also a well-known catalyst for propane ammoxidation [45–47]. Other mixed metal oxide materials included TiO_2-PO_4 [48], ZrO_2-PO_4 [49], Zr-Ti and Zr-W oxides [50], have also been reported. These materials can be synthesised using one of the several available routes; however, a general synthetic method remains a challenge due to the dissimilar condensation kinetics and the chemistry of different metal precursors.

This often leads to undesirable macro-scale phase separations that disrupt the co-assembly process, especially when synthesising multicomponent MMOs [35]. Fan and co-workers [35] have described a different method for the synthesis of multicomponent mesoporous metal oxides. The synthesis includes the use of acetic- and/or hydrochloric acid. The acetic acid acts as a complexing agent which modifies the condensation kinetics of the metal precursor, including metal alkoxides. The addition of acetylacetone can achieve the same. Zhang *et al*., [51] showed that during the synthesis of a multicomponent MMO using Ti, the addition of acetylacetone acts as a complexing agent and inhibits the hydrolysis rate of the titanium source. This prevents the rapid formation of precipitates which favours the formation of mesoporous networks.

With the controlled addition of strong aqueous acids such as hydrochloric or nitric acid, these acids partially hydrolyse, charge and modify the inorganic precursor to give it a higher affinity towards the hydrophilic block of the block co-polymers being used. These strong acids also act as a charge intermediate between the surfactant and inorganic species, which inhibits condensation of certain metal ions. And finally, using an amphoteric solvent (e.g. ethanol or acetic acid) ensures that all species are present in ionic form.

Lui and co-workers have also reported using the method described above, where they used acetic acid, HCl, ethanol and metal alkoxides as the metal precursor [36]. This method is also

known as the AcHE method, where the acetate ligands bind to the metal cores of the alkoxides in a bidentate fashion forming stable, nanosized metal-oxo-acetate clusters. These clusters act as building blocks and can co-assemble with organic amphiphilic block co-polymers into ordered mesostructures during the evaporation of the volatile solvent [36].

1.1.3 Supporting nanoparticles on mesoporous metal oxides

The use of metal nanoparticles (MNPs) for catalysis has attracted lots of attention. They are mostly used in the catalysis, electrical and optical industries. The downside of the MNPs is that the performance relies on the size, shape, crystal structure as well as textural parameters. Another disadvantage of these nanoparticles is that they tend to aggregate and agglomerate if they are not supported. MNPs can be supported onto several supports; these include porous materials such as alumina, zeolites and mesoporous solids [52]. The strength of the interaction of the nanoparticles and the support is crucial and can be controlled. A strong interaction favours high stability of the MNPs, but it may change their intrinsic catalytic properties. On the other hand, weak interactions favour the stability of the intrinsic properties but may lead to leaching of the MNPs as well as agglomeration during the catalytic process [52].

Oxides, especially MMOs [53], are among the support materials being used to support nanoparticles [54–58]. Not only will the support material protect the nanoparticles from aggregation and agglomeration, but it also enhances the catalytic activity of the nanoparticles through a synergistic effect. This is ascribed to an increase in the acid/base redox sites, as well as the desired metal/metal-oxide interfaces. The synthesis of metal oxides having metal nanoparticles within inorganic matrices possessing a pore network has become a popular subject of catalyst research and development [59]. The synthesis of these types of catalysts leads to high surface area materials where the shape-selective behaviour of the porous materials is combined with the catalytic performance of metal nanoparticles. Moreover, if the nanoparticles are uniform in size and shape, this may improve the selectivity of the reactions [59].

There are a few methods described in the literature for the preparation of bifunctional metal nanoparticle-loaded porous catalysts. The ion exchange of transition- or noble metal ions into zeolites followed by reduction is an example of such a method [59]. Initially, metal atoms are formed adjacent to the ion exchange position in the framework, where the atoms form

clusters, and as long as the clusters are smaller than the pores, these clusters can be encapsulated into the pores [59]. However, one disadvantage is the uniformity of the particle size. If the particles are not uniform in size, this might cause some of the particles to be formed inside the pores, and others on the outer surface. This might lead to reduced activity. Other methods for the preparation of supported MNPs in porous materials include wet preparation techniques such as impregnation [52]. However, these techniques rarely result in the formation of uniform distribution of the MNPs [52]. To overcome this, one can first prepare the MNP with a uniform shape and a narrow size distribution and then use the particles in the synthesis of the mesoporous materials [59]. Therefore, the supporting takes place *in situ*.

These metal nanoparticle metal oxide hybrids can be synthesised in two different ways. Firstly, the MNPs can be loaded onto the solid support material (usually MMO materials), or the nanoparticles and MMOs are formed at the same time. Although the former preparation method is mostly used for industrial-scale synthesis, it lacks structural and/or compositional control over the MMO supports. Not only that, the complex surface chemistry and porous networks of the MMOs might limit the diffusion of metal species during synthesis and ultimately leading to non-uniform distribution of MNPs. Therefore, it is better to use the latter method, where the nanoparticles and MMO supports are generated simultaneously. This method is a simple, one-pot process [36, 60]. However, some disadvantages, such as the challenge of dissimilar condensation/growth kinetics and chemistry of the nanoparticles and metal oxide precursors, may arise. This might lead to macro-scale phase separation that disrupts the co-assembly process or induces aggregation of the MNPs [36].

1.1.4 Application of mesoporous metal oxides as catalysts in oxidation reactions

Mesoporous metal oxide catalysts have been employed in numerous applications in recent years. These applications included oxygen evolution catalysis [61], photocatalytic reactions [62–64], methane conversion [65], esterification of levulinic acid [66], and numerous oxidation reactions.

This chapter will focus on oxidation reactions. Mesoporous metal oxide catalysts have been used for several oxidation reactions. These oxidation reactions include oxidation of hydrocarbons [7], CO [3, 67–69], benzyl alcohol [70], methane [71, 72], glycerol [73], and styrene [74].

Many studies focus on the oxidation of CO, in particularly low-temperature CO oxidation as a model reaction and for the use of air cleaning. The activation of oxygen molecules plays a very important role in the oxidation of CO [75]. It has been shown that supported gold nanoparticles on a solid support adsorbs CO molecules onto the catalyst effectively; however, these nanoparticles are not able to strongly adsorb and activate oxygen molecules, which is a crucial step in CO oxidation. It is therefore important to use an oxide as a support material, especially oxides with strong redox properties [2]. These include TiO_2 [76] Fe_2O_3, CeO_2 [3, 77], and ZrO_2 [68], supports. These can provide oxygen atoms during the oxidation reaction and improve the oxidation of CO [3]. Recently, it was also shown that MnO_x-CeO_2 catalysts exhibit multiple redox states and high oxygen storage capacity [7]. For ZrO_2 materials, it is known that anionic vacancies in the material lead to better oxygen mobility, resulting in a useful oxidation catalyst, even with lower surface areas as compared to Al_2O_3 and TiO_2 materials.

Moreover, it has been shown that ZrO_2 catalysts, impregnated with transition metals such as Co, Mn, Fe, Cu and Ni give excellent CO and soot oxidation catalysts [68]. This showed that the impregnation of ZrO_2 with Co and Mn resulted in better catalysts compared to the impregnation with Fe, Ni and Cu. The Co and Mn impregnated ZrO_2 showed activity around 80 °C, compared to the others, which only started showing activity above 100 °C. Another catalyst containing Ce and Mn ($Mn_{0.5}Ce_{0.5}O_x$) was also able to oxidise CO. The oxidation took place at 90 °C and gave a conversion of 100%. Moreover, this catalyst was able to oxidise the CO at room temperature (with a conversion of 19%). This activity is attributed to the abundant superoxide species that are formed on the surface of the catalyst [7]. Yen *et al*., [2] showed that using bimetallic supported nanoparticles such as Au:Ag in a ratio of 3:1 on a MCM-41 silica support gives good activity in the oxidation of CO. A conversion of 10% was achieved even at a temperature as low as -63.15 °C. The long-term stability of a similar catalyst (Au-Ag ratio of 8:1) also showed good activity [3]. After 1-year, comparable activity was observed. In another study, where Au-Ag bimetallic nanoparticles were supported onto a CeO_2 metal oxide, catalytic activity for the oxidation of CO was shown. Moreover, a catalyst with an Au-Ag ratio of 1:1 gave higher activity compared to the monometallic catalyst and other bimetallic catalysts with different ratios (9:1 and 7:3 Au-Ag) [3].

Another major application of MMOs is the oxidation of hydrocarbons. This includes the oxidation of styrene [74], methane [71, 72], glycerol [73], cyclohexane [7], and benzyl

alcohol [70] just to mention a few. Highly ordered mesoporous Co-Al catalysts have been used for the epoxidation of styrene, and it was shown that a synergistic effect occurred between the Co^{2+} ions coordinated to the Al(III) in the catalyst. The catalyst showed excellent activity in the epoxidation of styrene with a conversion of 75.8% with a selectivity of 56.6% towards styrene oxide. This catalyst also showed good stability and recyclability properties [74].

A well-known application in catalysis is the production of synthesis gas. This can be achieved by the oxidation of methane and employing a ZrO_2 catalyst with the incorporation of praseodymium (Pr). The use of Zr enhances the oxygen mobility of the Pr-Zr catalyst by effective enhancing the oxidation properties. Moreover, high selectivity towards CO and H_2 was achieved with a high methane conversion [71, 72]. Another example is the oxidation of glycerol, where the gold catalysts play an important role in the activity, but also the nature of the support. It was shown that bimetallic Cu/Au catalysts were more active compared to the monometallic catalysts under the same reaction conditions [73]. Furthermore, the turn-over-frequency (TOF) of the Cu/Au supported on ZrO_2 was the highest; however, a better selectivity for glyceric acid (2,3-dihydroxypropanoic acid) was achieved when the Cu/Au-$CeZrO_2$ (with a 1:1 ratio of Ce:Zr) was used [73]. This clearly shows that the support, as well as the supported catalysts, plays a major role in the activity and selectivity of the catalyst.

Catalysts such as Mn/CeO_2 are used for the oxidation of cyclohexane. It was shown that $Mn_{0.5}Ce_{0.5}O_x$ were able to oxidise cyclohexane at 100 °C, giving moderate conversion rates of approximately 6.5%. Although the conversion may not seem that high, this catalyst gave a high selectivity (95%) for cyclohexanone (also known as KA oil). Moreover, the conversion occurs at relatively low temperatures of around 100 °C. It was also found that the oxidation of cyclohexane did not proceed when CeO_2, MnO_x or a mixture of both, was used. This confirms the synergistic effect of the Mn and Ce species in the hybrid catalyst $Mn_{0.5}Ce_{0.5}O_x$. Another important reaction is the oxidation of benzyl alcohol to benzaldehyde. This oxidation reaction can be achieved by gold supported onto a TiO_2 catalyst. The reaction took place in the absence of a solvent. It was shown that the conversion increases with an increase in the gold loading on the TiO_2 catalyst, however, the selectivity towards benzaldehyde decreases [70].

For all the reactions mentioned above, a conventional catalyst evaluation approach was followed, whereby the catalysts are evaluated individually. This process can be time-consuming, and only a few catalysts can be successfully evaluated. Alternatively, one can use a high-throughput and/or combinatorial approach. This involves the massively parallel synthesis of the catalysts and the screening thereof. The combinatorial approach [78] is being used in many fields including pharmaceutical drug discovery [79], natural product synthesis [80], chemical biology [81, 82], catalyst discovery [79, 83–87], and materials science [88]. To use the combinatorial approach, a combinatorial synthesis method is needed to generate libraries. These include solid- and solution-phase synthesis including parallel synthesis [83, 89, 90], split-and-pool techniques [79, 82, 91–93], and encoding with deconvolution approaches [79, 84].

1.2 High-throughput approach to catalysis

The conventional method to produce, assess and validate catalysts or catalytic reactions, is by performing the synthesis and characterisation of the catalyst/sample individually, which can be a tedious and time-consuming approach. It can be said that the catalyst discovery and optimisation are done using a sequential method. Furthermore, the limitations of the method are often not mentioned, and only the best results and highest yields are presented. Realistically, the syntheses, applications and results are often far more complex than presented, and the limitations are endless [94]. High-throughput, combinatorial and miniaturisation techniques are therefore being developed as methods for catalyst discovery.

The exploration for catalysts has recently been growing, and for this reason, many researchers are exploring alternative methods for the synthesis and evaluation of new catalysts. High-throughput strategies have been used to explore catalysis in a fast way. The terms high-throughput refer to an automated parallel or rapid sequential synthesis or evaluation of materials [95]. The combinatorial approach is one example of a high-throughput method, where several different catalysts, reagents, or entities are evaluated simultaneously, using a high-throughput method. This approach generally involves the creation of a library containing several materials, and these materials are then screened for a specific property of interest, using a high-throughput process. The data is then processed to identify the most promising material in the library. This is referred to as a “hit”. Thereafter, the identified hit is further characterised by using general batch experiments [96].

The use of combinatorial chemistry is mostly applied in the pharmaceutical and biotechnology industries, where it is mostly used for drug discovery and the development of new lead structures [97]. This is an appealing technique that can also be applied to modern-day chemistry for the synthesis and discovery of solid-state materials. It is, therefore, being applied in the catalysis field where homogeneous and heterogeneous catalysts can be synthesised and discovered rapidly. Conventional methods for the synthesis and discovery of heterogeneous catalysts involves tedious and lengthy procedures. These procedures are often based on trial-and-error processes [98]. Using the combinatorial approach, one can synthesise and test a large number of catalysts simultaneously, which shortens the discovery process dramatically [99]. High-throughput screening has been applied in the fields of luminescence [86, 100], magnetoresistivity [101], ferroelectric/dielectric materials [102], and also solid-state catalysis [98].

A typical process cycle is followed when using high-throughput methods for the discovery of new materials. The first stage involves the identification of a group of related materials with certain variations. Moreover, these studies are performed based on two different objectives; discovery of new materials and/or optimisation of existing materials. The next stage is material preparation, and this includes physical and instrumental based deposition and chemical-based synthesis. After the materials have been synthesised, they are subjected to the high-throughput screening process. The screening process should be rapid and accurate. It is, therefore, important to validate the screening process. This will ensure that the results obtained can be reported with reliability. Finally, the data obtained is analysed, and the results can either be used as a final output or to give additional feedback [95].

The design and discovery of catalysts can be a complicated process. In the discovery process, when considering ten elements at 25 different concentrations, the possible combinations that can be achieved reaches more than 38 million [103]. When considering the different preparation methods and reaction conditions that a given catalyst may be subjected to, the number of combinations increases even more. Therefore, high-throughput experimentation in the discovery of catalysts is imperative. High-throughput screening of heterogeneous catalysis is often frowned upon since data collection is not done using the conventional reductionist approach (one-at-a-time) or Edisonian approach (trail-and-error). Therefore the results obtained are thought to be of lower quality [103]. However, as combinatorial chemistry became more popular, better experimental methodologies were developed to give

quantitative data which are comparable to the traditional single reaction studies. One of the drawbacks of combinatorial methods is the analysis and characterisation of the properties of the materials. This is due to the very small amount of each material that is synthesised. The materials are miniaturised to evaluate more targets at once. This makes it extremely difficult to characterise and analyse the materials [97].

1.2.1 High-throughput and/or combinatorial heterogeneous catalysis

1.2.1.1 Early approaches to high-throughput heterogeneous catalysis

Using conventional methods for the assessment of catalytic activity can be problematic. This is due to the unambiguous detection of a specific product on a small catalyst site. When multiple catalysts in a library are assessed, it becomes more difficult [98]. The first screening approach was done by Moates *et al.* in 1996 [104]. The screening was done by utilising an IR camera, and the hits were identified by the change in temperature when the reaction occurred. One of the first reported high-throughput methods for the screening of heterogeneous catalysts made use of a reactor that could accommodate 16 catalyst pellets, and the reaction was evaluated using infrared thermography. The technique uses an IR (infrared) camera for the detection of a temperature change in the pellets once the reaction occurred on the catalysts.

The system was used to test the activity of metal catalysts for the oxidation of H_2. An active catalyst would produce an exothermic reaction which was captured and recorded by the IR camera. Using a temperature change, they could determine the activity of 16 different metal catalysts on the pellets [103, 104]. However, the drawback of this technique is that no information regarding the formation of reaction products could be obtained. Another technique involves laser-induced resonance-enhanced multiphoton ionisation, in combination with Time-of-flight mass spectrometry (TOF-MS) from the conversion of cyclohexane to benzene by dehydrogenation [98]. Unfortunately, no quantitative data was given.

In 1998, Maier and co-workers developed a reactor where the libraries of materials could directly be synthesised, and the components could be identified automatically using X-ray microdiffraction. The volume of the reactor used could accommodate volumes of microliters, which made it possible to miniaturise the experiments [97]. The reactor had 100 chambers on an area of approximately 4 cm^2 with a silicon wafer at the bottom. The reactor was made

from Teflon and steel, both having the same number of holes. The reaction volumes used were approximately two μL, which were pipetted manually or by a robot. This made the theoretical amounts obtainable between 50 and 150 μg [97]. This technique was used to synthesise crystalline products which could be detected and identified by using X-ray microdiffraction.

The approaches discussed above makes mention of the synthesis and screening of only a few catalysts (no more than 100). However, to ensure that a wide range of catalysts is screened, larger libraries should be considered. This can be achieved by using the split-and-pool or inkjet printing (IJP) approaches, where heterogeneous catalyst discovery can be done on a large scale. The discovery stage involves the identification of hits from a large catalyst library. Therefore, the number of catalysts tested during this stage should be in the order of a few hundred, and the libraries should contain small amounts of different materials [105]. Inkjet printing and the split-and-pool approaches are discussed here. These approaches can be used for the massively parallel synthesis of combinatorial catalyst libraries which are then screened to identify hits.

1.2.1.2 Split-and-pool approach

The synthesis of combinatorial libraries has mostly been used for the massively parallel synthesis of pharmaceutically [79, 91] and biologically relevant compounds, such as peptides [82]. These combinatorial libraries, consisting of several different chemical entities, can be created by an approach known as the split-and-pool approach. The term “split-and-pool” was first described in 1988 [106]. In general, the starting material is divided into several batches which are then treated separately with a different reagent. For example, a number of small polymer beads are divided into equal amounts and placed in vials. A different substrate (e.g., an amino acid) is added to each vial. After the reaction is completed, the beads are washed to remove excess substrate [93]. This is followed by the pooling and mixing of the treated beads, which is then split into more batches (vials) for the second chemical treatment. With this, each portion now contains a mixture of compounds (**Figure 1.4**). This cycle can be repeated for each step of the library creation [79].

A few decades ago, the use of spatially addressable libraries was employed for the combinatorial screening of inorganic materials. This approach used continuous or discrete arrays where the composition and synthetic parameters could be systematically varied.

However, some disadvantages make this approach difficult to be used with heterogeneous catalysts. The disadvantages include that the arrays are limited to a few hundred members, the cost of the equipment is high (especially when lithographic or high-vacuum techniques are used for the synthesis of the arrays), and when using dense arrays, heterogeneous catalysts cannot be incorporated into these arrays [93]. To overcome these issues, researchers resorted to bead libraries, which were initially used for bioorganic combinatorial libraries [93]. These libraries are easy to synthesise and are relatively cheap. This approach is generally done with solid-state polymer resin beads, which are used as supports for the reaction and where the biomolecules are synthesised, for bioorganic combinatorial chemistry [92, 93].

These beads can also be used for the addition of inorganic metal precursors, to form inorganic combinatorial libraries. This was shown by Klein *et al*., [106], where they synthesised approximately 3000 Mo-Bi-Co-Fe-Ni/γ-Al_2O_3 combinatorial libraries using the split-and-pool approach. A similar approach was followed by Ramnarayanan *et al.*, [107], where they deposited inorganic precursors onto the γ-Al_2O_3 beads, and the libraries were created using well-plates and pipettes. One of the libraries were evaluated for the dehydrogenation of methylcyclohexane to toluene as a probe reaction.

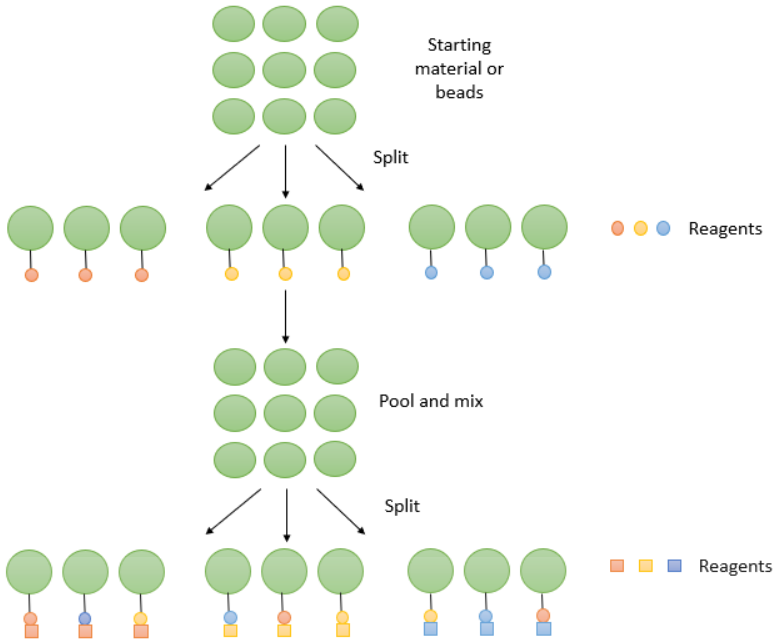

Figure 1.4: Split-and-pool approach to combinatorial library synthesis. In the first stage, the starting materials or the beads are split into equal portions. The portions are then treated with different reagents. The portions are then pooled and mixed and split again into equal portions. The new portions are then treated with different reagents. A mixture of compounds (either catalysts, reagents or products) is the result.

This is a suitable approach for the screening of individual beads for biological activity since this split-and-pool method results in solid-supported libraries with each bead containing only one compound [79]. However, one of the limitations of this approach is the quantity of material that can be supported onto a single bead. Only very small amounts, for example, sub-nanomolar amounts, can be prepared on a bead. Another limitation is the encoding or tagging of these libraries [83]. This was one of the challenges Ramnarayanan *et al.*, faced. A tagging system had to be developed to track the metal salt adsorbed onto the bead, to avoid mixing of components and dissolution of the polymer beads during the adsorption steps [107]. Without a tagging system, there was no control over the bead composition, and they could not identify individual beads without post-synthesis analysis.

These limitations can be overcome by using the IJP approach. No beads are required, and large libraries can be created in a fast way. Moreover, metal oxide materials, including mesoporous metal oxides, can be synthesised using IJP.

1.2.1.3 Inkjet printing catalyst libraries

Inkjet printing (IJP) is a familiar printing technique commonly used to print computer data onto paper as well as date information onto cans and bottles. The interest in this technique has been growing over recent years. It is now being used for many other applications, other than the normal text or image printing onto porous materials such as paper [108]. The IJP technique can operate in two different modes. These modes are known as the continuous or drop-on-demand (DOD) mode [109, 110]. With the continuous mode, the ink is pumped through a nozzle to give a liquid jet resulting in uniformly spaced and sized droplets. With the DOD method, smaller droplet sizes are generated, using pressure waves in a cavity filled with liquid created with a piezoelectric transducer. This is more accurate, and there are fewer restrictions on the properties of the inks that can be used [109].

The DOD method works by generating a droplet of ink through either an acoustic pulse or piezoelectrically. The droplet is generated from a reservoir through a nozzle [111]. This technique can generate picolitre droplets from many different parallel nozzles of micrometre sizes. The droplets can be deposited in specific patterns onto different surfaces and substrates [109]. This technology has been applied in many fields such as electronics [112], life sciences [113, 114] and chemistry [112, 115, 116]. The properties of the inks including the viscosity, surface tension and particle sizes should be well defined for IJP, and also free of agglomeration. For example, the particle sizes should typically be about 100 times smaller than that of the nozzle (20 μm), to prevent clogging of the nozzle [112]. The DOD is the preferred method used for the deposition of ceramic or metallic particle formulations or suspension, to be used as supports for catalytic active materials [109]. For the materials to be printed, the starting phase of the materials should be in liquid or ink form. The inks are then printed onto a specific substrate by making use of thermal or piezoelectric printheads (when the DOD mode is enabled), which can be used as-is, without any further modification.

Even though IJP is well known for the printing of texts and images, this technique has been used for the creation of 3D parts using the free-form production method. Moreover, this technique has been used for the nano-synthesis of inorganic materials; however, one drawback is that only a few inorganic materials can be inkjet printed. This is due to dissimilar condensation kinetics and chemistries of the metal precursors being used [83]. This ultimately leads to difficulties during the IJP of libraries for catalyst discovery. Some of the

materials that have already been inkjet printed include sol-gel materials, polymers, ceramics, as well as nanoparticles [117].

Inkjet printing can be used as a method for the massively parallel nano-synthesis of chemical entities for the high-throughput screening thereof [83, 118–120]. This technique is popular since it can reduce the cost of synthesis by simply using a desktop inkjet printer. Also, complex patterns can be printed on a wide range of substrates, the layer thickness can be adjusted, and the amount of material wasted is decreased. Inkjet printing has been used for many applications, including sensors, electronic devices such as solar cells, transistors and supercapacitors [118].

It can bridge the gap between small- and large-scale synthesis, in chemistry as well as other industries. Using this technique, one can synthesise a large amount of material or parallel material libraries. This technique has been used for the synthesis of indium-zinc tin oxide high field-effect mobility thin-film transistor arrays that can be used for low-cost displays. The DOD mode was used for the IJP of these transistors on Al_2O_3 gate insulators, labelling it as a green technology [115]. They could adjust the thickness of the film and hence the high field-effect mobility. It has already been adapted for the use in catalysis research. Nanoparticle catalysts have been used as inks to inkjet print catalysts. Using IJP, $GaPd_2$ nanoparticles were deposited onto micro-structured foils using the DOD printing method, and these catalysts were investigated for its catalytical performance in the selective hydrogenation of acetylene [121].

Inkjet printing has also been used for the deposition of certain catalysts used as electrochemical energy conversion devices such as polymer electrolyte membrane fuel cells (PEMFCs) [112, 122]. Lesch and co-workers [112] demonstrated that IJP could be used for the synthesis of nitrogen-doped reduced graphene oxide sheets coated with cobalt oxide nanocrystals. These electrocatalysts are mostly used for oxidation-reduction reactions. They also investigated the combination of IJP and photonic curing for the large-scale production of electrocatalysts. It was found that IJP could accurately deposit a formulated catalyst ink onto glassy carbon substrates, using precise catalyst loadings. Stabilisers including polyvinylpyrrolidone and ethyl cellulose were added to the formulations and could be removed by thermal post-processing using an oven.

Moreover, IJP can be used for the deposition of an ink formulation into small cavities, such as microstructure reactors [109]. Alumina films were deposited into microchannels with different geometries and materials. These alumina films or supports were generated from alumina ink which was doped with rhodium. These catalysts were then evaluated for its activity in methane conversion [109]. Inkjet printing has also recently been used for the synthesis of drug-loaded mesoporous silica nanoparticles [123]. Silver nanoparticles have also been synthesised using IJP. For example, these nanoparticles were synthesised on mesoporous silicon using IJP [124]. IJP was also recently used for the synthesis and screening of self-assembled nanoparticles. A polymer solution in DMSO was deposited into a 96-well plate, and 50 suspensions were screened for nanoparticle formation. The nanoparticles were then evaluated for effects on the metabolic activity of lung cancer cells [125]. Gold nanoparticles have also recently been synthesised using this approach. In the study, they combined block copolymer micelles nanolithography with IJP to give gold nanoparticles in the form of microstructures. Droplets of the micelle solution were deposited on surfaces, resulting in circular patterns containing the gold nanoparticles. This study was able to show that gold nanoparticles could be deposited on different surfaces (silicon and nickel-titanium surfaces) using IJP [126].

Metal oxides and mesoporous metal oxides have also recently been synthesised using IJP. The metal oxide and mesoporous metal oxide precursors are deposited onto a substrate, and upon thermal post-processing, these precursors decompose into its respective solid catalysts [112]. These include; SiO_2 [123, 127–130], SnO_2 [131], carbon-based printed Perovskite solar cells, NiO solar cells [132], and TiO_2 [116, 118, 133]. TiO_2 used for photocatalytic application has also been inkjet printed [116–118, 134]. High catalytically active nitrogen-doped reduced graphene oxide supported cobalt oxide nanosheets have been created using IJP. These catalysts, used in fuel cells are employed in oxidation-reduction reactions [112]. Metal oxides, such as NiO, Perovskites and TiO_2 as solar cells have also been inkjet printed [132, 135, 136]. Multicomponent metal oxides have also been inkjet printed for the use as catalysts [83, 96, 127, 130, 137]. Kimmich *et al*., used IJP for the synthesis of mixed Zn and Fe oxides, which were evaluated for water splitting reactions [96]. Another study by Haber *et al*., has also used IJP for the synthesis of multicomponent metal oxides. They synthesised Ni-Fe-Co-Ce containing oxides as oxygen evolution catalysts [137]. A $NiCo_2O_4$ film was also synthesised by IJP using the drop-on-demand approach. The multicomponent films were evaluated for their electrocatalytic activity in a water oxidation reaction [138].

Not only can this technique be used for the synthesis of metal oxide materials, but it can also be used for coating of functional metal oxides. This was recently shown by Maleki *et al.*, [118]. In this study, TiO_2 layers were inkjet printed onto a polymeric substrate in a microfluidic device. The as-synthesised TiO_2 catalysts were evaluated for their activity in the photocatalytic degradation of methylene blue. It was shown that the microreactor used for the study gave an efficient performance, and it was shown that the TiO_2 was stable during long-running reactions.

The IJP techniques have also been used for the synthesis of numerous solar cells. TiO_2 nanoparticles were used in the IJP of TiO_2 films onto FTO (fluorine-doped tin oxide) glass substrates. It was demonstrated that a crack-free film could be achieved by using IJP. These films were used to produce the photoelectrodes for dye-sensitised solar cells (DSSCs) [133]. Mesoporous NiO p-type dye-sensitised solar cells (used as photocathodes) have also been synthesised with IJP. This was achieved by the EISA method using $NiCl_2$ as a precursor and a water/ethanol solvent system to form a sol-gel ink [132]. Moreover, perovskite solar cells can also be infiltrated onto a device using IJP. This was shown by Hashmi *et al.*, [135], where carbon-based solar cells were inkjet infiltrated into a device which was able to show impressive photovoltaic performance.

In another study, it was shown that well-structured patterned silica microdot arrays could be functionalised with different functionalities, including a thiol functionality. This study employed the EISA and IJP techniques. The silica microdot array inks were deposited on a substrate and subsequently calcined to form the mesoporous material. By optimising different parameters in the IJP process, 3D microdot arrays were successfully synthesised with 25 stacked layers to give sensors that could potentially be used in the fields of heavy metal trapping, artificial noses as well as antibody detection in the diagnosis of infections [127]. Another study also employed the EISA and IJP techniques for the synthesis of mesoporous silica microdots. These microdots were used for click reactions which occurred within the mesoporous structures of the microdots. This study used the microdots for fluorescence or electrochemical detections [130]. These inkjet printed silica-based materials are also used as microdot arrays in the detection field.

The biggest advantage of using IJP is that a large number of materials or catalysts can be produced simultaneously. This makes it possible to construct libraries of catalysts to be used

for combinatorial high-throughput screening purposes. McFarland and co-workers reported one of the first combinatorial approaches for the screening of metal oxides in 2002. They used robotics to plate different metal oxide compositions and screen it as water photooxidation catalysts [119, 139]. A few years later in 2005, Woodhouse *et al*., used IJP to construct multicomponent metal oxide catalyst libraries for its evaluation in water photoelectrolysis. Inkjet printing was used to overlap patterns of soluble metal nitrate salts (which decomposes to metal oxides) onto a conductive glass substrate [119].

The ultimate aim in creating catalyst libraries using the combinatorial high-throughput approach is to identify an optimum catalyst formulation from the library. IJP can be used in parallel with a multidimensional group testing method. This allows for the ultrafast exploration of an entire candidate library space. Therefore, one can sequentially analyse the catalytical performance of a certain library, using analytical tools. This was shown by Liu *et al*., [83], where they used an IJP assisted cooperative-assembly (IJP-A) method to synthesise a large library of multicomponent mesoporous metal oxides (e.g. $Mg_{0.1}Ni_{0.1}Mn_{0.06}Cr_{0.1}Cu_{0.07}Fe_{0.1}Co_{0.1}Ti_{1.0}O_w$). This technique can be used to synthesise up to 1 000 000 formulations in one hour using up to eight-component compositions. The libraries were screened for hydrogen evolution in the liquid phase reforming of a formaldehyde-aqueous solution. They demonstrated the use of IJP assisted synthesis of mesoporous oxide materials.

The IJP technique uses a slightly different approach compared to the split-and-pool method. There are no mixing of the libraries after the splitting step. Each library is created on its own, containing a few thousand catalysts. The libraries are then used separately for a reaction and analysed. Thereafter, the libraries are split into smaller libraries, and the process is repeated. This approach is referred to as the deconvolution of catalyst libraries

1.2.1.4 Deconvolution of the libraries to identify hits

The deconvolution technique, also referred to as dereplication, was first described in 1991 by Houghten *et al.*, [79, 140] for the synthesis, screening and deconvolution of peptides. The approach is based on an iterative process, where a large library is screened and thereafter split and re-synthesised into smaller libraries for further screening (**Figure 1.5**). This aim is to fractionate a mixture to ultimately find the most active constituent [79].

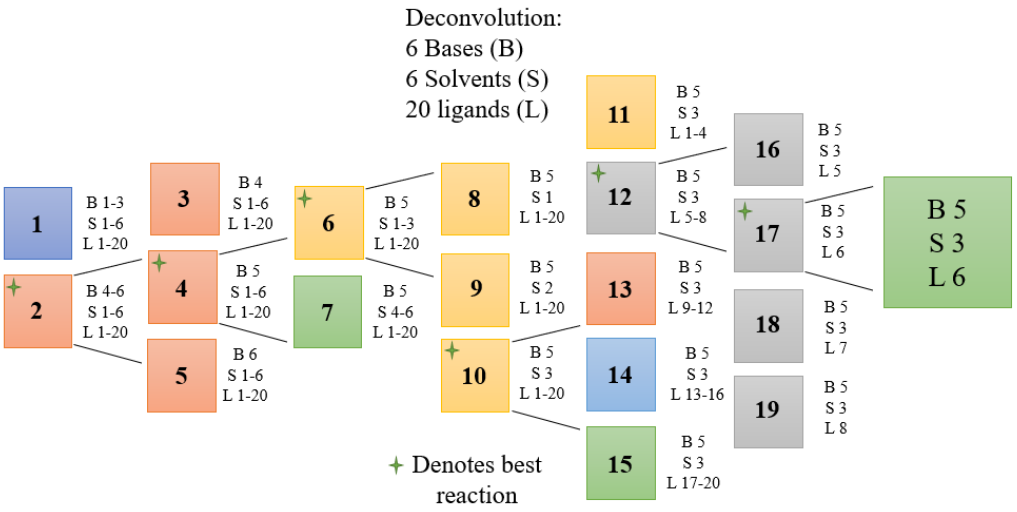

Figure 1.5: Schematic representation of a deconvolution process, where six bases (B), six solvents (S) and 20 ligands (L) are deconvoluted in a homogeneous catalytic reaction. Initially, the bases are deconvoluted, followed by the solvents then finally the ligands. A total of 19 reactions are performed to deconvolute to the best base, solvent and ligand. Conventionally 720 reactions are needed if one parameter is investigated at a time.

For this approach, a library is synthesised using a multistep approach, and the active compound or constituent is identified from a certain amount of pools, following the re-synthesis of the libraries in the subsequent steps. There are a few limitations to this approach. For example, the time and reagents spend in the re-synthesis of the libraries. With the re-synthesis of smaller libraries after the screening, it takes time and more reagents to make up the smaller libraries. However, the biggest limitation is the comparison of the activities of the pooled compounds.

It should be noted that the activity of a given pool or library is a cumulative activity of the entire pool. Therefore, the activity is represented by all the compounds in the pool. Moreover, pools with the same activity may contain less active and more active compounds and selecting the pool with the highest activity for deconvolution, will not always result in the identification of the most active compound. Even though this approach has some limitation, it has been successfully used in the screening of the most active compound from a combinatorial mixture [79]. The limitations become less prevalent if the goal is to only screen for new reactivity or new catalysts. However, when the optimisation of selectivity is

considered, the limitation increases [141]. Nevertheless, this approach has been used for homogeneous catalyst discovery [87, 141].

1.2.2 High-throughput and/or combinatorial homogeneous catalysis

Combinatorial libraries can also be generated for homogeneous catalyst discovery. This involves the synthesis of mixed-compound libraries in solution. Several screening and deconvolution procedures are available to identify hits from the libraries [84]. It is known that homogeneous catalyst discovery is a complex multidimensional problem [87]. For example, many parameters can be optimised during catalyst discovery. These include transition metals, counter ions, precatalysts, ligands, solvents, acid and bases, additives, temperature and pressure as well as the performance of the molecular entity under investigation [78, 87]. Fortunately, homogeneous metal catalysis is tremendously suitable for high-throughput synthesis of the catalyst libraries. Most homogeneous catalysts are prepared via coordination of a metal and a ligand. It is, therefore, relatively straightforward to synthesise these catalyst libraries, since it only requires the mixing of metal precursors and ligands under certain conditions [142].

Catalyst library generation for the high-throughput experimentation of homogeneous catalysis involves the synthesis of the libraries followed by the characterisation and quality control of the synthesised libraries. This is usually done with high-throughput nuclear magnetic resonance (NMR) techniques. The libraries are then screened to obtain information regarding the catalytic properties, for example, the Turn Over Frequency (TOF) also represented by the activity, the selectivity (in the case for enantioselective catalysts) and also Turn Over Number (TON). After screening, the results are compared to the chemical properties to determine the structure and properties of the catalyst [78]. Moreover, using the deconvolution approach, one can screen for different parameters simultaneously.

This approach has recently been used for deconvolution and hit identification of a complex mixture of precatalysts and ligands for the *in situ* generation of homogeneous catalysts [87, 141]. Wolf *et al*. [87] used this approach where the catalysts were screened for the dehydrative Friedel-Crafts reaction. Moreover, the conditions for the monoarylation in the catalytic ortho-C-H arylation of unsubstituted N-(quinoline-8-yl)benzamide were screened [87]. They assumed that the precatalysts and ligands could be screened as mixtures in a batch followed by the deconvolution of the batch after identifying the best reaction. A complex

mixture of boronic acids and bidentate O-ligand were used as precatalysts and ligands, respectively. During the first stage, all the precatalysts and ligands were mixed in each reaction of a block of 25 reactions. Using this approach, they could screen up to four reaction parameters at once, for example, solvents and acid/bases. After identifying the best result (conditions) out of the 25 reactions, those precatalysts and ligands were further deconvoluted with two additional steps, to identify the best precatalyst and ligand. The best reaction was identified through product formation. Some disadvantages and advantages are possible.

False negatives are one of the disadvantages of this approach. This might occur if an active catalyst is taken out of equilibrium or if the catalysts are being poisoned. However, since the reactivity is screened, only a small amount of an active catalyst is required in the mixture, making it feasible. One of the advantages is that more combinations can be tested, and expensive robotics are not required. Moreover, since catalysts are screened from a complex mixture (containing many inhibitors of poisons), the most robust catalyst is selected as the best catalyst [141].

A similar approach was followed by Reetz *et al.* [143], and Ding [144], where chiral catalyst libraries were generated using metal ions and ligands. It is important to create and screen large libraries of chiral catalysts with a large catalyst scope since it is known that no single catalyst is universal to all substrates in enantioselective catalysis. These chiral catalyst libraries were created for asymmetric transformations and consisted of binary ligands for the synergistic effect investigation, as well as metal ions [144]. With this approach, several highly efficient and cost-effective catalyst systems were identified, including Ti(IV), Zn(II), Rh(I) and Ru(II) complexes for asymmetric hetero-Diels-Alder, carbonyl-ene, alkylation and hydrogenation reactions, respectively [144]. This approach was also followed for the synthesis and screening of diastereoselective carbene insertion catalysts. The libraries were generated by chiral ligands and a variety of metal ion salts. The libraries were screened in a 96-well plate for reactivity and selectivity [145, 146].

Another approach to high-throughput combinatorial homogeneous catalysis was demonstrated by the *in situ* generation of Ir and Rh metal complexes with bidentate N-donor ligands, as catalysts. These catalyst libraries were screened for the hydroamination of 2-(2-phenylethynyl) aniline using a well plate and UV-Vis spectroscopy. Hits were identified by the ranking of the catalysts according to the ratio of product to starting material and product

at a specific time [147]. Combinatorial catalysis has also recently been applied to organocatalysis. Bifunctional organocatalyst libraries were generated through dynamic covalent chemistry (DCC) assembly. The catalysts are based on reversible imine chemistry and were evaluated for the Morita-Baylis-Hillmann reaction of enones with aldehydes or N-tosyl imines. The DCC method was used to screen the catalyst libraries, through a one-pot synthesis and *in situ* evaluation of the libraries.

Furthermore, it was shown that these catalysts could be optimised this way as well [148]. A similar study was done by Schaufelberger *et al.* [149], where they used dynamic deconvolution to identify catalyst precursors for C-H activation of imines by using hydroacylation as a model reaction. Metals, acids and directing groups could be screened by the interruption of the catalytic cycle and amplifying the reactive intermediate. The active compound containing the metal and the directing agent could be identified *in situ* using electrospray ionisation mass spectrometry (ESI-MS).

Another technique that has been employed for the identification of hits from a library include high-performance liquid chromatography (HPLC). This method can fraction a relatively large quantity (20 – 100 mg) of a solution-phase library consisting of approximately 25 – 1000 compounds. Portions of the library are collected, and the fraction that shows promising activity is then further purified to obtain a single compound [84, 150].

Combinatorial catalyst library generation and the high-throughput screening thereof can be achieved by employing robotic systems. For example, a liquid handling robot can dispense reagents, catalyst precursors, as well as catalysts (for example, nanoparticle catalysts) into well plates for high-throughput screening [147]. This approach is discussed in Chapter 3. Catalysts can also be prepared by using robotic acoustic liquid handlers such as inkjet printers and the ECHO liquid handler (discussed in Chapter 4)

1.3 The robotics approach to high-throughput chemistry

To a layperson, robotics might seem intimidating, because the term robotics are generally confused with artificial intelligence. However, robotics simply implies a smart device or system that can be automated to do specific tasks. Examples of robotics include liquid handling robots, microfluidic devices and 3D printers, just to mention a few. These systems

can be used for numerous applications including, life sciences (e.g. botany, biology and biochemistry), as well as physical sciences (such as chemistry). This section will mainly focus on the systems that can be used in chemistry.

1.3.1 Liquid handlers

The use of liquid handling robots and automated systems has the potential to improve sciences in academia as well as in the pharmaceutical industry [151–153]. Liquid handling systems are probably the most popular systems being used. These systems are capable of handling liquids with volumes ranging from millilitres to nanolitres, and applications ranging from compound synthesis to dilutions. These systems can either be simple or complex, and the complexity of the system determines the price. Numerous liquid handling robots are available commercially, but Open-Source robots (that allow the user to build it from beginning to end) are becoming more popular. There is a significant difference in the cost of these systems.

1.3.1.1 Commercially available liquid handlers

As mentioned above, commercially available liquid handlers are very expensive and are mostly used in biosciences. For example, in the field of protein crystallography, liquid handling robots are often used to screen as a specific drug target against numerous protein crystals. The Mosquito® HTS liquid handler (by TTP Lactech) makes protein crystallography screening much faster and more efficient. This instrument has a pipetting range of 25 nL up to 1.2 µL. This is especially useful for automated miniaturised chemistry, which can be used for drug discovery or natural product synthesis. This miniaturised, automated platform could enable high-throughput experimentation for synthetic route scouting to identify conditions for a specific reaction. This was shown by Santanilla *et al*., [154] where the Mosquito® HTS liquid handler was used for a test case using Pd-catalysed C-O, C-N and C-C cross-coupling reactions. In a matter of a day, 1500 experiments were carried out using as little as 0.02 mg of material per reaction.

The Hamilton liquid handler is suitable for numerous applications ranging from agriculture, forensic, protein, pharmaceutical, and industrial sciences. Even though this instrument is very popular, it is expensive ranging between £90 000 and £100 000 (more than R2 million based on an exchange rate of 1 GBP = 20.39 ZAR), for the entry-level instrument. Another liquid handler is the Tecan liquid handler and automated system. It is similar to the Hamilton, with

applications in genomics, protein science, analytical chemistry and cell biology. Most liquid handling robots are equipped with pipetting modules for the aspiration and dispensing of the liquids. However, acoustic waves can also be used for liquid handling.

1.3.2 Acoustic liquid handling

The ECHO acoustic liquid handler is an example of a liquid handler which generates small droplets using sound waves. This is a very powerful liquid handling instrument which does not use pipetting modules like regular liquid handlers. The ECHO liquid handler is a revolutionised liquid handler which uses acoustic energy to transfer liquids from a source to a destination which is suspended above the source. Sound waves eject precisely sized droplets from one source to another. The liquid can be transferred to a microplate, microscope slide or any other surface suspended above the source plate. Unlike the conventional liquid handlers, the acoustic liquid handler uses no tips, pin tools, or nozzles. Therefore there is no contact between the instrument and the liquid. This avoids contamination between samples. One disadvantage, however, is that such a liquid handler is very expensive. Despite being expensive, this instrument has been used for numerous high-throughput applications in the life sciences for high-throughput screening and miniaturisation of experiments. For example, it has been used for RNA interference screening [155], for cell culture and drug testing towards anticancer activity [156–159], drug testing which also involves the screening of the chemical libraries (including drug targets) against protein crystals using protein plates [160–162] as well as detection of secretory proteins [163], protein crystallisation [164] and many other biological applications [165–168].

1.3.2.1 Catalytic application of acoustic liquid handlers

This technique has not yet been fully explored for the high-throughput and miniaturisation of catalysis. Recently acoustic liquid handlers have been used for reaction scouting for specific organic reactions. In this study, acoustic droplet ejection (ADE) techniques were used, which involves the touchless nanolitre (nL) volume transfer of reagents for the synthesis of new isoquinoline reactions. A large number of novel compounds were synthesised in a very short time [94]. This technique has also been used for the investigation of free boronic acid building blocks in multicomponent reactions. The acoustic liquid handler was used for the creation of large libraries of diverse and complex boronic acid derivatives [169]. To the best of our knowledge, this technique has not been used for the synthesis of mesoporous metal oxide catalysts.

Most research laboratories have limited funds available to purchase such expensive and high-end equipment. In recent years, affordable commercial low-throughput liquid handlers have emerged; however, they are not extendable by the users and are not capable of performing reactive experiments [170]. However, there are several Open-Source liquid handlers available, which provides features comparable to high-end commercial liquid handlers. The Opentrons and the EvoBot are examples of Open-Source liquid handlers that will be discussed.

1.3.3 Open-Source liquid handling robots

1.3.3.1 The Opentrons

The Opentrons is an affordable Open-Source liquid handling robot, that can accurately dispense 1 µL into a 384-well plate. Apart from that, it is compatible with most tips and pipettes often used in laboratories. The Opentrons can be purchased for $5000 (approximately R82000, using an exchange rate of 1 ZAR = 0.061 US Dollar, 29.10.2020); however, it is Open-Source which means that all the parts and mechanical designs are freely available. The Opentrons can be used for numerous applications including, sample preparation, polymerase chain reaction (PCR), nucleic acid extraction and purification, protein preparation, DNA assembly as well as making dilutions. Although the Opentrons was developed for life science applications, it can be applied in chemistry research as well.

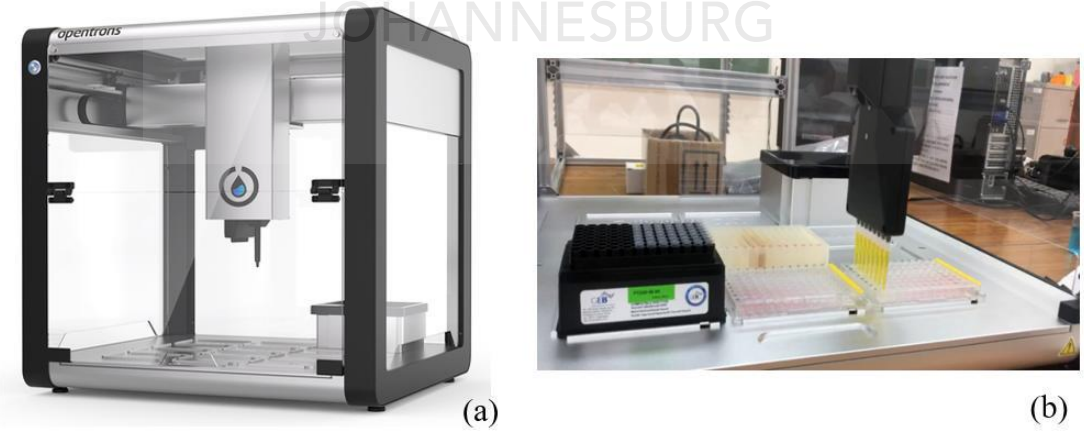

Figure 1.6: (a) Opentrons 2 (OT-2) (photo obtained from the Opentrons website) is the second version of an Open-Source liquid handling robot. (b) The transfer of reagents into a 96-well plate (photo by K. Potgieter)

Even though the Opentrons is a versatile robot, it is not extendable with new modules, for example with a pump or syringe module. This was overcome by the development of the EvoBot.

1.3.3.2 The EvoBot

The EvoBot is a modular Open-Source liquid handling robot that is not only affordable (production cost is estimated to be below R30 000) but can be built at home or in the laboratory (**Figure 1.7**). This robot focuses on research requiring low-throughput experiments; however, it can handle long-lasting experiments as well. The EvoBot's modularity enables the robot to be reconfigured and extended for the use in diverse experiments. One of the main features of the EvoBot is a real-time video that enables the experimenter to interact with the experiment while it is in progress.

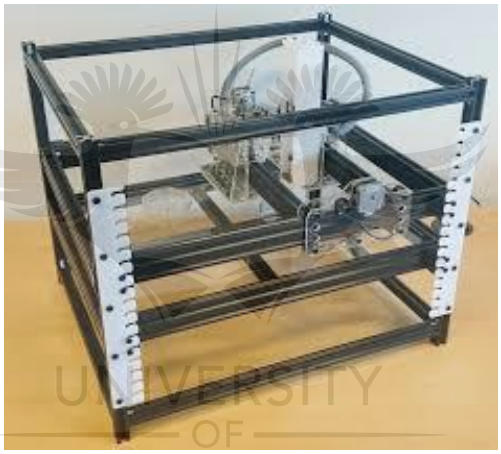

Figure 1.7: The EvoBot liquid handling robot [170].

The design of the EvoBot allows for the components to be printed using 3D printers, or to be laser or water cut from plastics, such as Perspex or POM (polyoxymethylene) materials. The system is controlled with an Open-Source electronic prototyping platform (an Arduino board and Ramps shield). The software of the EvoBot has been developed in Python, and the interpreting commands from the G-code file controls the motion accordingly. However, basic skills or experience with this technology (Arduino and Python) is necessary for the operation of the EvoBot.

The EvoBot can perform general liquid handling experiments by mixing the contents of a reaction vessel and washing or discarding the vessel. It can also aspirate a liquid from one source and dispense it into another or discard the content. It can also empty wells from a plate

and discard the content. The robot is intelligent enough to refill a syringe with the same solution when the syringe runs out of solution. Another application of the EvoBot is to perform serial dilutions for ELISA (enzyme-linked immunosorbent assay) as well as PCR [170]. Moreover, the EvoBot can also perform droplet placement, where drops are placed precisely in two or three dimensions as well as in specific patterns such as circles or rectangles or more complex shapes. The EvoBot has also been used for cell culturing and nurturing in microbiology studies [171].

1.3.3.3 Alternative custom-built liquid handler

Another interesting Open-Source liquid handling robot can be built from LEGO®. This robot was designed for science, technology engineering and mathematics (STEM) education and research. Riedel-Kruse and co-workers [151] used a LEGO® Mindstorms set to develop a LEGO® based pipetting robot that can handle volumes from 1 mL down to sub µL ranges. The robot can be directly built using the LEGO® Education EV3 core set alone. It can also operate on standard labware such as cuvettes and multi-well plates. The robot was successfully tested by elementary, middle and high school students [151].

From the information given above, it can be seen that simple yet powerful liquid handling robots can be built using Open-Source hard- and software. There is, therefore, no need to buy expensive liquid handling robot if Open-Source robots are freely available. Open-Source equipment might soon take over laboratories since it is much cheaper than the commercially available liquid handlers. Apart from that, students and academics get the chance to broaden their expertise and learn more about other fields.

1.4 Conclusion

Even though robotics plays a major role in high-throughput approaches to catalysis, other approaches can also be employed. Using a multidimensional group testing strategy, with a split-and-pool deconvolution approach, the ultra-fast reagent (base, solvent and ligands) optimisation can be achieved. Moreover, it can be seen that by employing a robotic system, catalysts discovery can be achieved in a much faster way. Robotics can be used for the massively parallel synthesis of catalyst libraries which can be evaluated for a specific reaction. It can also be used for the synthesis of complex and diverse small molecules.

High-throughput and/or combinatorial approaches are the future of catalyst discovery.

1.5 References

[1] M.E. Ali, M.M. Rahman, S.M. Sarkar, S.B.A. Hamid, Heterogeneous metal catalysts for oxidation reactions, J. Nanomater. 2014 (2014) 1–23.

[2] C.-W. Yen, M.-L. Lin, A. Wang, S.-A. Chen, J.-M. Chen, C.-Y. Mou, CO Oxidation Catalyzed by Au−Ag Bimetallic Nanoparticles Supported in Mesoporous Silica, J. Phys. Chem. C. 113 (2009) 17831–17839.

[3] N. Sasirekha, P. Sangeetha, Y.-W. Chen, Bimetallic Au–Ag/CeO_2 Catalysts for Preferential Oxidation of CO in Hydrogen-Rich Stream: Effect of Calcination Temperature, J. Phys. Chem. C. 118 (2014) 15226–15233.

[4] F. Rodríguez-Reinoso, The role of carbon materials in heterogeneous catalysis, Carbon. 36 (1998) 159–175.

[5] Y. Gao, Y. Zhang, Y. Zhou, C. Zhang, H. Zhang, S. Zhao, J. Fang, M. Huang, X. Sheng, Synthesis of ordered mesoporous La_2O_3-ZrO_2 composites with encapsulated Pt NPs and the effect of La-dopping on catalytic activity, J. Colloid Interface Sci. 503 (2017) 178–185.

[6] X. Liu, P. Ning, L. Xu, Q. Liu, Z. Song, Q. Zhang, Low-temperature catalytic oxidation of CO over highly active mesoporous Pd/CeO_2-ZrO_2-Al_2O_3 catalyst, RSC Adv. 6 (2016) 41181–41188.

[7] P. Zhang, H. Lu, Y. Zhou, L. Zhang, Z. Wu, S. Yang, H. Shi, Q. Zhu, Y. Chen, S. Dai, Mesoporous $MnCeO_x$ solid solutions for low temperature and selective oxidation of hydrocarbons, Nat. Commun. 6 (2015) 1–10.

[8] D.J. Kim, B.C. Dunn, P. Cole, G. Turpin, R.D. Ernst, R.J. Pugmire, M. Kang, J.M. Kim, E.M. Eyring, Enhancement in the reducibility of cobalt oxides on a mesoporous silica supported cobalt catalyst, Chem. Commun. 11 (2005) 1462–1464.

[9] A. Kumar, V.P. Kumar, B.P. Kumar, V. Vishwanathan, K.V.R. Chary, Vapor phase oxidation of benzyl alcohol over gold nanoparticles supported on mesoporous TiO2, Catal. Letters. 144 (2014) 1450–1459.

[10] C. Colella, A.F. Gualtieri, Cronstedt's zeolite, Microporous Mesoporous Mater. 105 (2007) 213–221.

[11] N.E.R. Zimmermann, M. Haranczyk, History and Utility of Zeolite Framework-Type Discovery from a Data-Science Perspective, Cryst. Growth Des. 16 (2016) 3043–3048.

[12] Y. Ni, A. Sun, X. Wu, G. Hai, J. Hu, T. Li, G. Li, Facile synthesis of hierarchical nanocrystalline ZSM-5 zeolite under mild conditions and its catalytic performance, J. Colloid Interface Sci. 361 (2011) 521–526.

[13] N. Pal, A. Bhaumik, Soft templating strategies for the synthesis of mesoporous materials: Inorganic, organic-inorganic hybrid and purely organic solids, Adv. Colloid Interface Sci. 189 (2013) 21–41.

[14] P. Behrens, Mesoporous inorganic solids, Adv. Mater. 5 (1993) 127–132.

[15] Y. Ren, Z. Ma, P.G. Bruce, Ordered mesoporous metal oxides: synthesis and applications, Chem. Soc. Rev. 41 (2012) 4909–4927.

[16] F. Schüth, Non-siliceous mesostructured and mesoporous materials, Chem. Mater. 13 (2001) 3184–3195.

[17] Y. Xie, D. Kocaefe, C. Chen, Y. Kocaefe, Review of Research on Template Methods in Preparation of Nanomaterials, J. Nanomater. 2016 (2016).

[18] H. Masuda, K. Fukuda, Ordered metal nanohole arrays made by a two-step replication of honeycomb structures of anodic alumina, Science. 268 (1995) 1466–1468.

[19] A.E.H. Machado, K.A. Borges, T.A. Silva, L.M. Santos, M.F. Borges, W.A. Machado, B.P. Caixeta, S.M. Oliveira, A.G. Trovó, A.O.T. Patrocínio, Applications of Mesoporous Ordered Semiconductor Materials — Case Study of TiO_2, in: Sol. Radiat. Appl., 2015: pp. 87–118.

[20] P. Van Der Voort, C. Vercaemst, D. Schaubroeck, F. Verpoort, Ordered mesoporous materials at the beginning of the third millennium: new strategies to create hybrid and non-siliceous variants, Phys. Chem. Chem. Phys. 10 (2008) 347–360.

[21] X. Deng, K. Chen, H. Tüysüz, Protocol for the nanocasting method: Preparation of ordered mesoporous metal oxides, Chem. Mater. 29 (2017) 40–52.

[22] T.-W. Kim, P.-W. Chung, V.S.-Y. Lin, Facile Synthesis of Monodisperse Spherical MCM-48 Mesoporous Silica Nanoparticles with Controlled Particle Size, Chem. Mater. 22 (2010) 5093–5104.

[23] J. Li, H. Ren, X. Zou, K. Cai, N. Zhao, G. Zhu, Hard-template synthesis of micro-mesoporous organic frameworks with controlled hierarchicity, Chem. Commun. 54 (2018) 8335–8338.

[24] H. Wang, H.Y. Jeong, M. Imura, L. Wang, L. Radhakrishnan, N. Fujita, T. Castle, O. Terasaki, Y. Yamauchi, Shape- and Size-Controlled Synthesis in Hard Templates: Sophisticated Chemical Reduction for Mesoporous Monocrystalline Platinum Nanoparticles, J. Am. Chem. Soc. 133 (2011) 14526–14529.

[25] L. Zhang, L. Jin, B. Liu, J. He, Templated Growth of Crystalline Mesoporous Materials: From Soft/Hard Templates to Colloidal Templates, Front. Chem. 7 (2019) 22.

[26] K. Zhu, B. Yue, W. Zhou, H. He, Preparation of three-dimensional chromium oxide porous single crystals templated by SBA-15, Chem. Commun. 1 (2003) 98–99.

[27] M. Marcos-Hernández, D. Villagrán, 11 - Mesoporous Composite Nanomaterials for Dye Removal and Other Applications, in: G.Z. Kyzas, A.C.B.T.-C.N. Mitropoulos (Eds.), Micro Nano Technol., Elsevier, 2019: pp. 265–293.

[28] E. Ramasamy, C. Jo, A. Anthonysamy, I. Jeong, J.K. Kim, J. Lee, Soft-template simple synthesis of ordered mesoporous titanium nitride-carbon nanocomposite for high performance dye-sensitized solar cell counter electrodes, Chem. Mater. 24 (2012) 1575–1582.

[29] Y. Cui, X. Lian, L. Xu, M. Chen, B. Yang, C. Wu, W. Li, B. Huang, X. Hu, Designing and Fabricating Ordered Mesoporous Metal Oxides for CO_2 Catalytic Conversion: A Review and Prospect, Materials. 12 (2019) 276.

[30] U. Ciesla, D. Demuth, R. Leon, P. Petroff, G. Stucky, K. Unger, F. Schüth, Surfactant controlled preparation of mesostructured transition-metal oxide compounds, J. Chem. Soc. Chem. Commun. 11 (1994) 1387–1388.

[31] M.F. Islam, E. Rojas, D.M. Bergey, A.T. Johnson, A.G. Yodh, High weight fraction surfactant solubilization of single-wall carbon nanotubes in water, Nano Lett. 3 (2003) 269–273.

[32] D. Zhao, Y. Peidong, H. Qisheng, C. Bradley F, S. Galen D, Topological construction of mesoporous materials, Curr. Opin. Solid State Mater. Sci. 3 (1998) 111–121.

[33] H.P. Lin, C.Y. Mou, Structural and morphological control of cationic surfactant-templated mesoporous silica, Acc. Chem. Res. 35 (2002) 927–935.

[34] S. Cheng, Y. Wei, Q. Feng, K.Y. Qiu, J. Bin Pang, S.A. Jansen, R. Yin, K. Ong, Facile synthesis of mesoporous gold-silica nanocomposite materials via sol-gel process with nonsurfactant templates, Chem. Mater. 15 (2003) 1560–1566.

[35] J. Fan, S.W. Boettcher, G.D. Stucky, Nanoparticle assembly of ordered multicomponent mesostructured metal oxides via a versatile sol-gel process, Chem. Mater. 18 (2006) 639.

[36] J. Liu, S. Zou, S. Li, X. Liao, Y. Hong, L. Xiao, J. Fan, A general synthesis of mesoporous metal oxides with well-dispersed metal nanoparticles via a versatile sol-gel process, J. Mater. Chem. A. 1 (2013) 4038–4047.

[37] A.E. Gash, T.M. Tillotson, J.H. Satcher, J.F. Poco, L.W. Hrubesh, R.L. Simpson, Use of epoxides in the sol-gel synthesis of porous iron(III) oxide monoliths from Fe(III) salts, Chem. Mater. 13 (2001) 999–1007.

[38] A.E. Danks, S.R. Hall, Z. Schnepp, The evolution of "sol-gel" chemistry as a technique for materials synthesis, Mater. Horizons. 3 (2016) 91–112.

[39] S. Esposito, "Traditional" Sol-Gel Chemistry as a Powerful Tool for the Preparation of Supported Metal and Metal Oxide Catalysts, Materials. 12 (2019) 668.

[40] D.P. Debecker, P.H. Mutin, Non-hydrolytic sol-gel routes to heterogeneous catalysts, Chem. Soc. Rev. 41 (2012) 3624–3650.

[41] M. Niederberger, Nonaqueous sol-gel routes to metal oxide nanoparticles, Acc. Chem. Res. 40 (2007) 793–800.

[42] J.J. Garcia-Jareno, D. Gimenez-Romero, F. Vicente, Correlationship between Microscopic Observations and Electrochemical Behaviour of Different Kind of Galvanized Steel, in: Mater. Sci. Forum, Trans Tech Publ, 2005: pp. 345–350.

[43] D. Grosso, F. Cagnol, G.J.D.A.A. Soler-Illia, E.L. Crepaldi, H. Amenitsch, A. Brunet-Bruneau, A. Bourgeois, C. Sanchez, Fundamentals of mesostructuring through evaporation-induced self-assembly, Adv. Funct. Mater. 14 (2004) 309–322.

[44] Q. Huo, D.I. Margolese, U. Ciesla, D.G. Demuth, P. Feng, T.E. Gier, P. Sieger, A. Firouzi, B.F. Chmelka, F. Schüth, G.D. Stucky, Organization of Organic Molecules with Inorganic Molecular Species into Nanocomposite Biphase Arrays, Chem. Mater. 6 (1994) 1176–1191.

[45] M.A. Carreon, V. V. Guliants, Ordered meso- and macroporous binary and mixed metal oxides, Eur. J. Inorg. Chem. 2005 (2005) 27–43.

[46] V. V. Guliants, J.B. Benziger, S. Sundaresan, I.E. Wachs, J.M. Jehng, J.E. Roberts, The effect of the phase composition of model VPO catalysts for partial oxidation of n-butane, Catal. Today. 28 (1996) 275–295.

[47] M.O. Guerrero-Pérez, J.L.G. Fierro, M.A. Bañares, Effect of the oxide support on the propane ammoxidation with Sb-V-O-based catalysts, Catal. Today. 78 (2003) 387–396.

[48] D.J. Jones, G. Aptel, M. Brandhorst, M. Jacquin, J. Jimenez-Jimenez, A. Jimenez-Lopez, P. Maireles-Torres, I. Piwonski, E. Rodriguez-Castellon, J. Zajac, J. Roziere, High surface area mesoporous titanium phosphate: Synthesis and surface acidity determination, J. Mater. Chem. 10 (2000) 1957–1963.

[49] U. Ciesla, M. Fröba, G. Stucky, F. Schüth, Highly ordered porous zirconias from

surfactant-controlled syntheses: Zirconium oxide-sulfate and zirconium oxo phosphate, Chem. Mater. 11 (1999) 227–234.

[50] P. Yang, D. Zhao, D.I. Margolese, B.F. Chmelka, G.D. Stucky, Block copolymer templating syntheses of mesoporous metal oxides with large ordering lengths and semicrystalline framework, Chem. Mater. 11 (1999) 2813–2826.

[51] Y. Zhang, M.C. Wang, H. He, H. Li, Effect of heat treatment on the crystalline structure and hydrophilic properties of TiO2 porous thin films, J. Sol-Gel Sci. Technol. 80 (2016) 881–892.

[52] C. Li, X. Li, X. Liu, Y. Yang, J. Zhao, Q. Yang, Entrapment of metal nanoparticles within nanocages of mesoporous silicas aided by co-surfactants, J. Mater. Chem. 22 (2012) 21045–21050.

[53] Y. Lu, R. Ganguli, C. Drewien, M.T. Anderson, C. Brinker, W. Gong, Y. Guo, H. Soyez, B. Dunn, M. Huang, J. Zink, Continuous formation of supported cubic and hexagonal mesoporous films by sol–gel dip-coating, Nature. 389 (1997) 364–368.

[54] C.M. Yang, H.S. Sheu, K.J. Chao, Templated synthesis and structural study of densely packed metal nanostructures in MCM-41 and MCM-48, Adv. Funct. Mater. 12 (2002) 143–148.

[55] M. Bandyopadhyay, H. Gies, W. Grünert, M. van den Berg, A. Birkner, Metal Oxide Nano-Particles Supported on Mesoporous Matrices: A Comparative Study on Structural Behavior, Adv. Porous Mater. 4 (2016) 166–178.

[56] S. Tanaka, J. Lin, Y.V. Kaneti, S.I. Yusa, Y. Jikihara, T. Nakayama, M.B. Zakaria, A.A. Alshehri, J. You, M.S.A. Hossain, Y. Yamauchi, Gold nanoparticles supported on mesoporous iron oxide for enhanced CO oxidation reaction, Nanoscale. 10 (2018) 4779–4785.

[57] T. Oh, S. Ryu, H. Oh, J. Kim, $MnCo_2O_4$ nanoparticles supported on nitrogen and sulfur co-doped mesoporous carbon spheres as efficient electrocatalysts for oxygen catalytic reactions, Dalt. Trans. 48 (2019) 945–953.

[58] J. Liu, S. Zou, L. Xiao, J. Fan, Well-dispersed bimetallic nanoparticles confined in mesoporous metal oxides and their optimized catalytic activity for nitrobenzene hydrogenation, Catal. Sci. Technol. 4 (2014) 441–446.

[59] Z. Kónya, V.F. Puntes, I. Kiricsi, J. Zhu, J.W. Ager, M.K. Ko, H. Frei, P. Alivisatos, G.A. Somorjai, Synthetic insertion of gold nanoparticles into mesoporous silica, Chem. Mater. 15 (2003) 1242–1248.

[60] V. Lordi, N. Yao, J. Wei, Method for supporting platinum on single-walled carbon

nanotubes for a selective hydrogenation catalyst, Chem. Mater. 13 (2001) 733–737.

[61] J. Rosen, G.S. Hutchings, F. Jiao, Ordered Mesoporous Cobalt Oxide as Highly Efficient Oxygen Evolution Catalyst, J. Am. Chem. Soc. 135 (2013) 4516–4521.

[62] T. Liu, B. Li, Y. Hao, F. Han, L. Zhang, L. Hu, A general method to diverse silver/mesoporous-metal-oxide nanocomposites with plasmon-enhanced photocatalytic activity, Appl. Catal. B Environ. 165 (2015) 378–388.

[63] S. Hao, J. Hou, P. Aprea, F. Pepe, Mesoporous Ce-Pr-O solid solution with efficient photocatalytic activity under weak daylight irradiation, Appl. Catal. B Environ. 160 (2014) 566–573.

[64] Y. Li, B.P. Zhang, J.X. Zhao, Enhanced photocatalytic performance of Au-Ag alloy modified ZnO nanocomposite films, J. Alloys Compd. 586 (2014) 663–668.

[65] R. Bacani, L.M. Toscani, T.S. Martins, M.C.A. Fantini, D.G. Lamas, S.A. Larrondo, Synthesis and characterization of mesoporous NiO_2/ZrO_2-CeO_2 catalysts for total methane conversion, Ceram. Int. 43 (2017) 7851–7860.

[66] W. Ciptonugroho, M.G. Al-Shaal, J.B. Mensah, R. Palkovits, One pot synthesis of WOx/mesoporous-ZrO2 catalysts for the production of levulinic-acid esters, J. Catal. 340 (2016) 17–29.

[67] C.W. Yen, M.L. Lin, A. Wang, S.A. Chen, J.M. Chen, C.Y. Mou, CO oxidation catalyzed by Au-Ag bimetallic nanoparticles supported in mesoporous silica, J. Phys. Chem. C. 113 (2009) 17831–17839.

[68] P. Doggali, S. Waghmare, S. Rayalu, Y. Teraoka, N. Labhsetwar, Transition metals supported on mesoporous ZrO_2 for the catalytic control of indoor CO and PM emissions, J. Mol. Catal. A Chem. 347 (2011) 52–59.

[69] N. Yang, F. Pang, J. Ge, One-pot and general synthesis of crystalline mesoporous metal oxides nanoparticles by protective etching: Potential materials for catalytic applications, J. Mater. Chem. A. 3 (2015) 1133–1141.

[70] V.R. Choudhary, D.K. Dumbre, S.K. Bhargava, Oxidation of Benzyl Alcohol to Benzaldehyde by tert-Butyl Hydroperoxide over Nanogold Supported on TiO_2 and other Transition and Rare-Earth Metal Oxides, Ind. Eng. Chem. Res. 48 (2009) 9471–9478.

[71] Y. Du, X. Zhu, H. Wang, Y. Wei, K. Li, Synthesis gas generation by chemical-looping selective oxidation of methane using $Pr_{1-x}Zr_xO_2-\delta$ oxygen carriers, J. Energy Inst. 89 (2016) 745–754.

[72] Y.P. Du, X. Zhu, H. Wang, Y.G. Wei, K.Z. Li, Selective oxidation of methane to

syngas using $Pr_{0.7}Zr_{0.3}O_2^-$: Stability of oxygen carrier, Trans. Nonferrous Met. Soc. China. 25 (2015) 1248–1253.

[73] P. Kaminski, M. Ziolek, J.A. Van Bokhoven, Mesoporous cerium-zirconium oxides modified with gold and copper-synthesis, characterization and performance in selective oxidation of glycerol, RSC Adv. 7 (2017) 7801–7819.

[74] D. Pan, Q. Xu, Z. Dong, S. Chen, F. Yu, X. Yan, B. Fan, R. Li, Facile synthesis of highly ordered mesoporous cobalt-alumina catalysts and their application in liquid phase selective oxidation of styrene, RSC Adv. 5 (2015) 98377–98390.

[75] M.M. Schubert, S. Hackenberg, A.C. Van Veen, M. Muhler, V. Plzak, J.J. Behm, CO oxidation over supported gold catalysts -"Inert" and “active” support materials and their role for the oxygen supply during reaction, J. Catal. 197 (2001) 113–122.

[76] F. Moreau, G.C. Bond, A.O. Taylor, Gold on titania catalysts for the oxidation of carbon monoxide: Control of pH during preparation with various gold contents, J. Catal. 231 (2005) 105–114.

[77] X.S. Huang, H. Sun, L.C. Wang, Y.M. Liu, K.N. Fan, Y. Cao, Morphology effects of nanoscale ceria on the activity of Au/CeO_2 catalysts for low-temperature CO oxidation, Appl. Catal. B Environ. 90 (2009) 224–232.

[78] S.A. Schunk, N. Böhmer, C. Futter, A. Kuschel, E. Prasetyo, T. Roussière, High throughput technology: approaches of research in homogeneous and heterogeneous catalysis, Catalysis. 25 (2013) 172–215.

[79] D. Maclean, J.R. Schullek, M.M. Murphy, Z.-J. Ni, E.M. Gordon, M.A. Gallop, Encoded combinatorial chemistry: synthesis and screening of a library of highly functionalized pyrrolidines, Proc. Natl. Acad. Sci. 94 (1997) 2805–2810.

[80] J. Nielsen, Combinatorial synthesis of natural products, Curr. Opin. Chem. Biol. 6 (2002) 297–305.

[81] M.T. Cancilla, M.M. He, N. Viswanathan, R.L. Simmons, M. Taylor, A.D. Fung, K. Cao, D.A. Erlanson, Discovery of an Aurora kinase inhibitor through site-specific dynamic combinatorial chemistry, Bioorg. Med. Chem. Lett. 18 (2008) 3978–3981.

[82] G. Lowe, Combinatorial chemistry, Chem. Soc. Rev. 24 (1995) 309–317.

[83] X. Liu, Y. Shen, R. Yang, S. Zou, X. Ji, L. Shi, Y. Zhang, D. Liu, L. Xiao, X. Zheng, S. Li, J. Fan, G.D. Stucky, Inkjet printing assisted synthesis of multicomponent mesoporous metal oxides for ultrafast catalyst exploration, Nano Lett. 12 (2012) 5733–5739.

[84] C. Barnes, S. Balasubramanian, Recent developments in the encoding and

deconvolution of combinatorial libraries, Curr. Opin. Chem. Biol. 4 (2000) 346–350.

[85] S. Bergh, P. Cong, B. Ehnebuske, S. Guan, A. Hagemeyer, H. Lin, Y. Liu, C.G. Lugmair, H.W. Turner, A.F. Volpe, Combinatorial heterogeneous catalysis: oxidative dehydrogenation of ethane to ethylene, selective oxidation of ethane to acetic acid, and selective ammoxidation of propane to acrylonitrile, Top. Catal. 23 (2003) 65–79.

[86] X.D. Sun, K.A. Wang, Y. Yoo, W.G. Wallace-Freedman, C. Gao, X.D. Xiang, P.G. Schultz, Solution-phase synthesis of luminescent materials libraries, Adv. Mater. 9 (1997) 1046–1049.

[87] E. Wolf, E. Richmond, J. Moran, Identifying lead hits in catalyst discovery by screening and deconvoluting complex mixtures of catalyst components, Chem. Sci. 6 (2015) 2501–2505.

[88] R. V Belosludov, S. Sakahara, K. Yajima, S. Takami, M. Kubo, A. Miyamoto, Combinatorial computational chemistry approach as a promising method for design of Fischer–Tropsch catalysts based on Fe and Co, Appl. Surf. Sci. 189 (2002) 245–252.

[89] S.R. Gilbertson, X. Wang, The combinatorial synthesis of chiral phosphine ligands, Tetrahedron Lett. 37 (1996) 6475–6478.

[90] J.G. de Vries, A.H.M. de Vries, The Power of High-Throughput Experimentation in Homogeneous Catalysis Research for Fine Chemicals, European J. Org. Chem. 2003 (2003) 799–811.

[91] N.K. Terrett, M. Gardner, D.W. Gordon, R.J. Kobylecki, J. Steele, Combinatorial synthesis—the design of compound libraries and their application to drug discovery, Tetrahedron. 51 (1995) 8135–8173.

[92] E.G. Derouane, V. Parmon, F. Lemos, F.R. Ribeiro, Principles and Methods for Accelerated Catalyst Design and Testing, Springer Science & Business Media, 2012.

[93] Y. Sun, B.C. Chan, R. Ramnarayanan, W.M. Leventry, T.E. Mallouk, S.R. Bare, R.R. Willis, Split-pool method for synthesis of solid-state material combinatorial libraries, J. Comb. Chem. 4 (2002) 569–575.

[94] Y. Wang, S. Shaabani, M. Ahmadianmoghaddam, L. Gao, R. Xu, K. Kurpiewska, J. Kalinowska-Tluscik, J. Olechno, R. Ellson, M. Kossenjans, V. Helan, M. Groves, A. Dömling, Acoustic Droplet Ejection Enabled Automated Reaction Scouting, ACS Cent. Sci. 5 (2019) 451–457.

[95] N.M. Nursam, X. Wang, R.A. Caruso, High-Throughput Synthesis and Screening of Titania-Based Photocatalysts, ACS Comb. Sci. 17 (2015) 548–569.

[96] D. Kimmich, D.H. Taffa, C. Dosche, M. Wark, G. Wittstock, Combinatorial screening

of photoanode materials - Uniform platform for compositional arrays and macroscopic electrodes, Electrochim. Acta. 259 (2018) 204–212.

[97] J. Klein, C.W. Lehmann, H.W. Schmidt, W.F. Maier, Combinatorial Material Libraries on the Microgram Scale with an Example of Hydrothermal Synthesis, Angew. Chemie - Int. Ed. 37 (1999) 3369–3372.

[98] S.M. Senkan, High-throughput screening of solid-state catalyst libraries, Nature. 394 (1998) 350–353.

[99] P. Cong, R.D. Doolen, Q. Fan, D.M. Giaquinta, S. Guan, E.W. Mcfarland, D.M. Poojary, K. Self, H.W. Turner, W.H. Weinberg, High-throughput Synthesis and Screening of Combinatorial Heterogeneous Catalyst Libraries, Angew. Chemie. 38 (1999) 483–488.

[100] E. Danielson, J.H. Golden, E.W. Mcfarland, A combinatorial approach to the discovery and optimization of luminescent materials, Nature. 389 (1997) 944–948.

[101] G. Brice o, H. Chang, X. Sun, P.G. Schultz, X.-D. Xiang, A Class of Cobalt Oxide Magnetoresistance Materials Discovered with Combinatorial Synthesis, Science. 270 (1995) 273–275.

[102] R.B. Van Dover, L.F. Schneemeyer, R.M. Fleming, Discovery of a useful thin-film dielectric using a composition-spread approach, Nature. 392 (1998) 162–164.

[103] R.J. Hendershot, C.M. Snively, J. Lauterbach, High-throughput heterogeneous catalytic science, Chem. - A Eur. J. 11 (2005) 806–814.

[104] F.C. Moates, M. Somani, J. Annamalai, J.T. Richardson, D. Luss, R.C. Willson, Infrared Thermographic Screening of Combinatorial Libraries of Heterogeneous Catalysts, Ind. Eng. Chem. Res. 35 (1996) 4801–4803.

[105] T. Zech, G. Bohner, J. Klein, High-throughput screening of supported catalysts in massively parallel single-bead microreactors: Workflow aspects related to reactor bonding and catalyst preparation, Catal. Today. 110 (2005) 58–67.

[106] J. Klein, T. Zech, J.M. Newsam, S.A. Schunk, Application of a novel Split&Pool-principle for the fully combinatorial synthesis of functional inorganic materials, Appl. Catal. A Gen. 254 (2003) 121–131.

[107] R. Ramnarayanan, B.C. Chan, M.A. Salvitti, T.E. Mallouk, F.M. Falih, J. Davis, D.B. Galloway, S.R. Bare, R.R. Willis, Directed-Sorting Method for Synthesis of Bead-Based Combinatorial Libraries of Heterogeneous Catalysts, J. Comb. Chem. 8 (2006) 199–212.

[108] P. Calvert, Inkjet printing for materials and devices, Chem. Mater. 13 (2001) 3299–

3305.

[109] S. Lee, T. Boeltken, A.K. Mogalicherla, U. Gerhards, P. Pfeifer, R. Dittmeyer, Inkjet printing of porous nanoparticle-based catalyst layers in microchannel reactors, Appl. Catal. A Gen. 467 (2013) 69–75.

[110] R. Waasdorp, O. Van Den Heuvel, F. Versluis, B. Hajee, M.K. Ghatkesar, Accessing individual 75-micron diameter nozzles of a desktop inkjet printer to dispense picoliter droplets on demand, RSC Adv. 8 (2018) 14765–14774.

[111] X. Liu, T.J. Tarn, F. Huang, J. Fan, Recent advances in inkjet printing synthesis of functional metal oxides, Particuology. 19 (2015) 1–13.

[112] V.C. Bassetto, J. Xiao, E. Oveisi, V. Amstutz, B. Liu, H.H. Girault, A. Lesch, Rapid inkjet printing of high catalytic activity Co_3O_4/N-rGO layers for oxygen reduction reaction, Applied Catal. A, Gen. 563 (2018) 9–17.

[113] T. Xu, J. Jin, C. Gregory, J.J. Hickman, T. Boland, Inkjet printing of viable mammalian cells, Biomaterials. 26 (2005) 93–99.

[114] R. Ahmad, M. Vaseem, N. Tripathy, Y.-B. Hahn, Wide linear-range detecting nonenzymatic glucose biosensor based on CuO nanoparticles inkjet-printed on electrodes, Anal. Chem. 85 (2013) 10448–10454.

[115] C. Avis, H.R. Hwang, J. Jang, Effect of channel layer thickness on the performance of indium-zinc-tin oxide thin film transistors manufactured by inkjet printing, ACS Appl. Mater. Interfaces. 6 (2014) 10941–10945.

[116] M. Černá, M. Veselý, P. Dzik, Physical and chemical properties of titanium dioxide printed layers, Catal. Today. 161 (2011) 97–104.

[117] I. Fasaki, K. Siamos, M. Arin, P. Lommens, I. Van Driessche, S.C. Hopkins, B.A. Glowacki, I. Arabatzis, Ultrasound assisted preparation of stable water-based nanocrystalline TiO_2 suspensions for photocatalytic applications of inkjet-printed films, Appl. Catal. A Gen. 411 (2012) 60–69.

[118] H. Maleki, V. Bertola, TiO2 Nanofilms on Polymeric Substrates for the Photocatalytic Degradation of Methylene Blue, ACS Appl. Nano Mater. 2 (2019) 7237–7244.

[119] M. Woodhouse, G.S. Herman, B.A. Parkinson, Combinatorial approach to identification of catalysts for the photoelectrolysis of water, Chem. Mater. 17 (2005) 4318–4324.

[120] J.R.G. Evans, M.J. Edirisinghe, P. V. Coveney, J. Eames, Combinatorial searches of inorganic materials using the ink-jet printer: Science, philosophy and technology, J. Eur. Ceram. Soc. 21 (2001) 2291–2299.

[121] M. Siebert, R.R. Zimmermann, M. Armbrüster, R. Dittmeyer, Inkjet Printing of GaPd2 into Micro-Channels for the Selective Hydrogenation of Acetylene, ChemCatChem. 9 (2017) 3733–3742.

[122] A.D. Taylor, E.Y. Kim, V.P. Humes, J. Kizuka, L.T. Thompson, Inkjet printing of carbon supported platinum 3-D catalyst layers for use in fuel cells, J. Power Sources. 171 (2007) 101–106.

[123] H. Wickström, E. Hilgert, J.O. Nyman, D. Desai, D.Ş. Karaman, T. De Beer, N. Sandler, J.M. Rosenholm, Inkjet printing of drug-loaded mesoporous silica nanoparticles—a platform for drug development, Molecules. 22 (2017) 2020.

[124] C. Novara, F. Petracca, A. Virga, P. Rivolo, S. Ferrero, A. Chiolerio, F. Geobaldo, S. Porro, F. Giorgis, SERS active silver nanoparticles synthesized by inkjet printing on mesoporous silicon, Nanoscale Res. Lett. 9 (2014) 527.

[125] I.D. Styliari, C. Conte, A.K. Pearce, A. Hüsler, R.J. Cavanagh, M.J. Limo, D. Gordhan, A. Nieto-Orellana, J. Suksiriworapong, B. Couturaud, High-Throughput Miniaturized Screening of Nanoparticle Formation via Inkjet Printing, Macromol. Mater. Eng. 303 (2018) 1800146.

[126] H.R. Neumann, C. Selhuber-Unkel, High-throughput micro-nanostructuring by microdroplet inkjet printing, Beilstein J. Nanotechnol. 9 (2018) 2372–2380.

[127] B. Fousseret, M. Mougenot, F. Rossignol, J.F.O. Baumard, B. Soulestin, C. Boissiére, F.O. Ribot, D. Jalabert, C. Carrion, C. Sanchez, M. Lejeune, Inkjet-printing-engineered functional microdot arrays made of mesoporous hybrid organosilicas, Chem. Mater. 22 (2010) 3875–3883.

[128] M. Mougenot, M. Lejeune, J.F. Baumard, C. Boissiere, F. Ribot, D. Grosso, C. Sanchez, R. Noguera, Ink jet printing of microdot arrays of mesostructured silica, J. Am. Ceram. Soc. 89 (2006) 1876–1882.

[129] B. Fousseret, M. Mougenot, M. Lejeune, F. Rossignol, J.F. Baumard, B. Soulestin, C. Boissière, C. Sanchez, D. Jalabert, D. Massiot, Ink-jet printing processed mesoporous silica microdot arrays: New possible plateforms for the design of multifunctional sensors, in: 4th IMAPS/ACerS Int. Conf. Exhib. Ceram. Interconnect Ceram. Microsystems Technol. 2008, CICMT 2008, 2008: pp. 644–651.

[130] O.D.L. De los Cobos, B. Fousseret, M. Lejeune, F. Rossignol, M. Dutreilh-colas, C. Carrion, M. Wong, C. Man, J. Durand, Tunable Multifunctional Mesoporous Silica Microdots Arrays by Combination of Inkjet Printing, EISA, and Click Chemistry, Chem. Mater. 24 (2012) 4337–4342.

[131] D.H. Lee, Y.J. Chang, W. Stickle, C.H. Chang, Functional porous tin oxide thin films fabricated by inkjet printing process, Electrochem. Solid-State Lett. 10 (2007) K51–K54.

[132] R. Brisse, R. Faddoul, T. Bourgeteau, D. Tondelier, J. Leroy, S. Campidelli, T. Berthelot, B. Geffroy, B. Jousselme, Inkjet printing NiO-based p-Type dye-sensitized solar cells, ACS Appl. Mater. Interfaces. 9 (2017) 2369–2377.

[133] R. Cherrington, D.J. Hughes, S. Senthilarasu, V. Goodship, Inkjet-Printed TiO_2 Nanoparticles from Aqueous Solutions for Dye-Sensitized Solar Cells (DSSCs), Energy Technol. 3 (2015) 866–870.

[134] M. Arin, P. Lommens, N. Avci, S.C. Hopkins, K. De Buysser, I.M. Arabatzis, I. Fasaki, D. Poelman, I. Van Driessche, Inkjet printing of photocatalytically active TiO_2 thin films from water based precursor solutions, J. Eur. Ceram. Soc. 31 (2011) 1067–1074.

[135] S.G. Hashmi, D. Martineau, X. Li, M. Ozkan, A. Tiihonen, M.I. Dar, T. Sarikka, S.M. Zakeeruddin, J. Paltakari, P.D. Lund, M. Grätzel, Air Processed Inkjet Infiltrated Carbon Based Printed Perovskite Solar Cells with High Stability and Reproducibility, Adv. Mater. Technol. 2 (2017) 1600183.

[136] R. Cherrington, D.J. Hughes, S. Senthilarasu, V. Goodship, Inkjet-printed TiO2 nanoparticles from aqueous solutions for dye-sensitized solar cells (DSSCs), Energy Technol. 3 (2015) 866–870.

[137] J.A. Haber, C. Xiang, D. Guevarra, S. Jung, J. Jin, J.M. Gregoire, High-Throughput Mapping of the Electrochemical Properties of (Ni-Fe-Co-Ce) O_x Oxygen-Evolution Catalysts, ChemElectroChem. 1 (2014) 524–528.

[138] R.D. Bacelis-Martínez, G. Oskam, G. Rodriguez Gattorno, M.A. Ruiz-Gómez, Inkjet Printing as High-Throughput Technique for the Fabrication of $NiCo_2O_4$ Films, Adv. Mater. Sci. Eng. 2017 (2017) 9647458.

[139] S.H. Baeck, T.F. Jaramillo, C. Brändli, E.W. McFarland, Combinatorial Electrochemical Synthesis and Characterization of Tungsten-Based Mixed-Metal Oxides, J. Comb. Chem. 4 (2002) 563–568.

[140] R.A. Houghten, C. Pinilla, S.E. Blondelle, J.R. Appel, C.T. Dooley, J.H. Cuervo, Generation and use of synthetic peptide combinatorial libraries for basic research and drug discovery, Nature. 354 (1991) 84–86.

[141] E. Richmond, J. Moran, Harnessing complex mixtures for catalyst discovery, Synlett. 27 (2016) 2637–2643.

[142] M. Renom-Carrasco, L. Lefort, Ligand libraries for high throughput screening of homogeneous catalysts, Chem. Soc. Rev. 47 (2018) 5038–5060.

[143] M.T. Reetz, T. Sell, A. Meiswinkel, G. Mehler, A New Principle in Combinatorial Asymmetric Transition-Metal Catalysis: Mixtures of Chiral Monodentate P Ligands, Angew. Chemie Int. Ed. 42 (2003) 790–793.

[144] K. Ding, Synergistic effect of binary component ligands in chiral catalyst library engineering for enantioselective reactions, Chem. Commun. (2008) 909–921.

[145] K. Burgess, H. Lim, A.M. Porte, G.A. Sulikowski, New Catalysts and Conditions for a C□ H Insertion Reaction Identified by High Throughput Catalyst Screening, Angew. Chemie Int. Ed. English. 35 (1996) 220–222.

[146] M.B. Francis, T.F. Jamison, E.N. Jacobsen, Combinatorial libraries of transition-metal complexes, catalysts and materials, Curr. Opin. Chem. Biol. 2 (1998) 422–428.

[147] D.F. Kennedy, B.A. Messerle, S.L. Rumble, Application of UV-vis spectroscopy to high throughput screening of hydroamination catalysts, New J. Chem. 33 (2009) 818–824.

[148] F. Schaufelberger, O. Ramström, Dynamic covalent organocatalysts discovered from catalytic systems through rapid deconvolution screening, Chem. Eur. J. 21 (2015) 12735–12740.

[149] F. Schaufelberger, B.J.J. Timmer, O. Ramström, Resolving a Reactive Organometallic Intermediate from Dynamic Directing Group Systems by Selective C− H Activation, Chem. Eur. J. 24 (2018) 101–104.

[150] R.H. Griffey, H. An, L.L. Cummins, H.J. Gaus, B. Haly, R. Herrmann, P.D. Cook, Rapid deconvolution of combinatorial libraries using HPLC fractionation, Tetrahedron. 54 (1998) 4067–4076.

[151] L.C. Gerber, A. Calasanz-Kaiser, L. Hyman, K. Voitiuk, U. Patil, I.H. Riedel-Kruse, Liquid-handling Lego robots and experiments for STEM education and research, PLoS Biol. 15 (2017) e2001413.

[152] T. Chapman, Lab automation and robotics: Automation on the move, Nature. 421 (2003) 661–663.

[153] F. Kong, L. Yuan, Y.F. Zheng, W. Chen, Automatic liquid handling for life science: a critical review of the current state of the art, J. Lab. Autom. 17 (2012) 169–185.

[154] A.B. Santanilla, E.L. Regalado, T. Pereira, M. Shevlin, K. Bateman, L.-C. Campeau, J. Schneeweis, S. Berritt, Z.-C. Shi, P. Nantermet, Nanomole-scale high-throughput chemistry for the synthesis of complex molecules, Science. 347 (2015) 49–53.

[155] N.M. Nebane, T. Coric, S. McKellip, L.K. Woods, M. Sosa, L. Rasmussen, M.A. Bjornsti, E.L. White, Acoustic Droplet Ejection Technology and Its Application in High-Throughput RNA Interference Screening, J. Lab. Autom. 21 (2016) 198–203.

[156] Y.C. Tung, A.Y. Hsiao, S.G. Allen, Y.S. Torisawa, M. Ho, S. Takayama, High-throughput 3D spheroid culture and drug testing using a 384 hanging drop array, Analyst. 136 (2011) 473–478.

[157] B.A. Brodin, K. Wennerberg, E. Lidbrink, O. Brosjö, S. Potdar, J.N. Wilson, L. Ma, L.N. Moens, A. Hesla, E. Porovic, Drug sensitivity testing on patient-derived sarcoma cells predicts patient response to treatment and identifies c-Sarc inhibitors as active drugs for translocation sarcomas, Br. J. Cancer. 120 (2019) 435–443.

[158] E. Kulesskiy, J. Saarela, L. Turunen, K. Wennerberg, Precision cancer medicine in the acoustic dispensing era: ex vivo primary cell drug sensitivity testing, J. Lab. Autom. 21 (2016) 27–36.

[159] K. Blom, P. Nygren, J. Alvarsson, R. Larsson, C.R. Andersson, Ex vivo assessment of drug activity in patient tumor cells as a basis for tailored cancer therapy, J. Lab. Autom. 21 (2016) 178–187.

[160] E. Teplitsky, K. Joshi, D.L. Ericson, A. Scalia, J.D. Mullen, R.M. Sweet, A.S. Soares, High throughput screening using acoustic droplet ejection to combine protein crystals and chemical libraries on crystallization plates at high density, J. Struct. Biol. 191 (2015) 49–58.

[161] F. Madoux, A. Tanner, M. Vessels, L. Willetts, S. Hou, L. Scampavia, T.P. Spicer, A 1536-well 3D viability assay to assess the cytotoxic effect of drugs on spheroids, SLAS Discov. Adv. Life Sci. R&D. 22 (2017) 516–524.

[162] G.K.Y. Chan, S. Wilson, S. Schmidt, J.G. Moffat, Unlocking the potential of high-throughput drug combination assays using acoustic dispensing, J. Lab. Autom. 21 (2016) 125–132.

[163] M.J. Iannotti, R. Macarthur, R. Jones, D. Tao, I. Singeç, S. Michael, J. Inglese, Detecting Secretory Proteins by Acoustic Droplet Ejection in Multiplexed High-Throughput Applications, ACS Chem. Biol. 14 (2019) 497–505.

[164] D.L. Ericson, X. Yin, A. Scalia, Y.N. Samara, R. Stearns, H. Vlahos, R. Ellson, R.M. Sweet, A.S. Soares, Acoustic Methods to Monitor Protein Crystallization and to Detect Protein Crystals in Suspensions of Agarose and Lipidic Cubic Phase, J. Lab. Autom. 21 (2016) 107–114.

[165] L.A. Mitchell, L.H. McCulloch, S. Pinglay, H. Berger, N. Bosco, R. Brosh, M. Bulajic,

E. Huang, J.A. Martin, M.S. Hogan, De novo assembly, delivery and expression of a 101 kb human gene in mouse cells, BioRxiv. (2019) 423426.

[166] J.J. Minich, G. Humphrey, R.A.S. Benitez, J. Sanders, A. Swafford, E.E. Allen, R. Knight, High-throughput miniaturized 16S rRNA amplicon library preparation reduces costs while preserving microbiome integrity, MSystems. 3 (2018) e00166-18.

[167] S.J. Moore, J.T. MacDonald, S. Wienecke, A. Ishwarbhai, A. Tsipa, R. Aw, N. Kylilis, D.J. Bell, D.W. McClymont, K. Jensen, Rapid acquisition and model-based analysis of cell-free transcription–translation reactions from nonmodel bacteria, Proc. Natl. Acad. Sci. 115 (2018) E4340–E4349.

[168] L. Ballell, R.H. Bates, R.J. Young, D. Alvarez-Gomez, E. Alvarez-Ruiz, V. Barroso, D. Blanco, B. Crespo, J. Escribano, R. González, Fueling open-source drug discovery: 177 small-molecule leads against tuberculosis, ChemMedChem. 8 (2013) 313–321.

[169] C.G. Neochoritis, S. Shaabani, M. Ahmadianmoghaddam, T. Zarganes-Tzitzikas, L. Gao, M. Novotná, T. Mitríková, A.R. Romero, M.I. Irianti, R. Xu, Rapid approach to complex boronic acids, Sci. Adv. 5 (2019) eaaw4607.

[170] F. Nejatimoharrami, A. Faina, K. Stoy, New Capabilities of EvoBot: A Modular, Open-Source Liquid-Handling Robot, SLAS Technol. Transl. Life Sci. Innov. 22 (2017) 500–506.

[171] P. Theodosiou, A. Faina, F. Nejatimoharrami, K. Stoy, J. Greenman, C. Melhuish, I. Ieropoulos, EvoBot: Towards a robot-chemostat for culturing and maintaining Microbial Fuel Cells (MFCs), in: Conf. Biomim. Biohybrid Syst., Springer, 2017: pp. 453–464.

Chapter 2

A multidimensional group testing approach to Mizoroki-Heck and Suzuki C-C coupling reactions catalysed by homogeneous Pd phosphine complexes

Chapter 2

A multidimensional group testing approach to Mizoroki-Heck and Suzuki C-C coupling reactions, catalysed by homogeneous Pd phosphine complexes.

Graphical Abstract

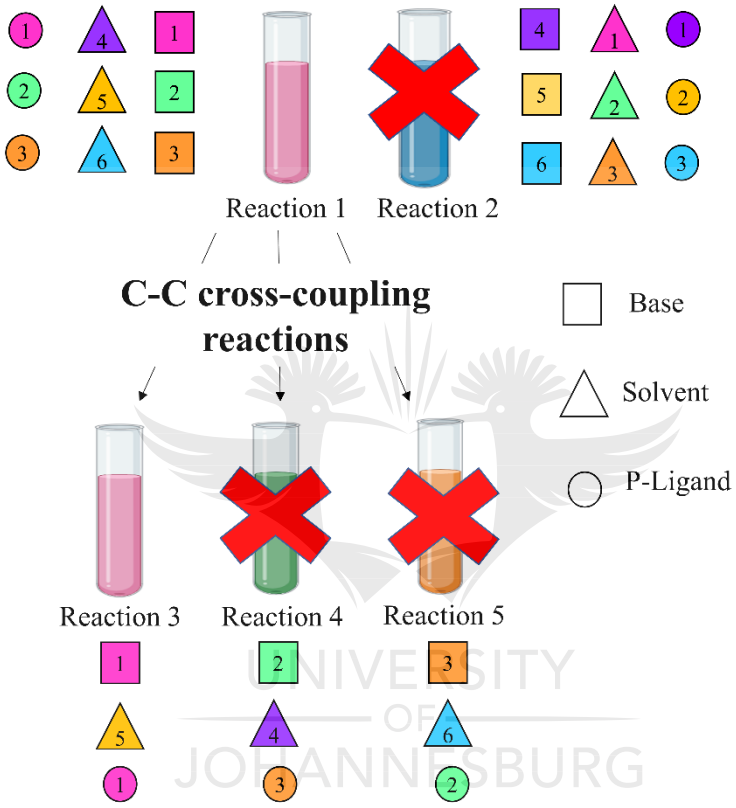

The deconvolution of reagents (bases, solvents and phosphine ligands) for common C-C cross coupling reactions.

Abstract

Conventional reaction optimisation involves the evaluation of different reagents such as bases, solvents and catalysts (or phosphine ligands), one reactant at a time. This is a time-consuming approach, and only a few reactants can be evaluated in this manner. By employing a multidimensional group testing strategy, a few reagents can be combined in one or more reaction vessels, and ultimately deconvolute the variables to find the optimal reagent. As a proof of principle, a multidimensional group testing approach was utilised for the deconvolution of six bases, six solvents and up to 20 phosphine ligands for the Pd catalysed Mizoroki-Heck and Suzuki C-C cross-coupling reactions. Conventionally, testing all the reagents mentioned, approximately 720 reactions are necessary. However, using a multidimensional group testing approach, the total reactions needed was reduced to 19 reactions for the Mizoroki-Heck reaction and 19 for the Suzuki reaction. The deconvolution resulted in K_2CO_3 as the optimal base for both the Mizoroki-Heck and Suzuki reactions. Acetonitrile and ethanol were found to be the optimal solvent for the Mizoroki-Heck and Suzuki reaction, respectively. Tricyclohexylphosphine and benzyldiphenylphosphine were the optimal phosphine ligands for these reactions, respectively. To confirm that such an approach can be used to optimise the system, a different approach was employed for the deconvolution of the Suzuki reagents. This resulted in the same outcome where the same optimal base and solvent were identified.

2.1 Introduction

Catalyst discovery includes evaluation of numerous reactions, catalysts and reagents and substrates to identify the best catalyst for a specific reaction. If one catalyst is evaluated at a time, the procedure can become very tedious and expensive. This is due to the synthesis of several materials which are purified and assayed separately [1], as well as a large number of reactions necessary to explore the intersection of a few parameters [2]. It is known that homogenous catalyst discovery requires knowledge about the mechanistic and empirical action of the catalyst since structure/function relationships are not always available for most catalyst [1]. Therefore, it is necessary to find alternative methods for faster catalyst discovery and screening.

A split and deconvolution approach is proposed. This approach does not require expensive instrumentation such as robotics which is sometimes used to reduce the number of reactions required. This approach can be done using basic wet chemistry involving the mixing of several reagents or substrates for a specific reaction in the same batch (or same reaction vessel). The mixtures are then screened for a specific reaction, the best reaction or mixture is identified and deconvoluted, in the steps that follow [2, 3]. This deconvolution is carried out until the optimal reagents or substrates are found.

This approach may accelerate homogenous catalyst discovery and development. It combines the parallel synthesis of numerous catalysts, as well as the creation of catalyst libraries using parallel assays, and rapidly screening these mixtures or catalyst libraries, then deconvoluting to ultimately find the optimised catalyst [1]. This technique is also known as combinatorial chemistry, and it usually involves three steps: 1) the synthesis of libraries of several compounds that are structurally related; 2) parallel evaluation of these libraries towards a specific reaction using an appropriate assay, and 3) the identification of the "hit" catalyst, that shows the best activity [1].

Combinatorial chemistry can be described as a systematic Edisonian approach to the discovery of new molecules and materials that have enhanced properties. In modern days, this method uses parallel synthesis and screening to reduce the time and expense of discovery and optimisation. This method is mainly applied to biomolecular problems, for example, in drug discovery. However, the method was adapted for the use in catalysis [4]. Over 90 years ago, this method was applied for the discovery of a better catalyst for ammonia synthesis. In this study, numerous catalysts combinations, supports and promoters were tested [5].

This field has not been explored to its full potential; however, it has been growing. Combinatorial methods include many different areas of chemistry, for example, therapeutic drug discovery and drug synthesis, material science, as well as homogeneous and heterogeneous catalysis. The main purpose for the use of combinatorial methods is to synthesise and screen large libraries of specific chemical entities, narrowing down the best entity in the fastest possible way. This is a parallel method and is less time-consuming compared to the traditional sequential method [6]. This approach was mainly designed to reduce the time-to-market for new and optimised products such as catalysts that are being manufactured by industry [7].

It is well known that the science behind catalysis is very precise, and the catalytic reaction can be described mechanistically to the point where the catalyst can be designed based on chemical principles that are already known [4]. Catalysis is an attractive subject for combinatorial methods. This is due to the element of empiricism in catalyst development. Since the first combinatorial approach to finding the best catalyst numerous studies have been reported involving transition metal complexes (where ligands are varied) [8], heterogeneous catalysts where multiple metals are employed [2, 9–12], supported metals [13, 14] as well as metal oxides [15, 16], resin bound organic catalysts (oligopeptides) [17, 18]. The combinatorial approach is used to discover new molecules or catalysts rapidly. Therefore, the first stage of this approach is a rapid synthesis/screening method to find new leads. This is also called the discovery phase. Thereafter, more reliable methods are used for full testing and characterisation of the newly discovered catalyst or molecule [4].

This approach can be used for homogeneous catalysis, and it involves the optimisation of reaction conditions which include temperature variations, pressure, additives, ligands and/or metal ions [2, 19]. Suppose the optimisation of one of these parameters is missed. In that case, the ultimate catalyst hit may also be missed, which would result in the failure of the discovery of the best catalyst for the reaction [2]. To date, mostly polymer-bound ligands have been used in these systems [19].

Cross-coupling reactions are popular reactions mostly being applied in pharmaceutical, materials and polymer chemistry as well as natural product synthesis [20, 21]. These reactions can transform two different chemical entities into one useful entity [22]. These reactions are also known as C-C cross-coupling reactions since it involves the formation of a new C-C bond [23, 24]. The reaction is a one-step procedure which can result in different aryl derivatives with high yields and good selectivity [25]. There are a few different C-C coupling reactions that can be performed. The Mizoroki-Heck reaction converts alkenes to aryl derivatives, while the Suzuki, Hiyama, Kumada and Stille reactions form non-symmetric biphenyls, and the Sonogashira coupling reaction produces diaryl-alkyne derivatives [25–27]. These reactions are mostly catalysed by palladium or palladium complexes.

The Mizoroki-Heck reaction was first described by Heck and Mizoroki more than 50 years ago. The reaction involves the arylation or vinylation of alkenes with aryl or vinyl halides. In this reaction, there is formation of a new C-C bond, and it is generally catalysed by palladium

(Pd) species which are formed from either Pd(0) compounds or Pd(II) salts. One of the limitations of these systems is the precipitation of Pd black, which limits the lifetime of the active species. However, with the addition of phosphine ligands, it was found that the stability of the Pd complex is greatly improved [28]. It is, therefore, necessary to form stable Pd-phosphine complexes that can catalyse the reaction. The Suzuki cross-coupling reaction occurs between an organoboron compound and organic halides, mostly aryl halides. These reactions result in the formation of biaryls, which are often used as building blocks in organic chemistry. The reaction is used to produce fine chemicals as well as complex pharmaceutical compounds [23].

The cross-coupling reactions are similar in the sequence of the steps in the mechanism. The general mechanism for cross-coupling reactions involves three basic steps. The first step is an oxidative addition of an electrophilic halide (aryl halides are most often used), to a Pd(0) species with act as the catalyst. Followed by this, a transmetalation of an organometallic reactant with the Pd complex takes place. Ultimately a reductive elimination occurs. This step forms the new carbon-carbon bond, and the catalyst is regenerated (**Figure 2.1**). A base is necessary for the final stage of the cycle. Numerous bases, solvents and phosphine ligands have been used in C-C cross-coupling reactions through the years.

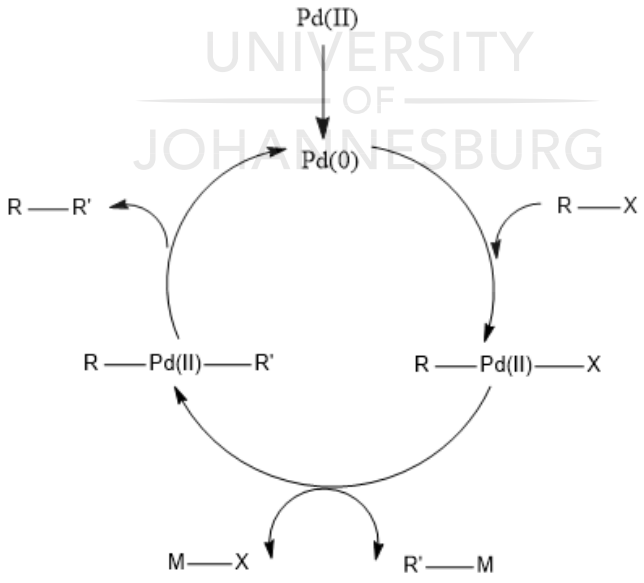

Figure 2.1: Schematic representation of a generic C-C cross-coupling reaction.

Therefore, in this chapter, as proof of principle, a multidimensional group testing strategy is employed for the screening of six different bases, six different solvents and up to 20 different

substituted trialkylphosphine ligands (**Table 2.1**) in the Mizoroki-Heck and Suzuki C-C coupling reactions. We propose that a multidimensional group testing approach could be a lower-cost alternative to high-throughput experimentation to determine the optimised system for C-C cross-coupling reactions, and indeed other homogeneously catalysed reactions.

2.2 Experimental

2.2.1 Materials

All the reagents used in the Mizoroki-Heck and Suzuki C-C coupling reactions were purchased from Sigma-Aldrich and were used as received with no further purification. The reagents include butyl acrylate (99%), iodobenzene (99%), bromobenzene (99%), chlorobenzene (99%), potassium tetrachloropalladate (98%). The bases used included sodium hydroxide (NaOH, 99%), sodium carbonate (Na_2CO_3, 99%), triethyl amine (NEt_3), potassium hydroxide (KOH, 99%), potassium carbonate (K_2CO_3, 99%) and caesium carbonate ($CsCO_3$, 99%). The solvents included; ethanol, butanol, toluene, 1,4-dioxane, dimethyl formide (DMF) and acetonitrile (MeCN). A range of the most commonly used monodentate alkyl and aryl phosphine ligands were investigated. These ligands have different steric and electronic properties [29].

Table 2.1: Phosphine ligands with their respective numbering, used for the Heck and Suzuki C-C coupling deconvolution reactions.

Number	Phosphine ligand
L1	Tri(4-tolyl)phosphine, 97%
L2	Tris(4-chlorophenyl)phosphine, 95%
L3	Tris(4-methoxyphenyl)phosphine, 95%
L4	Triphenylphosphine, 99.9%
L5	Cyclohexyldiphenylphosphine, 95%
L6	Dicyclohexyl(2-methylphenyl)phosphine, 95%
L7	Tricyclohexylphosphine, 99%
L8	Dicyclohexylphenylphosphine, 95%
L9	4-(diphenylphosphino)styrene, 97%
L10	(2-Biphenyl)di-tert-butylphosphine, 97%
L11	Tri-1-naphthylphosphine, 97%
L12	Diphenyl(p-tolyl)phosphine, 96%
L13	Tris(2,4,6-trimethylphenyl)phosphine, 97%
L14	Diphenyl-2-pyridylphosphine, 97%
L15	4-(Dimethylamino)-phenyldiphenylphosphine, 95%
L16	Tris(3,5-dimethylphenyl)phosphine, 96%
L17	Benzyldiphenylphosphine, ≥95%
L18	O-methoxyphenyldiphenylphosphine, 98%
L19	Tri(m-tolyl)phosphine, 97%
L20	Tri(o-tolyl)phosphine, 97%
L21	Diphenyl(o-tolyl) phosphine, 97%
L22	Dicyclo(2,6-diisopropylphenyl)phosphine, 97%

2.2.2 Method

For both the Mizoroki-Heck and Suzuki C-C coupling combinatorial deconvolution reactions, the optimal base, solvent and phosphine ligand were investigated. Therefore, six bases, six solvents and phosphine ligands (20 for the Mizoroki-Heck reaction and 14 for the Suzuki reaction) were deconvoluted using a split-and-pool approach. For the first deconvolution step

(deconvolution of the bases), a mixture of the solvents was used, and a mixture of the phosphine ligands was prepared to be added to the reactions.

2.2.2.1 Solvent mixture

A mixture of all the solvents under investigation was prepared to be used in the first deconvolution step. Therefore, equal volumes of ethanol, butanol, toluene, 1,4-dioxane, dimethylformamide (DMF) and acetonitrile (MeCN) were mixed and used as a solvent.

2.2.2.2 Phosphine ligand mixture

A mixture of phosphine ligands was prepared to be used in the deconvolution steps preceding the phosphine ligand deconvolution steps. Equal amounts (0.01 mol) of all the phosphine ligands under investigation were mixed. The mixture was used in the reactions.

2.2.2.3 A general description of the split-and-pool deconvolution approach

In general, all the reagents under investigation were mixed in one reaction flask. The metal precursor (K_2PdCl_4) and substrates were also included. For the Mizoroki-Heck reaction, butyl acrylate and an aryl halide (iodobenzene, bromobenzene, or chlorobenzene) were used as substrates whilst phenylboronic acid with 4-bromotoluene as substrates for the Suzuki reaction. External calibration was used for Heck reactions, and decane was used as the internal standard in the Suzuki reaction. The reactions were carried out at approximately 80 °C, and sampling was performed at time 0, followed by 30 or 60 min intervals for a total of 4 hrs. The final sampling was done at 24 hrs. The samples were diluted with dichloromethane (DCM) and analysed using GC-FID (gas chromatography flame ionisation detector). The fastest product formation (as with the Heck reaction) or the highest conversion of the substrate to product (as with the Suzuki reaction) was used to identify the best reaction. Following the identification of the best reaction, the subsequent reagent was investigated using a split-and-pool deconvolution strategy.

Initially, the bases were deconvoluted, followed by the solvents and, finally, the phosphine ligands. Two reaction flasks were prepared for the deconvolution of the bases, each containing three bases with six solvents and the up to 20 phosphine ligands. After the best reaction was identified, the bases were further split and deconvoluted into three reactions containing one base each. The reactions were carried out for a second time, and the optimal base was identified from the previous three reactions. Following the identification of the optimal base, the solvents

were deconvoluted. The same approach was followed, where two reaction flasks were prepared, containing three solvent in each, with the best-identified base from the previous deconvolution step. The reactions were carried out, and the best reaction was identified, split into three subsequent reactions, and deconvoluted to find the optimal solvent. Finally, the phosphine ligands were deconvoluted using several different reaction flasks containing the optimal base and solvent. The best reaction was identified and split further to be deconvoluted to only one phosphine ligand per reaction vessel, from where the best phosphine ligand was identified.

To substantiate the results obtained from the split-and-pool approach for the Suzuki reaction, the deconvolution of reagents was repeated using a second approach. Instead of combining the reagents under investigation, the reagents were split into several reactions containing one reagent per reaction. For example, the six bases were split into six reactions (one base per reaction) with the solvent and phosphine mixture in each reaction. The same was done for the solvent and phosphine deconvolution steps (**Table 2.4**).

The optimal combination of base, solvent and phosphine ligand could be identified using approximately 19 split-and-pool deconvolution reactions. A general deconvolution strategy is illustrated in **Figure 2.2**. Conventionally (varying one parameter or reagent at a time), it would have taken approximately 720 reactions to achieve the same result.

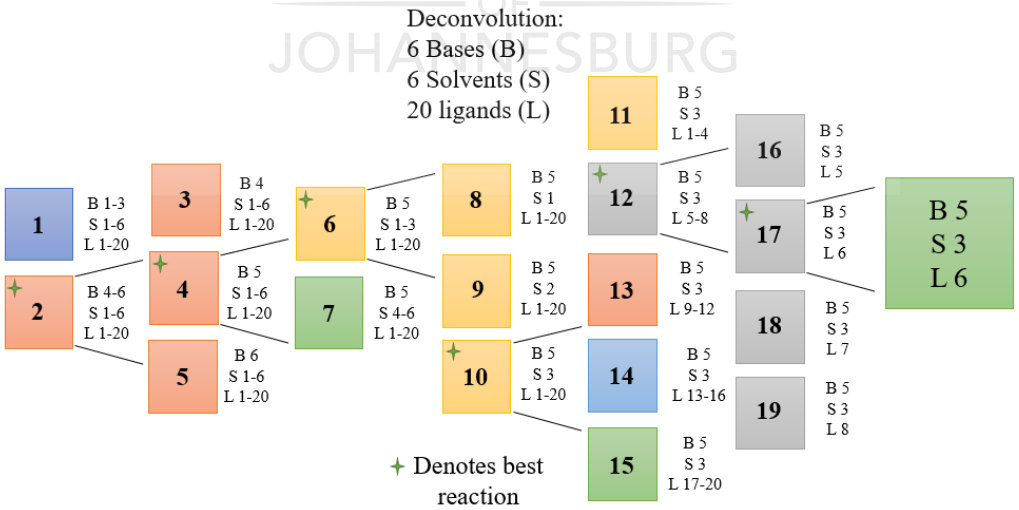

Figure 2.2: Schematic representation of a general split-and-pool deconvolution approach. This approach was used to deconvolute six bases, six solvents, and up to 20 phosphine ligands. This multidimensional group testing strategy was used for reagent optimisation for the Heck and Suzuki cross-coupling reactions.

The tables below (**Table 2.2**, **Table 2.3**, **Table 2.4** and **Table 2.5**) indicate the reaction numbers (for both the Mizoroki-Heck and Suzuki reactions) and the reagents under investigation. A detailed description of the experiment is given in the SI of chapter 2.

Table 2.2: Reaction numbers and reagents under investigation for the Mizoroki-Heck cross-coupling between iodobenzene (PhI) and butyl acrylate.

Deconvolution step	Reaction number	Bases	Solvents	Phosphine ligand
Base deconvolution	1a	NEt_3, Na_2CO_3 NaOH	DMF, 1,4-Dioxane, Acetonitrile, Ethanol, Butanol, Toluene	L1 – L20
	*2a	K_2CO_3 Cs_2CO_3 KOH	DMF, 1,4-Dioxane, Acetonitrile, Ethanol, Butanol, Toluene	L1 – L20
	*3a	K_2CO_3	DMF, 1,4-Dioxane, Acetonitrile, Ethanol, Butanol, Toluene	L1 – L20
	4a	Cs_2CO_3	DMF, 1,4-Dioxane, Acetonitrile, Ethanol, Butanol, Toluene	L1 – L20
	5a	KOH	DMF, 1,4-Dioxane, Acetonitrile, Ethanol, Butanol, Toluene	L1 – L20
Solvent deconvolution	*6a	K_2CO_3	DMF, 1,4-Dioxane, Acetonitrile	L1 – L20
	7a	K_2CO_3	Ethanol, Butanol, Toluene	L1 – L20
	8a	K_2CO_3	DMF	L1 – L20
	9a	K_2CO_3	1,4-Dioxane	L1 – L20
	*10a	K_2CO_3	Acetonitrile	L1 – L20
Phosphine deconvolution	11a	K_2CO_3	Acetonitrile	L1, L2, L3, L4, L5
	*12a	K_2CO_3	Acetonitrile	L6, L7, L8, L9, L10
	13a	K_2CO_3	Acetonitrile	L11, L12, L13, L14, L15
	14a	K_2CO_3	Acetonitrile	L16, L17, L18, L19, L20
	15a	K_2CO_3	Acetonitrile	L6
	*16a	K_2CO_3	Acetonitrile	L7
	17a	K_2CO_3	Acetonitrile	L8
	18a	K_2CO_3	Acetonitrile	L9
	19a	K_2CO_3	Acetonitrile	L10

*Represents the best reaction.

Table 2.3: Reaction numbers and reagents under investigation for the Mizoroki-Heck cross-coupling between bromobenzene (PhBr) and butyl acrylate.

Deconvolution step	Reaction number	Bases	Solvents	Phosphine ligand
Base deconvolution	1b	NEt_3 Na_2CO_3 NaOH	DMF, 1,4-Dioxane, Acetonitrile, Ethanol, Butanol, Toluene	L1 – L20
	*2b	K_2CO_3 Cs_2CO_3 KOH	DMF, 1,4-Dioxane, Acetonitrile, Ethanol, Butanol, Toluene	L1 – L20
	*3b	K_2CO_3	DMF, 1,4-Dioxane, Acetonitrile, Ethanol, Butanol, Toluene	L1 – L20
	4b	Cs_2CO_3	DMF, 1,4-Dioxane, Acetonitrile, Ethanol, Butanol, Toluene	L1 – L20
	5b	KOH	DMF, 1,4-Dioxane, Acetonitrile, Ethanol, Butanol, Toluene	L1 – L20
Solvent deconvolution	*6b	K_2CO_3	DMF, 1,4-Dioxane, Acetonitrile	L1 – L20
	7b	K_2CO_3	Ethanol, Butanol, Toluene	L1 – L20
	8b	K_2CO_3	DMF	L1 – L20
	9b	K_2CO_3	1,4-Dioxane	L1 – L20
	*10b	K_2CO_3	Acetonitrile	L1 – L20
Phosphine deconvolution	11b	K_2CO_3	Acetonitrile	L1, L2, L3, L4, L5
	*12b	K_2CO_3	Acetonitrile	L6, L7, L8, L9, L10
	13b	K_2CO_3	Acetonitrile	L11, L12, L13, L14, L15
	14b	K_2CO_3	Acetonitrile	L16, L17, L18, L19, L20
	15b	K_2CO_3	Acetonitrile	L6
	*16b	K_2CO_3	Acetonitrile	L7
	17b	K_2CO_3	Acetonitrile	L8
	18b	K_2CO_3	Acetonitrile	L9
	19b	K_2CO_3	Acetonitrile	L10

*Represents the best reaction.

Table 2.4: Reaction numbers and reagents under investigation for the Suzuki cross-coupling between phenylboronic and 4-bromotoluene.

Deconvolution step	Reaction number	Bases	Solvents	Phosphine ligands
Base deconvolution	1c	NEt_3 Na_2CO_3 NaOH	Toulene, DMF, 1,4-Dioxane, Ethanol, Butanol, Acetonitrile	L1 – L14
	*2c	KOH Cs_2CO_3 K_2CO_3	Toulene, DMF, 1,4-Dioxane, Ethanol, Butanol, Acetonitrile	L1 – L14
	3c	KOH	Toulene, DMF, 1,4-Dioxane, Ethanol, Butanol, Acetonitrile	L1 – L14
	4c	Cs_2CO_3	Toulene, DMF, 1,4-Dioxane, Ethanol, Butanol, Acetonitrile	L1 – L14
	*5c	K_2CO_3	Toulene, DMF, 1,4-Dioxane, Ethanol, Butanol, Acetonitrile	L1 – L14
Solvent deconvolution	6c	K_2CO_3	Toulene, DMF, 1,4-Dioxane	L1 – L14
	7c	K_2CO_3	Ethanol, Butanol, Acetonitrile	L1 – L14
	*8c	K_2CO_3	Ethanol	L1 – L14
	9c	K_2CO_3	Butanol	L1 – L14
	10c	K_2CO_3	Acetonitrile	L1 – L14
Phosphine ligand deconvolution	11c		Ethanol	L1 – L8
	*12c		Ethanol	L11, L12, L16, L17, L19, L20, L21
	13c		Ethanol	L11
	14c		Ethanol	L12
	*15c		Ethanol	L16
	*16c		Ethanol	L17
	17c		Ethanol	L19
	18c		Ethanol	L20
	*19c		Ethanol	L21

*Represents the best reaction or reagent

Table 2.5: Reaction numbers and reagents under investigation for the Suzuki cross-coupling between phenylboronic and 4-bromotoluene using a different deconvolution approach.

Deconvolution step	Reaction number	Bases	Solvents	Phosphine ligands
Base deconvolution	1d	NaOH	Toulene, DMF, 1,4-Dioxane, Ethanol, Butanol, Acetonitrile	L1 – L14
	2d	Na_2CO_3	Toulene, DMF, 1,4-Dioxane, Ethanol, Butanol, Acetonitrile	L1 – L14
	3d	NEt_3	Toulene, DMF, 1,4-Dioxane, Ethanol, Butanol, Acetonitrile	L1 – L14
	*4d	K_2CO_3	Toulene, DMF, 1,4-Dioxane, Ethanol, Butanol, Acetonitrile	L1 – L14
	5d	KOH	Toulene, DMF, 1,4-Dioxane, Ethanol, Butanol, Acetonitrile	L1 – L14
	6d	Cs_2CO_3	Toulene, DMF, 1,4-Dioxane, Ethanol, Butanol, Acetonitrile	L1 – L14
Solvent deconvolution	*7d	K_2CO_3	Ethanol	L1 – L14
	8d	K_2CO_3	Butanol	L1 – L14
	9d	K_2CO_3	Acetonitrile	L1 – L14
	10d	K_2CO_3	Toluene	L1 – L14
	11d	K_2CO_3	1,4-Dioxane	L1 – L14
	12d	K_2CO_3	DMF	L1 – L14
Phosphine ligand deconvolution	13d	K_2CO_3	Ethanol	L11
	14d	K_2CO_3	Ethanol	L12
	*15d	K_2CO_3	Ethanol	L16
	*16d	K_2CO_3	Ethanol	L17
	17d	K_2CO_3	Ethanol	L19
	18d	K_2CO_3	Ethanol	L20
	*19d	K_2CO_3	Ethanol	L21
	20d	K_2CO_3	Ethanol	L1
	21d	K_2CO_3	Ethanol	L2
	22d	K_2CO_3	Ethanol	L3
	23d	K_2CO_3	Ethanol	L4
	24d	K_2CO_3	Ethanol	L5
	25d	K_2CO_3	Ethanol	L7
	26d	K_2CO_3	Ethanol	L8

*Represents the best reaction or reagent

2.2.2.4 Gas chromatography flame ionisation detector (GC-FID) analysis

The reaction mixtures were analysed using GC-FID (Shimadzu 2010 Plus or Perkin Elmer Clarus 580 GC). For the Mizoroki-Heck reaction, a sample (100 µL) was collected from the reaction flask at specific time intervals. The sample was syringe filtered to remove any solid particles. After that, the samples were diluted (1:200) with dichloromethane (DCM). The

retention time of the product (butyl cinnamate) was confirmed by analysing a standard. This was used to identify the best reaction.

For the Suzuki reactions, a sample (300 μL) was collected from the reaction flask at the specific time intervals. The sample was subjected to a small silica column for the removal of inorganic species in the sample. The samples were then syringe filtered and diluted (1:200) with DCM.

2.3 Results and discussion

2.3.1 Mizoroki-Heck C-C coupling between butyl acrylate and aryl halides (PhI, PhBr, PhCl)

The ultra-fast deconvolution of bases, solvents and phosphine ligands used for a model Mizoroki-Heck C-C coupling reaction (**Figure 2.3**) was evaluated. The coupling of butyl acrylate with iodobenzene (PhI), bromobenzene (PhBr) as well as chlorobenzene (PhCl) was investigated.

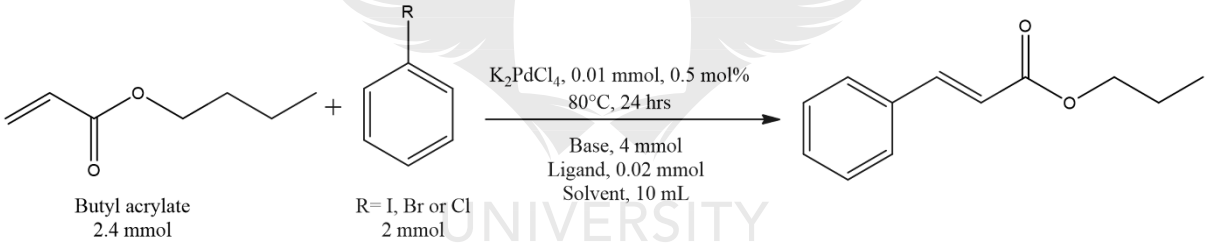

Figure 2.3: Reaction equation for the Mizoroki-Heck C-C coupling between butyl acrylate and an aryl halide.

The reagents were split-and-pooled into several reactions, and activity of each reaction was analysed. The best reaction was further split-and-pooled and deconvoluted. The process was continued until one reagent (i.e. optimal base, solvent, and phosphine ligand) was identified.

The Mizoroki-Heck C-C coupling reaction between an aryl halide and butyl acrylate resulted in the formation of butyl cinnamate. The reaction, which showed an initial product formation at the shortest time interval, was taken as the best reaction. The conversion was calculated for that specific time interval using an external calibration (see chapter 2 SI for the conversions). The best reaction was then further split and deconvoluted. This approach was performed for all the deconvolution steps.

2.3.1.1 Coupling between iodobenzene (PhI) and butyl acrylate

In **Figure 2.4**, a schematic representation of the deconvolution approach followed to identify the best reagents is shown. **Table 2.2** show the reaction numbers corresponding to the reagents under investigation for the deconvolution. For the deconvolution of the bases, two reactions, reaction 1a and 2a, were compared. The GC analysis of reaction 2a showed a product peak appearance at the 2.5 hr time interval, compared to 24 hrs for reaction 1a. Therefore, it was concluded that reaction 2a was the fastest, and it was further split into reactions 3a, 4a and 5a. The reactions were completed, and the GC results indicated that reaction 3a (K_2CO_3) was the fastest, with the product peak appearing at the 2.5 hr time interval. Reaction 4a showed the product formation at 24 hrs. No reaction was observed for reaction 5a. For the following deconvolution steps, K_2CO_3 was used as the base.

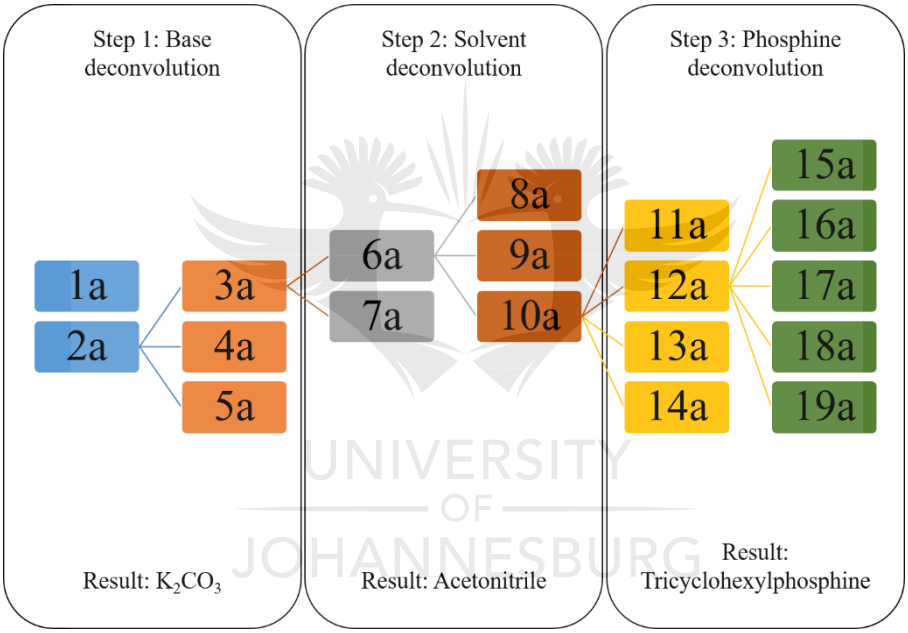

Figure 2.4: Schematic representation of the deconvolution approach followed to identify the best base, solvent, and phosphine ligand in the Mizoroki-Heck C-C coupling reaction between iodobenzene and butyl acrylate. The best base, solvent, and phosphine ligand were identified as K_2CO_3, acetonitrile, and tricyclohexylphosphine.

For the solvent deconvolution, the solvents were split into two reactions, reactions 6a and 7a. Following GC-FID analyses, it was observed that reaction 6a gave the product peak at the 1.5 hr time interval, whilst reaction 7a did not show any product formation; hence no reaction occurred. The reagents used in reaction 6a were further split into reaction 8a, 9a, and 10a. Reaction 10a was identified as the best reaction with a product peak appearing at the 0.5 hr

time interval, compared to 1 and 24 hrs for reaction 8a and 9a, respectively. Acetonitrile was therefore used as the best solvents in the subsequent deconvolution step.

For the final deconvolution step, the phosphine ligands were deconvoluted. This step was carried out by split-and-pooling the 20 phosphine ligands into reactions 11a, 12a, 13a and 14a (**Figure 2.4**), each containing five phosphine ligands. Reaction 12a was identified as the best reaction and was subsequently split into reactions 15a – 19a. The results showed that reaction 16a, containing phosphine L7, gave the fastest product formation around 0.5 hr. Overall, a multidimensional group testing approach could be used to deconvolute bases, solvents, and phosphine ligands, resulting in K_2CO_3, acetonitrile, and tricyclohexylphoshine as the best reagents.

2.3.1.2 Coupling between bromobenzene (PhBr) and butyl acrylate:

The same multidimensional group testing approach was used to deconvolute the bases, solvents and phosphine ligand for the reaction between PhBr and butyl acrylate. The deconvolution was also conducted in 19 reactions, as illustrated in **Table 2.3** and **Figure 2.5**.

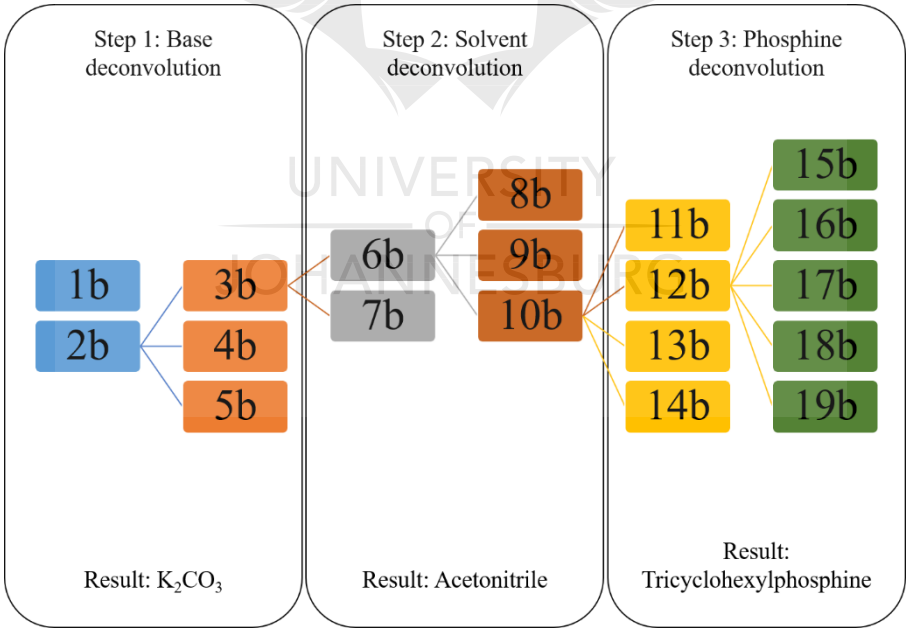

Figure 2.5: Schematic representation of the deconvolution approach followed to identify the best base, solvent, and phosphine ligand in the Mizoroki-Heck C-C coupling reaction between bromobenzene and butyl acrylate. The best base, solvent, and phosphine ligand were identified as K_2CO_3, acetonitrile, and tricyclohexylphosphine.

For both reactions between PhI and PhBr with butyl acrylate, the deconvolution steps resulted in the same optimal base, solvent and phosphine ligand.

2.3.1.3 Coupling between chlorobenzene (PhCl) and butyl acrylate

The C-C coupling of PhCl and butyl acrylate was attempted using the same multidimensional group testing approach; however, no product formation or conversion was observed in the first two reactions. It was therefore concluded that no reaction took place, and the reaction was not further deconvoluted. This is due to the reactivity of the aryl halides that decrease in the order of ArI > ArBr >> ArCl [23, 30, 31]. This indicates that PhCl is not likely to react with the butyl acrylate to form the product butyl cinnamate under the reaction conditions presented here.

2.3.2 Suzuki C-C coupling between phenylboronic acid and 4-bromotoluene

The same strategy was followed for the split-and-pool deconvolution of reagents for a Suzuki reaction to further investigate if the multidimensional group testing strategy can be employed for other reactions. For the Suzuki reaction, phenylboronic acid was used for the C-C coupling to 4-bromotoluene, as illustrated in **Figure 2.6**.

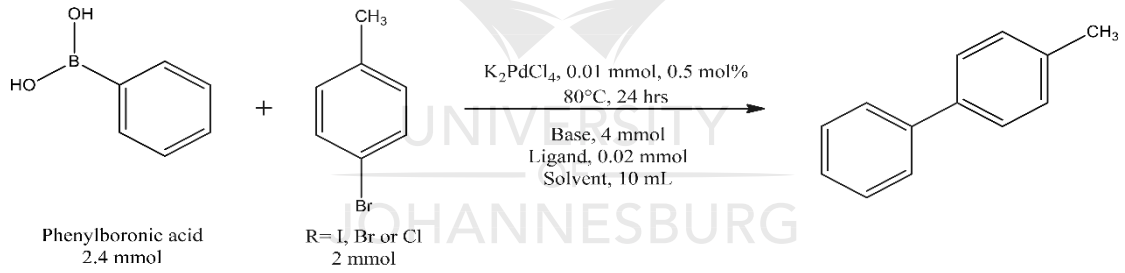

Figure 2.6: Reaction equation for the Suzuki C-C coupling between phenylboronic acid and an aryl halide.

The samples were analysed using GC-FID, and the conversion of the 4-bromotoluene substrate was calculated for each interval using decane as an internal standard. The conversions at 24 hrs were compared to identify the best reaction.

Refer to **Table 2.4** and **Figure 2.7** for the various reactions performed. The six bases were split-and-pooled into two reactions 1c and 2c. The reactions were carried out for 24 hrs, and the results showed that reaction 2c gave the highest conversion in 24 hrs (36%). This reaction was then split into reactions 3c, 4c, and 5c, and all three of the reactions gave a 100% conversion. Therefore, the best reaction was chosen based on the reaction that achieved 100%

conversion the fastest. The best reaction was chosen as reaction 5c (K_2CO_3), which gave a 100% conversion in 1.5 hrs (**Figure S2.4,** chapter 2 SI).

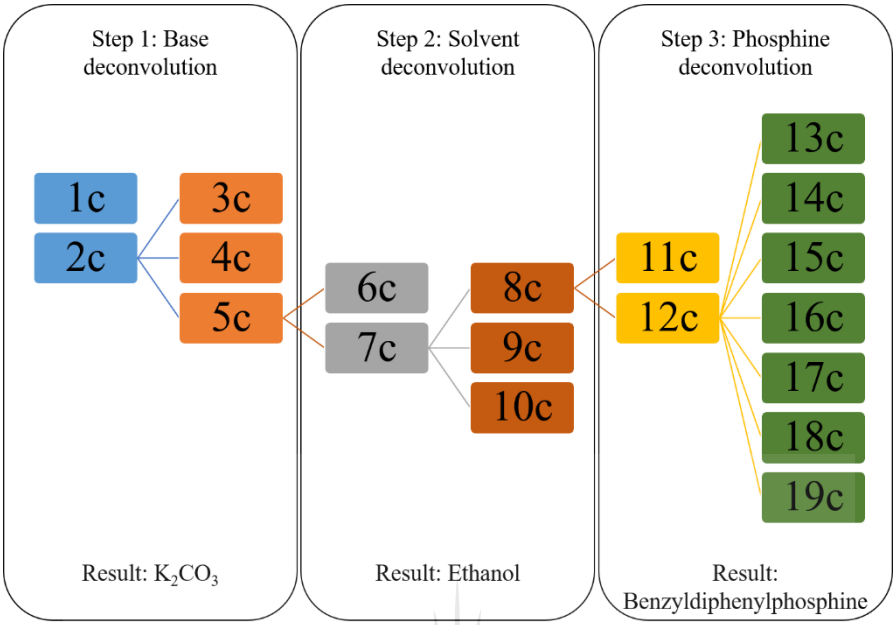

Figure 2.7: Schematic representation of the deconvolution approach to identify the best base, solvent, and phosphine ligand in the Suzuki C-C coupling reaction between phenylboronic acid and 4-bromotoluene. The best base, solvent, and phosphine ligand were identified as K_2CO_3, ethanol, and benzyldiphenylphosphine.

The solvents were split-and-pooled into two reactions 6c and 7c. From the GC results, it was confirmed that reaction 7c was the best reaction since a conversion of 59% was obtained in 24 hrs. Therefore, it was split into reactions 8c, 9c, and 10c. Reaction 8c gave a 98% conversion at 24 hrs and was subsequently identified as the best reaction. Therefore, ethanol was chosen as the optimal solvent. It was observed that the K_2CO_3 base is poorly soluble in the solvent.

For the phosphine ligand deconvolution, 14 phosphine ligands were used (see **Table S2.1**), and split-and-pooled into reactions 11c and 12c, each containing seven phosphine ligands. The reactions were analysed, and the results showed that reaction 12c gave the highest conversion of 95% in 24 hrs, compared to reaction 11c, which gave an 84% conversion for the same time (**Figure S2.7**, chapter 2 SI).

Reaction 12c was then further split into reactions 13c – 19c. Most of the phosphine ligand reactions gave a relatively high conversion of 80% and higher at 24 hrs (**Figure S2.8**). Reaction 15c and 16c both gave a conversion of 98% for 24 hrs. Therefore, reactions 15c and 16c had

to be compared to identify the optimal phosphine ligand. Reaction 16c reached an 80% conversion in 1 hr, compared to 15c, which gave a conversion of 15% at 1 hr (**Figure S2.9**). Therefore, the optimal phosphine ligand was found to be benzyldiphenylphosphine.

2.3.2.1 A variation in the deconvolution strategy for the Suzuki reaction

The deconvolution of the Suzuki reaction reagents was investigated by using a different approach. Initially, the solvents were deconvoluted in the first step, by split-and-pooling the solvents into two reactions containing three solvents each. The six bases and the phosphine ligand mixture were also added. The reactions were carried out for 24 hrs and resulted in 0% conversion. Similarly, starting with the phosphine deconvolution, the same results were obtained (0% conversions). It was concluded that solubility issues arise with all six bases present in the one reaction flask.

Subsequently, the reagents were split into reactions containing only one reagent at a time, as indicated in **Table 2.5** and **Figure 2.8**.

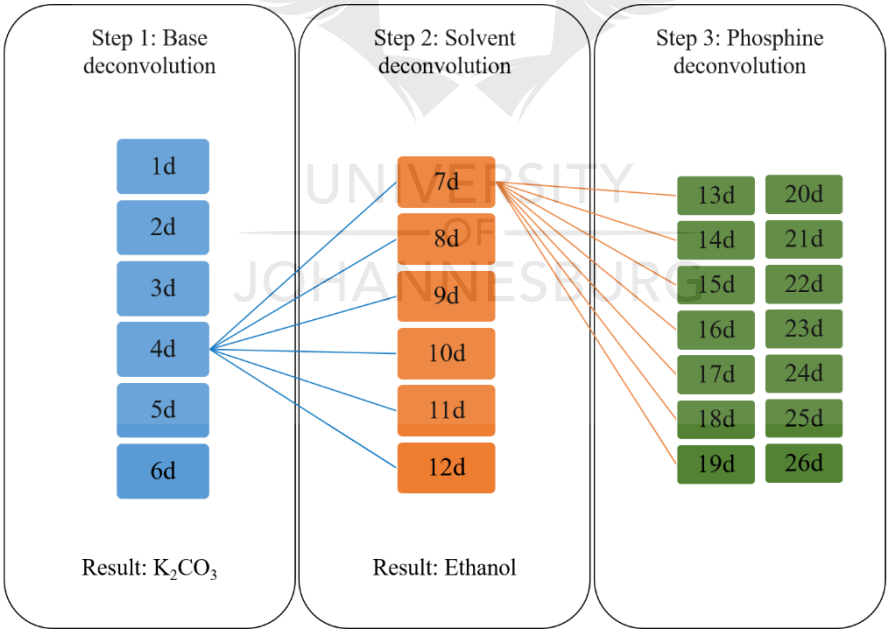

Figure 2.8: Schematic representation of the variation in deconvolution setup for the Suzuki reaction between phenylboronic acid and 4-bromotoluene. This was done to confirm the previous findings (section 2.3.2) determine if the same system can be identified as previously found. The best base and solvent were also found to be K_2CO_3 and ethanol. All phosphine reactions gave similar results (conversions > 90%).

For the deconvolution of the bases, six reactions (reactions 1d – 6d) were used with one base in each. It was observed that the reactions containing K_2CO_3 and Cs_2CO_3, gave similar results each time. A *t*-test was performed to determine if there is a significant difference between the two bases. For each base (K_2CO_3 and $CsCO_3$), there were three replicate experiments where the reaction mixture contained all the solvents and all the phosphine ligands. The null (H_0) and the alternative hypothesis (H_a) is as follows: H_0: $\mu_1 = \mu_2$ (the average conversions of the K_2CO_3 and Cs_2CO_3 reactions are equal) and H_a: $\mu_1 \neq \mu_2$ (the average conversions of K_2CO_3 and Cs_2CO_3 reaction is not equal). The test statistic (*t*) had a value of -0.1887, and the critical value of *t* at a 95% confidence level for 4 degrees of freedom is 2.78. Therefore, the null hypothesis is accepted. This indicates that there is no statistically significant difference between the conversions obtained for K_2CO_3 and Cs_2CO_3. K_2CO_3 was used as the base for the subsequent deconvolution reactions.

For the solvent deconvolution step, the solvents were split into six reactions (Fig. 3). Each reaction, containing K_2CO_3, one solvent and all the ligands. Reaction 7d gave the highest conversion, and it was concluded that ethanol was the best solvent. For the phosphine ligand deconvolution, all the phosphines were evaluated separately (reactions 13d – 26d). As with the first approach, all the phosphine ligands gave high conversions. Conversions of 98%, 98% and 100%, were obtained for reaction 15d, 16d and 19d after 24 hrs, respectively. Therefore, any of these phosphine ligands will be suitable for the reaction

It is known that palladium nanoparticles (PdNPs) form *in-situ* during C-C cross-coupling reactions in the presence of phosphine ligands [20]. These NPs are responsible for the catalytic activity. It is believed that when Pd(0) is formed, the ligands coordinated to the PdNPs to form phosphine ligand stabilised PdNPs. Even though several phosphine ligands were investigated, the results indicated that any of these phosphine ligands could be used in the Suzuki reaction, to form phosphine ligand stabilised NPs.

2.3.3 General aspects of the Mizoroki-Heck and Suzuki cross-coupling reactions

2.3.3.1 The role of the base

The base plays numerous roles in cross-coupling reactions. When palladium acetate ($Pd(OAc)_2$) is used as the Pd precursor with a phosphine ligand such as triphenylphosphine (PPh_3), the base stabilises the $[Pd(0)(PPh_3)_2(OAc)]$ complex. The base also decreases the rate of the oxidative addition step [31]. Most importantly, it is believed that the role of the base in

the Mizoroki-Heck and Suzuki cross-coupling reactions have to do with the elimination of the HX precursor to ultimately regenerate the Pd(0) species, which acts as the catalyst [24]. During this step, the base shifts the equilibrium towards the Pd(0) specie (catalyst), by quenching the HX specie [31, 32].

Moreover, the base also plays an important role in facilitating the slow transmetalation of the boronic acid in the Suzuki reaction. This forms a more stable boronate species which can interact with the Pd centre to facilitate the transmetalation in an intramolecular fashion. It is believed that the base replaces the halide specie in the coordination sphere of the Pd complex, which leads to the transmetalation, which takes place intramolecularly. Secondary or tertiary amines, sodium or potassium acetates, carbonates or bicarbonates can be used as bases [27]; however, K_2CO_3 has been commonly used for both reactions. However, there are no general rules for the selection of the base [33].

2.3.3.2 Role of the solvent

The solvent also plays an important role in Pd-catalysed cross-coupling reactions. The solvent can influence the rate, selectivity and the equilibria of the reactions, and it can determine if the oxidative additions will be the rate-determining step. Solvents are important to ensure that the reactants and products remain in the solution. This is necessary for the dissolution of many species, for example, lipophilic reactants, organometallic, inorganic metal complexes and also the bases and other additives of the reactions [20]. Therefore, the correct solvent has to be selected. Moreover, coordinating solvents might compete with the ligands by coordinating to the Pd species instead of the ligands; this can influence the stability of the catalyst. The solvent can also regulate the temperature of the reaction.

The Mizoroki-Heck reaction is most commonly performed in a dipolar aprotic solvent such as DMF. This is a cheap, highly polar and aprotic solvent capable of coordinating as a ligand to a metal complex, and most organic compounds and inorganic salts can dissolve in DMF [20]. However, with the deconvolution of the solvents, acetonitrile was found to be the best solvent. Zhao *et al.*, [34] showed that when two equivalents of a triphenylphosphine ligand were used with the Pd precursor and acetonitrile as a solvent, good reactivity was seen for the coupling between methyl acrylate and iodobenzene. Moreover, the Mizoroki-Heck reaction was demonstrated in flow chemistry set up using an acetonitrile/water azeotrope as the solvent mixture, in a heterogeneous catalytical system on supported ionic liquid-like phases [35].

As for the Suzuki reaction, very high conversion rates are obtained when a deactivated bromotoluene substrate is used with an alcoholic solvent [20, 23, 36, 37]. Hoffmann *et al.* [23], showed that the catalytic activity of the Suzuki cross-coupling reaction increases in the following sequences, 1,4-dioxane < water < 1,4-dioxane/water (1:1) < ethanol/water (1:1). This clearly shows that the addition of ethanol to the solvent system increases the reactivity. The conversions for the reaction between phenylboronic acid and 4-bromotoluene (using K_2CO_3 as a base) for the above-mentioned solvent systems were as follows, 1,4-dioxane resulted in a conversion of 20%, pure water 88%, and both the 1,4-dioxane/water and ethanol/water solvent systems gave a >99% conversion. It was also observed that the K_2CO_3 base had a higher solubility in the water and alcoholic solvent systems, which explains the increased reactivity. Sarmah *et al.*, [36] obtained similar results (95% yield in 5 min) for Suzuki coupling between 4-bromotoluene and a methoxy-substituted phenylboronic acid in ethanol.

This reasoning can be used to explain why the deconvolution of the solvents resulted in ethanol as the optimal solvent for the Suzuki reaction between 4-bromotoluene and phenylboronic acid. Moreover, it was shown that a deactivated bromotoluene substrate, such as 4-bromotoluene, enhanced the activity of the reaction [23].

2.3.3.3 Role of the phosphine ligand

It is known that phosphine ligands (used to form stable Pd-phosphine complexes) can enhance the efficiency and selectivity of cross-coupling reactions. Trialkyl- and aryl phosphine ligands are mostly used, along with bulky dialkylbiarylphosphines and *N*-heterocyclic carbenes [33]. Moreover, the ligand to Pd ratio (Pd:L) also plays a role in the reactivity of the catalyst for these cross-coupling reactions [33, 34]. This is due to their electron density as well as the bulkiness of the phosphine ligands. Phosphines, having a high electron density, are believed to increase the reactivity of the oxidative addition stage from the metal centre, where the bulkiness increases the reductive elimination process. For example, *tert*-butyl or cyclohexyl substituted phosphines are more reactive compared to triarylphosphine, which has a lower electron density [33, 38].

Bulky and electron-donating phosphine ligands can stabilise the monoligated PdLx complexes, which are formed as an intermediate, and this species is believed to be crucial for the catalytic cycle. It has been shown that monoligated Pd complexes show better reactivity compared to more highly coordinated complexes. This is due to the smaller size of the monoligated

complex, and this can allow the substrate to approach the complex more easily, resulting in a faster reaction [33]. Sometimes when using phosphine ligands, PdNPs are formed *in situ* [25], and it is believed that these NPs are responsible for the catalytic activity of the Pd. Even though PdNPs are assumed to be responsible, it could also be assumed that during the reduction stage (Pd(II) to Pd(0)), the released ligands can coordinate to the PdNPs which are formed. This will ultimately prevent agglomeration of the PdNPs. Therefore, it can be said that phosphine ligands also play an important role in cross-coupling reactions.

It is possible to perform the C-C cross-coupling reactions using a ligand-free system (without the use of any ligands) [22, 26, 39, 40]. However, these systems are less stable, and the reduction of Pd(II) to Pd(0) can result in other forms of Pd, including Pd nanoparticles (PdNPs) or Pd black.

2.4 Conclusion

In conclusion, a multidimensional group testing strategy was employed for the deconvolution of six bases, six solvents and up to 20 phosphine ligands in the Mizoroki-Heck and Suzuki C-C cross-coupling reactions. The optimal base, solvent and phosphine ligand for the Mizoroki-Heck reaction was K_2CO_3, acetonitrile and tricyclohexylphosphine, respectively. For the Suzuki reaction, it was found that K_2CO_3, ethanol and benzyldiphenylphosphine ligand were the optimal reagents. The optimal reagents which resulted from the deconvolution strategy are comparable to literature reagents used for these specific cross-coupling reactions. Using this strategy, one can significantly reduce the number of reactions necessary to optimise each reaction. The number of reactions was reduced from approximately 720 reactions to 19 reactions for each of the cross-coupling reactions evaluated in this paper.

2.5 Acknowledgements

This work was supported by the National Research Foundation of South Africa {Grant specific unique reference number (UID) 5386}, and the University of Johannesburg with funding. We would like to acknowledge Mr D. Harris and Dr R. Meyer from Shimadzu South Africa (Pty) Ltd for their analytical instruments.

2.6 References

[1] R. Crabtree, Combinatorial and rapid screening approaches to homogeneous catalyst discovery and optimization, Chem. Commun. (1999) 1611–1616.

[2] E. Wolf, E. Richmond, J. Moran, Identifying lead hits in catalyst discovery by screening and deconvoluting complex mixtures of catalyst components, Chem. Sci. 6 (2015) 2501–2505.

[3] M.T. Reetz, T. Sell, A. Meiswinkel, G. Mehler, A New Principle in Combinatorial Asymmetric Transition-Metal Catalysis: Mixtures of Chiral Monodentate P Ligands, Angew. Chemie Int. Ed. 42 (2003) 790–793.

[4] T.E. Mallouk, E.S. Smotkin, Combinatorial catalyst development methods, in: Handb. Fuel Cells, 2010.

[5] A. Mittasch, W. Frankenburg, Early Studies of Multicomponent Catalysts, Adv. Catal. 2 (1950) 81–104.

[6] M.T. Reetz, Combinatorial Methods in Catalysis by Metal Complexes, Compr. Coord. Chem. II. 9 (2004) 509–548.

[7] S. Bergh, P. Cong, B. Ehnebuske, S. Guan, A. Hagemeyer, H. Lin, Y. Liu, C.G. Lugmair, H.W. Turner, A.F. Volpe, Combinatorial heterogeneous catalysis: oxidative dehydrogenation of ethane to ethylene, selective oxidation of ethane to acetic acid, and selective ammoxidation of propane to acrylonitrile, Top. Catal. 23 (2003) 65–79.

[8] K.D. Shimizu, B.M. Cole, C.A. Krueger, K.W. Kuntz, M.L. Snapper, A.H. Hoveyda, Search for Chiral Catalysts Through Ligand Diversity: Substrate-Specific Catalysts and Ligand Screening on Solid Phase, Angew. Chemie Int. Ed. English. 36 (1997) 1704–1707.

[9] F.C. Moates, M. Somani, J. Annamalai, J.T. Richardson, D. Luss, R.C. Willson, Infrared Thermographic Screening of Combinatorial Libraries of Heterogeneous Catalysts, Ind. Eng. Chem. Res. 35 (1996) 4801–4803.

[10] S.M. Senkan, High-throughput screening of solid-state catalyst libraries, Nature. 394 (1998) 350–353.

[11] A.M. Cassell, S. Verma, L. Delzeit, M. Meyyappan, J. Han, Combinatorial optimization of heterogeneous catalysts used in the growth of carbon nanotubes, Langmuir. 17 (2001) 260–264.

[12] P. Cong, R.D. Doolen, Q. Fan, D.M. Giaquinta, S. Guan, E.W. Mcfarland, D.M. Poojary, K. Self, H.W. Turner, W.H. Weinberg, High-throughput Synthesis and Screening of

Combinatorial Heterogeneous Catalyst Libraries, Angew. Chemie. 38 (1999) 483–488.

[13] A. Holzwarth, H.W. Schmidt, W.F. Maier, Detection of catalytic activity in combinatorial libraries of heterogeneous catalysts by IR thermography, Angew. Chemie - Int. Ed. 37 (1998) 2644–2647.

[14] K. Krantz, S. Ozturk, S. Senkan, Application of combinatorial catalysis to the selective reduction of NO by C3H6, Catal. Today. 62 (2000) 281–289.

[15] D.E. Akporiaye, I.M. Dahl, A. Karlsson, R. Wendelbo, Combinatorial approach to the hydrothermal synthesis of zeolites, Angew. Chemie - Int. Ed. 37 (1998) 609–611.

[16] J. Klein, C.W. Lehmann, H.W. Schmidt, W.F. Maier, Combinatorial Material Libraries on the Microgram Scale with an Example of Hydrothermal Synthesis, Angew. Chemie - Int. Ed. 37 (1999) 3369–3372.

[17] A.C. Cooper, L.H. McAlexander, D.-H. Lee, M.T. Torres, R.H. Crabtree, Reactive Dyes as a Method for Rapid Screening of Homogeneous Catalysts, J. Am. Chem. Soc. 120 (1998) 9971–9972.

[18] S.J. Taylor, J.P. Morken, Thermographic selection of effective catalysts from an encoded polymer- bound library, Science. 280 (1998) 267–270.

[19] P.J. Fagan, E. Hauptman, R. Shapiro, A. Casalnuovo, Using Intelligent/Random Library Screening To Design Focused Libraries for the Optimization of Homogeneous Catalysts: Ullmann Ether Formation, J. Am. Chem. Soc. 122 (2000) 5043–5051.

[20] J. Sherwood, J.H. Clark, I.J.S. Fairlamb, J.M. Slattery, Solvent effects in palladium catalysed cross-coupling reactions, Green Chem. 21 (2019) 2164–2213.

[21] K. Suzuki, Y. Hori, Y. Nakayama, T. Kobayashi, Development of new phosphine ligands (BRIDPs) for efficient palladium-catalyzed coupling reactions and their application to industrial processes, J. Synth. Org. Chem. Japan. 69 (2011) 1231–1240.

[22] Y. Sun, K. Meng, J. Zhang, M. Jin, N. Huang, G. Zhong, Additive- and Ligand-Free Cross-Coupling Reactions between Alkenes and Alkynes by Iridium Catalysis, Org. Lett. 21 (2019) 4868–4872.

[23] I. Hoffmann, B. Blumenröder, S.O. neé Thumann, S. Dommer, J. Schatz, Suzuki cross-coupling in aqueous media, Green Chem. 17 (2015) 3844–3857.

[24] A.F.P. Biajoli, C.S. Schwalm, J. Limberger, T.S. Claudino, A.L. Monteiro, Recent progress in the use of Pd-catalyzed CC cross-coupling reactions in the synthesis of pharmaceutical compounds, J. Braz. Chem. Soc. 25 (2014) 2186–2214.

[25] A.M. Trzeciak, A.W. Augustyniak, The role of palladium nanoparticles in catalytic C–C cross-coupling reactions, Coord. Chem. Rev. 384 (2019) 1–20.

[26] S.N. Jadhav, A.S. Kumbhar, C. V Rode, R.S. Salunkhe, Ligand-free Pd catalyzed cross-coupling reactions in an aqueous hydrotropic medium, Green Chem. 18 (2016) 1898–1911.

[27] S. Jagtap, Heck reaction—state of the art, Catalysts. 7 (2017) 267.

[28] A. Biffis, M. Zecca, M. Basato, Palladium metal catalysts in Heck C-C coupling reactions, J. Mol. Catal. A Chem. 173 (2001) 249–274.

[29] M.R. Wilson, D.C. Woska, A. Prock, W.P. Giering, The quantitative analysis of ligand effects (QALE). The aryl effect, Organometallics. 12 (1993) 1742–1752.

[30] M.T. Reetz, G. Lohmer, R. Schwickardi, A new catalyst system for the Heck reaction of unreactive aryl halides, Angew. Chemie Int. Ed. 37 (1998) 481–483.

[31] A. Jutand, Mechanisms of the Mizoroki–Heck reaction, Mizoroki–Heck React. 1 (2009) 1.

[32] C.B. Ziegler Jr, R.F. Heck, Palladium-catalyzed vinylic substitution with highly activated aryl halides, J. Org. Chem. 43 (1978) 2941–2946.

[33] R. Martin, S.L. Buchwald, Palladium-catalyzed Suzuki− Miyaura cross-coupling reactions employing dialkylbiaryl phosphine ligands, Acc. Chem. Res. 41 (2008) 1461–1473.

[34] F. Zhao, B.M. Bhanage, M. Shirai, M. Arai, Effect of triphenylphosphine concentration on the kinetics of homogeneous Heck reaction in different solvents, J. Mol. Catal. A Chem. 142 (1999) 383–388.

[35] C. Petrucci, G. Strappaveccia, F. Giacalone, M. Gruttadauria, F. Pizzo, L. Vaccaro, An E-Factor Minimized Protocol for a Sustainable and Efficient Heck Reaction in Flow, ACS Sustain. Chem. Eng. 2 (2014) 2813–2819.

[36] G. Sarmah, M. Mondal, U. Bora, Alcoholic solvent-assisted ligand-free room temperature Suzuki–Miyaura cross-coupling reaction, Appl. Organomet. Chem. 29 (2015) 495–498.

[37] X. Rao, C. Liu, J. Qiu, Z. Jin, A highly efficient and aerobic protocol for the synthesis of N-heteroaryl substituted 9-arylcarbazolyl derivatives via a palladium-catalyzed ligand-free Suzuki reaction, Org. Biomol. Chem. 10 (2012) 7875–7883.

[38] D.S. Surry, S.L. Buchwald, Biaryl phosphane ligands in palladium-catalyzed amination, Angew. Chemie Int. Ed. 47 (2008) 6338–6361.

[39] C. Pan, M. Liu, L. Zhang, H. Wu, J. Ding, J. Cheng, Palladium catalyzed ligand-free Suzuki cross-coupling reaction, Catal. Commun. 9 (2008) 508–510.

[40] B. Luo, J. Wang, D. Ge, X. Li, X. Cao, Y. Pan, H. Gu, Efficient and ligand free palladium

catalyst for Suzuki and Heck cross-coupling reactions, Sci. China Chem. 57 (2014) 1310–1314.

Chapter 3

Robotics-Assisted High-throughput Catalytic Investigation of PVP Nanoparticles in the Oxidation of Morin

Chapter 3

Robotics-Assisted High-throughput Catalytic Investigation of PVP Nanoparticles in the Oxidation of Morin

Graphical Abstract

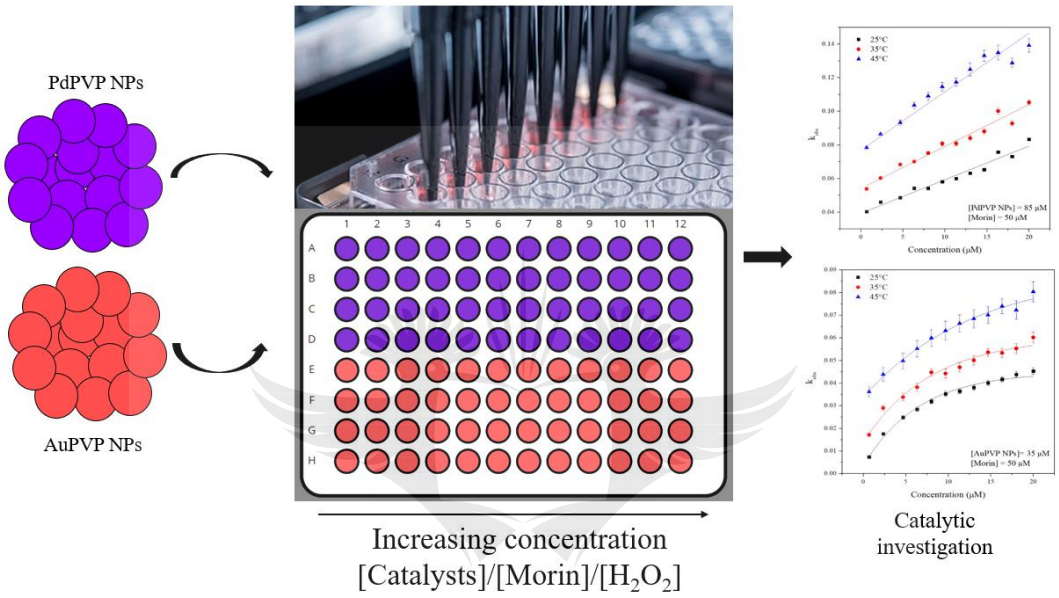

By employing a pipetting robot, one can investigate the kinetics of nanoparticle catalysts for the oxidation or morin.

Abstract

A robotics-assisted high-throughput system for the fast and effective catalytic evaluation of Pd- and Au-PVP nanoparticles (NPs) was investigated. Palladium and gold PVP NPs were synthesised by employing ethylene glycol in the polyol method. These NPs were evaluated for the oxidation of morin using a high-throughput system including a liquid handling robot, a 96-well plate and a microplate reader. The catalyst concentration variation step for both catalysts (Pd- and Au-PVP NPs) was performed in one experiment in a 96-well plate. A concentration range including 12 concentrations, in four replicates, was investigated simultaneously. Therefore, with one experiment, the optimal concentration of both catalysts could be determined. A similar approach was followed for the concentration variation steps of the morin and the hydrogen peroxide at different temperatures. This was done to determine the effect of the concentration on the observed rate (k_{obs}). The catalytic oxidative degradation of morin can be an investigation in a fast and effective way by employing robotics and a high-throughput system. This system can also potentially be applied for the screening of catalysts (homogeneous and heterogeneous catalyst), as well as the parallel synthesis of nanoparticles, particularly dendrimer encapsulated nanoparticles.

3.1 Introduction

The catalysis industry is a fast-growing multi-billion dollar industry, which is responsible for numerous processes such as polymerisation, plastic manufacturing, pharmaceuticals, detergents, and many more [1]. It is known that more than 85% of industrial products are made using a catalyst. The use of metal nanoparticles (MNPs) has attracted lots of attention in recent years, especially in catalysis, electrical and optical industries. This is attributed to the particles that show enhanced electronic, optical, catalytic, and biological activity compared to its bulk material [2, 3]. Nanoparticles are defined as small particles with sizes ranging from 1 - 100 nm. To be classified as nanoparticles, the particles should contain at least one dimension in the nanometer range [4]. Metal nanoparticles are widely used in industries such as catalysis, medical and pharmaceutical industries as well as the paint industry *etc.* due to their unique properties and their small size. The physicochemical properties of NPs include intrinsic and extrinsic properties. Intrinsic properties include electrical, magnetic and/or optical properties whereas extrinsic properties include the ability of the particles to aggregate and/or agglomerate due to their high surface area (or surface-to-volume ratio) [5].

Metal nanoparticle catalysts are an important class of catalysts since they are involved in many industrial reactions such as hydrogenation [6, 7], dehydrogenation, hydrogenolysis, isomerisation as well as oxidation [8–10]. This is due to extensive research that indicates that these MNPs are active due to their high surface-to-volume ratio. This advantage of nanoparticles gives them the ability to lower the activation energy of a reaction, increasing the reaction rate, and ultimately gives rise to the desired products [2]. Moreover, noble MNPs, such as Au-, Pd-, Ag-, Ru-, and Pt-NPs, are used more extensively due to their close-packed structure and valence bands which allows electrons to move freely, making them even more reactive [11]. The performance of MNPs relies on their size, shape, crystal structure as well as textural parameters, which can sometimes lead to aggregation and agglomeration of the nanoparticles. This may be due to the lack of a stabilisation coating around the nanoparticles, or if the NPs are not immobilised onto a support. Most commonly, nanoparticles are synthesised in the presence of a coating or a stabilising agent, to keep the nanoparticles stable, preventing aggregation and agglomeration.

The synthesis of stable MNPs involves the reduction of metal ions in the presence of a stabiliser. A stabiliser (usually polymers, ligands, or surfactants) is used to control the size of the particles and also to keep the particles stable in solution preventing aggregation, agglomeration or precipitation. It is important to note that the stabiliser used may also passivate the surface of NPs, and for the application of catalysis, fully passivated surfaces should be avoided since it should be possible for the substrates to interact with the surface [12]. It is therefore important to prepare NPs using a method that may stabilise the particles and control the particle size without blocking active sites.

Organic stabilisers are most commonly used in the control of nanoparticle growth and size. Some of the organic stabilisers include: polyethylene oxide (PEO) [13], poly(N-vinyl-2-pyrrolidone or polyvinylpyrrolidone (PVP) [14] and polyvinyl carbazole (PVK) [15]. When the nanoparticles are synthesised, one of these stabilisers is added to the reaction flask to cap and stabilise the surface of the nanoparticle [16]. For this study, the nanoparticles were synthesised using a polyvinylpyrrolidone (PVP) stabilising agent. The PVP coats and stabilises the particles by repulsive forces that occur due to its hydrophobic groups that come into contact with the solvent [17]. Polyvinylpyrrolidone is an organic polymer consisting of C=O, C-N and CH_2 groups. This stabilising agent is very commonly used in the synthesis of nanoparticles. This is because the polymer contains strong hydrophilic groups (the pyrrolidone moiety) as

well as a hydrophobic component, the alkyl group [17]. The polar amide group within the pyrrolidone ring and the apolar methylene and methine groups make it possible to dissolve PVP in water or other non-aqueous solvents [18].

In the synthesis of PVP nanoparticles, the polyol method can be used. The polyol method employs ethylene glycol as a solvent and a reducing agent [19]. The PVP, along with the metal salt is dissolved in the ethylene glycol, and the resulting mixture is heated up. During the heating stage, the ethylene glycol reduces the metal ions to nanoparticles and the PVP caps the particles, stabilising them to prevent aggregation and agglomeration. Many metallic NPs have been synthesised using the polyol method with PVP as a capping agent. These include gold nanoparticles [20–23], silver nanoparticles [24–27], palladium nanoparticles [28–31], and copper nanoparticles [32] just to mention a few. Other particles, including Pt, Co, Ni, and bimetallic NPs have also been synthesised using this method [17]. The polyol method for nanoparticle synthesis was first described by Fievet *et al.* [33] in 1989, and in recent years it has not only been used for the synthesis of metal nanoparticles but also many other metal nanostructures [27].

There is a growing concern regarding the pollution of dyes into the environment. Dyes are extensively used in many industries including; textiles, the printing of paper, food processing, cosmetics, as well as in the pharmaceutical industry, and the list go on. This is of major concern since this pollution may cause various environmental and health hazards [34]. Therefore, much research is ongoing to find methods for the removal of such dyes from the environment.

Organic dyes are most commonly degraded by methods such as catalytic oxidation, adsorption, photodegradation, and electrochemical methods [34]. Other methods that can also be used include biodegradation and coagulation [9]. Among these techniques, catalytic oxidation is likely the best method for the degradation or removal of organic dyes. Morin is a dye that is found in teas, fruits, and vegetables, as well as the chemical industry [34–36]. It is a non-toxic flavonoid (unlike other dyes found in the effluent from the industrial sector) and is mostly used as a polyphenolic dye for the catalytic study of bleaching in laundry detergents [37]. Morin is often used as a dye for model oxidation reaction (**Scheme 3.1** and **Scheme 3.2**) to study different catalytic systems [2, 36, 37].

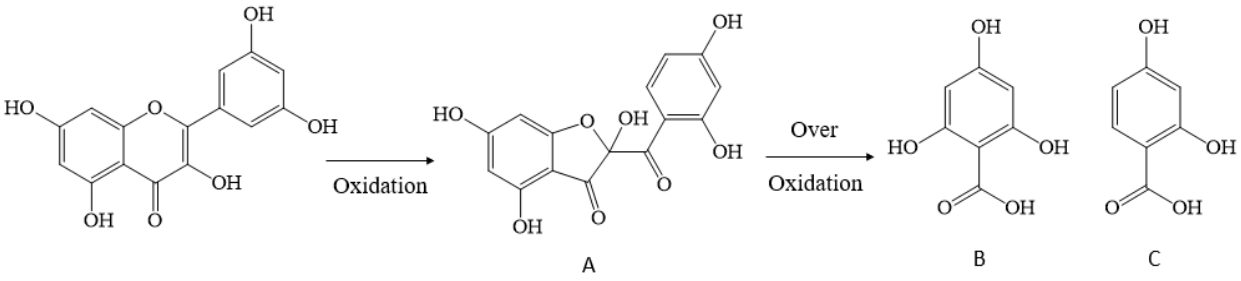

Scheme 3.1: The oxidation and over-oxidation of morin.

In this study, PVP NPs (Au and Pd) were employed as catalysts for the oxidative degradation of morin. Noble-metal NPs such as palladium [34, 38] and gold nanoparticles [2, 39] are often used for the catalytic degradation of pollutants due to their high catalytic activity. Gold nanoparticles are used due to their unique electromagnetic and chemical properties [40] and are relatively stable and can remain in solution for longer periods with less aggregation [36]. However, Pd-NPs are more easily aggregated due to their high specific surface energy [34].

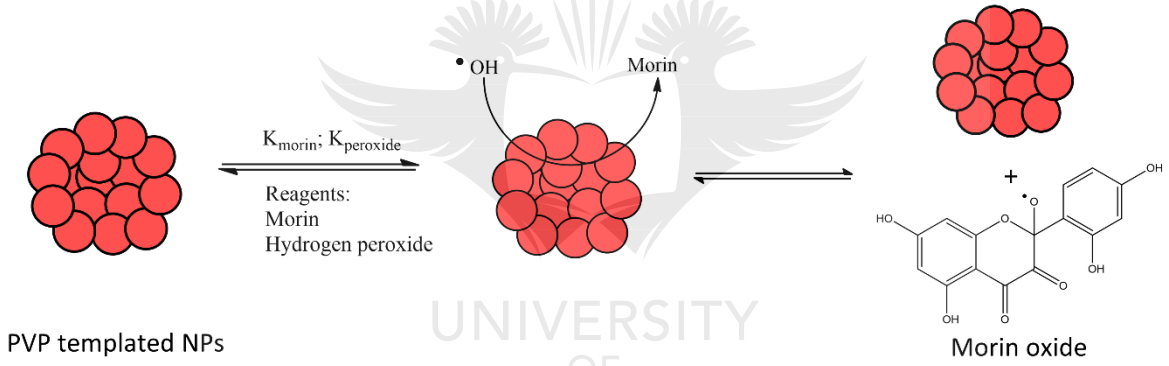

Scheme 3.2: Pseudo-first kinetic scheme of the oxidation of morin by PVP templated nanoparticles. Both the morin and hydrogen peroxide adsorbs to the surface of the particle for the reaction to take place.

Catalyst discovery using the conventional method involves the synthesis and characterisation of one catalyst at a time. This method, referred to as a sequential method, is tedious and only a few catalysts or reactions can be successfully discovered or evaluated. Often limitations and struggles are not mentioned, and the best results or highest yields of a reaction, are reported. However, it is known that the synthesis, applications and results are far more complex, and the limitations are never-ending [41]. Researchers are now exploring alternative methods for catalyst discovery and implementing high-throughput, combinatorial and/ or miniaturisation techniques for this. High-throughput strategies, also sometimes referred to as combinatorial approach, have become a trend to explore catalysis rapidly. The terms high-throughput and/or

combinatorial approach refers to an automated parallel or rapid sequential synthesis or evaluation of materials and reactions [42].

The pharmaceutical and biotechnology industries initially introduced the use of high-throughput or combinatorial chemistry for drug discovery [43]. This approach is rapidly expanding and can now also applied to modern-day chemistry. This technique is also being applied for catalysis, where homogeneous and heterogeneous catalysts are synthesised, screened, and discovered swiftly. The conventional one at a time approach is usually based on trial-and-error processes [44]. However, using the high-throughput or combinatorial strategy, a large number of catalysts can be evaluated simultaneously, shortening the discovery process dramatically [45]. This technique has already been used in fields such as luminescence [46, 47], magnetoresistivity [48], ferroelectric/dielectric materials [49] and also solid-state catalysis [44].

Numerous robotics techniques can be employed to shorten this process even more. The robots can pipette the required amount of catalyst and reagents into destination plates to be screened. The Opentrons liquid handling pipetting robot is an example of such a robot. The Opentrons is an Open-source liquid handling robot that can accurately dispense small volumes of 1 µL into a 384-well plate. Other microtiter plates can also be used, which includes 6-, 12-, 24- and 96-well plates. The first version of this robot, the OT1, is compatible with most tips and pipettes being used in the labs. However, the second version, the OT2, comes with a custom-made pipetting module/s which can accommodate any tips. The applications mostly include life sciences where it is used for polymerase chain reaction (PCR), nucleic acid extraction and purification, enzyme-linked immunosorbent assay (ELISA), dilutions, and basic pipetting. To the best of our knowledge, the Opentrons robots have not been used for the evaluation of the catalytic degradation of morin, nor the screening of catalysts for specific reactions.

The Opentrons was used for the fast and effective evaluation of Au- and Pd-PVP NPs in the oxidation of morin. Such a pipetting robot makes the transfer of the NPs and the reagents (water, hydrogen peroxide, and morin) into a 96-well plate fast and effective. The plate is then transferred to a microplate reader to monitor the decrease in absorbance.

3.2 Experimental

3.2.1 Materials

Morin hydrate ($C_{13}H_{10}O_7.xH_2O$, ≥98.0%), K_2PdCl_4 salt (99%), gold(III) chloride salt (99%), polyvinylpyrrolidone (PVP, 10 000 average mol weight), ethylene glycol (99%), sodium hydroxide (NaOH, 99%) and hydrogen peroxide (50% w/v) were all purchased from Sigma-Aldrich. All chemicals were used as received, without any further purification.

3.2.2 Instrumentation

3.2.2.1 Opentrons – liquid handling robot (pipetting robot)

To determine the activity of the nanoparticles in a fast and effective way, a liquid handling robot (also known as a pipetting robot) was used for pipetting all the reagents into a microtiter plate. An Opentrons liquid handling robot was used for pipetting of the reagents into a 96-well microtiter plate. This robot was purchased from www.opentrons.com. This allows for the miniaturisation of the reaction and to simultaneously determine the optimum concentration of the Au- and Pd-PVP NPs for the oxidation of morin. All the volumes for the miniaturised reactions were calculated for the use of a 96-well plate (maximum volume of 360 μL). The protocol was designed using the Opentrons protocol designer app. This is a user-friendly protocol designer that allows the user to input all solutions and volumes that are needed in each well. The protocol is then exported and imported into the Opentrons software. The Opentrons can then pipette a specific volume of each solution that is needed in each well.

3.2.2.2 UV/vis microplate reader

Following the addition of the reagents, which include; H_2O, H_2O_2, PVP NPs and morin, the degradative oxidation of morin by the PVP NPs was followed using UV/vis at a wavelength of λ 410 nm. This was accomplished using a microplate reader (PowerWave HT.Biotek microplate reader). A plate reader can simultaneously read the absorbance for 96 wells over a specific time.

3.2.2.3 High-resolution transmission electron microscopy (HR-TEM)

A high-resolution transmission electron microscope (HR-TEM) was used to determine the size and morphology of the synthesised nanoparticles. A JOEL JEM-2100F electron microscope with an acceleration voltage of 200 kV was used. The nanoparticles were diluted with dH_2O

and deposited onto a copper grid for the HR-TEM analysis. The sizes of the nanoparticles were determined by using the Image-J software.

3.2.2.4 Data fitting

The catalytic data were fitted and processed using Kinetic Studio using eq 1 to find the observed rate constants (k_{obs}), and Origin Pro 8.5 graphing and modelling software was used for the fittings of the morin and hydrogen peroxide concentration studies (eq 2).

$$y = -Ae^{-k_{obs}[cat]} + C \quad \text{eq 1}$$

$$y = A^{\exp\left(-\frac{x}{t1}\right)} + y_0 \quad \text{eq 2}$$

$$y = A_2 + (A_1 + A_2)/\left(1 + exp\left((x - x_0)/d_x\right)\right) \quad \text{eq 3}$$

$$y = mx + c \quad \text{eq 4}$$

3.2.3 Methods

3.2.3.1 Synthesis of PVP stabilised nanoparticles

The nanoparticles (gold and palladium) were synthesised using the polyol method. The metal salts were dissolved in ethylene glycol in the presence of polyvinylpyrrolidone (PVP). The ethylene glycol serves as both a solvent and a reducing agent [27]. The Pd-PVP NPs were synthesised with a slight modification from Jones *et al*. [50]. The Au-PVP NPs were synthesised using a modified method from Zhou *et al*. [51].

Pd-PVP NPs:

The appropriate amount of K_2PdCl_4 (0.979 g) was weighed out to give a 0.3 M solution. It was dissolved in 10 mL ethylene glycol. Polyvinyl pyrrolidone (0.2775 g) was added to the mixture. The mixture was heated to 120 °C for 2 hrs. During the heating process, the ethylene glycol reduces the Pd^{2+} to Pd^0. The solution changed colour from dark orange to brown. The particles were used without further purification.

Au-PVP NPs:

Au-PVP NPs were also synthesised using the polyol method in ethylene glycol. A solution of PVP (0.5095 g) in ethylene glycol (5 mL) was prepared. The mixture was stirred for 2 hrs at 80 °C, to dissolve all the PVP. A solution of $AuCl_3$ (0.1558 g) was prepared in water (2.5 mL). The Au solution was added to the PVP solution, and the mixture was stirred for approximately

15 min. The pH of the solution was adjusted to 9 by the addition of NaOH (1 M, 2.5 mL). The solution was then heated to 100 °C, and the particles were subsequently formed. The solution changed from dark brown to wine-red. This is a visual indicator that the particles did form [52].

3.2.3.2 Catalytic oxidation of morin

The catalytic oxidation of morin was performed in a 96-well microtiter plate. The morin solution was made up using a 0.1 M carbonate buffer (Na_2CO_3 and $NaHCO_3$). All the reagents which include the water, PVP nanoparticles, hydrogen peroxide, and morin solution were pipetted into each well using the Opentrons liquid handling pipetting robot. Initially, the optimal concentration of the catalysts (Au- and Pd-PVP NPs) was determined. The concentrations were varied from 5 μM to 150 μM, whilst keeping the concentration of the morin and peroxide constant at 50 μM and 0.45 mM, respectively. The concentration range (12 concentrations) of each catalyst was evaluated in four replicates in the 96-well plate. This means that the concentration of each catalyst was increased over 12 columns in 4 rows, respectively. This was done to find the best catalyst concentration for this specific reaction.

Following the optimisation of catalyst concentration, kinetic runs were performed by varying the concentration of morin and the concentration of hydrogen peroxide at three different temperatures, including 25 °C, 35 °C and 45 °C. For the variation of the morin concentration between 3.3 μM and 100 μM, the concentration of the catalysts were kept constant at 35 μM for the Pd-PVP NPs and 85 μM for the Au-PVP NPs. The concentration for the hydrogen peroxide was also kept constant at 0.45 mM. For the variation of the hydrogen peroxide concentration between 0.67 mM and 20 mM, the concentrations of the catalysts were kept constant at 35 μM and 85 μM for the Pd- and Au-PVP NPs, respectively. Moreover, for these runs, the morin concentration was kept constant at 50 μM.

For optimisation of the catalyst concentration, 12 concentrations (final concentrations in the reactions) for both the catalysts (Pd- and Au-PVP NPs) were investigated using four replicates. The concentrations ranged between 5 and 150 μM, as illustrated in **Figure 3.1 (a)**. This is the final concentration of the catalysts in the wells. The maximum volume of each well in a 96-well plate is 360 μL. The volumes (10 – 300 μL) of the NP solutions were increased from columns 1 to 12, to give an increase in the final concentration of each particle. Therefore, the volume of the water over the 12 columns was decreased from 290 μL to 0 μL (in column 12), as illustrated in **Figure 3.1 (b)**. The volumes of the morin and the hydrogen peroxide solutions

were kept constant at 30 μL each, using stock solutions with the concentrations of 600 μM for the morin solution and 5.5 mM for the hydrogen peroxide solution. The concentrations of the stock solutions had to be calculated in such a way that 30 μL of the solutions could be pipetted into 96-well plate, to make up a specific concentration with a maximum volume of 360 μL in each well.

The same principle was followed with the experiments where the morin and hydrogen peroxides concentrations were varied. With the variation in concentration of morin, the volumes for the NP and hydrogen peroxide solutions were kept constant at 30 μL, whilst the volume (10 – 300 μL) of the morin solution was increased over the 12 columns, and the volume of the water was decreased. For the peroxide concentration variation, the volumes of the morin solution and NPs were kept constant at 30 μL, and the volume for the water and the peroxide was decreased and increased over the 12 columns, respectively. For all the studies performed, the morin solution was added last to prevent the reaction from starting before all reagents were added to the wells (See SI for a schematic representation of the well plates).

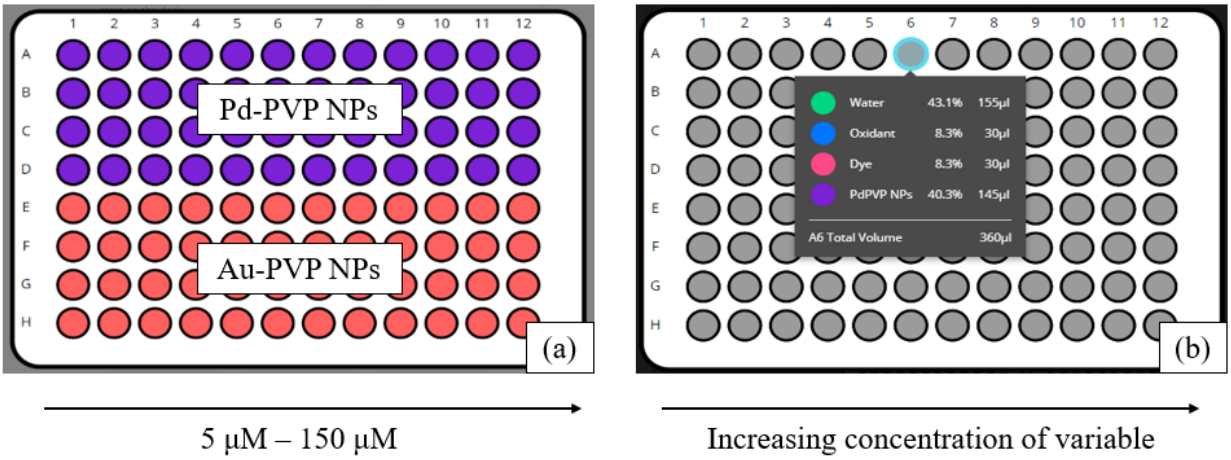

Figure 3.1: **(a)** Representation of the 96-well microtiter plate with the 12 final concentrations of each catalyst, using four replicates. Row A – D represents the four replicates used for the Pd-PVP NPs, and row E – H represents the four replicates used for the Au-PVP NPs. The columns 1 – 12 represents the concentration range of the catalysts increasing from 5 µM to 150 µM. **(b)** Final plate representation, following the addition of all the reagents by the Opentrons for the catalyst concentration variation study. This figure shows the composition of well A6 as an example. This well contains 155 µL water, 30 µL oxidant or hydrogen peroxide (0.45 mM), 30 µL dye or morin solution (50 µM) and 145 µL of PdPVP NPs. For this plate, concentrations (5 – 150 µM) and the volume of the NPs were increased from A1 – D1 to A12 – D12 for the PdPVP NPs, and from E1 – H1 to E12 – H12 for the AuPVP NPs, in a range of 10 – 300 µL.

The Opentrons can fill the 96-well plate in approximately 3 min. Once the plate had been filled with all the reagents, it was placed into a UV/visible light microplate reader to follow the oxidation of morin over 2 hrs.

3.2.4 Plate reader

A microplate reader is a multimodal instrument that can be used for absorbance, fluorescence, and luminescence measurements. This instrument is mostly used in life sciences, for techniques such as cell counting, histology, cell proliferation studies, genotoxicity, and enzyme-linked immunosorbent assay (ELISA), just to mention a few. This instrument can perform a variety of experiments and measurements simultaneously. Numerous microplates can be used in such experiments; these include, 6-, 12-, 24-, 96- and 384-well microtiter plates. A microplate reader made it possible to follow the oxidation of morin for the 96-wells. Therefore, 96 different experiments can be done and measured simultaneously.

This strategy can be used to measure 96 wells simultaneously. Therefore, it can be used to screen different concentrations of multiple catalysts (in this case, two different nanoparticles) and perform concentration varying studies of morin and peroxide simultaneously. This approach makes the catalytic evaluation rapid. The oxidation of morin was followed by using the kinetic method of the microplate reader. The absorbance of the morin was read at λ 410 nm over 2 hrs, at 2 min intervals. The decrease in absorbance of morin at λ 410 nm over time gives an indication of the degradation over time.

3.3 Results and Discussion

3.3.1 Synthesis of polyvinyl pyrrolidone nanoparticles (PVP NPs)

Polyvinylpyrrolidone (PVP) is a homogeneous amphiphilic polymer used in the synthesis of some nanoparticles. This polymer contains a strong hydrophilic component, the amide group, and a hydrophobic group that comprises six carbons per monomer unit. This makes the PVP polymer a suitable capping agent for nanoparticles since it can stabilise surfaces of nanoparticles [27]. Not only this, but PVP can also facilitate the reduction of the metal to metal nanoparticles. This was shown by Wu *et al*. [53] in the synthesis of AgNPs using PVP as a capping agent. They showed that the silver interacted with the PVP by forming an Ag^{+}-O interaction in the carbonyl group. This interaction facilitates an electron exchange between the Ag^{+} and the adjacent nitrogen atom on the pyrrolidone ring. The N atoms contain lone pairs of electrons donated to the Ag, ultimately reducing the Ag^{+} to Ag^{0}, forming the capped Ag-PVP NPs. Some reports have shown that PVP is capable of initiating the nucleation of gold seed particles by the interaction of the gold with the PVP. This not only prevents aggregation from taking place, but it also controls the shape of the nanostructures [17, 21, 54]. The interaction keeping the nanoparticles stable can be attributed to the interaction through the carbonyl or nitrogen atoms in the repeating unit and the metal surface [17].

The PVP stabilising agent and the metal precursors are dissolved in the ethylene glycol. When the mixture is heated, the ethylene glycol reduces the metal ions to zerovalent metal NPs. The size distribution of both the Au-and PdPVP NPs was determined by Transmission Electron Microscopy imaging. For the Pd-PVP NPs, it was found that the average size is approximately 16 nm, and for the Au-PVP NPs, approximately 10 nm (**Figure 3.2**).

3.3.1.1 Transmission Electron Microscopy (TEM) imaging

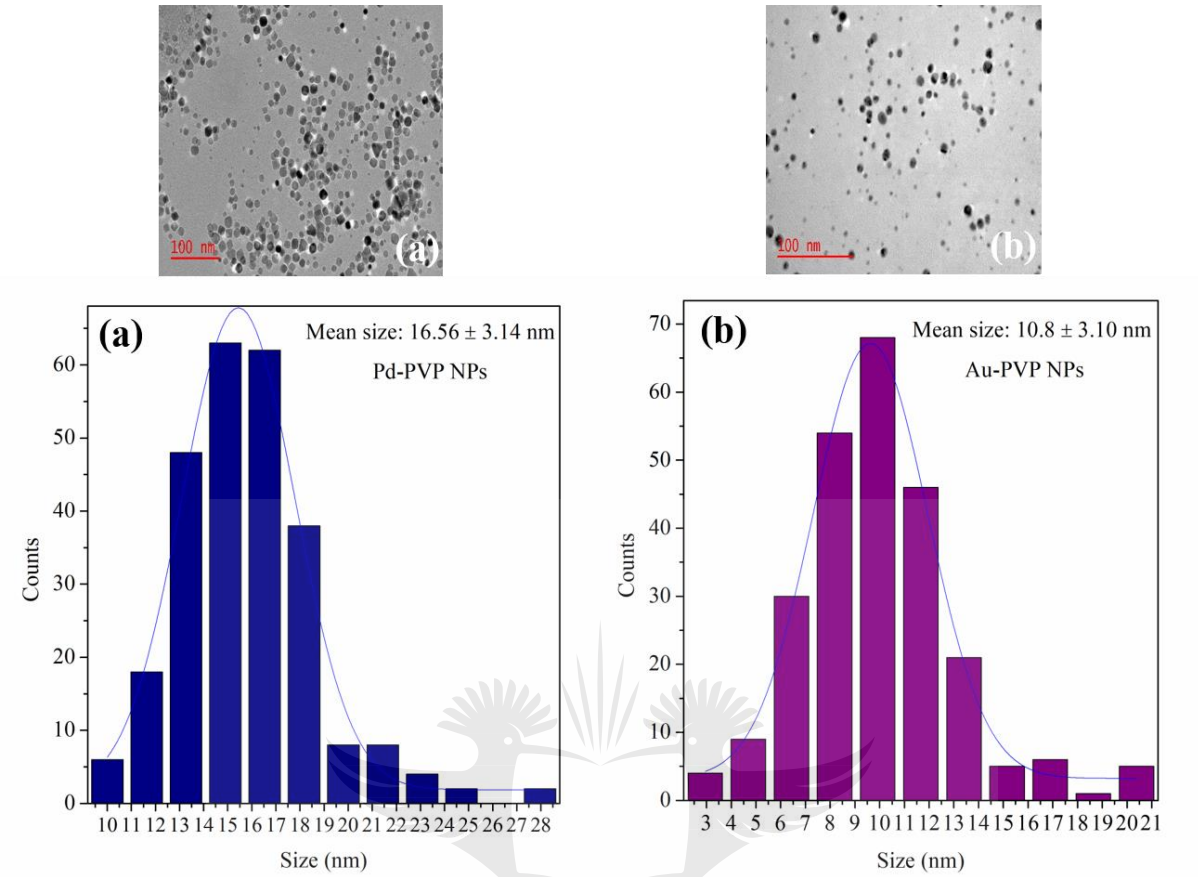

Figure 3.2: Transmission electron microscopy imaging of the **(a)** Pd- and **(b)** Au-PVP NPs synthesised using the polyol method. The Pd-PVP NPs had an average size of 16.56 nm, and the Au-PVP NPs have an average size of 10.8 nm.

Both the Pd-PVP NPs and Au-PVP NPs were spherical in shape (**Figure 3.2**) and had average sizes of 16.56 nm and 10.8 nm, respectively. The synthesised PVP NPs were used for the catalytic oxidative degradation of morin in a 96-well plate.

3.3.2 Opentrons setup for the catalytic study

For this study, the Opentrons was used for pipetting the different reagents needed for the kinetic study of morin oxidation by PVP NPs. The water, hydrogen peroxide, NPs as well as the morin solution could precisely be pipetted into several different wells. The kinetic study of Au- and Pd-PVP NPs involves three stages. Initially, the optimisation of the catalyst concentrations was performed. This optimal concentration is found in the dynamic concentration range, where the k_{obs} increases as the concentration increases. Once a certain concentration is reached, the k_{obs} will form a plateau without any change. The k_{obs} will become constant and independent of the catalyst concentration. Thereafter, different concentrations of morin and peroxide were

investigated at temperatures of 25 °C, 35 °C, and 45 °C. During this stage, the optimal concentration for both catalysts was used.

3.3.3 Catalytic oxidation of morin

Using a high-throughput system, such as a 96-well plate for catalytic evaluation of NPs, small volumes need to be pipetted into each well. When doing this by hand, human error during pipetting may influence the results. Therefore, employing a liquid handling robot for the pipetting of such small volumes can greatly improve the precision and reproducibility of the results. For the catalyst concentration optimisation stage, 12 different concentrations were evaluated simultaneously, using four replicates. When this is done using a conventional approach, replicate experiments are included for the calculation of the average value to improve the accuracy of the result. However, a liquid handling robot may eliminate human error.

The oxidation of morin dye was investigated using a high-throughput approach. During the first few minutes of the reaction, the dye is oxidised to only one product, product A, then upon over-oxidation, two products are formed, products B and C, as illustrated in **Scheme 3.1**. This was observed by Bingwa *et al*. [37]. They observed one absorption band formation at λ 310 nm (with isosbestic points), indicating only one product. Over time, isosbestic points disappeared, indicating the formation of more than one product due to over oxidation. The products were identified by Ali *et al*. [2]. For this study, the oxidation of morin was evaluated for 120 min, which might lead to the over oxidation of the morin resulting in two oxidised products and not one.

3.3.3.1 Catalyst concentration variation

For the concentration optimisation of the Au- and Pd-PVP NPs, the k_{obs} (the observed rate constant, or the decrease of a particular reagent in solution) of each concentration of each replicate were calculated. The average k_{obs} for the four replicates were calculated, as well as the standard deviation, as shown in **Figure 3.3** and **Figure 3.4**.

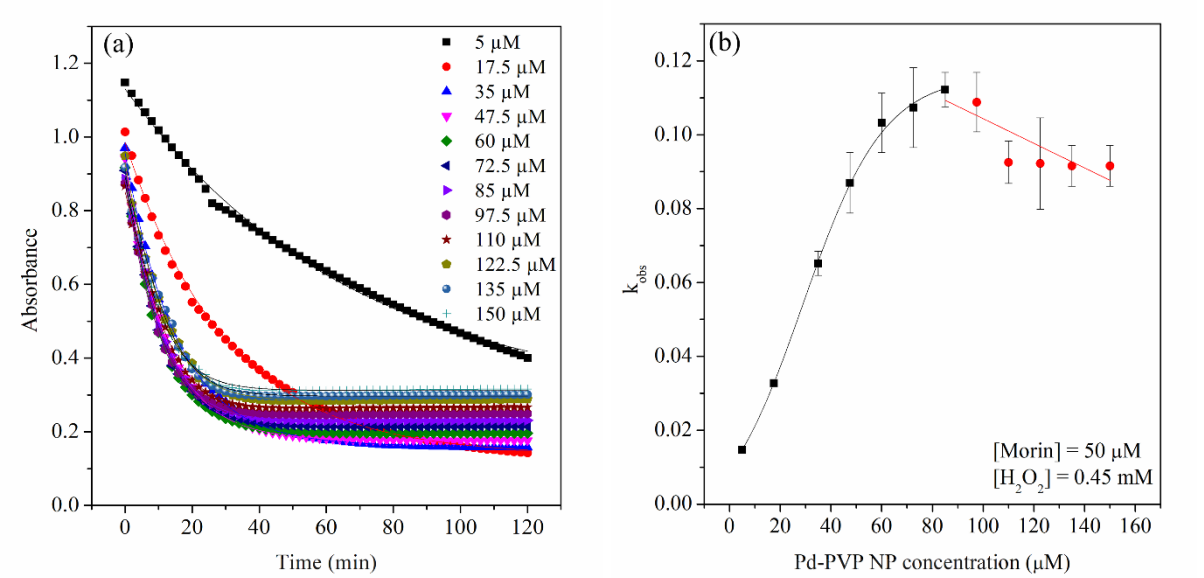

Figure 3.3: (a) The decrease in absorbance at λ 410 nm of morin over time, using Pd-PVP NPs as a catalyst. The points correspond to the concentration of the Pd-PVP NPs. (b) The graph shows the influence of Pd-PVP NP concentration on the observed rate (k_{obs}) for the oxidation of morin at 25 °C. The concentration of morin was 50 µM and for H_2O_2 0.45 mM. Each k_{obs} value corresponds to a certain concentration of Pd-PVP NPs. The black square points represent the catalytic dynamic range, and the red circle points represent the diffusion limitation domain.

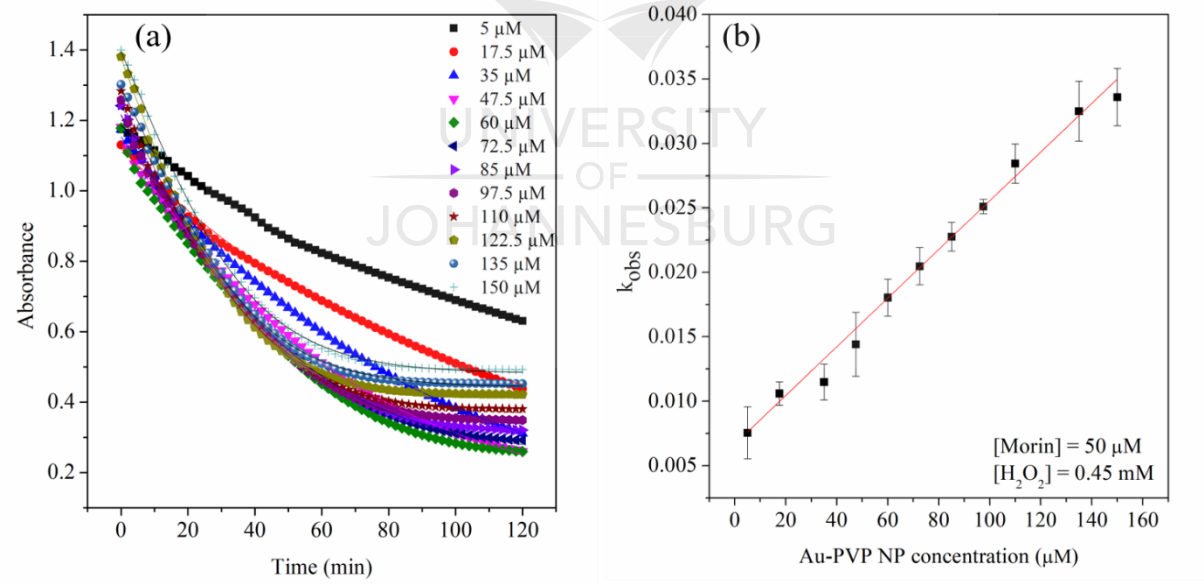

Figure 3.4: (a) The decrease in absorbance of morin at λ 410 nm, over 2 hrs when using Au-PVP NPs as a catalyst. (b) The graph shows the influence of Au-PVP NP concentration on the observed rate (k_{obs}) for the oxidation of morin at 25 °C, using a concentration of 50 µM for morin and 0.45 mM for H_2O_2. Each k_{obs} value corresponds to a certain concentration of Au-PVP NPs. The catalytic dynamic range is represented by the red fitted linear curve.

For the oxidation of morin, a decrease in the absorbance at λ 410 nm can be observed over time. This exponential decrease in absorbance over time is an indication of a pseudo first-order kinetic reaction [38]. Moreover, hydrogen peroxide was added in excess, which will ultimately lead to a pseudo first-order reaction. In the catalytic dynamic range, the k_{obs} increases as the concentration increases. However, only up to a specific point, where the k_{obs} remain constant without increasing. This is referred to as the diffusion limitation domain [2], and it can be seen for the Pd-PVP NPs from **Figure 3.3** but not for the AuPVP NPs from **Figure 3.4**. The linear relationship that is seen in the dynamic range between the k_{obs} and the concentration indicates a catalytic process on the surface of the NPs, with a dependency on the total surface area of the NPs [2]. The optimal catalyst concentration for the other catalytic studies of morin oxidation was chosen from the dynamic range. Therefore, the optimal concentration for the Pd-PVP NPs was 35 μM, and for the Au-PVP NPs was 85 μM. From **Figure 3.3** (b), it can be seen that the standard deviation increases slightly as the concentration increase. This might be due to the homogeneity of the nanoparticle solution. If the solution is not completely homogeneous, inconsistencies might occur, reducing the precision of the replicates.

3.3.3.2 Morin concentration variation

The influence of the morin concentration was investigated by varying the concentration of morin from 3.33 – 100 μM, whilst keeping the concentration of both catalysts constant at 35 μM for the Pd-PVP NPs and 85 μM for the Au-PVP NPs. The concentration of the hydrogen peroxide was also kept constant at 0.45 mM. The concentration of morin was varied to determine the effect on the k_{obs} at different temperatures (**Figure 3.5**).

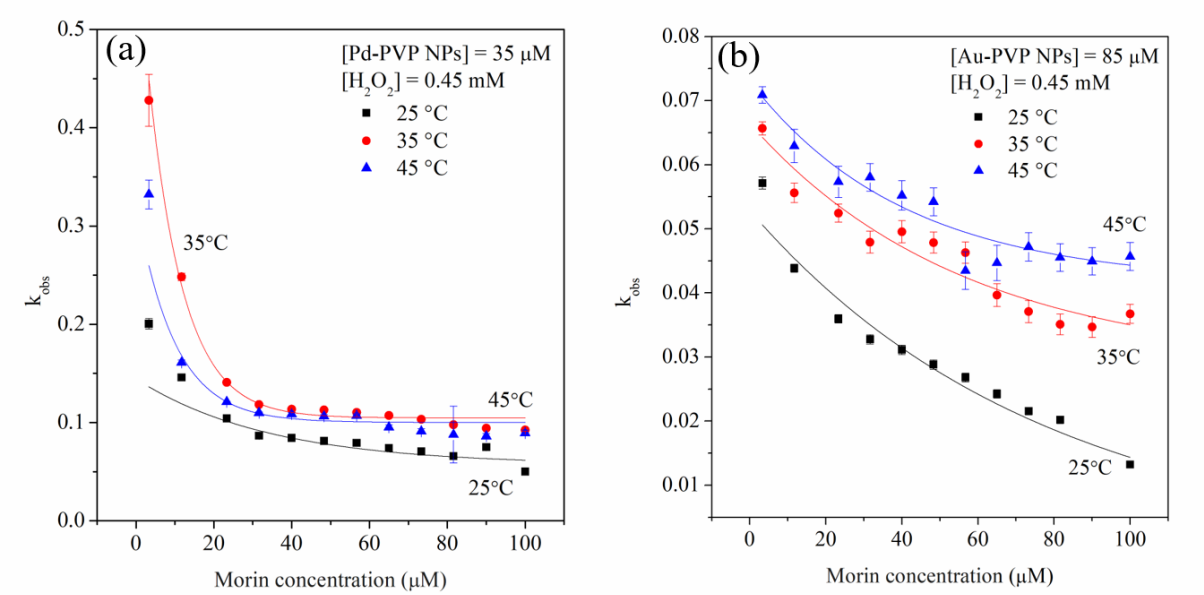

Figure 3.5: The influence of the concentration of morin on the k_{obs} using a constant concentration of **(a)** 35 µM for the Pd-PVP NPs, and **(b)** 85 µM for the Au-PVP NPs. The influence was investigated at 25 °C, 35 °C, and 45 °C. All the experiments were conducted at a constant concentration of 0.45 mM of the H_2O_2.

From **Figure 3.5**, it can be seen that the k_{obs} decrease as the morin concentration increases for all the temperatures under investigation. It is assumed that both the morin and hydrogen peroxide competes for an active site on the catalyst since both these reagents needs to be adsorbed onto the surface of the catalyst for the reaction to take place [2]. As the concentration of the morin increases, the surface of the catalyst gets saturated with the substrate (morin). This means that most active sites are occupied with either the morin or the hydrogen peroxide. This ultimately decreases the observed rate since no more active sites are available on the catalyst for the morin to adsorb and be catalysed. As illustrated in the **Scheme 3.2**, both the morin and hydrogen peroxide adsorbs to the surface of the catalyst and compete for active site. This is in agreement with literature as well [38].

3.3.3.3 Hydrogen peroxide concentration variation

Similar to the morin concentration variation study, the concentration of hydrogen peroxide was also varied to determine the effect on the k_{obs}. The concentration was varied from 0.67 – 20 mM, keeping the Pd- and Au-PVP NPs catalyst concentration constant at 35 µM and 85 µM, respectively. The concentration of the morin was also kept constant at 50 µM.

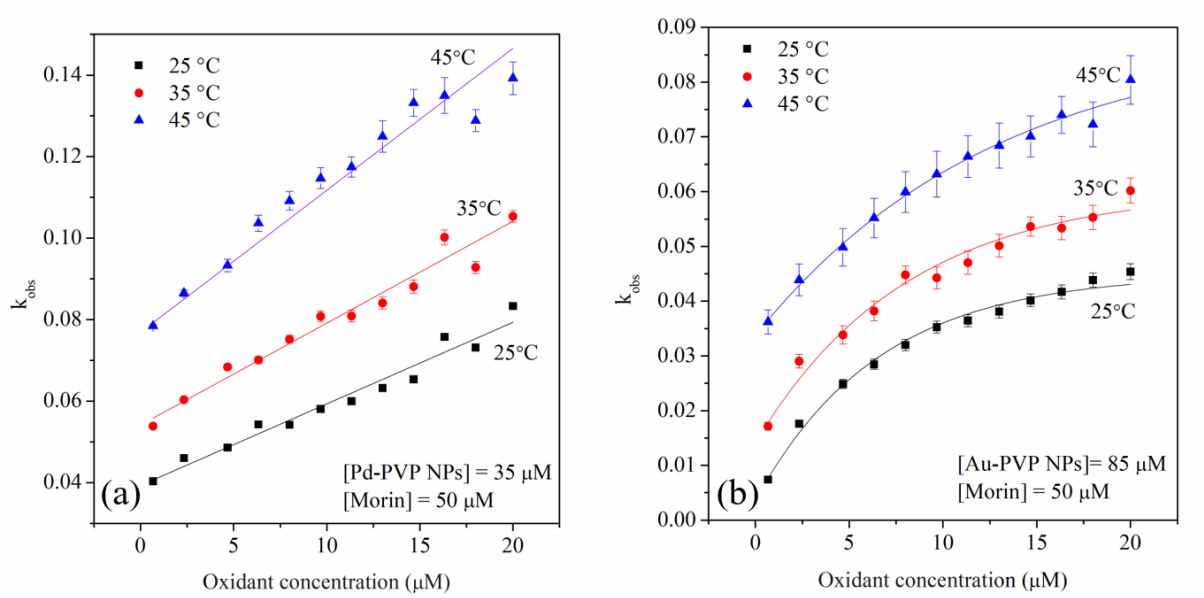

Figure 3.6: The variation of the concentration of the hydrogen peroxide from 0.67 – 20 mM, and the influence on the k_{obs}. A constant concentration of 50 µM morin was used for all experiments. The catalyst concentration was also kept constant at **(a)** 35 µM for the Pd-PVP NPs, and **(b)** 85 µM for the Au-PVP NPs.

It can be seen that the observed rate increases as the concentration of the hydrogen peroxide increases. This can be seen for the Pd-PVP NPs (**Figure 3.6 (a)**) as well as the Au-PVP NPs (**Figure 3.6 (b)**). This is true of the reaction taking place at 25 °C, 35 °C and 45 °C. Therefore, more hydrogen peroxide molecules are available and hence compete with the morin substrate for the active sites on the catalysts. The observed rate increases up to a certain point where it plateaus and becomes constant. This may be due to the saturation of the active sites on the catalyst.

The conventional method for the catalytic study of the degradation of dye involves using cuvettes and an ultraviolet-visible light spectrometer (UV/Vis spectrophotometer). The maximum number of cuvettes that most instruments can accommodate is six cuvettes. This means that only six experiments can be performed simultaneously, which is a tedious approach. However, using robotics, and a high-throughput approach, one can investigate the catalytic degradation of a dye in a fast and effective way. Using this approach, one can limit the number of experiments conducted as well as the reagents being used. This is due to the miniaturisation of reactions in a microtiter plate. There is also the possibility to investigate a greater concentration range. Moreover, a few replicates can be included in one experiment to improve the precision of the results.

A high-throughput approach for the catalytic oxidative degradation of morin was successfully achieved. These studies were conducted rapidly by employing a robotic liquid handler and a high-throughput system consisting of a 96-well plate. The plate enables the user to conduct 96 experiments simultaneously and using a microplate reader for the analysis thereof.

Such a high-throughput system can potentially be used for many applications, including the fast and effective catalytic studies of oxidative degradation of a dye, screening of homogeneous catalysts (including NPs) for a specific reaction which can be monitored using UV/Vis spectroscopy. For example, oxidative or reductive degradation of a substrate, or the synthesis of a UV active compound. It can also be used for the parallel synthesis of dendrimer encapsulated nanoparticles (DENs). Moreover, heterogeneous catalysts such as mesoporous metal oxides can also be screened for the oxidative or reductive degradation of a dye.

This approach could also potentially be employed for screening of other catalysts, reaction or systems. Preliminary studies showed that mesoporous metal oxide catalysts could also be screened for the oxidation of morin, using a 96-well plate. Different concentrations of mesoporous metal oxides (8 catalysts) were evaluated for the oxidation of morin in a 96-well plate. See SI for more information (**Figure S3.4**). Furthermore, it was also shown that it is possible to synthesise DENs in a 96-well plate. An appropriate volume of a dendrimer solution (made before the NP synthesis) was added to the 96-well plate, along with a gold chloride solution (serving as the metal precursor). The metal was allowed to coordinate to the dendrimer, followed by the reduction using a solution of sodium borohydride. A plasmon resonance peak at approximately λ 520 nm confirmed the formation of a dendrimer encapsulated gold NP (**Figure S3.5**). The synthesised DEN was used for the reduction of 4-nitrophenol (4-NP) in the 96-well plate. A slight decrease was seen in the absorbance of 4-NP at λ 400 nm (See SI for more information **Figure S3.6**).

From this, it can be seen that the parallel synthesis of 96 or more different NPs is possible, which can then be screened for a specific reaction. Therefore, the high-throughput screening of NPs and mesoporous metal oxides are possible using this approach. Moreover, using the Opentrons for the pipetting of the reagents to the well plate will further speed up the process, making more experiments possible.

3.4 Conclusion

In this study, it was demonstrated that by using a liquid handling robot and high-throughput systems, one can evaluate the catalytic oxidative degradation of morin in a fast and effective way. The optimal catalyst concentration of Pd- and Au-PVP NPs for the oxidation of morin, were determined using a 96-well plate and a microplate reader. The catalytic study of morin and hydrogen peroxide concentration at three different temperatures was evaluated. By using this approach, the number of experiments and time taken to perform these experiments are drastically reduced. The use of a 96-well plate also makes it possible to evaluate a larger concentration range for both the catalyst and substrate concentration variation. It also makes it possible to include replicates in a single experiment. Therefore, one experiment can be performed, which includes the concentration variation as well as replicates. This approach also shows the possibility for the screening of mesoporous metal oxides and the parallel synthesis of NPs.

3.5 Acknowledgements

This work was funded by the National Research Foundation of South Africa {Grant specific unique reference number (UID) 5386}, and the University of Johannesburg. We greatly appreciated Mr D. Harris and Dr R. Meyer from Shimadzu South Africa (Pty) Ltd for their analytical instruments

3.6 References

[1] S. Bagheri, N. Muhd Julkapli, S. Bee Abd Hamid, Titanium dioxide as a catalyst support in heterogeneous catalysis, Sci. World J. 2014 (2014) 1–21.

[2] A.K. Ilunga, R. Meijboom, Synthesis of narrowly dispersed silver and gold nanoparticles and their catalytic evaluation for morin oxidation, Appl. Catal. A Gen. 509 (2016) 17–29.

[3] A. Tavakoli, M. Sohrabi, A. Kargari, A review of methods for synthesis of nanostructured metals with emphasis on iron compounds, Chem. Pap. 61 (2007) 151–170.

[4] K.M.M. Abou El-Nour, A. Eftaiha, A. Al-Warthan, R.A.A. Ammar, Synthesis and applications of silver nanoparticles, Arab. J. Chem. 3 (2010) 135–140.

[5] J. Rose, M. Auffan, O. Proux, V. Niviere, J.-Y. Bottero, Physicochemical Properties of Nanoparticles in Relation with Toxicity, in: Encycl. Nanotechnol., Springer, 2012: p. 2085.

[6] M. Liu, J. Zhang, J. Liu, W.Y. William, Synthesis of PVP-stabilized Pt/Ru colloidal nanoparticles by ethanol reduction and their catalytic properties for selective hydrogenation of ortho-chloronitrobenzene, J. Catal. 278 (2011) 1–7.

[7] C.H. Campos, B.F. Urbano, C.C. Torres, J.A. Alderete, A Novel Synthesis of Gold Nanoparticles Supported on Hybrid Polymer/Metal Oxide as Catalysts for p-Chloronitrobenzene Hydrogenation, J. Chem. 2017 (2017) 1–9.

[8] C. Li, X. Li, X. Liu, Y. Yang, J. Zhao, Q. Yang, Entrapment of metal nanoparticles within nanocages of mesoporous silicas aided by co-surfactants, J. Mater. Chem. 22 (2012) 21045–21050.

[9] G. Bandekar, N.S. Rajurkar, I.S. Mulla, U.P. Mulik, D.P. Amalnerkar, P. V. Adhyapak, Synthesis, characterization and photocatalytic activity of PVP stabilized ZnO and modified ZnO nanostructures, Appl. Nanosci. 4 (2014) 199–208.

[10] A.R. Prasad, A. Joseph, Synthesis, characterization and investigation of methyl orange dye removal from aqueous solutions using waterborne poly vinyl pyrrolidone (PVP) stabilized poly aniline (PANI) core-shell nanoparticles, RSC Adv. 7 (2017) 20960–20968.

[11] R. Rajesh, S.S. Kumar, R. Venkatesan, Efficient degradation of azo dyes using Ag and Au nanoparticles stabilized on graphene oxide functionalized with PAMAM dendrimers, New J. Chem. 38 (2014) 1551–1558.

[12] R.M. Crooks, M. Zhao, L. Sun, V. Chechik, L.K. Yeung, Dendrimer-encapsulated metal nanoparticles: synthesis, characterization, and applications to catalysis, Acc. Chem. Res. 34 (2001) 181–190.

[13] Y. Yang, H. Chen, X. Bao, Synthesis and optical properties of cds semiconductor nanocrystallites encapsulated in a poly (ethylene oxide) matrix, J. Cryst. Growth. 252 (2003) 251–256.

[14] R. He, X.F. Qian, J. Yin, H.A. Xi, L.J. Bian, Z.K. Zhu, Formation of monodispersed PVP-capped ZnS and CdS nanocrystals under microwave irradiation, Colloids Surfaces A Physicochem. Eng. Asp. 220 (2003) 151–157.

[15] K.R. Choudhury, M. Samoc, A. Patra, P.N. Prasad, Charge Carrier Transport in Poly(N-vinylcarbazole):CdS Quantum Dot Hybrid Nanocomposite, J. Phys. Chem. B. 108 (2004) 1556–1562.

[16] G. Ghosh, M.K. Naskar, A. Patra, M. Chatterjee, Synthesis and characterization of PVP-encapsulated ZnS nanoparticles, Opt. Mater. (Amst). 28 (2006) 1047–1053.

[17] K.M. Koczkur, S. Mourdikoudis, L. Polavarapu, S.E. Skrabalak, Polyvinylpyrrolidone (PVP) in nanoparticle synthesis, Dalt. Trans. 44 (2015) 17883–17905.

[18] C. Graf, S. Dembski, A. Hofmann, E. Rühl, A General Method for the Controlled Embedding of Nanoparticles in Silica Colloids, Langmuir. 22 (2006) 5604–5610.

[19] I.A. Safo, M. Werheid, C. Dosche, M. Oezaslan, The role of polyvinylpyrrolidone (PVP) as a capping and structure-directing agent in the formation of Pt nanocubes, Nanoscale Adv. 1 (2019) 3095–3106.

[20] Y. Nakazato, K. Taniguchi, S. Ono, T. Eitoku, K. Katayama, Formation dynamics of gold nanoparticles in poly(vinylpyrrolidone) and other protective agent solutions, Phys. Chem. Chem. Phys. 11 (2009) 10064–10072.

[21] M. Verma, A. Kedia, M.B. Newmai, P.S. Kumar, Differential role of PVP on the synthesis of plasmonic gold nanostructures and their catalytic and SERS properties, RSC Adv. 6 (2016) 80342–80353.

[22] W. Wang, Q. Chen, C. Jiang, D. Yang, X. Liu, S. Xu, One-step synthesis of biocompatible gold nanoparticles using gallic acid in the presence of poly-(N-vinyl-2-pyrrolidone), Colloids Surfaces A Physicochem. Eng. Asp. 301 (2007) 73–79.

[23] M. Tsuji, M. Hashimoto, Y. Nishizawa, T. Tsuji, Synthesis of gold nanorods and nanowires by a microwave-polyol method, Mater. Lett. 58 (2004) 2326–2330.

[24] Y. Sun, Y. Xia, Large-scale synthesis of uniform silver nanowires through a soft, self-seeding, polyol process, Adv. Mater. 14 (2002) 833–837.

[25] H. Mao, J. Feng, X. Ma, C. Wu, X. Zhao, One-dimensional silver nanowires synthesized by self-seeding polyol process, J. Nanoparticle Res. 14 (2012) 887.

[26] C. Chen, L. Wang, H. Yu, G. Jiang, Q. Yang, J. Zhou, W. Xiang, J. Zhang, Study on the growth mechanism of silver nanorods in the nanowire-seeding polyol process, Mater. Chem. Phys. 107 (2008) 13–17.

[27] T.M.D. Dang, T.T.T. Le, E. Fribourg-Blanc, M.C. Dang, Influence of surfactant on the preparation of silver nanoparticles by polyol method, Adv. Nat. Sci. Nanosci. Nanotechnol. 3 (2012) 035004.

[28] D. Berger, G.A. Trăistaru, B.Ş. Vasile, I. Jitaru, C. Matei, Palladium nanoparticles synthesis with controlled morphology obtained by polyol method, UPB Sci. Bull. Ser. B Chem. Mater. Sci. 72 (2010) 113–120.

[29] K. Patel, S. Kapoor, D.P. Dave, T. Mukherjee, Synthesis of Pt, Pd, Pt/Ag and Pd/Ag

nanoparticles by microwave-polyol method, J. Chem. Sci. 117 (2005) 311–316.

[30] N.V. Long, D.C. Nguyen, H. Hirata, M. Ohtaki, T. Hayakawa, M. Nogami, Chemical synthesis and characterization of palladium nanoparticles, Adv. Nat. Sci. Nanosci. Nanotechnol. 1 (2010) 035012.

[31] H. Hei, R. Wang, X. Liu, L. He, G. Zhang, Controlled Synthesis and Characterization of Nobel Metal Nanoparticles, Soft Nanosci. Lett. (2012).

[32] B.T. Meshesha, N. Barrabés, F. Medina, J.E. Sueiras, Polyol mediated synthesis & characterization of Cu nanoparticles : Effect of 1-hexadecylamine as stabilizing agent, Nanotechnology. 1 (2009) 87–91.

[33] F. Fievet, J.P. Lagier, B. Blin, B. Beaudoin, M. Figlarz, Homogeneous and heterogeneous nucleations in the polyol process for the preparation of micron and submicron size metal particles, Solid State Ionics. 32 (1989) 198–205.

[34] H. Xiao, R. Wang, L. Dong, Y. Cui, S. Chen, H. Sun, G. Ma, D. Gao, L. Wang, Biocompatible Dendrimer-Encapsulated Palladium Nanoparticles for Oxidation of Morin, ACS Omega. 4 (2019) 18685–18691.

[35] J.J. Dannacher, Catalytic bleach: Most valuable applications for smart oxidation chemistry, J. Mol. Catal. A Chem. 251 (2006) 159–176.

[36] M. Nemanashi, R. Meijboom, Catalytic Behavior of Different Sizes of Dendrimer-Encapsulated Au $_n$ Nanoparticles in the Oxidative Degradation of Morin with H_2O_2, Langmuir. 31 (2015) 9041–9053.

[37] N. Bingwa, S. Bewana, M. Haumann, R. Meijboom, Revisiting kinetics of morin oxidation: Surface kinetics analysis, Appl. Surf. Sci. 426 (2017) 497–503.

[38] A.K. Ilunga, R. Meijboom, Catalytic and kinetic investigation of the encapsulated random alloy (Pd_n-Au110-$_n$) nanoparticles, Appl. Catal. B Environ. 189 (2016) 86–98.

[39] M.S. Xaba, R. Meijboom, Kinetic and catalytic analysis of mesoporous Co_3O_4 on the oxidation of morin, Appl. Surf. Sci. 423 (2017) 53–63.

[40] M.J. Ndolomingo, R. Meijboom, Determination of the surface area and sizes of supported copper nanoparticles through organothiol adsorption—Chemisorption, Appl. Surf. Sci. 390 (2016) 224–235.

[41] Y. Wang, S. Shaabani, M. Ahmadianmoghaddam, L. Gao, R. Xu, K. Kurpiewska, J. Kalinowska-Tluscik, J. Olechno, R. Ellson, M. Kossenjans, V. Helan, M. Groves, A. Dömling, Acoustic Droplet Ejection Enabled Automated Reaction Scouting, ACS Cent. Sci. 5 (2019) 451–457.

[42] N.M. Nursam, X. Wang, R.A. Caruso, High-Throughput Synthesis and Screening of

Titania-Based Photocatalysts, ACS Comb. Sci. 17 (2015) 548–569.

[43] J. Klein, C.W. Lehmann, H.W. Schmidt, W.F. Maier, Combinatorial Material Libraries on the Microgram Scale with an Example of Hydrothermal Synthesis, Angew. Chemie - Int. Ed. 37 (1999) 3369–3372.

[44] S.M. Senkan, High-throughput screening of solid-state catalyst libraries, Nature. 394 (1998) 350–353.

[45] P. Cong, R.D. Doolen, Q. Fan, D.M. Giaquinta, S. Guan, E.W. Mcfarland, D.M. Poojary, K. Self, H.W. Turner, W.H. Weinberg, High-throughput Synthesis and Screening of Combinatorial Heterogeneous Catalyst Libraries, Angew. Chemie. 38 (1999) 483–488.

[46] E. Danielson, J.H. Golden, E.W. Mcfarland, A combinatorial approach to the discovery and optimization of luminescent materials, Nature. 389 (1997) 944–948.

[47] X.D. Sun, K.A. Wang, Y. Yoo, W.G. Wallace-Freedman, C. Gao, X.D. Xiang, P.G. Schultz, Solution-phase synthesis of luminescent materials libraries, Adv. Mater. 9 (1997) 1046–1049.

[48] G. Brice o, H. Chang, X. Sun, P.G. Schultz, X.-D. Xiang, A Class of Cobalt Oxide Magnetoresistance Materials Discovered with Combinatorial Synthesis, Science. 270 (1995) 273–275.

[49] R.B. Van Dover, L.F. Schneemeyer, R.M. Fleming, Discovery of a useful thin-film dielectric using a composition-spread approach, Nature. 392 (1998) 162–164.

[50] S. Jones, S.M. Fairclough, M. Gordon-Brown, W. Zheng, A. Kolpin, B. Pang, W.C.H. Kuo, J.M. Smith, S.C.E. Tsang, Dual doping effects (site blockage and electronic promotion) imposed by adatoms on Pd nanocrystals for catalytic hydrogen production, Chem. Commun. 51 (2015) 46–49.

[51] M. Zhou, B. Wang, Z. Rozynek, Z. Xie, J.O. Fossum, X. Yu, S. Raaen, Minute synthesis of extremely stable gold nanoparticles, Nanotechnology. 20 (2009) 505606.

[52] R. State, F. Papa, C. Munteanu, I. Balint, A. Ion, A. Volceanov, Synthesis and Characterization of PVP (Polyvinly Pyrrolidone) Stablized Gold Nanoparticles, Rom. J. Mater. 45 (2015) 262–266.

[53] C. Wu, B.P. Mosher, K. Lyons, T. Zeng, Reducing ability and mechanism for polyvinylpyrrolidone (PVP) in silver nanoparticles synthesis., J. Nanosci. Nanotechnol. 10 (2010) 2342–2347.

[54] J. Xiao, L. Qi, Surfactant-assisted, shape-controlled synthesis of gold nanocrystals, Nanoscale. 3 (2011) 1383–1396.

Chapter 4

Robotic Catalysis: A High-throughput Method for Miniature Screening of Mesoporous Metal Oxides

Chapter 4

Robotic Catalysis: A High-throughput Method for Miniature Screening of Mesoporous Metal Oxides

Graphical Abstract

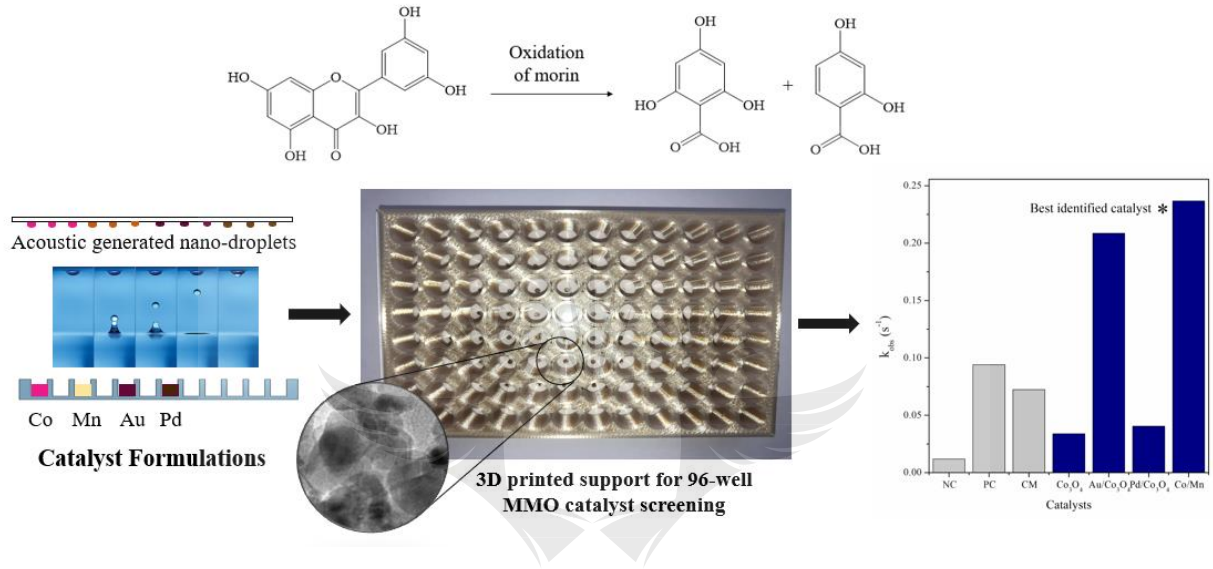

The use of robotics and 3D printing to design a custom system for the screening of mesoporous catalysts in the oxidation of morin.

Abstract

We have developed a high-throughput system to synthesise and explore up to 96 heterogeneous catalysts at the same time. The system was developed as a proof of concept, using a standard glass plate and a 3D printed 96-well plate. Nano-droplets of catalyst formulations were transferred to the glass plate using an acoustic liquid handler, and upon heat treatments, the miniature mesoporous metal oxide catalysts were formed. The 3D printed bottomless 96-well plate was fixed to the glass plate, to give 96 individual wells, each containing a catalyst. Four catalyst plates were prepared (Co_3O_4-, Au/Co_3O_4-, Pd/Co_3O_4 and Co/Mn-MMO) to be screened for their activity in the oxidation of morin, as a model reaction. The observed reaction rates (k_{obs}) for each catalyst were calculated to identify the most active catalyst. The general method described herein requires microscopic amounts of catalysts with derivates of the catalyst's composition.

4.1 Introduction

Conventional catalyst development and discovery is a tedious process and often based on trial-and-error [1]. Using a high-throughput and/or combinatorial approach, one can synthesise and evaluate multiple catalysts simultaneously, increasing the efficiency of the process [2, 3]. With a combinatorial approach, a large number of new materials can be discovered by using different combinations of specific building blocks of atoms and/or molecules [4]. These methods, including parallel synthesis and screening, were first established for early-stage drug discovery in the pharmaceutical industry, where libraries of compounds were screened against a target to identify a potential drug treatment [5]. High-throughput screening methods have been applied in the fields of luminescence [6, 7], magnetoresistivity [8], ferroelectric/dielectric materials [9], and also solid-state catalysis [1].

In recent years, automated parallel synthesis methods have also been adapted for the discovery and optimisation of catalysts [10]. This includes the rapid sequential synthesis of materials followed by the evaluation of these materials [11]. Some of the initial high-throughput combinatorial experiments for catalyst discovery involved the synthesis of crystalline compounds in libraries that could be identified using X-ray micro-diffraction. Recently, inkjet printing has become a popular technique to produce large numbers of

materials in parallel. It has the potential to be used for combinatorial and high-throughput screening of different materials or catalysts [12–14]. Metal oxides and mesoporous metal oxides (including multicomponent metal oxides) have also recently been synthesised using inkjet printing, for the high-throughput discovery of catalysts [12–17].

Silica [18], carbon [19], clay, zeolites and metal oxides [20–22] are mostly used as heterogeneous catalysts or supports. Among these solid supports, mesoporous materials (with pores sizes ranging from 2 – 50 nm) are particularly interesting. Increased surface area and uniformity of the pore network create spaces where the catalysts and reactants can interact [23–25]. Mesoporous metal oxide materials can be used as oxidation catalysts, and materials including oxides of Co, Mn and Fe have mostly been used as oxidation catalysts due to their stability at multiple oxidation states [26]. Not only has Co mesoporous metal oxide been used for oxidation reactions, but also as a support material [27] for noble metals such as Pd and Au nanoparticles [28].

One of the challenges of high-throughput experiments is that instruments suitable for high-throughput analysis are required. When using a high-throughput method, the amount of sample generated is often miniaturised, to increase the range of targets being evaluated. This makes it difficult to analyse and characterise the properties of the materials under investigation [5]. The assessment of catalytic activity using a high-throughput method can be challenging since it requires the unambiguous detection of a specific product above a small catalyst site. Using multiple catalysts in a library can make it even more difficult [1].

This study aimed to design and use a custom high-throughput setup for the parallel synthesis and screening of 96 mesoporous metal oxide oxidation catalysts. To achieve this, tools and techniques typically used for biological applications were considered, therefore bridging the gap between biology and chemistry. Specifically, liquid handlers (an acoustic liquid handler [29–32] and the Opentrons [33–36]) and a microplate reader were utilised. The acoustic liquid handler dispenses nano-droplet (as small as 2.5 nL droplets) of a solution into a 96-well plate. This acoustic liquid handler is mostly used in biological applications such as drug discovery [37], RNA interference studies [38], for cell culturing and anti-cancer studies [39–42], and many other biological applications [43–46]. Recently, an acoustic liquid handler was used for the preparation of boronic acid libraries [47]. The Opentrons is a liquid handler

typically used for biological applications such as polymer chain reaction (PCR) [33, 34], nucleic acid extraction and purification, DNA assembly [35], protein preparation [36] as well as fungal sample preparation [48]. It can also be used for making dilutions. And finally, a UV/Vis microplate reader is often/commonly used for biological absorption and fluorescence assays.

In this study, as proof of concept, up to 96 catalysts were evaluated for the oxidation of morin as a model reaction. Morin is a flavonoid dye which is extracted from plants. It is known to be a quercetin compound, which can be detected analytically using UV/Vis spectroscopy, making it ideal for high-throughput experimentation. To the best of our knowledge, acoustic transfer of mesoporous metal oxide catalyst formulations has yet to be exploited for the synthesis of mesoporous metal oxide catalysts.

4.2 Experimental

4.2.1 Chemicals and materials

Cobalt (II) nitrate hexahydrate (99%), Manganese (II) nitrate hexahydrate (99%), Pluronic surfactant F127, ethanol (absolute), ethylene glycol, K_2PdCl_2 (99%), $AuCl_3$ (99%) and polyvinylpyrrolidone (avg mol weight 10 000) were all purchased from Merck (formerly known as Sigma-Aldrich). Dimethyldichlorosilane and hydrogen peroxide (30%) were purchased from Fischer Scientific All the chemicals were used as received without any further purification.

Lipidic cubic phase (LCP) sandwich glass plate set was purchased from Marienfeld. Ultem 3D printing filament was purchased from Stratasys. The slow-curing epoxy glue, manufacturer 3M, DP490 epoxy AD BK 50 mL CAR 12/CV, was purchased from RS Components (UK), RS stock no 189-3159, MFr part no DP-490 50ML 1.

4.2.2 Synthesis of mesoporous metal oxide (MMO) formulations

The synthesis of the mesoporous metal oxides was adapted from Lui, *et al*. [12].

4.2.2.1 Synthesis of mesoporous cobalt oxide formulation

The surfactant, F127 (1.6 g) was dissolved in ethanol (15 mL). Cobalt (II) nitrate hexahydrate (2.9 g, 10 mmol) was added to the mixture. The mixture was stirred until all the solids had dissolved. Ethylene glycol (15 mL) was added to the mixture, and it was further stirred for 2 hrs.

4.2.2.2 Synthesis of mesoporous manganese oxide formulation

The surfactant, F127 (1.6 g) was dissolved in ethanol (15 mL). Manganese (II) nitrate tetrahydrate (2.5 g, 10 mmol) was added to the mixture. The mixture was stirred until all the solids had dissolved. Ethylene glycol (15 mL) was added to the mixture, and it was further stirred for 2 hrs.

4.2.3 Synthesis of polyvinyl pyrrolidone (PVP) stabilised nanoparticles (NPs)

4.2.3.1 Pd-PVP NPs

The Pd-PVP NPs were synthesised in ethylene glycol serving the dual role of solvent and reducing agent.[49] The appropriate amount of K_2PdCl_4 (0.979 g, 0.003 mol) was weighed out to give a 0.3 M solution. It was dissolved in 10 mL ethylene glycol. PVP (0.28 g, average Mw = 10 000) was added to the mixture. The mixture was heated to 120 °C for 2 hours. During the heating process and favoured by the presence of ethylene glycol, palladium species are formally reduced from Pd(II) to Pd(0), which can be observed by a change of colour of the solution from dark orange to a brown.[49] The synthesised nanoparticle formulation was used without further purification.

4.2.3.2 Au-PVP NPs

The synthesis of the Au-PVP NPs was modified from the method used by State, *et al*. [50]. A solution of PVP (0.51 g, average Mw = 10 000) in ethylene glycol (5 mL) was prepared. The mixture was stirred for 2 hours at 80 °C, to dissolve all the PVP. A solution of $AuCl_3$ (0.16 g) was prepared in water (2.5 mL). The Au solution was added to the PVP solution, and the mixture was stirred for 15 min. The pH of the solution was adjusted to ~9 by the addition of

NaOH (1 M, 2.5 mL). The solution was then heated to 100 °C for 2 hrs after which the nanoparticles formed, evidenced by the change of colour of the reaction mixture, from dark brown to burgundy.

4.2.4 Customised catalyst plate/s

4.2.4.1 Dispensing of the catalyst formulation onto the glass plate

Catalysts droplets were transferred from a source plate (containing the catalyst formulation and/or PVP-NPs, 384PP Labcyte) onto the glass plate (or destination plate) using a Labcyte ECHO 550 acoustic liquid handler following a 96-well plate template. Thereafter, the glass plate was subjected to different heat treatments to form the mesoporous metal oxide materials.

4.2.4.2 Heat treatment of the glass plate to form the catalyst plate:

After catalyst formulation transfer to the glass plate/s, the glass plate was placed into an oven for heat treatments of the catalysts. The catalyst plates were aged between 50 – 80 °C overnight. Then dried between 100 – 150 °C for 6 hours. The catalysts were formed after calcination of the plates at 400 °C for 4 hrs (using a ramped temperature of 1 – 2 °C/min).

4.2.4.3 Custom 3D printed catalyst plate:

A 3D model of a bottomless 96-well plate was designed using the Onshape software (academic license). The model was printed on a Stratasys Fortus 450 (F-450) 3D printer using Ultem (polyetherimide) printing material. The 3D print was fixed to the glass plate using a slow curing (4 – 6 hrs) epoxy glue (3M Scotch-Weld DP490). The glue was dispensed onto the 3D print using a 2D pattern with a Nordson EFD Pro 4 glue dispensing robot. The 3D print was fixed to the plate containing the calcined catalysts and was slightly pressed down to ensure an even distribution of the glue around each well was achieved. The glued plate was left overnight to complete the curing process.

4.2.5 Characterisation of bulk and miniature catalysts:

4.2.5.1 Surface area analysis

The surface area of the bulk samples was determined by the Brunauer-Emmett-Teller (BET) analysis. Before the analysis of the samples (approximately 20 mg) were weighed out and degassed under nitrogen at 200 °C overnight. The BET surface area, pore volume and pore

size (diameter) analyses were carried out at a temperature of -196 °C using N_2 gas. The Brunauer-Emmett-Teller (BET) method was used to calculate the surface area. The pore size and volume were calculated using the adsorption-desorption curves using the Barrett-Joyner-Halenda (BJH) model (results are shown in the SI).

4.2.5.2 Transmission electron microscopy (TEM) imaging

The mesoporous metal oxide and/or PVP-NP formulations (1000 µL x 96) were transferred to the glass plates. The miniature catalysts were formed by subjection to the heat treatments, and after that, the catalysts were scraped off the plate and collected. The catalysts (miniature and bulk) were then dispersed in deionised H_2O using a sonicator and deposited onto a copper TEM grid. The images were analysed using Transmission Electron Microscopy (TEM) JEOL JEM-2100.

4.2.6 Catalytic evaluation of the catalyst

After the formation of the catalysts on the glass plate, the catalysts were evaluated for their potential oxidation activity. To each well, water (100 µL), aqueous morin dye (50 µL, 150 µM) and hydrogen peroxide (50 µL, 7.5 mM) were added using an Opentrons OT2 pipetting robot. The catalyst plates were evaluated for the activity in the oxidation of morin. The decrease in absorbance was measured at λ 410 nm over time using a SpectraMax M2e microplate reader.

For the catalytic evaluation of the bulk Co_3O_4-MMO catalyst using the conventional method (CM), the bulk sample was dispersed in deionised water (1 mg/mL), and a concentration of 0.05 mg/mL was used in a round bottom flask. A concentration of 150 µM and 10 mM was used for the morin and hydrogen peroxide, respectively. The reaction was evaluated for 1 hour by sampling (150 µL) every 10 min. The reaction was followed on a microplate reader (SpectraMax M2e) at a wavelength of λ 410 nm.

4.2.7 Data fitting

The catalytic data were fitted and processed using Kinetic Studio and Origin Pro 8.5 graphing and modelling software.

4.3 Results and Discussion

To set up an efficient workflow for high-throughput catalyst evaluation, the synthesis of the catalysts should be done in a fast way and using small amounts. While difficult with conventional methods, an acoustic liquid handler is capable of accurately and precisely dispensing multiple nano-droplets (2.5 – 5000 nL) of different formulations from a source plate (containing the catalyst formulations) into or onto destination plates of various format and material. For this study, a glass plate was used. After catalyst synthesis, a customised 3D printed bottomless 96-well plate was adhered over the catalysts, to subject each catalyst to an individual reaction. For this study, the catalysts were evaluated for the oxidation of morin as a model reaction.

4.3.1 Morphological comparison between the miniature and bulk catalysts

Since the catalysts were synthesised using small volumes of the formulation/s (2.5 – 5000 nL), a morphological study was included to compare the miniature catalysts and the bulk catalyst. It had to be confirmed that the mesoporous metal oxides could be formed when small volumes of the formulation were used. Transmission electron microscopy (TEM) characterisation of bulk and miniature samples (Co_3O_4-MMO) was used to compare the morphology.

4.3.1.1 TEM imaging

The morphology of the bulk and the miniature Co_3O_4-MMO catalysts were compared using TEM imaging, as illustrated in **Figure 4.1** and **Figure 4.2**. From the images, it can be seen that morphology is comparable. The particle sizes for both catalysts are consistent around 20 nm. The porous networks can also be seen in both samples. This indicates that the catalysts can be formed on a small scale (using the same catalyst formulation as the bulk catalyst), by using nano-droplets generated by an ECHO acoustic liquid handler.

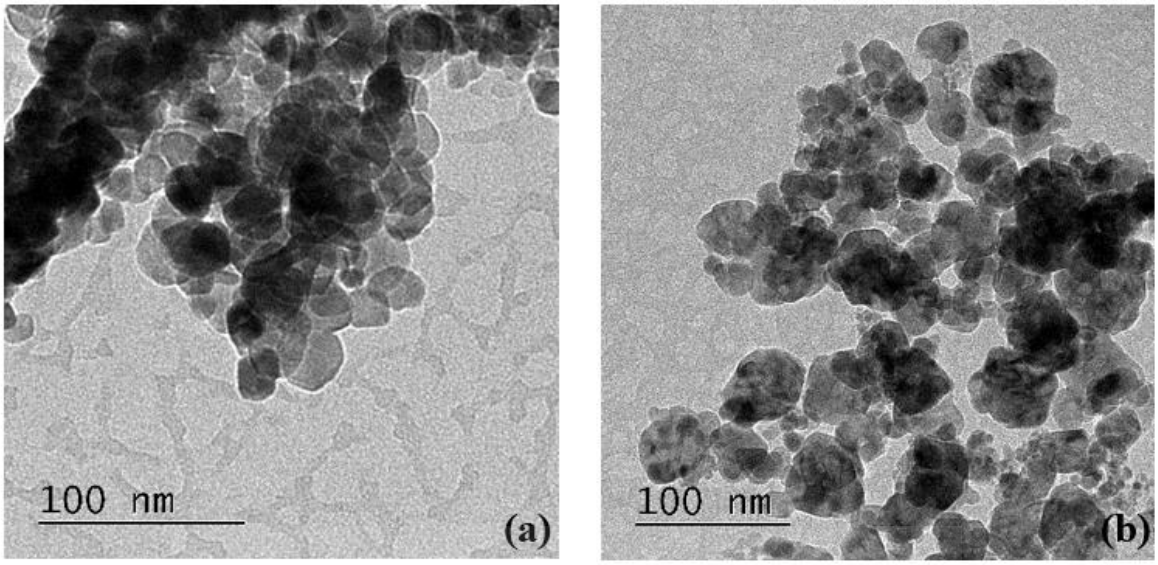

Figure 4.1: TEM images of **(a)** the bulk Co_3O_4-MMO sample, and for **(b)** the miniature Co_3O_4-MMO sample. Comparing the images of both samples, it can be seen that the particles size is uniform, approximately 20 nm.

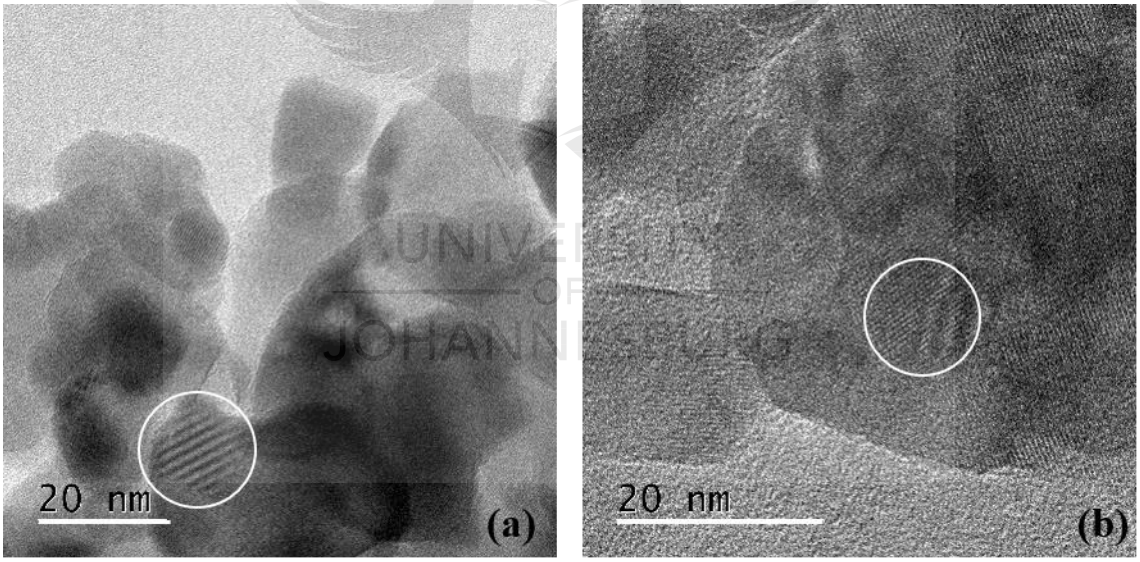

Figure 4.2: TEM images of **(a)** the bulk Co_3O_4-MMO sample, and for **(b)** the miniature Co_3O_4-MMO sample. From these images, the pore network structures (represented by the parallel lines, and circled in white) can be seen for both the bulk and the miniature samples.

The images for the Au/Co_3O_4-MMO, Pd/Co_3O_4-MMO and the multicomponent Co/Mn-MMO miniature samples, are comparable to the bulk catalyst as well. This is illustrated in **Figure 4.3**.

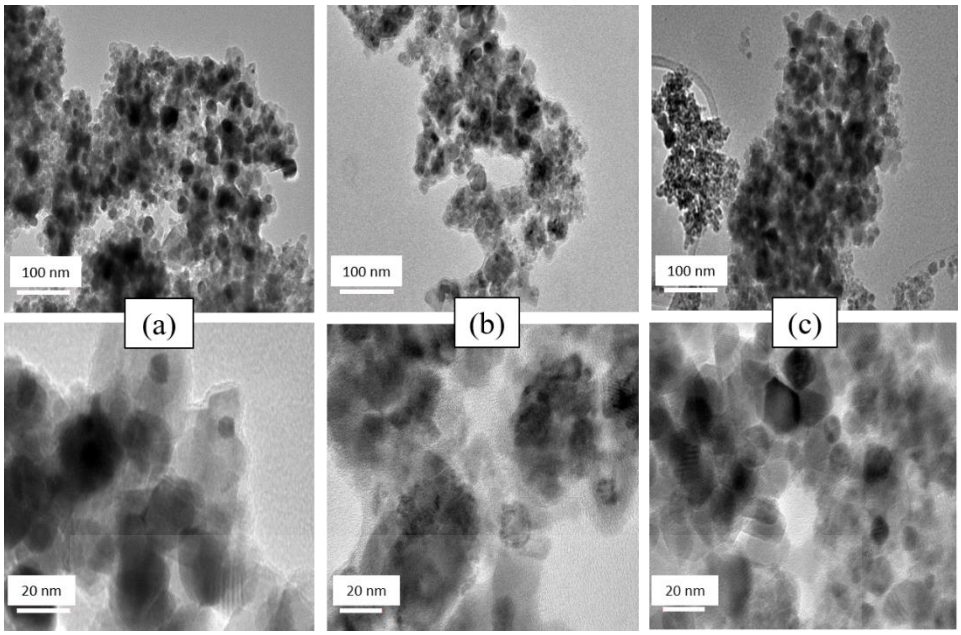

Figure 4.3: A comparison of **(a)** the Au/Co_3O_4-MMO, **(b)** Pd/Co_3O_4-MMO and **(c)** Co/Mn-MMO miniature catalysts using TEM. The particles sizes are comparable to the bulk sample, approximately 20 nm. The white bars represent the scale of the TEM images.

The Au- and Pd-PVP nanoparticles can be seen as the black spots on the MMO catalysts. Due to the high concentration of Au- and Pd-PVP NPs that had to be used to achieve relatively low percentages (1% - 13% for Pd, and 0.3% - 4% for Au) of the Au and Pd supported onto the catalyst, some agglomeration can also be observed.

4.3.2 The High-throughput catalyst screening system

The mesoporous metal oxide catalysts were subsequently formed after a few heat treatments. Using a customised 96-well plate over the calcined catalysts, these catalysts were screened for the oxidation of morin. Generally, ethanol is used as a solvent for the mesoporous metal oxide formulations. However, droplets generated with the liquid handler was not stable on the glass plate. It could visually be observed that droplets evaporated from the glass plate. The formulations were, therefore, stabilised with ethylene glycol. The addition of the ethylene glycol to the formulations and the synthesis on a small scale (using nL droplets of the formulations) are factors that might influence the formation of the mesopores. Morphological and surface area (found in the SI of chapter 4) analyses were performed to determine the influence of these factors on the catalysts. From **Figure 4.1, Figure 4.2** and **Figure 4.3**, it was confirmed that the ethylene glycol didn't affect the morphology of the catalysts.

4.3.2.1 Nano-droplet transfers to the glass plate

For high-throughput catalyst screening, the system requires the parallel synthesis of the catalysts on a small scale. Small amounts of catalyst formulation/s were transferred onto a glass plate (treated with a silane solution) which was then aged, dried and calcined to form the catalysts in small amounts (**Figure 4.4**). For this study, up to 96 different catalysts could be synthesised in this way. A 96-matrix pattern was used for the deposition of the catalyst formulation/s on to the glass plate, i.e. a droplet was placed in the same position on the glass plate, as it would have been in a 96-well plate.

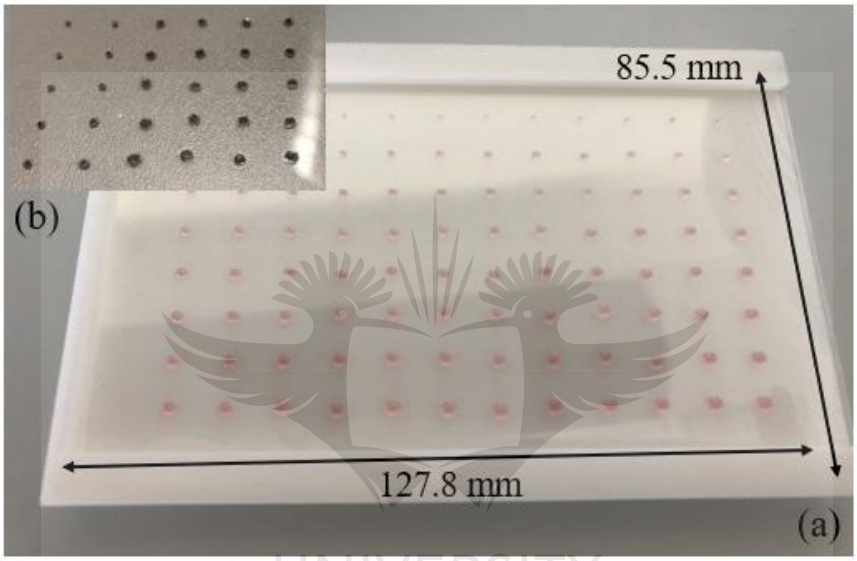

Figure 4.4: **(a)** The glass plate (LCP sandwich set glass plate, 1 mm thick) used as a support for the catalysts synthesis as well as evaluation of the catalysts for the oxidation of morin. The catalyst formulation (Co_3O_4 formulation) was deposited onto the glass plate using an acoustic liquid handler. The volume of the formulation was increased over the 96-well areas. A glass plate holder was designed, and 3D printed to hold the glass plate in the instrument during formulation deposition. **(b)** Catalysts after calcination at 400 °C.

4.3.2.2 Glass as a catalyst support

For biological application, high-throughput screening methods are generally achieved using commercially available microtiter well plates which are made of plastic. To synthesise the mesoporous metal oxide materials, plastic microtiter well plates cannot be used since the catalysts are formed at a high temperature (400 °C). It was, therefore, necessary to use an alternative system to synthesise the catalysts in parallel. Moreover, the catalysts were screened for the oxidation of morin. This reaction was evaluated using UV/Vis spectroscopy.

The decrease in absorbance of the morin is followed as oxidation takes place. Therefore, it was important to deposit the catalysts onto a material suitable for high temperatures and which was compatible to be used in a UV/Vis plate reader. The UV/Vis plate reader measures the absorbance of a particular solution in a microtiter plate. This reading takes place from the bottom of the plate. Hence, to evaluate the catalysts for the oxidation of morin, a clear substrate was needed for the catalyst deposition, to enable the UV/Vis plate reader to analyse each well.

A glass substrate was the only appropriate material for this use since it can withstand a temperature of 400 °C, and it is a transparent material/substrate, which allows the UV/Vis light to penetrate and evaluate the reaction. An LCP sandwich set glass plate (SI) was used as a substrate or support for the synthesis and evaluation of each catalyst activity. These LCP sandwich set glass plates are usually used for the screening of membrane proteins in lipidic mesophase.

4.3.2.3 The customised 3D printed catalyst plate

Following the calcination of the catalyst formulations on the glass plate, a custom bottomless 96-well plate was designed, and 3D printed to be placed over the catalyst on top of the glass plate, to ensure that each catalyst was contained in an individual well (**Figure 4.5**). A chemically resistant 3D printing filament (Ultem, polyetherimide) was used to print the 96-well plate. The custom 96-well plate was glued to the glass plate after catalyst calcination. A slow curing epoxy glue was dispensed, in a specific pattern, onto the 96-well plate using a Nordson EFD Pro4 glue dispensing robot. This robot ensured that the glue was dispensed accurately in between each well to secure the well plate onto the glass plate preventing leakages between neighbouring wells. The plate was then fixed to the glass plate and left overnight for curing. After that, the catalyst plate was evaluated for the oxidation of morin.

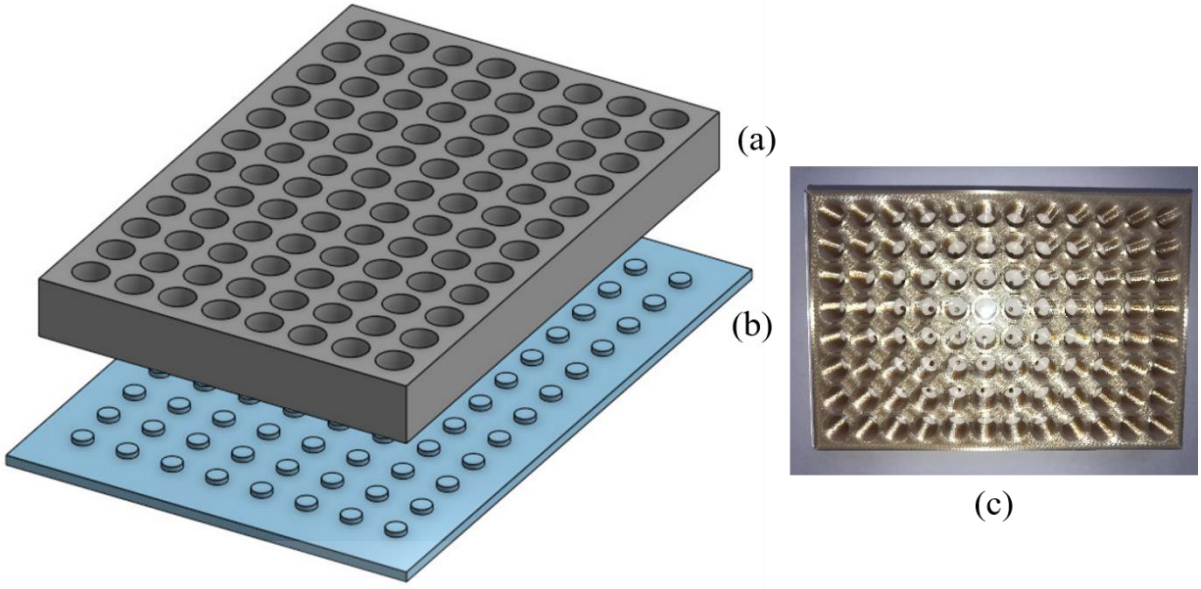

Figure 4.5: **(a)** The 3D printed bottomless 96-well plate fixed to **(b)** the glass plate (containing the already calcined catalysts) using epoxy glue, dispensed with a Nordson EFD Pro4 glue dispensing robot. **(c)** The actual catalyst plate, with the glass plate and catalysts in individual wells.

4.3.3 Evaluation of the catalyst plates for the oxidation of morin

Initially, a Co_3O_4-MMO plate with increasing volumes (ultimately increasing amount of catalyst formed, hence, increasing the final concentration of the catalysts in the reaction) of the formulation was used on the glass plate. This was used as a proof of concept, to show that miniature catalysts can be synthesised using this method, and be active in the oxidation of morin. After the creation of the initial Co_3O_4-MMO catalyst plate, the morin reaction was set up using the conditions mentioned in the experimental section. A decrease in the absorbance of morin was seen with the Co_3O_4-MMO plate, indicating that this system could potentially be used to screen the activity of catalysts. Therefore, plates containing different derivates of Co_3O_4-MMO catalysts (Au and Pd immobilised nanoparticles, and a Co_3O_4/MnO_x-MMO) were subsequently synthesised and evaluated for activity in the oxidation of morin.

Three other plates were prepared to determine if other variables can also be screened in this way, where the concentration of each variable was increased over the plate. Nanoparticles (NPs) supported onto the Co_3O_4, and a multicomponent MMO was investigated. These plates include the addition of PVP nanoparticle in the MMO catalysts, Au/Co_3O_4-MMO and Pd/Co_3O_4-MMO and also a multicomponent MMO catalyst plate (Co/Mn-MMO). As with

the Co_3O_4-MMO plate, the concentration of the variables (Au, Pd or Mn) was increased over 80 catalysts (using 80 well areas). The other 16 well areas on each plate were used for the inclusion of a negative (the absence of a catalyst) and positive (0.025 mg/mL bulk Co_3O_4-MMO) controls. Negative (NC) and positive controls (PC) were included with each plate as reference measurements. The negative control was included as a blank measurement, to show that the reaction occurs slowly in the absence of a catalyst. The positive control showed that the Co_3O_4-MMO bulk catalyst (synthesised the conventional way) could be used as a catalyst for the oxidation of morin.

The reagents for the oxidation reactions were added to each well using an Opentrons OT2 pipetting robot. The robot can accurately dispense the appropriate volume of water, peroxide (H_2O_2) and aqueous morin solution into each well before the analysis. Thereafter, the decrease in absorbance of the morin at λ 410 nm was followed using a UV/Vis plate reader. An exponential decrease in the absorbance of the morin over time indicates a pseudo first-order reaction. The reaction was followed for two hours, with a reading interval of 2 min. The rate of reactions, i.e. observed rate constant (k_{obs}), was determined from the decrease in absorbance over time. The best catalyst from each plate was identified by the highest k_{obs} value (**Figure 4.6**). The k_{obs} represent the observed rate constant for the reaction, and it implies the decrease of a specific reagent in solution.

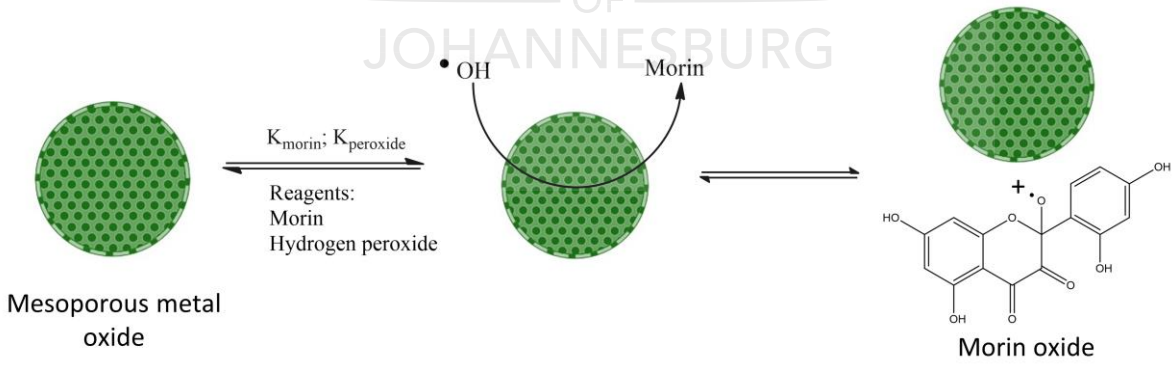

Scheme 4.1: Pseudo first-order kinetic scheme for the oxidation of morin by the mesoporous metal oxides.

During the oxidation reaction, both the morin and hydrogen peroxide adsorbs to the mesoporous metal oxide surface, as illustrated in **Scheme 4.1**. When both reagents are absorbed, the reaction can take place. Hydrogen peroxide is used in excess; therefore, a pseudo first-order reaction can be expected.

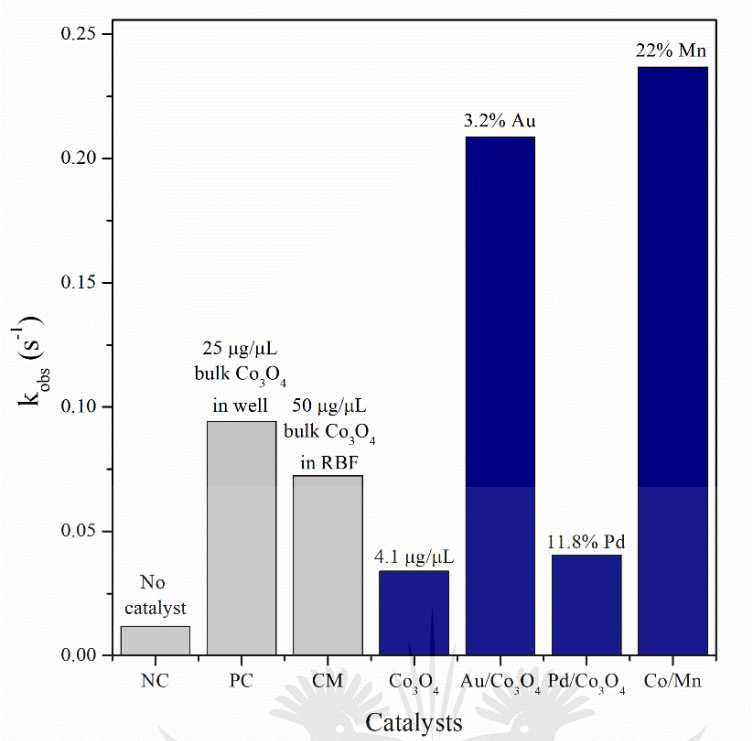

Figure 4.6: The observed rate constant (k_{obs}) obtained for the best catalyst from each catalyst plate. Negative and positive controls were included for all the catalyst plates, and the average rate was calculated for each control and is represented in the figure. The rate of reaction for the bulk Co_3O_4 catalyst determined using the conventional method (CM) in a round bottom flask (RBF) for 1 hour is given. A negative control (NC), as a blank measurement, was included to show that the reaction takes place slowly in the absence of a catalyst, and a positive control (PC, 0.025 mg/mL bulk Co_3O_4 dispersed in deionised water and added to empty well in the custom catalyst plate before the analysis in the plate reader) to show that Co_3O_4 is active in the oxidation of morin.

The morin dye is oxidised to only one product, product A, during the first few minutes of the reaction, however, upon over-oxidation, two products are formed, products B and C, as illustrated in **Scheme 4.2**. This was observed by Bingwa *et al*. [51] by the formation of one absorption band at λ 310 nm (with isosbestic points) which indicate the presence of only one product. However, over time it was seen that the isosbestic points disappeared indicating the formation of more than one product due to over oxidation. For this study, the oxidation of morin was evaluated over two hours which might lead to the over oxidation of the morin resulting in two oxidised products and not one.

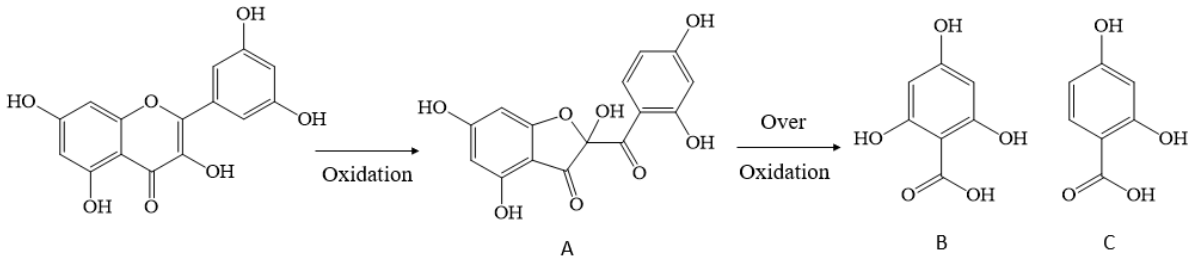

Scheme 4.2: The schematic representation of the oxidation and over-oxidation of morin

As expected, the negative control gave the lowest k_{obs} (0.012 s^{-1}) value. This shows that the reaction takes place in the absence of a catalyst; however, slowly. The k_{obs} (0.094 s^{-1}) value for the positive control is much higher (8 folds) than the negative control, indicating that the Co_3O_4-MMO bulk catalyst is active towards the oxidation of morin. The k_{obs} for Co_3O_4-MMO plate is lower than the positive control. Moreover, the rate was also decreased (2 folds) compared to the rate of the Co_3O_4 bulk catalyst determined in a round bottom flask. Even though the rate for the miniature Co_3O_4-MMO catalyst is lower compared to the positive control and for the reaction in the round bottom flask, the concentration is also lower (25 and 50 µg/µL for the positive (PC) and conventional method (CM), compared to 4.1 µg/µL for the miniature catalyst). This may indicate that the rate for the miniature catalysts might increase when the amount is upscaled or if the catalyst is properly dispersed in the reaction solution.

The positive control, as well as the catalyst in the round bottom flask reaction, were prepared by the dispersion of the bulk Co_3O_4-MMO using a sonicator bath. For the positive control, the dispersed catalyst was subsequently added to empty wells of each catalyst plate under investigation. Sonication ensures that all the particles are properly dispersed, making the entire surface area available for adsorption of reagents. When the particles are not sonicated and dispersed, it decreases the available active sites on the catalyst. The Co_3O_4-MMO plate was not sonicated. The particles were, therefore agglomerated, which decreased the surface area, explaining why the k_{obs} might have been lower than expected. All plates were subsequently sonicated.

For the plate containing an incremental ratio of Au-PVP NPs (0.05 M, 0.4 to 4%) in a fixed (2500 nL) amount of Co_3O_4 formulation the k_{obs} for the best identified Au/Co_3O_4-MMO catalyst (3.2%) is higher than the Co_3O_4-MMO and positive control. This indicates the Au

supported onto the Co_3O_4 catalyst shows a synergistic effect, increasing the rate [28]. The Au-PVP NPs increase the surface to volume ratio of the catalyst hence increasing the activity of the catalyst. This was previously shown by Ilunga *et al*.[28] They showed a synergistic effect between Au/Pd supported nanoparticles on Co_3O_4 in the oxidation of morin. Similarly, with the Pd/Co_3O_4-MMO plate, fixed amounts of the Co_3O_4-MMO (2500 nL) catalyst was used with an increasing amount of Pd-PVP NPs (0.3 M). The Pd loading was approximately 1 – 13%. The k_{obs} of the best-identified catalyst (11.8%) is slightly higher than the Co_3O_4-MMO catalyst but lower than the Au/Co_3O_4-MMO catalyst. This indicates that Pd-PVP NPs also increases the activity of the catalyst, however, not as much as the Au-PVP NPs.

A multicomponent MMO plate was also investigated, and it contained Co/Mn-MMO catalysts. A fixed amount for the Co_3O_4 formulation was used, and the amount of Mn formulation was increased over the plate. From **Figure 4.6**, it can be seen that the Co/Mn-MMO, with 22% Mn, catalyst gave the highest k_{obs}. This is ascribed to a synergistic effect between the Co and Mn in the catalyst. Both catalysts are active; however, in combination, the k_{obs} for the catalyst is increased considerably by approximately 20-fold.

The results in **Figure 4.6** highlights the following: (i) for all systems, the reaction rate was faster than the reaction rate of the negative control, for which no catalyst was added. (ii) the rate for the Co_3O_4-MMO synthesised on the glass plate is slower compared to the positive control (0.025 mg/mL bulk Co_3O_4-MMO synthesised traditionally) dispersed in deionised water by sonication before the addition into the custom catalyst plate. Moreover, the rate is also decreased (ca two folds) compared to the rate of bulk Co_3O_4 catalyst when determined using the conventional method (CM) in a round bottom flask. Even though the rate of the miniature Co_3O_4-MMO catalyst is decreased compared to the bulk, it should be mentioned that the concentration is much lower. This is both expected and interesting. Expected because the catalyst synthesised on the glass plate hasn't been dispersed properly in the reaction mixture; hence fewer active sites are available. Interesting because it means that the activity of a screened catalyst will almost certainly be higher when scaled-up and/or properly dispersed by sonication. (iii) Cobalt and Pd/Co_3O_4 increase the rate slightly by approximately 3-fold compared to the negative control. (iv) Both Au/Co_3O_4-MMO and Mn/Co-MMO species increase the rate by more than 18-folds (18- and 20-fold, respectively).

The success in the parallel synthesis of the MMO catalyst on the glass plate, and the screening thereof implies that this high-throughput screening system can be used to identify the most active catalyst on the glass plate. It can also be developed further as a combinatorial high-throughput system, where multicomponent MMO catalysts can be synthesised and screened. The established workflow can be further standardised and accommodated to other reactions which will be reported in due course.

4.4 Conclusion

High-throughput miniaturisation of catalysis can be achieved by using microscopic amounts of mesoporous metal oxide formulations, for the miniature synthesis of heterogeneous mesoporous metal oxide catalysts. In this study, a workflow was set up for the rapid screening of miniature multi-metallic species of mesoporous metal oxides catalyst for their activity towards the oxidation of morin. This was conducted by using a combination of acoustic liquid handling (ECHO acoustic handler) as well as affordable Open-Source (Opentrons and 3D printing) technologies. In this study, a customised 96-well plate was created by using a 3D printed bottomless plate fixed to a glass plate containing the catalysts. Catalysts such as Co_3O_4-MMO as well other derivatives (immobilisation of Mn, Au-PVP NPs and Pd-PVP NPs on the Co_3O_4-MMO) could also be synthesised and screened in this manner.

The most active catalyst could be identified from the highest k_{obs} value obtained. It can, therefore, be concluded that this high-throughput technique can be used for the simultaneous synthesis and evaluation of numerous catalysts, ultimately for catalyst screening for a specific reaction. This technique can be further developed for the screening of multicomponent mesoporous metal oxides using a combination of different metals. As well as supported NPs on the multicomponent MMOs (for example Au/Co-Mn MMO). For the high-throughput synthesis of 96 different molecules, equipment such as the ECHO acoustic liquid handler might not be available in many research groups. However, the same study can be conducted using an affordable liquid handling robot such as the Opentrons for the liquid handling for catalyst formulations.

4.5 Acknowledgements

We thank Dr Craig Sawyer from Particle Physics Department at Science and Technology Facilities Council (STFC) Rutherford Appleton Laboratory, UK, and Dr Emma Buchanan, Institute of High Energy Physics (IHEP), Chinese Academy of Sciences, Beijing, for the assistance and training of the Nordson EFP Pro4 glue dispensing robot. The authors thank the beamline scientists of Diamond Light Source beamline I04-1 and the XChem laboratory for the use of the state-of-the-art equipment. As well as the Science and Technology Facilities Council (STFC), Research Complex at Harwell (RCaH) laboratories and for the assistance with analytical instruments such as the TEM and SEM. Spectrum facilities at the University of Johannesburg are also acknowledged for the TEM analysis. We appreciate Mr D. Harris and Dr R. Meyer from Shimadzu South Africa (Pty) Ltd for their analytical instruments.

This work was supported through the Global Challenges Research Fund (GCRF) through Science & Technology Facilities Council (STFC), grant number ST/R002754/1: Synchrotron Techniques for African Research and Technology (START). This work was also supported financially by the National Research Foundation of South Africa {Grant specific unique reference number (UID) 5386}, and the University of Johannesburg.

4.6 References

[1] S.M. Senkan, High-throughput screening of solid-state catalyst libraries, Nature. 394 (1998) 350–353.

[2] D. Wolf, O. V. Buyevskaya, M. Baerns, Evolutionary approach in the combinatorial selection and optimisation of catalytic materials, Appl. Catal. A Gen. 200 (2000) 63–77.

[3] P. Cong, R.D. Doolen, Q. Fan, D.M. Giaquinta, S. Guan, E.W. Mcfarland, D.M. Poojary, K. Self, H.W. Turner, W.H. Weinberg, High-throughput Synthesis and Screening of Combinatorial Heterogeneous Catalyst Libraries, Angew. Chemie. 38 (1999) 483–488.

[4] S.H. Baeck, T.F. Jaramillo, C. Brändli, E.W. McFarland, Combinatorial Electrochemical Synthesis and Characterization of Tungsten-Based Mixed-Metal Oxides, J. Comb. Chem. 4 (2002) 563–568.

[5] J. Klein, C.W. Lehmann, H.W. Schmidt, W.F. Maier, Combinatorial Material Libraries on the Microgram Scale with an Example of Hydrothermal Synthesis, Angew. Chemie - Int. Ed. 37 (1999) 3369–3372.

[6] E. Danielson, J.H. Golden, E.W. Mcfarland, A combinatorial approach to the discovery and optimisation of luminescent materials, Nature. 389 (1997) 944–948.

[7] X.D. Sun, K.A. Wang, Y. Yoo, W.G. Wallace-Freedman, C. Gao, X.D. Xiang, P.G. Schultz, Solution-phase synthesis of luminescent materials libraries, Adv. Mater. 9 (1997) 1046–1049.

[8] G. Brice o, H. Chang, X. Sun, P.G. Schultz, X.-D. Xiang, A Class of Cobalt Oxide Magnetoresistance Materials Discovered with Combinatorial Synthesis, Science. 270 (1995) 273–275.

[9] R.B. Van Dover, L.F. Schneemeyer, R.M. Fleming, Discovery of a useful thin-film dielectric using a composition-spread approach, Nature. 392 (1998) 162–164.

[10] T.E. Mallouk, E.S. Smotkin, Combinatorial catalyst development methods, in: Handb. Fuel Cells, 2010.

[11] N.M. Nursam, X. Wang, R.A. Caruso, High-Throughput Synthesis and Screening of Titania-Based Photocatalysts, ACS Comb. Sci. 17 (2015) 548–569.

[12] X. Liu, Y. Shen, R. Yang, S. Zou, X. Ji, L. Shi, Y. Zhang, D. Liu, L. Xiao, X. Zheng, S. Li, J. Fan, G.D. Stucky, Inkjet printing assisted synthesis of multicomponent mesoporous metal oxides for ultrafast catalyst exploration, Nano Lett. 12 (2012) 5733–5739.

[13] O.D.L. De los Cobos, B. Fousseret, M. Lejeune, F. Rossignol, M. Dutreilh-colas, C. Carrion, M. Wong, C. Man, J. Durand, Tunable Multifunctional Mesoporous Silica Microdots Arrays by Combination of Inkjet Printing, EISA, and Click Chemistry, Chem. Mater. 24 (2012) 4337–4342.

[14] B. Fousseret, M. Mougenot, F. Rossignol, J.F.O. Baumard, B. Soulestin, C. Boissiére, F.O. Ribot, D. Jalabert, C. Carrion, C. Sanchez, M. Lejeune, Inkjet-printing-engineered functional microdot arrays made of mesoporous hybrid organosilicas, Chem. Mater. 22 (2010) 3875–3883.

[15] R. Ahmad, M. Vaseem, N. Tripathy, Y.-B. Hahn, Wide linear-range detecting nonenzymatic glucose biosensor based on CuO nanoparticles inkjet-printed on electrodes, Anal. Chem. 85 (2013) 10448–10454.

[16] M. Černá, M. Veselý, P. Dzik, Physical and chemical properties of titanium dioxide

printed layers, Catal. Today. 161 (2011) 97–104.

[17] I. Fasaki, K. Siamos, M. Arin, P. Lommens, I. Van Driessche, S.C. Hopkins, B.A. Glowacki, I. Arabatzis, Ultrasound assisted preparation of stable water-based nanocrystalline TiO_2 suspensions for photocatalytic applications of inkjet-printed films, Appl. Catal. A Gen. 411 (2012) 60–69.

[18] C.-W. Yen, M.-L. Lin, A. Wang, S.-A. Chen, J.-M. Chen, C.-Y. Mou, CO Oxidation Catalysed by Au−Ag Bimetallic Nanoparticles Supported in Mesoporous Silica, J. Phys. Chem. C. 113 (2009) 17831–17839.

[19] F. Rodríguez-Reinoso, The role of carbon materials in heterogeneous catalysis, Carbon. 36 (1998) 159–175.

[20] Y. Gao, Y. Zhang, Y. Zhou, C. Zhang, H. Zhang, S. Zhao, J. Fang, M. Huang, X. Sheng, Synthesis of ordered mesoporous La_2O_3-ZrO_2 composites with encapsulated Pt NPs and the effect of La-dopping on catalytic activity, J. Colloid Interface Sci. 503 (2017) 178–185.

[21] X. Liu, P. Ning, L. Xu, Q. Liu, Z. Song, Q. Zhang, Low-temperature catalytic oxidation of CO over highly active mesoporous Pd/CeO_2-ZrO_2-Al_2O_3 catalyst, RSC Adv. 6 (2016) 41181–41188.

[22] P. Zhang, H. Lu, Y. Zhou, L. Zhang, Z. Wu, S. Yang, H. Shi, Q. Zhu, Y. Chen, S. Dai, Mesoporous $MnCeO_x$ solid solutions for low temperature and selective oxidation of hydrocarbons, Nat. Commun. 6 (2015) 1–10.

[23] M.E. Ali, M.M. Rahman, S.M. Sarkar, S.B.A. Hamid, Heterogeneous metal catalysts for oxidation reactions, J. Nanomater. 2014 (2014) 1–23.

[24] D.J. Kim, B.C. Dunn, P. Cole, G. Turpin, R.D. Ernst, R.J. Pugmire, M. Kang, J.M. Kim, E.M. Eyring, Enhancement in the reducibility of cobalt oxides on a mesoporous silica supported cobalt catalyst, Chem. Commun. 11 (2005) 1462–1464.

[25] A. Kumar, V.P. Kumar, B.P. Kumar, V. Vishwanathan, K.V.R. Chary, Vapor phase oxidation of benzyl alcohol over gold nanoparticles supported on mesoporous TiO_2, Catal. Letters. 144 (2014) 1450–1459.

[26] W. Song, A.S. Poyraz, Y. Meng, Z. Ren, S.Y. Chen, S.L. Suib, Mesoporous Co_3O_4 with controlled porosity: Inverse micelle synthesis and high-performance catalytic CO oxidation at -60 °C, Chem. Mater. 26 (2014) 4629–4639.

[27] M.S. Xaba, R. Meijboom, Kinetic and catalytic analysis of mesoporous Co3O4 on the oxidation of morin, Appl. Surf. Sci. 423 (2017) 53–63.

[28] A.K. Ilunga, R. Meijboom, Random alloy nanoparticles of Pd and Au immobilised on reducible metal oxides and their catalytic investigation, Appl. Catal. B Environ. 203 (2017) 505–514.

[29] L. Wang, G. Dalglish, Z. Ouyang, D.G. David-Brown, C. Chiriac, J. Duo, A. Kozhich, Q.C. Ji, J.E. Peterson, Integration of Acoustic Liquid Handling into Quantitative Analysis of Biological Matrix Samples, SLAS Technol. Transl. Life Sci. Innov. (2020) 2472630320915844.

[30] E.K. Sackmann, L. Majlof, A. Hahn-Windgassen, B. Eaton, T. Bandzava, J. Daulton, A. Vandenbroucke, M. Mock, R.G. Stearns, S. Hinkson, Technologies that enable accurate and precise nano-to milliliter-scale liquid dispensing of aqueous reagents using acoustic droplet ejection, J. Lab. Autom. 21 (2016) 166–177.

[31] B. Edwards, J. Lesnick, J. Wang, N. Tang, C. Peters, Miniaturization of high-throughput epigenetic methyltransferase assays with acoustic liquid handling, J. Lab. Autom. 21 (2016) 208–216.

[32] A.S. Xiao, E.S. Lightcap, D.C. Bouck, Acoustic Liquid Handling for Rapid siRNA Transfection Optimization, J. Biomol. Screen. 20 (2015) 957–964.

[33] J. Rader, K. Watson, Sequence ready library preparation fully automated for microbial and human DNA template, (n.d.).

[34] A.C. Ma, M.S. McNulty, T.L. Poshusta, J.M. Campbell, G. Martínez-Gálvez, D.P. Argue, H.B. Lee, M.D. Urban, C.E. Bullard, P.R. Blackburn, T.K. Man, K.J. Clark, S.C. Ekker, FusX: A Rapid One-Step Transcription Activator-Like Effector Assembly System for Genome Science., Hum. Gene Ther. 27 (2016) 451–463.

[35] M. Storch, M.C. Haines, G.S. Baldwin, DNA-BOT: a low-cost, automated DNA assembly platform for synthetic biology, Synth. Biol. 5 (2020).

[36] K.M. Poulsen, T. Pho, J.A. Champion, C.K. Payne, Automation and low-cost proteomics for characterisation of the protein corona: experimental methods for big data, Anal. Bioanal. Chem. 412 (2020) 6543–6551.

[37] P.M. Collins, J.T. Ng, R. Talon, K. Nekrosiute, T. Krojer, A. Douangamath, J. Brandao-Neto, N. Wright, N.M. Pearce, F. von Delft, Gentle, fast and effective crystal soaking by acoustic dispensing, Acta Crystallogr. Sect. D Struct. Biol. 73 (2017) 246–255.

[38] N.M. Nebane, T. Coric, S. McKellip, L.K. Woods, M. Sosa, L. Rasmussen, M.A. Bjornsti, E.L. White, Acoustic Droplet Ejection Technology and Its Application in

High-Throughput RNA Interference Screening, J. Lab. Autom. 21 (2016) 198–203.

[39] Y.C. Tung, A.Y. Hsiao, S.G. Allen, Y.S. Torisawa, M. Ho, S. Takayama, High-throughput 3D spheroid culture and drug testing using a 384 hanging drop array, Analyst. 136 (2011) 473–478.

[40] B.A. Brodin, K. Wennerberg, E. Lidbrink, O. Brosjö, S. Potdar, J.N. Wilson, L. Ma, L.N. Moens, A. Hesla, E. Porovic, Drug sensitivity testing on patient-derived sarcoma cells predicts patient response to treatment and identifies c-Sarc inhibitors as active drugs for translocation sarcomas, Br. J. Cancer. 120 (2019) 435–443.

[41] E. Kulesskiy, J. Saarela, L. Turunen, K. Wennerberg, Precision cancer medicine in the acoustic dispensing era: ex vivo primary cell drug sensitivity testing, J. Lab. Autom. 21 (2016) 27–36.

[42] K. Blom, P. Nygren, J. Alvarsson, R. Larsson, C.R. Andersson, Ex vivo assessment of drug activity in patient tumor cells as a basis for tailored cancer therapy, J. Lab. Autom. 21 (2016) 178–187.

[43] L.A. Mitchell, L.H. McCulloch, S. Pinglay, H. Berger, N. Bosco, R. Brosh, M. Bulajic, E. Huang, J.A. Martin, M.S. Hogan, De novo assembly, delivery and expression of a 101 kb human gene in mouse cells, BioRxiv. (2019) 423426.

[44] J.J. Minich, G. Humphrey, R.A.S. Benitez, J. Sanders, A. Swafford, E.E. Allen, R. Knight, High-throughput miniaturised 16S rRNA amplicon library preparation reduces costs while preserving microbiome integrity, MSystems. 3 (2018) e00166-18.

[45] S.J. Moore, J.T. MacDonald, S. Wienecke, A. Ishwarbhai, A. Tsipa, R. Aw, N. Kylilis, D.J. Bell, D.W. McClymont, K. Jensen, Rapid acquisition and model-based analysis of cell-free transcription–translation reactions from nonmodel bacteria, Proc. Natl. Acad. Sci. 115 (2018) E4340–E4349.

[46] L. Ballell, R.H. Bates, R.J. Young, D. Alvarez-Gomez, E. Alvarez-Ruiz, V. Barroso, D. Blanco, B. Crespo, J. Escribano, R. González, Fueling open-source drug discovery: 177 small-molecule leads against tuberculosis, ChemMedChem. 8 (2013) 313–321.

[47] C.G. Neochoritis, S. Shaabani, M. Ahmadianmoghaddam, T. Zarganes-Tzitzikas, L. Gao, M. Novotná, T. Mitríková, A.R. Romero, M.I. Irianti, R. Xu, Rapid approach to complex boronic acids, Sci. Adv. 5 (2019) eaaw4607.

[48] Y. Xiong, V. Shapaval, A. Kohler, J. Li, P.J. From, A Fully Automated Robot for the Preparation of Fungal Samples for FTIR Spectroscopy Using Deep Learning, IEEE Access. 7 (2019) 132763–132774.

[49] S. Jones, S.M. Fairclough, M. Gordon-Brown, W. Zheng, A. Kolpin, B. Pang, W.C.H. Kuo, J.M. Smith, S.C.E. Tsang, Dual doping effects (site blockage and electronic promotion) imposed by adatoms on Pd nanocrystals for catalytic hydrogen production, Chem. Commun. 51 (2015) 46–49.

[50] R. State, F. Papa, C. Munteanu, I. Balint, A. Ion, A. Volceanov, Synthesis and Characterisation of PVP (Polyvinly Pyrrolidone) Stablized Gold Nanoparticles, Rom. J. Mater. 45 (2015) 262–266.

[51] N. Bingwa, S. Bewana, M. Haumann, R. Meijboom, Revisiting kinetics of morin oxidation: Surface kinetics analysis, Appl. Surf. Sci. 426 (2017) 497–503.

Chapter 5

The Use of Robotics and 3D Printing in Chemistry – An Open-Source Approach

Chapter 5

The Use of Robotics and 3D Printing in Chemistry – An Open-Source Approach

Abstract

Open-source hardware is the development of equipment made available for anyone to use. This means that design is made to be distributed freely, for anyone to obtain and build. Liquid handling robots and 3D printers are among the open-source hardware that is freely available. Liquid handling robots are mostly used in life sciences for dilutions etc. However, in chemistry, liquid handling robots are also required for high-throughput experiments, especially for catalyst screening. Here, we discuss the assembly of the EvoBot to be used in catalysis. A few issues were encountered; however, these were resolved, using techniques such as 3D printing. We also demonstrate the use of 3D printing of labware for the improvement of productivity. The labware was either designed using a CAD program or printed from open-source files.

5.1 Introduction

In the scientific field, researchers are reliant on laboratory equipment to carry out specific tasks. Equipment is often very expensive and can only be purchased from major companies or the supplier. In recent years, there have been ongoing efforts to produce free and open-source hardware (FOSH) to replace laboratory equipment [1, 2]. FOSH can also be used for the development and production of components and tools to be used for the creation of new laboratory instruments [3]. This gives an opportunity to drastically reduce the cost of laboratory equipment as well as experimentation in research [2, 4]. Moreover, this can improve productivity in research and expand the knowledge and skill set of the researcher.

The term open-source originated from hackers (referring to a computer programmer who develops free and open-source software) which were involved in the early open software movement. Initially, open-source software was designed and released for free. The success in creating open-source software led to the development of open-source hardware [2]. The same principles for free and open-source software (FOSS) can be applied to free and open-source hardware (FOSH). This indicates that free and open-source hardware can be designed and made available to the public for anyone to study, modify, distribute, make, or sell [2].

The most successful open-source hardware project to date is the Arduino project [2, 3]. This is an electronic prototyping platform that is easy to learn and use. The Arduino is an affordable microcontroller that is capable of running many scientific apparatuses. Projects that have employed the Arduino microcontroller include an environmental chamber or sensor [5], pH meter [6], oscilloscope [7], and an open-source polymerase chain reaction (PCR) machine [8] for DNA analysis. It has also been used for analytical chemistry [3] applications such as electrochemical [9] and optical detection [10], mass spectrometry [11–13], separations [14, 15] and microfluidics [13, 16] and auto titrations [17]. The Arduino microcontroller can also be used to operate a 3D printer with the employment of RepRap [2]. RepRap is an acronym for Replicating Rapid-prototyper which is used in a series of open-source 3D printers. It was initially created for the self-replication of 3D printers to reduce the cost of instrumentation. It was created to transform commercial/industrial instruments to benchtop instruments which can be used by academic laboratories as well as hobbyists [3].

The process referred to as 3D printing involves the deposition of building material in layers to construct a 3D object. The object is constructed by the building up of layers that are placed on top of each other. The material is deposited at coordinates given by a digital model that has been created by a computer-controlled positioning system [18]. This is referred to as a layer-based approach. This process does not involve predetermined moulds; hence objects constructed can be tailored for a specific application. Moreover, it is not used for large-volume production such as injection moulding, but instead for the manufacturing of small or large unique objects. Different materials can be used for different applications. Hobbyists usually use materials such as polylactic acid (PLA), acrylonitrile butadiene styrene (ABS), and polyethylene terephthalate glycol (PETG). However, nylon or polypropylene is used for the chemical application of 3D printing since it is chemically inert [19].

To create a 3D object, the object model is initially designed using computer-aided design (CAD) software. The design is exported as a printable file format (STL, or STEP file format), imported into a program, known as a slicer, which can convert the model into 3D coordinates for the printer to read. The slicer program converts the model to a series of layers in the Z-direction [20]. A thermoplastic is used to translate the computer model to a physical 3D object which can be held [21]. As mentioned above, the coordinates denote the layers to be placed on top of each other. Therefore, the deposition of 2D layers on top of each other will create a 3D object [18]. By adjusting the material, using materials with diversity and strength, the print

resolution and speed, 3D printing becomes competitive with conventional fabrication and prototyping methods [22].

The 3D printing technique is not only used by hobbyists, but it can also be used to create microreactors (or reaction ware) [23], microfluidic devices [20], and analytical equipment [24] for the use in chemistry. Recently, Alimi *et al.*, [21] used the 3D printing technique for the manufacturing of a microfluidic device for the reduction of 4-nitrophenol (4-NP) to 4-aminophenol (4-AP) using a Pd/Co_3O_4 mesoporous metal oxide heterogeneous catalyst. The microfluidic device was 3D printed using PLA. There was no need to use chemically inert materials since the reaction was performed in an aqueous solution. It was shown that the 4-NP could be converted (98% conversion) to 4-AP in approximately 8 min, using a continuous-flow system.

Moreover, continuous-flow systems created using 3D printing can also be used for the synthesis of organic compounds. This was illustrated by Dragone *et al.* [19], for the synthesis as well as the reduction of the imine compounds. The reactions were followed used an ATR-IR flow cell. Polypropylene was used as the 3D printing material since chemically inert materials were required.

Not only can 3D printing be used for creating reactors and laboratory equipment, but it can also be used to create labware for increased productivity. With a 3D printer on hand in the laboratory; vial, sample, and tube holders can be 3D printed easily. This decreases the running costs of the laboratories tremendously. Instead of ordering labware from a company and waiting weeks for delivery (as is the case in South Africa), one could just print labware to be used immediately. Moreover, with a skill set to design using a CAD program, this enables the researcher to design unique labware or prototypes to be transformed to labware or laboratory equipment.

The production of reactors, microfluidic devices, and 3D printers are not the only entities that are open-source. Recently, liquid handling robots have also been designed and built to be used for life sciences. The Opentrons and EvoBot are examples of open-source liquid handling robots [25–29]. The Opentrons can also be bought commercially; however, the EvoBot was designed and created to be built by researchers. The EvoBot is a modular open-source liquid handling robot with a production cost estimated at R25 000 ($1500). This is very affordable

compared to other commercially available liquid handling robots which can be priced at over R500 000. This robot can be built at home or in the laboratory. Even though the EvoBot focusses on low-throughput research experiments, it can be used for long-running experiments as well. As mentioned early, it is a modular robot which means that the robot can be reconfigured and extended for use in diverse experiments. Furthermore, a camera for real-time video recording can be incorporated, which enables the experimenter to interact with the experiment while in progress.

The EvoBot was designed as part of the EVOBLISS project [29]. This project is part of cluster projects which were funded by the E.C.'s Future and Emergent technologies proactive on evolving living technologies (EVLIT). The projects are aimed at the exploration of the potential of the computational self-adapting properties of a living organism for the future. The EVOBLISS project focussed on living organisms for energy production and using state-of-the-art technologies of microbial fuel cells (https://blogit.itu.dk/evoblissproject/).

Initially, with the design of the EvoBot, the components were meant to be laser or water cut from specific materials such as Perspex or polyoxymethylene (POM). However, it was designed in such a way that the components could also be 3D printed. The 2D patterns (for laser or water cutting) of components were given and could be extruded to a 3D model, using a CAD program. This allows the components also to be 3D printed. The electronics of the EvoBot consists of an open-source prototyping platform which includes an Arduino board and Ramps shield. The software has been developed in Python, and the motions of the robot are controlled by interpreting commands from a G-code file. It should be noted that basic skills or experience with these technologies (the Arduino board and Python coding) are necessary to control and operate the EvoBot.

The EvoBot was designed to perform basic liquid handling experiments, whereby the content of reaction vessels can be mixed and also to pre-rinse vessels before the addition of a particular solution. Moreover, liquids can be aspirated from one source and dispense it into another. A waste container can be included for the disposal of a pre-rinse solution or when the robot empties a well-plate. Once a syringe has been emptied, the robot can automatically detect the empty syringe and refill it with the same liquid. The EvoBot has already been used for numerous applications including serial dilutions for ELISA (enzyme-linked immunosorbent assay) as well as PCR [30]. The EvoBot has also been used for microbiology applications

where it was used for cell culturing and nurturing of cells [31]. Moreover, droplet placement can be achieved using this open-source robot. This application involves the precise placement of drops in two or three dimensions, including circle or rectangular patterns or more complex shapes.

Recently, the EvoBot has been upgraded to extend the modularity of the robot. This includes a moveable head that allows the mount of self-contained pipetting modules as well as sensors and grippers. Moreover, new modules and standalone controllers have been introduced and can be applied to new experiments such as nurturing microbial fuel cells. It has also been shown that an Optical Coherence Tomography (OCT) scanner can precisely be positioned and chemotaxis of droplets can be analysed and optimised [28].

The EvoBot can potentially be modified to be used for chemistry, particularly catalysis. It can be used for the synthesis of homo- and heterogeneous catalysts, and also the screening thereof. Moreover, reagents can be pipetted into a high-throughput system such as microtiter plates for parallel reactions. In this study, it was shown that 3D printing (from a CAD model) could be used for the production of labware and also to build the EvoBot. Moreover, challenges faced with the assembly of the EvoBot are also discussed.

5.2 Experimental

5.2.1 Materials

5.2.1.1 EvoBot

All parts for the construction of the EvoBot were purchased from RS Components (www.za.rs-online.com), the 3D printing store (www.3dprintingstore.co.za), Micro Robotics (www.robotics.org.za) and the local hardware store. The head and syringe printed circuit boards (PCB's) were assembled by JP Electronics. See the bill of materials (BOM) in the supplementary information (**Table S5.1, S5.2, S5.3, and S5.s4**).

5.2.1.2 3D printing

The 3D printers were purchased from www.prusa3d.com and included an Original Prusa i3 MK2S, Original Prusa i3 MK2.5, and Original Prusa i3 MK3. The labware was 3D printed using polylactic acid (PLA) thermoplastic which was purchased from www.3dprintingstore.co.za.

To print the objects, the .stl files were imported into a slicing program (PrusaSlicer based on Slic3r) which converted the .stl files to a G-code file containing the XYZ coordinates for the 3D printer to deposit the layers.

5.2.2 Method

5.2.2.1 EvoBot

The EvoBot forms part of the EVOBLISS project. The instructions were obtained from the EVOBLISS project website. The files are obtainable from the internet (https://bitbucket.org/afaina/evobliss-hardware, https://bitbucket.org/afaina/evobliss-software, and https://www.thingiverse.com/thing:2776125). The EvoBot was assembled according to the assembly document. The aluminium V-slot profiles were used to construct the frame, the experimental layer, and the actuator layer. An observation layer was not included with this EvoBot. The carriage plates and electronic covers for the syringe module were 3D printed using PLA filament. The height control plates and corner brackets were laser-cut from aluminium sheets.

5.2.2.2 3D printing

Some of the labware was printed from pre-existing Open-Source files available online (www.thingiverse.com). Others were designed using the Onshape (Onshape.com) CAD online program and 3D printed from the exported .stl file.

5.3 Results and discussion

5.3.1 Assembly of the EvoBot robot

The documentation for the EvoBot included a bill of materials for the robot module, the syringe module, the head, and printed circuit boards (PCB's) for the syringe, as well as building instructions for the frame, the carriage (carriage plates), syringe module (with the electronic covers) as well as the actuator and experimental layer. Building instructions for each section of the robot was clearly stated, with a description as well as figures (**Figure 5. 1**).

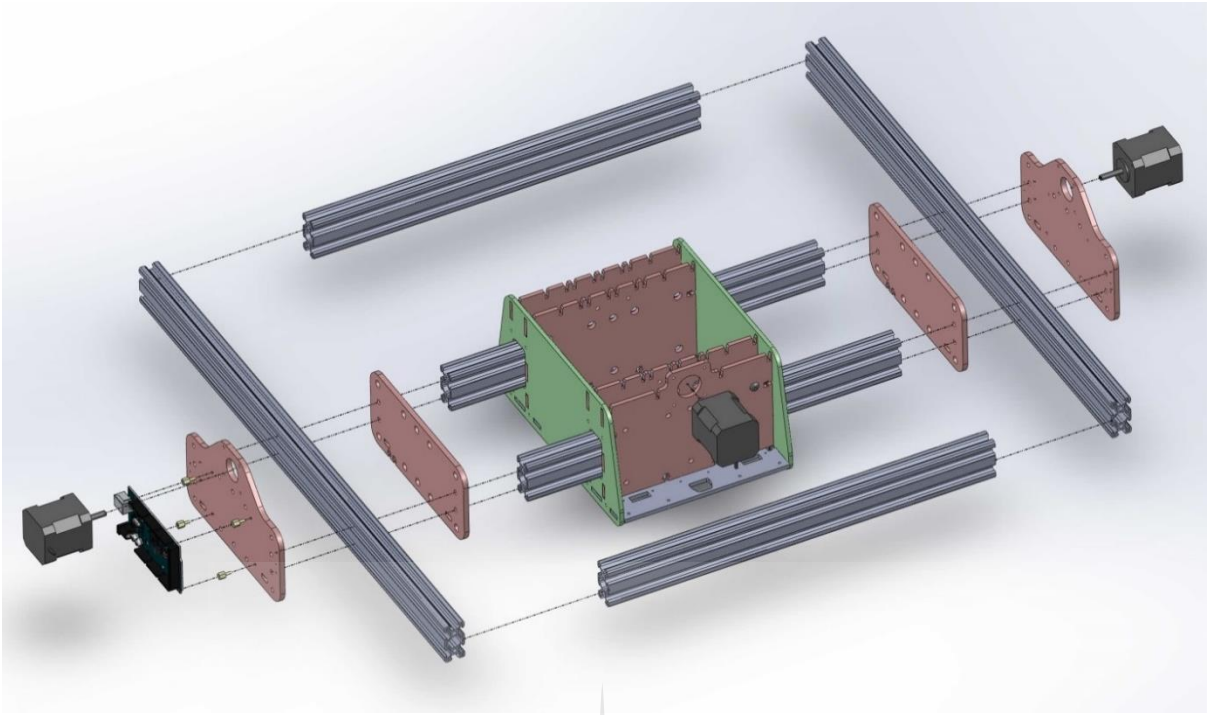

Figure 5. 1: An example of a figure provided in the building instruction documentation of the EvoBot. The figure represents the assembly of the actuator layer (https://bitbucket.org/afaina/evobliss-hardware and https://bitbucket.org/afaina/evobliss-software).

The frame of the EvoBot was constructed using aluminium V-slot profiles. A total of 12 aluminium V-slots were used to assemble the frame. This consisted of a top and bottom frame connected with four profiles, which forms the side frame (**Figure 5.2**). The profiles were attached using aluminium brackets and bolts and nuts.

Figure 5.2: The frame of the EvoBot constructed using aluminium V-slot profiles. The height controls can also be seen in the figure.

Originally the carriage plates, electronic covers for the syringe modules as well as the height control plates and corner brackets of the EvoBot were designed to be constructed from materials such as poly(methyl methacrylate) (PMMA) and polyoxymethylene (POM). The .dxf files were provided, and the parts could be laser-cut from these materials. The carriage plates were supposed to be laser-cut from 4 mm PMMA sheets. The height control and corner brackets from 3 mm POM sheets and the electronic covers for the syringe module from 1 mm POM sheets. Many issues were encountered in finding a local manufacturer or distributor for these specific sheets and also to find the correct sizes.

Moreover, we also could not find a laser-cutting company that could assist with cutting these specific sheets. It was, therefore, decided to cut the parts from aluminium sheets (**Figure 5.3**). It was possible to obtain aluminium sheets as thin (1, 3 and 4 mm) as stipulated in the assembly document.

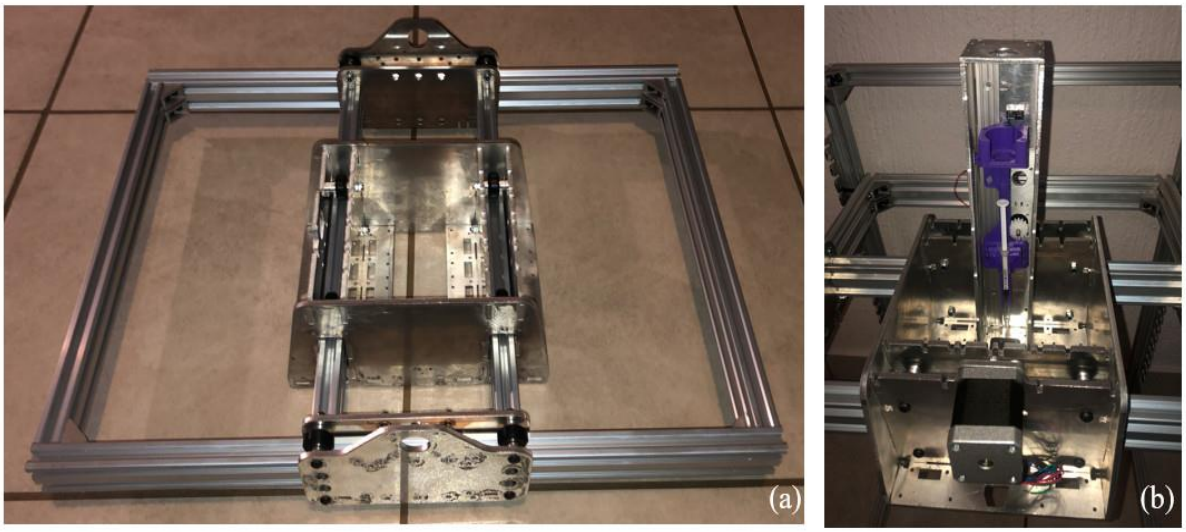

Figure 5.3: Carriage plates **(a)** and electronic cover parts, **(b)** laser-cut from 3 mm and 1 mm aluminium sheets, respectively.

Unfortunately, it was noted that the aluminium parts were too heavy, and the stepper motors would not have been able to move the carriages easily. As the .dxf files of the carriage plates and electronic covers for the syringe module were provided, the 2D files were imported into the Onshape CAD program, extruded to the specific heights needed, 1 mm for the syringe module electronic covers and 4 mm for the carriage plates, to give a 3D model (**Figure 5.4** and **Figure 5.5**).

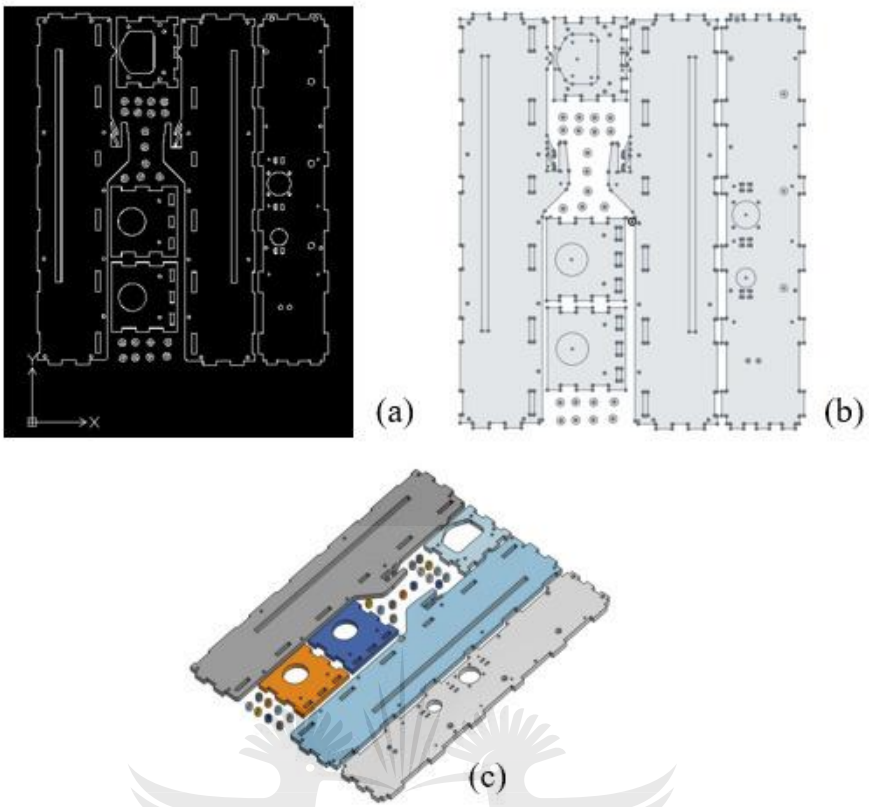

Figure 5.4: **(a)** Design files for the syringe module electronic cover, **(b)** the .dxf files converted to a 2D model and **(c)** extruded to a 1 mm 3D model using Onshape CAD program.

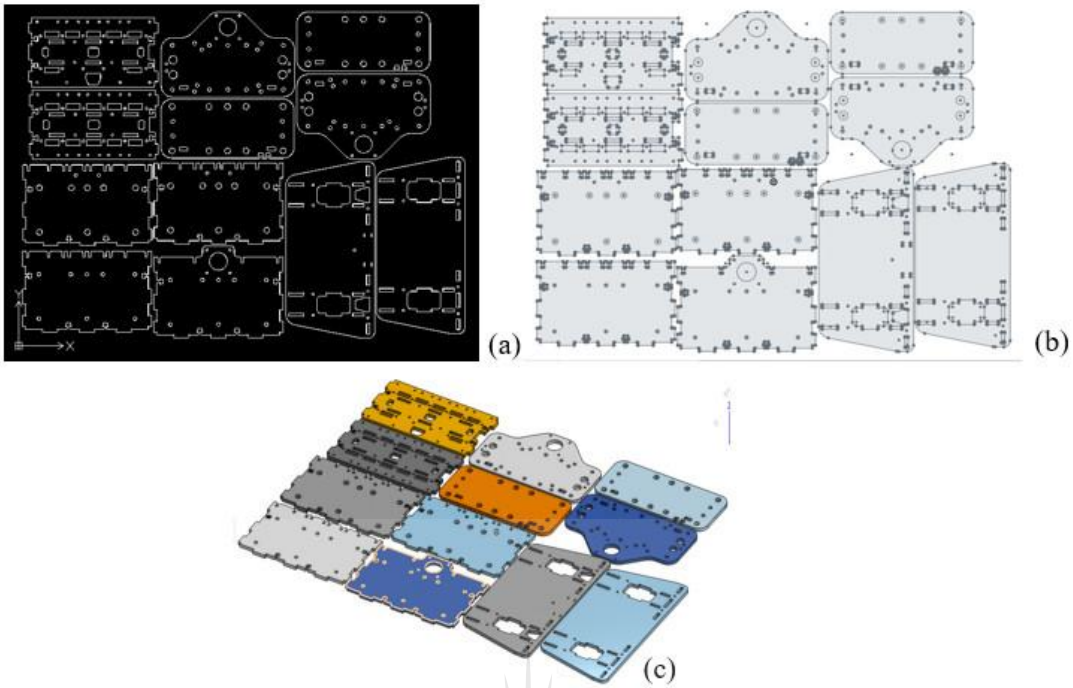

Figure 5.5: **(a)** Design files for the carriage plates, **(b)** the .dxf files converted to 2D models, and **(c)** extruded to a 4 mm 3D model using the Onshape CAD program.

The 3D models for the carriage plates and syringe module electronic covers were exported, and 3D printed using PLA filament (**Figure 5.6**). It was relatively easy to assemble the carriage and syringe module. The parts were designed with a lock-and-key model so that the plates and electronic covers fit easily into one another. By 3D printing these parts, it made the carriage and syringe module lighter compared to the aluminium parts, and hence can be moved easier by the stepper motors.

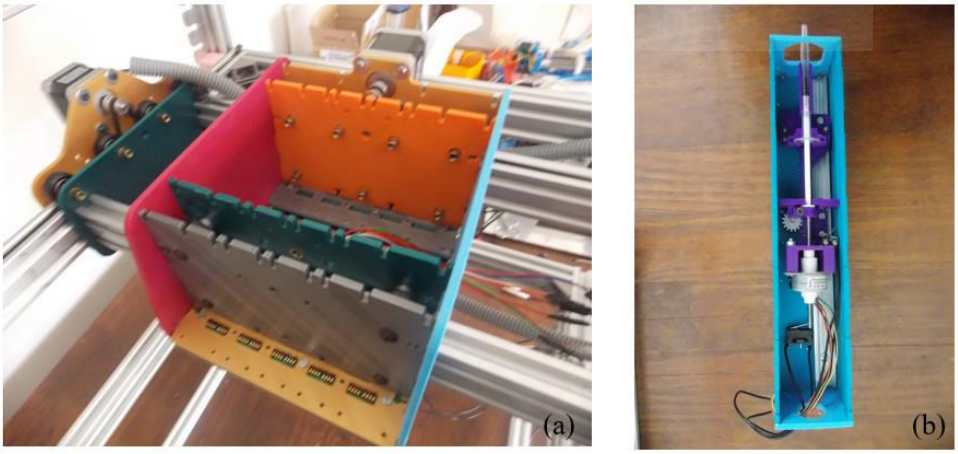

Figure 5.6: **(a)** 3D printed carriage plates and **(b)** the syringe module electronic covers. The parts were 3D printed using PLA filament.

The parts listed in the original BOM for the robot module provided by the developers of the EvoBot were not detailed enough, making it challenging to obtain some of the parts. Moreover, some parts, such as the stepper motors could not be obtained in South Africa. See **Table 5.1** for the list.

Table 5.1: List of stepper motors originally used for the EvoBot which had to be substituted with different motors due to availability in South Africa.

Stepper motor	**Orginal stepper motor used**	**Stepper motor purchased**
Z stepper motors	NEMA 17 Bipolar Step Motor 2.9 V 0.7 A 18 N·cm (25.5 oz·in)	NEMA 17 × 40 mm, 1.8 deg/step
X stepper motor	NEMA 17 Bipolar Stepper 5.4 V 0.85 A 36 N·cm (51 oz·in)	NEMA 17 × 48 mm, 1.8 deg/step
Syringe stepper motor	NEMA 8 Bipolar 0.6 A 4 N·cm (5.7 oz·in) mini stepper motor	NEMA 8, 1.8 N·cm, 1.8 deg/step, micro stepper motor
Linear stepper motor	25NCLA Non-Captive Linear stepper motor 25NCLA-B01	N-type, linear actuator, 28.1 N, 12 V dc, 48 mm stroke

5.3.2 Electronics and coding

The EvoBot was assembled successfully; however, the assembly of the electronics was challenging. Challenges were encountered since our expertise is in Chemistry, and not setting up electronics. Therefore, the EvoBot is not yet fully operational. The challenges faced with the set up of the electronics include: that the assembly instructions were not clearly stated. The files for the printed circuit boards (PCB's), as shown in **Figure 5.7**, didn't contain much detail. Additional holes were added to the PCB's to secure the boards to the robot.

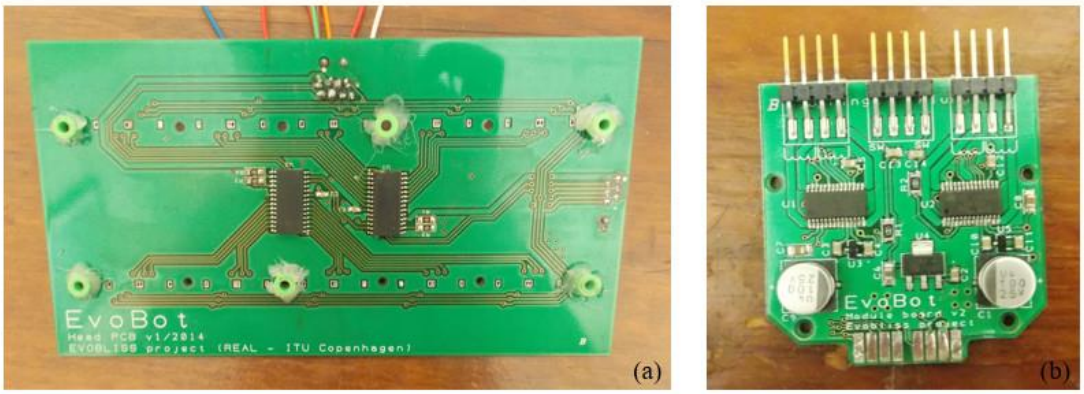

Figure 5.7: **(a)** PCB for the EvoBot robot and the **(b)** syringe module.

The quality of the wiring diagrams for the RAMPS 1.4 board, as well as for the Arduino (**Figure 5.8**), was poor. This may be since these files were obtained from the website. Moreover, the wiring diagrams for the syringe modules could not be obtained from the website. Despite these issues, an attempt was made with the wiring (**Figure 5.9**).

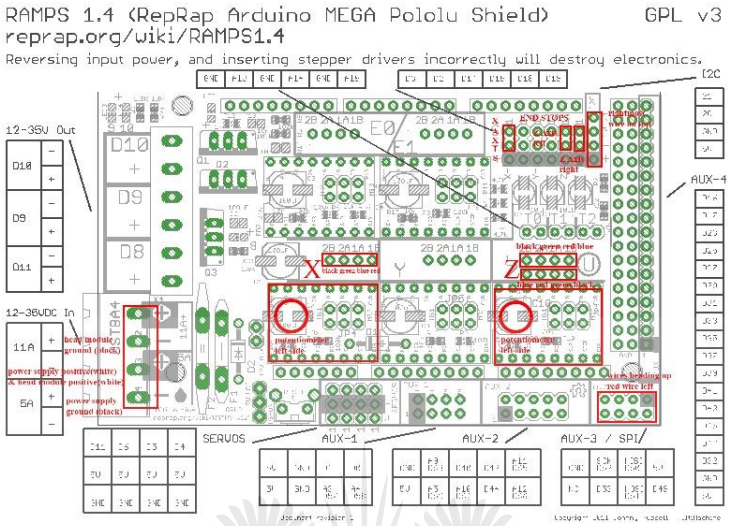

Figure 5.8: An example of the RAMPS and Arduino wiring diagram provided with the building instructions of the EvoBot.

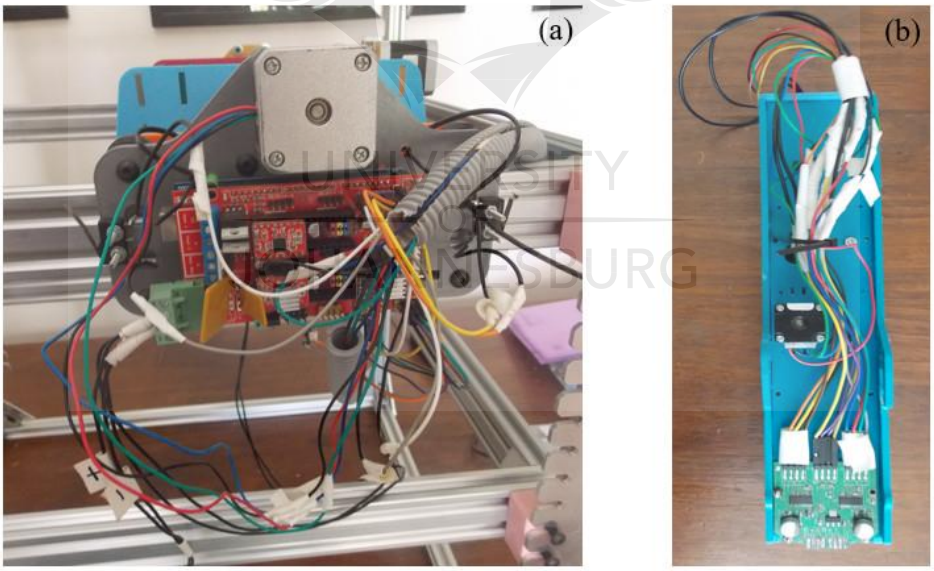

Figure 5.9: The wiring of the EvoBot robot – **(a)** RAMPS 1.4 and the **(b)** syringe module.

Another issue encountered was with the bill of materials (BOM) and the CAD files. These files were not annotated clearly, and a general descript of the part was not given,

Following the assembly of the robot and the connection of the electronics, the robot had to be evaluated. The code for the EvoBot was written in Python 2.7. Unfortunately, Python 2.7 is no

longer supported as of January 2020. The Python 2.7 code has been ported to Python 3.0, where possible. This made it challenging testing the robot thus far.

5.3.3 3D printing in the laboratory

5.3.3.1 Custom-designed 3D printed labware

Unique labware was designed using the Onshape CAD program, specifically for the increased productivity in the laboratory. Openscad is another CAD designing program that can be used for designed 3D models; however, some coding skills are required to use this program. Labware designed and 3D printed includes a cuvette insert for the centrifuge (**Figure 5.10**), a tube holder of an oil bath and a BET tube holder (**Figure 5.11**) to weigh out samples to be analysed by the BET accurately. A tube holder was also designed to be placed on top of an oil bath to heat samples (**Figure 5.12**). The models were designed; the .stl files were exported and sliced to obtain the G-code for 3D printing.

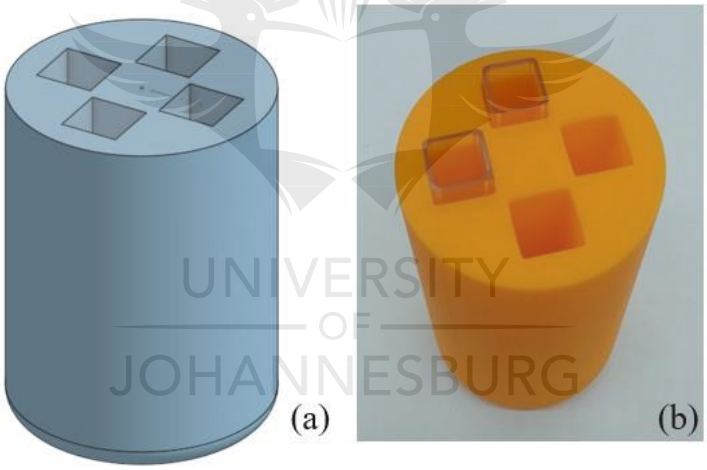

Figure 5.10: **(a)** The CAD model of the cuvette insert or holder for the centrifuge. This was designed in Onshape and **(b)** 3D printed using PLA filament. This was designed for plastic cuvettes with a path length of 1 cm.

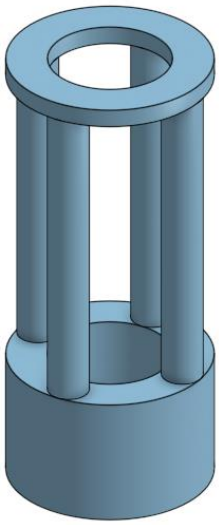

Figure 5.11: BET tube holder for accurately weigh out samples to be analysed on the BET.

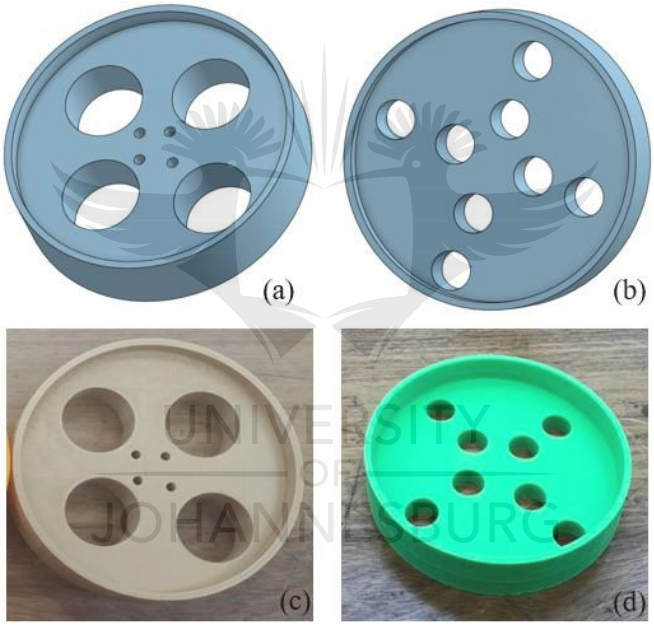

Figure 5.12: Oil bath test tube holders. **(a)** For larger test tubes, **(b)** for smaller test tubes, and **(c)** and **(d)** the 3D printed models of test tube holders printed with PLA filament.

5.3.3.2 Open-Source 3D printed labware

Labware was also 3D printed from open-source files obtained from the 3D printing community (www.thingiverse.com). The files were downloaded and sliced to obtain the G-code to be 3D printed. These models included vial holders, centrifuge tube holders, pipette stands, and GC vial holders (**Figure 5.13**).

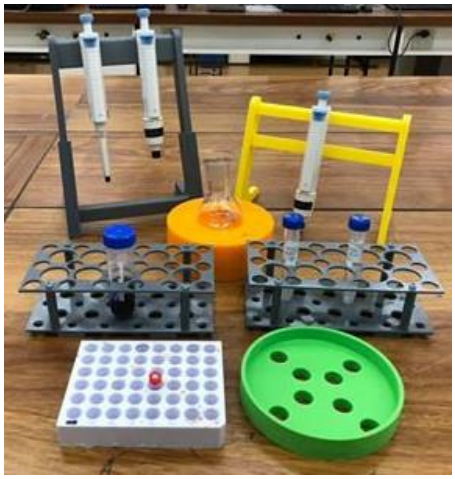

Figure 5.13: Labware 3D printed from open-source files obtained and downloaded from thingiverse.com.

By 3D printing labware, it has the potential to decrease the running costs of a laboratory greatly. It is cheaper to 3D print labware than to purchase it from designated companies. Moreover, the labware can be 3D printed immediately when needed and customised to suit individual needs, instead of waiting weeks or months for ordered labware to be delivered.

5.4 Future work

For future work, the EvoBot has the potential to be used for many projects and experiments in catalysis. Such a liquid handling robot is not only used to make simple dilutions but can be employed for more complex experiments. Such experiments may include, the miniaturisation of the catalytic and kinetic studies of hetero- and homogeneous catalysts since the EvoBot can be used to pipette the different reagents, the catalyst, oxidant, and dye, into a microtiter plate. These experiments can be used for the high-throughput miniaturisation of kinetic studies. This includes the investigation of more than one concentration and replicates at the same time, using one microtiter plate, as discussed in one of the previous chapters.

Moreover, it also has the potential to pipette different catalysts into a microtiter plate for the high-throughput screening of hetero- and homogeneous catalysts for a specific reaction. If a 96-well plate is used, 96 different catalysts can be screened simultaneously. The EvoBot could also be used for the combinatorial parallel synthesis of heterogeneous mesoporous metal oxide (MMO) libraries, for the high-throughput screening thereof. The robot could deposit small volumes of the different mesoporous metal oxide formulations onto a glass substrate.

Following the calcination of the glass substrate containing the MMO formulations, the catalysts can be combined or pooled to form an MMO library. The synthesis of many different libraries is possible, each having a different combination of MMO catalysts. These libraries can then be screened, further split-and-pooled, and then deconvoluted for ultra-fast catalyst exploration. It is also possible to adapt the robot modules for other applications. For example, the syringe module can be adapted for a syringe pump. This creates even more opportunities for the EvoBot.

Three-dimensional printing has had more applications in chemistry and catalysis compared to liquid handling robots. Therefore, the potential novel uses of 3D printing in the laboratory, especially chemistry and catalysis, is not as great as with the liquid handling robots. However, it can be used for the fabrication of microfluidic devices, flow cells, separation devices, and custom-made 3D-printed labware.

5.5 Conclusions

Open-source hardware allows researchers to create and build laboratory equipment as well as labware. This creates the opportunity to customise laboratory equipment, and also to adapt it for other applications. Moreover, open-source hardware is cheaper compared to commercially available laboratory equipment. The EvoBot, which is an Open-Source liquid handling robot, was assembled and built by following the building instructions provided by the creators. Some issues were encountered with the parts purchases, electronics as well as the assembly of the robot and electronics. However, many of these issues could be resolved. The EvoBot has the potential for many applications in catalysis, from miniaturisation of kinetic studies to combinatorial parallel high-throughput screening of catalyst and catalyst libraries.

Three-dimensional printing is another Open-Source technique that is used to create laboratory equipment and labware. Moreover, unique customised labware can be designed, and 3D printed to improve productivity in the laboratory. Numerous customised labware was designed, and 3D printed. Using 3D printing, one has the potential to fabricate microfluidic devices, flow cells, and separation devices.

The use of Open-Source hardware can improve productivity in the laboratory and also allow researchers to create unique laboratory equipment and labware.

5.6 Acknowledgements

Funding of this work was supported by the National Research Foundation of South Africa {Grant specific unique reference number (UID) 5386}, and the University of Johannesburg. We would like to acknowledge Mr D. Harris and Dr R. Meyer from Shimadzu South Africa (Pty) Ltd for their analytical instruments

5.7 References

[1] P.S. Gromski, J.M. Granda, L. Cronin, Universal Chemical Synthesis and Discovery with 'The Chemputer,' Trends Chem. 2 (2020) 4–12.

[2] J.M. Pearce, Open-source lab: how to build your own hardware and reduce research costs, Newnes, 2013.

[3] M.D.M. Dryden, R. Fobel, C. Fobel, A.R. Wheeler, Upon the shoulders of giants: open-source hardware and software in analytical chemistry, Anal. Chem. 89 (2017) 4330–4338.

[4] J.M. Pearce, Building research equipment with free, open-source hardware, Science. 337 (2012) 1303–1304.

[5] S.K. Lau, J. Subbiah, HumidOSH: A self-contained environmental chamber with controls for relative humidity and fan speed, HardwareX. 8 (2020) e00141.

[6] K. Hsu, S. Tan, C. Chiu, Y. Chang, I. Ng, ARduino-pH Tracker and screening platform for characterisation of recombinant carbonic anhydrase in Escherichia coli, Biotechnol. Prog. 35 (2019) e2834.

[7] A. Elfasi, M.A. Shawesh, W.T. Shanab, A.K. Thabet, Oscilloscope using arduino interface labview, in: 2017 Int. Conf. Green Energy Convers. Syst., IEEE, 2017: pp. 1–5.

[8] G. Wong, I. Wong, K. Chan, Y. Hsieh, S. Wong, A rapid and low-cost PCR thermal cycler for low resource settings, PLoS One. 10 (2015) e0131701.

[9] S.C. Bürgel, L. Diener, O. Frey, J.-Y. Kim, A. Hierlemann, Automated, multiplexed electrical impedance spectroscopy platform for continuous monitoring of microtissue spheroids, Anal. Chem. 88 (2016) 10876–10883.

[10] J.C. Miranda, M.Y. Kamogawa, B.F. Reis, Development of a portable setup and a multicommuted flow analysis procedure for the photometric determination of Fe (III) and Fe (II) in fresh water, Sensors Actuators B Chem. 207 (2015) 811–818.

[11] S.-H. Chiu, P.L. Urban, Robotics-assisted mass spectrometry assay platform enabled by open-source electronics, Biosens. Bioelectron. 64 (2015) 260–268.

[12] C.-L. Chen, T.-R. Chen, S.-H. Chiu, P.L. Urban, Dual robotic arm "production line" mass spectrometry assay guided by multiple Arduino-type microcontrollers, Sensors Actuators B Chem. 239 (2017) 608–616.

[13] J.-B. Hu, T.-R. Chen, C.-H. Chang, J.-Y. Cheng, Y.-C. Chen, P.L. Urban, A compact 3D-printed interface for coupling open digital microchips with Venturi easy ambient sonic-spray ionisation mass spectrometry, Analyst. 140 (2015) 1495–1501.

[14] T.D. Mai, M.D. Le, J. Sáiz, H.A. Duong, I.J. Koenka, H.V. Pham, P.C. Hauser, Triple-channel portable capillary electrophoresis instrument with individual background electrolytes for the concurrent separations of anionic and cationic species, Anal. Chim. Acta. 911 (2016) 121–128.

[15] J.P. Grinias, J.T. Whitfield, E.D. Guetschow, R.T. Kennedy, An inexpensive, open-source USB Arduino data acquisition device for chemical instrumentation, (2016).

[16] E.T. da Costa, M.F. Mora, P.A. Willis, C.L. do Lago, H. Jiao, C.D. Garcia, Getting started with open-hardware: Development and control of microfluidic devices, Electrophoresis. 35 (2014) 2370–2377.

[17] K.J. Mohsenian, A.T. Connolly, M.D. Johnson, Multijoint Rigidity-Testing Device for Titrating Medication and Deep Brain Stimulation Therapies, J. Med. Device. 8 (2014).

[18] C. Parra-Cabrera, C. Achille, S. Kuhn, R. Ameloot, 3D printing in chemical engineering and catalytic technology: structured catalysts, mixers and reactors, Chem. Soc. Rev. 47 (2018) 209–230.

[19] V. Dragone, V. Sans, M.H. Rosnes, P.J. Kitson, L. Cronin, 3D-printed devices for continuous-flow organic chemistry, Beilstein J. Org. Chem. 9 (2013) 951–959.

[20] Y. He, Y. Wu, J. Fu, Q. Gao, J. Qiu, Developments of 3D printing microfluidics and applications in chemistry and biology: a review, Electroanalysis. 28 (2016) 1658–1678.

[21] O.A. Alimi, N. Bingwa, R. Meijboom, Homemade 3-D printed flow reactors for heterogeneous catalysis, Chem. Eng. Res. Des. 150 (2019) 116–129.

[22] B. Gross, S.Y. Lockwood, D.M. Spence, Recent advances in analytical chemistry by 3D printing, Anal. Chem. 89 (2017) 57–70.

[23] R.D. Johnson, Custom labware: Chemical creativity with 3D printing, Nat. Chem. 4 (2012) 338.

[24] F. Li, N.P. Macdonald, R.M. Guijt, M.C. Breadmore, Increasing the functionalities of 3D printed microchemical devices by single material, multimaterial, and print-pause-

print 3D printing, Lab Chip. 19 (2019) 35–49.

[25] J. Rader, K. Watson, Sequence ready library preparation fully automated for microbial and human DNA template, (n.d.).

[26] M. Storch, M.C. Haines, G.S. Baldwin, DNA-BOT: a low-cost, automated DNA assembly platform for synthetic biology, Synth. Biol. 5 (2020).

[27] K.M. Poulsen, T. Pho, J.A. Champion, C.K. Payne, Automation and low-cost proteomics for characterisation of the protein corona: experimental methods for big data, Anal. Bioanal. Chem. 412 (2020) 6543–6551.

[28] A. Faiña, F. Nejatimoharrami, K. Stoy, EvoBot: An Open-Source, Modular, Liquid Handling Robot for Scientific Experiments, Appl. Sci. 10 (2020) 814.

[29] I. Ieropoulos, B. Taylor, P. Theodosiou, K. Stoy, F. Nejatimoharrami, A. Faíña, EvoBot: An open-source, modular liquid handling robot for nurturing microbial fuel cells, in: Proc. Artif. Life Conf. 2016 13, MIT Press, 2016: pp. 626–633.

[30] F. Nejatimoharrami, A. Faina, K. Stoy, New Capabilities of EvoBot: A Modular, Open-Source Liquid-Handling Robot, SLAS Technol. Transl. Life Sci. Innov. 22 (2017) 500–506.

[31] P. Theodosiou, A. Faina, F. Nejatimoharrami, K. Stoy, J. Greenman, C. Melhuish, I. Ieropoulos, EvoBot: Towards a robot-chemostat for culturing and maintaining Microbial Fuel Cells (MFCs), in: Conf. Biomim. Biohybrid Syst., Springer, 2017: pp. 453–464.

[32] O.A. Alimi, T.B. Ncongwane, R. Meijboom, Design and fabrication of a monolith catalyst for continuous flow epoxidation of styrene in polypropylene printed flow reactor, Chem. Eng. Res. Des. (2020).

Chapter 6

Conclusions, Recommendations and Future work

Chapter 6

Conclusions, Recommendations and Future work

The aim of this research was the development of high-throughput approaches, as proof of principle, to be used in homogeneous and heterogeneous catalysis. These approaches include the high-throughput combinatorial approach for the ultra-fast optimisation of reagents such as the bases, solvents and phosphine ligand. This was done for the C-C cross-coupling reactions such as the Mizoroki-Heck and Suzuki reactions. Robotics and a microtiter plate were used for fast and effective kinetic analysis of Au-and Pd-PVP NPs. This allows for the fast determination of the optimal concentration of the catalysts, morin dye and hydrogen peroxide oxidant. A high-throughput system using robotics and 3D printing was developed for the parallel synthesis of up to 96 mesoporous metal oxides, with the screening of the catalysts based on UV active reactions, such as the oxidation of morin. Moreover, And finally, an open-source liquid handling robot was build using Open-Source hardware, including 3D printing. The robot has the potential to be used for catalytic experiments such as the parallel synthesis of mesoporous metal oxides as well as the fast and effective kinetic studies of catalysts using a dye. Following conclusions were made.

1. The high-throughput combinatorial approach to the Mizoroki-Heck and Suzuki reactions were successfully demonstrated. This is also known as a multidimensional group testing strategy. A split-and-pool followed by a deconvolution approach was introduced for the ultra-fast discovery of the optimal reagents for these reactions. K_2PdCl_4 was used as the Pd precursor and six bases, six solvents and up to twenty phosphine ligands were investigated for both reactions. For the Mizoroki-Heck reaction, iodobenzene and bromobenzene were used as substrates for the coupling with butyl acrylate. For the first deconvolution step, the bases were split-and-pooled into two reactions. Both reactions were set up in a solvent and phosphine mixture containing all the solvents and ligands under investigation.

The best reaction was identified from the fastest product formation, and that reaction was further deconvoluted. The best base for both reactions involving iodo- and bromobenzene with butyl acrylate was found to be K_2CO_3. Following the best base identification, the solvents and phosphine ligands were deconvoluted. The best solvent for both reactions was found to be acetonitrile. For the phosphine ligand; it was determined that tricyclohexylphosphine was the optimal phosphine for both the iodo- and bromobenzene reactions.

The same approach was followed for the identification of the optimal reagents in the cross-coupling Suzuki reaction between 4-bromotoluene and phenylboronic acid. For these deconvolution reactions, the highest conversion of 4-bromotoluene was used to indicate the best reaction. From this, it was found that the best base was K_2CO_3, the best solvent was ethanol, and the best phosphine ligand was identified as benzyldiphenylphosphine.

The deconvolution of the Suzuki reaction was also evaluated with a different approach. Starting with the deconvolution of the phosphine ligands, however, none of the reactions showed any conversions. The deconvolution was then attempted starting with the solvents; again, none of the reactions gave a conversion. This might be due to limited solubility with all the bases in one reaction. The approach was altered, and each reagent under investigation was split into an individual reaction (one reagent per reaction flask). With this approach, the same base and solvent were obtained as the best reagents; however, with the phosphine ligand, all the reactions gave relatively high conversions, which indicated that any phosphine ligands might be suitable for this reaction. From this, it can be concluded that by using a multidimensional group testing strategy, the number of reactions can dramatically be reduced from approximately 720 reactions to 19 reactions.

2. For the kinetic study of Au-and Pd-PVP NPs for the oxidation of morin, it can be concluded that using a liquid handling robot made the study fast and effective. By employing robotics and a microtiter plate, it was shown that the optimal concentrations for both the PVP NPs could be determined in one reaction. This was done by evaluating 12 concentrations of each NP using four replicates simultaneously. The k_{obs} of both nanoparticles increased as the concentration increases and from this, the optimal concentration for the Au-PVP NPs was found to be 85 μM, and for the Pd-PVP NPs 35 μM. The same approach was done for the concentration studies of the morin and hydrogen peroxide. The concentration studies could be done in a fast way by using more that one replicates per experiment. For the morin studies, it was seen that the k_{obs} decrease with an increase in the concentration of morin. However, for the hydrogen peroxide studies, an increase in the k_{obs} was observed with an increase in the concentration of the hydrogen peroxide. This occurs only up to a certain point, where the k_{obs} plateaus. It can thus be concluded that the morin and hydrogen peroxide competes for active sites on the catalyst surface. The reaction rate decreases as the surface become saturated with the morin and hydrogen peroxide molecules.

From this, it can be concluded that robotics can be used of the fast and effective kinetic analysis of nanoparticles acting as catalysts. Therefore, this technique can also be employed for the screening of catalyst, such as nanoparticles and mesoporous metal oxide catalysts. For future work, the synthesis of dendrimer encapsulated nanoparticles in a microtiter plate could be investigated. The particles could be synthesised in the well plate, characterised using the plate reader and screened by performing a reaction that has UV-active reagents and/or products. Using robotics, human error could potentially be eliminated. It is recommended to do a comparative study between using robotic experimentation and manual experimentation to show that using a robot eliminates human error. If this could be confirmed, then a microtiter plate can be used for the kinetic analysis of 96 different catalysts without including replicates.

3. A high-throughput system was successfully developed for the parallel synthesis of up to 96 different mesoporous metal oxide catalysts. The system consisted of a glass plate and a 3D printed bottomless 96-well microtiter plate. A Co_3O_4 mesoporous metal oxide formulation was deposited on the glass plate with increasing volumes (to give an increase in a final concentration of the catalyst in each well). It was accomplished using an acoustic liquid handling robot. By using robotics and 3D printing, a high-throughput system was successfully developed for the parallel synthesis of up to 96 different catalysts and the screening of the catalysts for their activity in the oxidation of morin. A customised 96-well plate was created using a glass plate for the deposition of the formulations. After the formation of the catalysts by calcination, a bottomless 96-well 3D printed plate was adhered to the glass plate using epoxy glue and a glue-dispensing robot. This was done for proof of concept to show that this the miniaturisation of catalysis can be done using such a high-throughput system.

Moreover, other derivatives of the Co_3O_4 catalyst was synthesised using this approach and screened for the oxidation of morin. These catalysts include Mn incorporated with the Co_3O_4 catalyst as well as Au-PVP NPs, and Pd-PVP NPs immobilised onto Co_3O_4-MMO catalyst. It was shown that the derivatives of the Co_3O_4 catalyst resulted in different k_{obs} values, and with that, the most active catalyst could be identified from the highest k_{obs} value. These results showed that such a high-throughput system could be used for the parallel synthesis and evaluation of mesoporous metal oxide catalysts. This can ultimately be used for catalyst screening where it can be further developed for the screening of up to 96 different mesoporous metal oxide catalysts. Moreover, multicomponent mesoporous metal oxides using a combination of 2, 3, 4, and up to 8 different metals, which allows for rapid catalyst discovery.

Some issues were encountered with the catalysts on the glass plate. Static electricity caused the catalysts to come loose from the plate and get stuck on the 3D printed bottomless 96-well plate. This would ultimately change the final concentration of the catalysts in the wells. It was attempted to immobilise the catalysts on the glass plate, by treating the plate with a super hydrophilic layer (glass etching with a piranha solution). The catalyst could be immobilised on the glass using that method; however, due to the high hydrophilic layer on the glass plate, the glue did not stick to the plate and came loose during the reaction. For future work, this should be investigated further since it would be beneficial for the catalysts to be immobilised on the glass plate. Other catalysts could also be immobilised on a glass plate for other applications, such as organic compound synthesis.

4. From the previous sections, it can be seen that robotics can be used for many applications; however, high-throughput experimentation, using liquid handling robots, is the applications we are we focused on. Numerous liquid handling robots are commercially available; however, they are expensive. The emergence of Open-Source hardware made it possible to build a more affordable liquid handling robot. The EvoBot is an example of an Open-Source hardware liquid handler. The EvoBot was build using the Open-Source data available. A few issues were encountered with the assembly. The materials originally used for the creation of the carriage plates and syringe electronics covers could not be obtained in South Africa. This, however, was overcome by employing 3D printing, and the plates were 3D printed. Other parts, such as the electronics, could not be obtained South Africa and were replaced. It was also noted that some of the instructions were not clear enough. Despite all the issues encountered, the EvoBot was successfully assembled.

It is, however, recommended to do thorough research on the parts and assembly of the EvoBot, before purchasing the parts. Future work for the EvoBot includes the parallel synthesis of mesoporous metal oxide catalyst as well as nanoparticles. It could also potentially be used for the screening of catalysts in a microtiter plate. Moreover, it can be used for basic dilutions and other chemical experiments. Three-dimensional printing is another Open-Source hardware technique that is used to improve productivity in the lab. This technique was successfully used for the 3D printing of unique custom labware, such as cuvette inserts for the centrifuge, BET tube holders and test tube holders for oil baths.

From this, it can be concluded that high-throughput approaches can be employed to find the optimal reagents, for example, the bases, solvents and phosphine ligands used in cross-coupling reactions. Moreover, it can also be used for the ultra-fast discovery of catalysts, either homogeneous or heterogeneous catalysts, by synthesising and screening multiple catalysts simultaneously. It can also be used for the fast and effective kinetic analysis of catalysts, such as nanoparticles for the oxidation of the morin. By using either a split-and-pool deconvolution method or robotics, commercially available or Open-Source robots, high-throughput approaches are the future of catalysis.

Appendices

Supplementary information

Chapter 2

A multidimensional group testing approach to Heck and Suzuki C-C coupling reactions catalysed by homogeneous Pd phosphine complexes

Supplementary information

2.1 GC-FID methods

2.1.1 Shimadzu 2010 Plus

The Shimadzu 2010 Plus is equipped with a split/splitless inlet using a Restek RTX-5 (5% diphenyl/95% dimethylpolysiloxane) column (30 m x 0.25 mm x 0.25 μm). Nitrogen gas was used as the carrier gas with a flow rate of 1.82 mL/min. Samples (1 μL) were injected with a split ratio of 20:1 at 200 °C. The oven temperature was kept constant at 40 °C for 2 min and increased to 280 °C, at a rate of 10 °C/min, and kept constant for 5 min. A flame ionisation detector (FID) was used at 350 °C.

2.1.2 Perkin Elmer Clarus 580 GC

The Perkin Elmer Clarus 580 GC is equipped with a split/splitless inlet using an Elite-5 (5% diphenyl/95% dimethylpolysiloxane) column (30 m x 0.25 mm x 0.25 μm). Helium gas was used as the carrier gas with a flow rate set as 1 mL/min. Samples (1 μL) were injected with a split flow of 20 mL/min at 250 °C. The oven temperature was kept constant at 50 °C for 5 min. It was then increased to 330 °C, at a rate of 20 °C or 40 °C/min, and kept constant for 5 min. A flame ionisation detector (FID) was used at 300 °C.

Table S2.1: Phosphine ligands with their respective numbering, used for the Heck and Suzuki C-C coupling deconvolution reactions.

Number	Phosphine ligand
L1	Tri(4-tolyl)phosphine
L2	Tris(4-chlorophenyl)phosphine
L3	Tris(4-methoxyphenyl)phosphine
L4	Triphenylphosphine
L5	Cyclohexyldiphenylphosphine
L6	Dicyclohexyl(2-methylphenyl)phosphine
L7	Tricyclohexylphosphine
L8	Dicyclohexylphenylphosphine
L9	4-(diphenylphosphino)styrene
L10	(2-Biphenyl)di-tert-butylphosphine
L11	Tri-1-naphthylphosphine
L12	Diphenyl(p-tolyl)phosphine
L13	Tris(2,4,6-trimethylphenyl)phosphine
L14	Diphenyl-2-pyridylphosphine
L15	4-(Dimethylamino)-phenyldiphenylphosphine
L16	Tris(3,5-dimethylphenyl)phosphine
L17	Benzyldiphenylphosphine
L18	O-methoxyphenyldiphenylphosphine
L19	Tri(m-tolyl)phosphine
L20	Tri(o-tolyl)phosphine
L21	Diphenyl(o-tolyl) phosphine
L22	Dicyclo(2,6-diisopropylphenyl)phosphine

2.2 Proof of principle using nine phosphine ligands

Initial this concept was investigated using a less complex approach, with less complex mixtures. Only the phosphine ligands were deconvoluted to confirm if we could identify one phosphine from a mixture.

As proof of principle, this approach was initially used to deconvolute nine phosphine ligands in a Mizoroki-Heck C-C coupling reaction of butyl acrylate and iodobenzene (PhI). Triethylamine (NEt_3) and DMF were used as the base and solvent. The deconvolution of nine phosphine ligands, L1, L2, L3, L7, L8, L12, L13, L14, and L22, were investigated. Furthermore, K_2PdCl_4 salt was used as the Pd metal precursor to give a 1:2 (Pd:phosphine) Pd-phosphine complex catalyst. Results are shown in chapter 2, supplementary information (SI chapter 2).

2.2.1 Reaction A: L1, L2, L3

For reaction A, K_2Cl_4Pd (0.00326 g, 0.010 mmol, 0.5 mol %), L1 (0.0122g, 0.04 mmol), L2 (0.0146 g, 0.040 mmol) and L3 (0.0141 g, 0.04 mmol) was added to a flask containing DMF (10 mL). To the mixture, NEt_3 (557 µL, 4 mmol), butyl acrylate (344 µL, 2.4 mmol) and PhI (223 µL, 2 mmol) were added, and the reaction was heated to 80 °C. Sampling was done every 30 min for the first 4 hrs and then at 24 hrs again. The reaction was monitored by GC-FID. For the GC-FID samples, approximately 300 µL were sampled and syringe filtered into a GC vial. It was diluted with DCM.

2.2.2 Reaction B: L7, L8, L22

For reaction B, K_2Cl_4Pd (0.00326 g, 0.010 mmol, 0.5 mol %), L7 (0.0112 g, 0.04 mmol), L8 (0.0109 g, 0.040 mmol) and L22 (0.0143 g, 0.04 mmol) was added to a flask containing DMF (10 mL). To the mixture, NEt_3 (557 µL, 4 mmol), butyl acrylate (344 µL, 2.4 mmol) and PhI (223 µL, 2 mmol) were added, and the reaction was heated to 80 °C. Sampling was done every 30 min for the first 4 hrs and then at 24 hrs again. The reaction was monitored by GC-FID. For the GC-FID samples, approximately 300 µL were sampled and syringe filtered into a GC vial. It was diluted with DCM.

2.2.3 Reaction C: L12, L13, L14

For reaction C, K_2Cl_4Pd (0.00326 g, 0.010 mmol, 0.5 mol %), L12 (0.01105 g, 0.04 mmol), L13 (0.0155 g, 0.040 mmol) and L14 (0.0105 g, 0.04 mmol) was added to a flask containing DMF (10 mL). To the mixture, NEt_3 (557 µL, 4 mmol), butyl acrylate (344 µL, 2.4 mmol) and PhI (223 µL, 2 mmol) were added, and the reaction was heated to 80 °C. Sampling was done every 30 min for the first 4 hrs and then at 24 hrs again. The reaction was monitored by GC-FID. For the GC-FID samples, approximately 300 µL were sampled and syringe filtered into a GC vial. It was diluted with DCM.

From the GC analysis, it was concluded that reaction C gave the fastest product formation and it was hence further deconvoluted to find the optimum ligand for this reaction.

2.2.4 Reaction D: L12

For reaction D, K_2Cl_4Pd (0.00326 g, 0.010 mmol, 0.5 mol %), L12 (0.01105 g, 0.04 mmol) was added to a flask containing DMF (10 mL). To the reaction, NEt_3 (557 µL, 4 mmol), butyl acrylate (344 µL, 2.4 mmol) and PhI (223 µL) were added, and the reaction was heated to 80 °C. Sampling was done every 30 min for the first 4 hrs and then at 24 hrs again. The reaction was monitored by GC-FID. For the GC-FID samples, approximately 300 µL were sampled and syringe filtered into a GC vial. It was diluted with DCM.

2.2.5 Reaction E: L13

For reaction E, K_2Cl_4Pd (0.00326 g, 0.010 mmol, 0.5 mol%), L13 (0.0155 g, 0.04 mmol) was added to a flask containing DMF (10 mL). To the reaction, NEt_3 (557 µL, 4 mmol), butyl acrylate (344 µL, 2.4 mmol) and PhI (223 µL) were added, and the reaction was heated to 80°C. Sampling was done every 30 min for the first 4 hrs and then at 24 hrs again. The reaction was monitored by GC-FID. For the GC-FID samples, approximately 300 µL were sampled and syringe filtered into a GC vial. It was diluted with DCM.

2.2.6 Reaction F: L14

For reaction F, K_2Cl_4Pd (0.00326 g, 0.010 mmol, 0.5 mol %), L14 (0.0105 g, 0.04 mmol) was added to a flask containing DMF (10 mL). To the reaction, NEt_3 (557 µL, 4 mmol), butyl acrylate (344 µL, 2.4 mmol) and PhI (223 µL) were added, and the reaction was heated to 80 °C. Sampling was done every 30 min for the first 4 hrs and then at 24 hrs again. The reaction was monitored by GC-FID. For the GC-FID samples, approximately 300 µL were sampled and syringe filtered into a GC vial. It was diluted with DCM.

From the GC analysis, it was concluded that reaction F gave the fastest product formation. It was therefore concluded that L14 (Diphenyl-2-pyridyl phosphine) was the best ligand for these reactions.

2.3 Deconvolution of bases, solvents and phosphine ligands in the Mizoroki-Heck and Suzuki C-C cross-coupling reactions

2.4 Heck C-C coupling between iodobenzene and butyl acrylate

2.4.1 Base deconvolution – Step 1

The Heck reaction can be carried out using several bases. It was decided to deconvolute six bases to find the best suitable base for the reaction. The bases include; sodium hydroxide (NaOH), sodium carbonate (Na_2CO_3), triethylamine (NEt_3), potassium hydroxide (KOH), potassium carbonate (K_2CO_3) and caesium carbonate ($CsCO_3$). The bases were split and pooled into two reactions, each containing three bases.

2.4.1.1 Reaction 1a: Bases – NEt3, Na_2CO_3 and NaOH

In a reaction flask, K_2Cl_4Pd (0.01 mmol, 0.5 mol%), a mixture of the 20 phosphine ligands (0.02 mmol) was added to the solvent mixture (10 mL). To the reaction, NEt_3 (4 mmol), Na_2CO_3 (4 mmol) and NaOH (4 mmol) were added. Followed by the reactants, butyl acrylate (2.4 mmol) and iodobenzene (2 mmol). The reaction was heated to 80 °C. Sampling was done every 30 min for the first 4 hrs and then at 24 hrs again. The reaction was monitored by GC-FID. For the GC-FID samples, 100 µL were sampled and syringe filtered into a GC vial. It was diluted to 1 mL with DCM.

2.4.1.2 Reaction 2a: Bases – K_2CO_3, Cs_2CO_3 and KOH

The reagents, K_2Cl_4Pd (0.01 mmol, 0.5 mol%) and a mixture of the phosphine ligands (0.02 mmol) were added to a flask containing the solvents mixture (10 mL). To this, K_2CO_3 (4 mmol), Cs_2CO_3 (4 mmol) and KOH (4 mmol) were added. Followed by the reactants, butyl acrylate (2.4 mmol) and PhI (2 mmol). The reaction was heated to 80 °C. Sampling was done every 30 min for the first 4 hrs and then at 24 hrs again. The reaction was monitored by GC-FID. For the GC-FID samples, 100 µL were sampled and syringe filtered into a GC vial. It was diluted to 1 mL with DCM.

Reaction 2a gave the best results; it was therefore further split, pooled and deconvoluted

2.4.1.3 Reaction 3a: K_2CO_3

Solid K_2Cl_4Pd (0.01 mmol, 0.5 mol%) and the 20 phosphine ligand mixture (0.02 mmol) was added to a flask containing a mixture of solvents (10 mL). To the reaction, K_2CO_3 (4 mmol),

was added. Followed by the reactants, butyl acrylate (2.4 mmol) and PhI (2 mmol). The reaction was heated to 80 °C. Sampling was done every 30 min for the first 4 hrs and then at 24 hrs again. The base did not dissolve in the reaction. The reaction was monitored by GC-FID. For the GC-FID samples, 100 µL were sampled and syringe filtered into a GC vial. It was diluted to 1 mL with DCM.

2.4.1.4 Reaction 4a: $CsCO_3$

Solid K_2Cl_4Pd (0.01 mmol, 0.5 mol%), a mixture of the 20 phosphine ligands (0.02 mmol) was added to a flask containing the solvent mixture (10 mL). To the reaction, $CsCO_3$ (4 mmol), was added. Followed by the reactants, butyl acrylate (2.4 mmol) and PhI (2 mmol). The reaction was heated to 80 °C. The base did not dissolve in the reaction. Sampling was done every 30 min for the first 4 hrs and then at 24 hrs again. The reaction was monitored by GC-FID. For the GC-FID samples, 100 µL were sampled and syringe filtered into a GC vial. It was diluted to 1 mL DCM.

2.4.1.5 Reaction 5a: KOH

Solid K_2Cl_4Pd (0.01 mmol, 0.5 mol%), a mixture of the 20 phosphine ligands (0.02 mmol) was added to a flask containing the solvent mixture (10 mL). To the reaction, KOH (4 mmol), was added. Followed by the reactants, butyl acrylate (2.4 mmol) and PhI (2 mmol). The reaction was heated to 80 °C. Sampling was done every 30 min for the first 4 hrs and then at 24 hrs again. The reaction was monitored by GC-FID. For the GC-FID samples, 100 µL were sampled and syringe filtered into a GC vial. It was diluted to 1 mL with DCM.

The optimal base was identified as K_2CO_3.

The same approach was followed for the second and third deconvolution steps

2.4.2 Solvent deconvolution – Step 2

For the solvent deconvolution step, the six solvents under investigation were initially split and pooled into two reactions, each containing three solvents. For the first two reactions, a mixture of the three solvents was prepared beforehand the mixture was used as the reaction solvent.

2.4.2.1 Reaction 6a: Solvents – DMF, 1,4-Dioxane and acetonitrile

Solid K_2Cl_4Pd (0.01 mmol, 0.5 mol%), a mixture of the 20 phosphine ligands (0.02 mmol) was added to a flask containing a solvent mixture of DMF, 1,4-Dioxane and acetonitrile (10 mL). To the reaction, K_2CO_3 (4 mmol), was added, followed by the reactants, butyl acrylate (2.4 mmol) and PhI (2 mmol). The reaction was heated to 80 °C. The base did not dissolve in the reaction. Sampling was done every 30 min for the first 4 hrs and then at 24 hrs again. The reaction was monitored by GC-FID. For the GC-FID samples, 100 μL were sampled and syringe filtered into a GC vial. It was diluted to 1 mL with DCM.

2.4.2.2 Reaction 7a: Solvents – ethanol, butanol and toluene

Solid K_2Cl_4Pd (0.01 mmol, 0.5 mol%), a mixture of the 20 phosphine ligands (0.02 mmol) was added to a flask containing a mixture of 3 solvents (EtOH, BuOH, Toluene, 10 mL). To the reaction, K_2CO_3 (4 mmol), was added, followed by the reactants, butyl acrylate (2.4 mmol) and PhI (2 mmol). The reaction was heated to 80 °C. The base did not dissolve in the reaction. Sampling was done every 30 min for the first 4 hrs and then at 24 hrs again. The reaction was monitored by GC-FID. For the GC-FID samples, 100 μL were sampled and syringe filtered into a GC vial. It was diluted to 1 mL with DCM.

Reaction 6a containing DMF, 1,4-Dioxane and acetonitrile, was identified to be the best

2.4.2.3 Reaction 8a: DMF

Solid K_2Cl_4Pd (0.01 mmol, 0.5 mol%), a mixture of the 20 phosphine ligands (0.02 mmol) was added to a flask containing DMF (10 mL). To the reaction, K_2CO_3 (4 mmol), was added. Followed by the reactants, butyl acrylate (2.4 mmol) and PhI (2 mmol). The reaction was heated to 80 °C. The base did not dissolve in the reaction. Sampling was done every 30 min for the first 4 hrs and then at 24 hrs again. The reaction was monitored by GC-FID. For the GC-FID samples, 100 μL were sampled and syringe filtered into a GC vial. It was diluted to 1 mL with DCM.

2.4.2.4 Reaction 9a: 1,4-Dioxane

Solid K_2Cl_4Pd (0.01 mmol, 0.5 mol%), a mixture of the 20 phosphine ligands (0.02 mmol) was added to a flask containing 1,4-Dioxane (10 mL). To the reaction, K_2CO_3 (4 mmol), was added. Followed by the reactants, butyl acrylate (2.4 mmol) and PhI (2 mmol). The reaction was heated to 80 °C. The base did not dissolve in the reaction. Sampling was done every 30 min for the

first 4 hrs and then at 24 hrs again. The reaction was monitored by GC-FID. For the GC-FID samples, 100 μL were sampled and syringe filtered into a GC vial. It was diluted to 1 mL with DCM.

2.4.2.5 Reaction 10a: Acetonitrile

Solid K_2Cl_4Pd (0.01 mmol, 0.5 mol%), a mixture of the 20 phosphine ligands (0.02 mmol) was added to a flask containing acetonitrile (10 mL). To the reaction, K_2CO_3 (4 mmol), was added. Followed by the reactants, butyl acrylate (2.4 mmol) and PhI (2 mmol). The reaction was heated to 80 °C. The base did not dissolve in the reaction. Sampling was done every 30 min for the first 4 hrs and then at 24 hrs again. The reaction was monitored by GC-FID. For the GC-FID samples, 100 μL were sampled and syringe filtered into a GC vial. It was diluted to 1 mL with DCM.

Acetonitrile gave the best results; hence it was identified as the best solvent.

2.4.3 Phosphine ligand deconvolution – Step 3

Following the deconvolution of the bases and solvents, the phosphine ligands were also deconvoluted. The 20 phosphine ligands under investigation were split-and-pooled into four smaller batches each containing five phosphine ligands. The reactions were carried out, and the phosphine ligands were further split, pooled and deconvoluted to find the optimal ligand

2.4.3.1 Reaction 11a: Phosphines – L1, L2, L3, L4, L5

Solid K_2Cl_4Pd (0.01 mmol, 0.5 mol%), L1 (0.02 mmol), L2 (0.02 mmol), L3 (0.02 mmol), L4 (0.02 mmol) and L5 (0.02 mmol) was added to a flask containing acetonitrile (10 mL). To the reaction, K_2CO_3 (4 mmol), was added, followed by the reactants, butyl acrylate (2.4 mmol) and PhI (2 mmol). The reaction was heated to 80 °C. The base did not dissolve in the reaction. Sampling was done every 30 min for the first 4 hrs and then at 24 hrs again. The reaction was monitored by GC-FID. For the GC-FID samples, 100 μL were sampled and syringe filtered into a GC vial. It was diluted to 1 mL with DCM.

2.4.3.2 Reaction 12a: Phosphines – L6, L7, L8, L9, L10

Solid K_2Cl_4Pd (0.01 mmol, 0.5 mol%), L6 (0.02 mmol), L7 (0.02 mmol), L8 (0.02 mmol), L10 (0.02 mmol) and L11 (0.02 mmol) was added to a flask containing Acetonitrile (10 mL). To

the reaction, K_2CO_3 (4 mmol), was added, followed by the reactants, butyl acrylate (2.4 mmol) and PhI (2 mmol). The reaction was heated to 80 °C. The base did not dissolve in the reaction. Sampling was done every 30 min for the first 4 hrs and then at 24 hrs again. The reaction was monitored by GC-FID. For the GC-FID samples, 100 μL were sampled and syringe filtered into a GC vial. It was diluted to 1 mL with DCM.

2.4.3.3 Reaction 13a: Phosphines – L11, L12, L13, L14, L15

Solid K_2Cl_4Pd (0.01 mmol, 0.5 mol%), L12 (0.02 mmol), L13 (0.02 mmol), L14 (0.02 mmol), L15 (0.02 mmol) and L17 (0.02 mmol) was added to a flask containing acetonitrile (10 mL). To the reaction, K_2CO_3 (0.558 g, 4 mmol), was added. Followed by the reactants, butyl acrylate (2.4 mmol) and PhI (2 mmol). The reaction was heated to 80 °C. The base did not dissolve in the reaction. Sampling was done every 30 min for the first 4 hrs and then at 24 hrs again. The reaction was monitored by GC-FID. For the GC-FID samples, 100 μL were sampled and syringe filtered into a GC vial. It was diluted to 1 mL with DCM.

2.4.3.4 Reaction 14a: Phosphines – L16, L17, L18, L19, L20

Solid K_2Cl_4Pd (0.01 mmol, 0.5 mol%), L18 (0.02 mmol), L20 (0.02 mmol), L22 (0.02 mmol), L23 (0.02 mmol) and L25 (0.02 mmol) was added to a flask containing acetonitrile (10 mL). To the reaction, K_2CO_3 (4 mmol), was added, followed by the reactants, butyl acrylate (2.4 mmol) and PhI (2 mmol). The reaction was heated to 80 °C. The base did not dissolve in the reaction. Sampling was done every 30 min for the first 4 hrs and then at 24 hrs again. The reaction was monitored by GC-FID. For the GC-FID samples, 100 μL were sampled and syringe filtered into a GC vial. It was diluted to 1 mL with DCM.

GC-FID analysis showed that Reaction 12 gave the best results. Therefore, this reaction was further split into five reactions, each containing a single phosphine ligand to be deconvoluted.

2.4.3.5 Reaction 15a: Phosphine L6

Solid K_2Cl_4Pd (0.01 mmol, 0.5 mol%), L6 (0.02 mmol), was added to a flask containing acetonitrile (10 mL). To the reaction K_2CO_3 (4 mmol), was added, followed by the reactants, butyl acrylate (2.4 mmol) and PhI (2 mmol). The reaction was heated to approx 80 °C. The base did not dissolve in the reaction. Sampling was done every 30 min for the first 4 hrs and then at 24 hrs again. The reaction was monitored by GC-FID. For the GC-FID samples, 100 μL were sampled and syringe filtered into a GC vial. It was diluted to 1 mL with DCM.

2.4.3.6 Reaction 16a: Phosphine L7

Solid K_2Cl_4Pd (0.01 mmol, 0.5 mol%), L7 (0.02 mmol) was added to a flask containing acetonitrile (10 mL). To the reaction K_2CO_3 (4 mmol) was added, followed by the reactants, butyl acrylate (2.4 mmol) and PhI (2 mmol). The reaction was heated to 80 °C. The base did not dissolve in the reaction. Sampling was done every 30 min for the first 4 hrs and then at 24 hrs again. The reaction was monitored by GC-FID. For the GC-FID samples, 100 µL were sampled and syringe filtered into a GC vial. It was diluted to 1 mL with DCM.

2.4.3.7 Reaction 17a: Phosphine L8

Solid K_2Cl_4Pd (0.01 mmol, 0.5 mol%), L8 (0.02 mmol) was added to a flask containing acetonitrile (10 mL). To the reaction, K_2CO_3 (4 mmol) was added, followed by the reactants, butyl acrylate (2.4 mmol) and PhI (2 mmol). The reaction was heated to 80 °C. The base did not dissolve in the reaction. Sampling was done every 30 min for the first 4 hrs and then at 24 hrs again. The reaction was monitored by GC-FID. For the GC-FID samples, 100 µL were sampled and syringe filtered into a GC vial. It was diluted to 1 mL with DCM.

2.4.3.8 Reaction 18a: Phosphine L9

Solid K_2Cl_4Pd (0.01 mmol, 0.5 mol%), L9 (0.02 mmol) was added to a flask containing acetonitrile (10 mL). To the reaction, K_2CO_3 (4 mmol) was added, followed by the reactants, butyl acrylate (2.4 mmol) and PhI (2 mmol). The reaction was heated to 80 °C. The base did not dissolve in the reaction. Sampling was done every 30 min for the first 4 hrs and then at 24 hrs again. The reaction was monitored by GC-FID. For the GC-FID samples, 100 µL were sampled and syringe filtered into a GC vial. It was diluted to 1 mL with DCM.

2.4.3.9 Reaction 19a: Phosphine L10

Solid K_2Cl_4Pd (0.01 mmol, 0.5 mol%), and L10 (0.02 mmol) was added to a flask containing acetonitrile (10 mL). To the reaction, K_2CO_3 (4 mmol) was added, followed by the reactants, butyl acrylate (2.4 mmol) and PhI (2 mmol). The reaction was heated to 80 °C. The base did not dissolve in the reaction. Sampling was done every 30 min for the first 4 hrs and then at 24 hrs again. The reaction was monitored by GC-FID. For the GC-FID samples, 100 µL were sampled and syringe filtered into a GC vial. It was diluted to 1 mL with DCM.

The best ligand was identified as L7, tricyclohexylphosphine

2.5 Heck C-C coupling between bromobenzene and butyl acrylate

The same approach was followed for the deconvolution of the bases, solvents and phosphine ligands for the Heck C-C coupling reactions between bromobenzene and butyl acrylate. Reactions are numbered as reaction 1a – 19a.

2.5.1 Base deconvolution

2.5.1.1 Reaction 1b: Bases – NEt_3, Na_2CO_3, NaOH

In a reaction flask, K_2Cl_4Pd (0.01 mmol, 0.5 mol%), a mixture of the 20 phosphine ligands (0.02 mmol) was added to the solvent mixture (10 mL). To the reaction, NEt_3 (4 mmol), Na_2CO_3 (4 mmol) and NaOH (4 mmol) were added. Followed by the reactants, butyl acrylate (2.4 mmol) and bromobenzene (2 mmol). The reaction was heated to 80 °C. Sampling was done every 30 min for the first 4 hrs and then at 24 hrs again. The reaction was monitored by GC-FID. A sample of 100 µL was taken and syringe filtered into a GC vial. It was diluted with DCM. As soon as the sampling was done, the reaction mixture solidified in the syringe. Therefore it was concluded that this reaction did not work.

2.5.1.2 Reaction 2b: Bases – K_2CO_3, Cs_2CO_3, KOH

The reagents, K_2Cl_4Pd (0.01 mmol, 0.5 mol%) and a mixture of the phosphine ligand mixture (0.02 mmol) were added to a flask containing the solvents mixture (10 mL). To this, K_2CO_3 (4 mmol), Cs_2CO_3 (4 mmol) and KOH (4 mmol) were added. Followed by the reactants, butyl acrylate (2.4 mmol) and PhBr (2 mmol). The reaction was heated to 80 °C. Sampling was done every 30 min for the first 4 hrs and then at 24 hrs again. The reaction was monitored by GC-FID. For the GC-FID samples, 100 µL were sampled and syringe filtered into a GC vial and diluted with DCM.

Reaction 2b gave the best results; it was therefore further split, pooled and deconvoluted

2.5.1.3 Reaction 3b: K_2CO_3

Solid K_2Cl_4Pd (0.01 mmol, 0.5 mol%) and the 20 phosphine ligand mixture (0.02 mmol) was added to a flask containing a mixture of solvents (10 mL). To the reaction, K_2CO_3 (4 mmol), was added. Followed by the reactants, butyl acrylate (2.4 mmol) and PhBr (2 mmol). The reaction was heated to 80 °C. Sampling was done every 30 min for the first 4 hrs and then at 24 hrs again. The base did not dissolve in the reaction. The reaction was monitored by GC-

FID. For the GC-FID samples, 100 μL were sampled and syringe filtered into a GC vial and diluted with DCM.

2.5.1.4 Reaction 4b: $CsCO_3$

Solid K_2Cl_4Pd (0.01 mmol, 0.5 mol%), a mixture of the 20 phosphine ligands (0.02 mmol) was added to a flask containing the solvent mixture (10 mL). To the reaction, $CsCO_3$ (4 mmol), was added. Followed by the reactants, butyl acrylate (2.4 mmol) and PhBr (2 mmol). The reaction was heated to 80 °C. The base did not dissolve in the reaction. Sampling was done every 30 min for the first 4 hrs and then at 24 hrs again. The reaction was monitored by GC-FID. For the GC-FID samples, 100 μL were sampled and syringe filtered into a GC vial. It was diluted with DCM.

2.5.1.5 Reaction 5b: KOH

Solid K_2Cl_4Pd (0.01 mmol, 0.5 mol%), a mixture of the 20 phosphine ligands (0.02 mmol) was added to a flask containing the solvent mixture (10 mL). To the reaction, KOH (4 mmol), was added. Followed by the reactants, butyl acrylate (2.4 mmol) and PhBr (2 mmol). The reaction was heated to 80 °C. Sampling was done every 30 min for the first 4 hrs and then at 24 hrs again. The reaction was monitored by GC-FID. For the GC-FID samples, 100 μL were sampled and syringe filtered into a GC vial. It was diluted to 1 mL with DCM.

For the following deconvolution steps, K_2CO_3 was used as the optimal base

The same approach was followed for the second (solvents) and third (phosphine ligands) deconvolution steps

2.5.2 Solvent deconvolution – Step 2

The same deconvolution approach was used for the of the solvents as with the PhI reaction

2.5.2.1 Reaction 6b: Solvents – DMF, 1,4-Dioxane and acetonitrile

Solid K_2Cl_4Pd (0.01 mmol, 0.5 mol%), a mixture of the 20 phosphine ligands (0.02 mmol) was added to a flask containing a solvent mixture of DMF, 1,4-Dioxane and acetonitrile (10 mL). To the reaction, K_2CO_3 (4 mmol), was added, followed by the reactants, butyl acrylate (2.4 mmol) and PhBr (2 mmol). The reaction was heated to 80 °C. The base did not dissolve in the

reaction. Sampling was done every 30 min for the first 4 hrs and then at 24 hrs again. The reaction was monitored by GC-FID. For the GC-FID samples, 100 μL were sampled and syringe filtered into a GC vial. It was diluted with DCM.

2.5.2.2 Reaction 7b: Solvents – ethanol, butanol and toluene

Solid K_2Cl_4Pd (0.01 mmol, 0.5 mol%), a mixture of the 20 phosphine ligands (0.02 mmol) was added to a flask containing a mixture of 3 solvents (ethanol, butanol and toluene, 10 mL). To the reaction, K_2CO_3 (4 mmol), was added, followed by the reactants, butyl acrylate (2.4 mmol) and PhBr (2 mmol). The reaction was heated to 80 °C. The base did not dissolve in the reaction. Sampling was done every 30 min for the first 4 hrs and then at 24 hrs again. The reaction was monitored by GC-FID. A sample of 100 μL was taken and syringe filtered into a vial. It was diluted with DCM.

Reaction 6a containing DMF, 1,4-Dioxane and acetonitrile, gave the fastest product formation as was further deconvoluted.

2.5.2.3 Reaction 8b: DMF

Solid K_2Cl_4Pd (0.01 mmol, 0.5 mol%), a mixture of the 20 phosphine ligands (0.02 mmol) was added to a flask containing DMF (10 mL). To the reaction, K_2CO_3 (4 mmol), was added. Followed by the reactants, butyl acrylate (2.4 mmol) and PhBr (2 mmol). The reaction was heated to 80 °C. The base did not dissolve in the reaction. Sampling was done every 30 min for the first 4 hrs and then at 24 hrs again. The reaction was monitored by GC-FID. For the GC-FID samples, 100 μL were sampled and syringe filtered into a GC vial. It was diluted with DCM.

2.5.2.4 Reaction 9b: 1,4-dioxane

Solid K_2Cl_4Pd (0.01 mmol, 0.5 mol%), a mixture of the 20 phosphine ligands (0.02 mmol) was added to a flask containing 1,4-dioxane (10 mL). To the reaction, K_2CO_3 (4 mmol), was added. Followed by the reactants, butyl acrylate (2.4 mmol) and PhBr (2 mmol). The reaction was heated to 80 °C. The base did not dissolve in the reaction. Sampling was done every 30 min for the first 4 hrs and then at 24 hrs again. The reaction was monitored by GC-FID. For the GC-FID samples, 100 μL were sampled and syringe filtered into a GC vial. It was diluted with DCM.

2.5.2.5 Reaction 10b: acetonitrile

Solid K_2Cl_4Pd (0.01 mmol, 0.5 mol%), a mixture of the 20 phosphine ligands (0.02 mmol) was added to a flask containing acetonitrile (10 mL). To the reaction, K_2CO_3 (4 mmol), was added. Followed by the reactants, butyl acrylate (2.4 mmol) and PhBr (2 mmol). The reaction was heated to 80 °C. The base did not dissolve in the reaction. Sampling was done every 30 min for the first 4 hrs and then at 24 hrs again. The reaction was monitored by GC-FID. For the GC-FID samples, 100 µL were sampled and syringe filtered into a GC vial. It was diluted with DCM.

Acetonitrile was identified as the optimal solvent.

2.5.3 Phosphine ligand deconvolution – Step 3

The same approach was followed, as discussed above.

2.5.3.1 Reaction 11b: Phosphines – L1, L2, L3, L4, L5

Solid K_2Cl_4Pd (0.01 mmol, 0.5 mol%), L1 (0.02 mmol), L2 (0.02 mmol), L3 (0.02 mmol), L4 (0.02 mmol) and L5 (0.02 mmol) was added to a flask containing acetonitrile (10 mL). To the reaction, K_2CO_3 (4 mmol), was added, followed by the reactants, butyl acrylate (2.4 mmol) and PhBr (2 mmol). The reaction was heated to 80 °C. The base did not dissolve in the reaction. Sampling was done every 30 min for the first 4 hrs and then at 24 hrs again. The reaction was monitored by GC-FID. For the GC-FID samples, 100 µL were sampled and syringe filtered into a GC vial. It was diluted with DCM.

2.5.3.2 Reaction 12b: Phosphines – L6, L7, L8, L9, L10

Solid K_2Cl_4Pd (0.01 mmol, 0.5 mol%), L6 (0.02 mmol), L7 (0.02 mmol), L8 (0.02 mmol), L10 (0.02 mmol) and L11 (0.02 mmol) was added to a flask containing acetonitrile (10 mL). To the reaction, K_2CO_3 (4 mmol), was added, followed by the reactants, butyl acrylate (2.4 mmol) and PhBr (2 mmol). The reaction was heated to 80 °C. The base did not dissolve in the reaction. Sampling was done every 30 min for the first 4 hrs and then at 24 hrs again. The reaction was monitored by GC-FID. For the GC-FID samples, 100 µL were sampled and syringe filtered into a GC vial. It was diluted with DCM.

2.5.3.3 Reaction 13b: Phosphines – L11, L12, L13, L14, L15

Solid K_2Cl_4Pd (0.01 mmol, 0.5 mol%), L12 (0.02 mmol), L13 (0.02 mmol), L14 (0.02 mmol), L15 (0.02 mmol) and L17 (0.02 mmol) was added to a flask containing acetonitrile (10 mL). To the reaction, K_2CO_3 (0.558 g, 4 mmol), was added. Followed by the reactants, butyl acrylate (2.4 mmol) and PhBr (2 mmol). The reaction was heated to 80 °C. The base did not dissolve in the reaction. Sampling was done every 30 min for the first 4 hrs and then at 24 hrs again. The reaction was monitored by GC-FID. For the GC-FID samples, 100 µL were sampled and syringe filtered into a GC vial. The sample was diluted DCM.

2.5.3.4 Reaction 14b: Phosphines – L16, L17, L18, L19, L20

Solid K_2Cl_4Pd (0.01 mmol, 0.5 mol%), L18 (0.02 mmol), L20 (0.02 mmol), L22 (0.02 mmol), L23 (0.02 mmol) and L25 (0.02 mmol) was added to a flask containing acetonitrile (10 mL). To the reaction, K_2CO_3 (4 mmol), was added, followed by the reactants, butyl acrylate (2.4 mmol) and PhBr (2 mmol). The reaction was heated to 80 °C. The base did not dissolve in the reaction. Sampling was done every 30 min for the first 4 hrs and then at 24 hrs again. The reaction was monitored by GC-FID. For the GC-FID samples, 100 µL were sampled and syringe filtered into a GC vial. It was diluted with DCM.

Reaction 12b was identified as the most active reaction and was, therefore, further deconvoluted to find the optimal phosphine ligand.

2.5.3.5 Reaction 15b: Phosphine L6

Solid K_2Cl_4Pd (0.01 mmol, 0.5 mol%), L6 (0.02 mmol), was added to a flask containing acetonitrile (10 mL). To the reaction K_2CO_3 (4 mmol), was added, followed by the reactants, butyl acrylate (2.4 mmol) and PhBr (2 mmol). The reaction was heated to approx 80 °C. The base did not dissolve in the reaction. Sampling was done every 30 min for the first 4 hrs and then at 24 hrs again. The reaction was monitored by GC-FID. For the GC-FID samples, 100 µL were sampled and syringe filtered into a GC vial. It was diluted with DCM.

2.5.3.6 Reaction 16b: Phosphine L7

Solid K_2Cl_4Pd (0.01 mmol, 0.5 mol%), L7 (0.02 mmol) was added to a flask containing acetonitrile (10 mL). To the reaction K_2CO_3 (4 mmol) was added, followed by the reactants, butyl acrylate (2.4 mmol) and PhBr (2 mmol). The reaction was heated to 80 °C. The base did not dissolve in the reaction. Sampling was done every 30 min for the first 4 hrs and then at 24

hrs again. The reaction was monitored by GC-FID. A sample of 100 µL was syringe filtered into a GC vial. It was diluted with DCM.

2.5.3.7 Reaction 17b: Phosphine L8

Solid K_2Cl_4Pd (0.01 mmol, 0.5 mol%), L8 (0.02 mmol) was added to a flask containing acetonitrile (10 mL). To the reaction, K_2CO_3 (4 mmol) was added, followed by the reactants, butyl acrylate (2.4 mmol) and PhBr (2 mmol). The reaction was heated to 80 °C. The base did not dissolve in the reaction. Sampling was done every 30 min for the first 4 hrs and then at 24 hrs again. The reaction was monitored by GC-FID. For the GC-FID samples, 100 µL were sampled and syringe filtered into a GC vial. It was diluted to 1 mL with DCM.

2.5.3.8 Reaction 18b: Phosphine L9

Solid K_2Cl_4Pd (0.01 mmol, 0.5 mol%), L9 (0.02 mmol) was added to a flask containing acetonitrile (10 mL). To the reaction, K_2CO_3 (4 mmol) was added, followed by the reactants, butyl acrylate (2.4 mmol) and PhBr (2 mmol). The reaction was heated to 80 °C. The base did not dissolve in the reaction. Sampling was done every 30 min for the first 4 hrs and then at 24 hrs again. The reaction was monitored by GC-FID. For the GC-FID samples, 100 µL were sampled and syringe filtered into a GC vial. It was diluted to 1 mL with DCM.

2.5.3.9 Reaction 19b: Phosphine L10

Solid K_2Cl_4Pd (0.01 mmol, 0.5 mol%), and L10 (0.02 mmol) was added to a flask containing acetonitrile (10 mL). To the reaction, K_2CO_3 (4 mmol) was added, followed by the reactants, butyl acrylate (2.4 mmol) and PhBr (2 mmol). The reaction was heated to 80 °C. The base did not dissolve in the reaction. Sampling was done every 30 min for the first 4 hrs and then at 24 hrs again. The reaction was monitored by GC-FID. For the GC-FID samples, 100 µL were sampled and syringe filtered into a GC vial. It was diluted to 1 mL with DCM.

The optimal ligand was identified as L7, Tricyclohexylphosphine.

2.6 Heck C-C coupling between chlorobenzene and butyl acrylate

The C-C coupling of chlorobenzene and butyl acrylate was also investigated. For the first two reactions, the deconvolution of the bases, there was no product formation. It was, therefore, concluded that the chlorobenzene was not active enough.

2.7 Suzuki C-C coupling between phenylboronic acid and aryl halides (4-Bromotoluene)

2.7.1 Base deconvolution: Step 1

2.7.1.1 Reaction 1c: Bases – NEt_3, Na_2CO_3 and NaOH

In a reaction flask, K_2Cl_4Pd (0.01 mmol, 0.5 mol%), a mixture of the 14 phosphine ligands (0.02 mmol) was added to the solvent mixture (10 mL). To the reaction, NEt_3 (4 mmol), Na_2CO_3 (4 mmol) and NaOH (4 mmol) were added. Followed by the reactants, phenylboronic acid (2.4 mmol) and 4-bromotoluene (2 mmol), and decane (2 mmol) as an internal standard. The reaction was heated to 80 °C. Sampling was done every 30 min for the first 4 hrs and then at 24 hrs again. The reaction was monitored by GC-FID. For the GC-FID samples, 100 μL were sampled and subjected to a silica column and then syringe filtered into a GC vial. It was diluted with DCM (1:200).

2.7.1.2 Reaction 2c: K_2CO_3, Cs_2CO_3 and KOH

In a reaction flask, K_2Cl_4Pd (0.01 mmol, 0.5 mol%), a mixture of the 14 phosphine ligands (0.02 mmol) was added to the solvent mixture (10 mL). To the reaction, K_2CO_3 (4 mmol), Cs_2CO_3 (4 mmol) and KOH (4 mmol) were added. Followed by the reactants, phenylboronic acid (2.4 mmol) and 4-bromotoluene (2 mmol), and decane (2 mmol) as an internal standard. The reaction was heated to 80 °C. Sampling was done every 30 min for the first 4 hrs and then at 24 hrs again. The reaction was monitored by GC-FID. For the GC-FID samples, 100 μL were sampled and subjected to a silica column and then syringe filtered into a GC vial. It was diluted (1:200) with DCM.

The GC-FID results indicated that Reaction 2c gave the highest conversion. This reaction was, therefore, further split and deconvoluted.

2.7.1.3 Reaction 3c: KOH

In a reaction flask, K_2Cl_4Pd (0.01 mmol, 0.5 mol%), a mixture of the 14 phosphine ligands (0.02 mmol) was added to the solvent mixture (10 mL). To the reaction, KOH (4 mmol) was added, followed by the reactants, phenylboronic acid (2.4 mmol), 4-bromotoluene (2 mmol), and decane (2 mmol) as an internal standard. The reaction was heated to 80 °C. Sampling was done every 30 min for the first 4 hrs and then at 24 hrs again. The reaction was monitored by GC-FID. For the GC-FID samples, 100 μL were sampled and subjected to a silica column and then syringe filtered into a GC vial. It was diluted (1:200) with DCM.

2.7.1.4 Reaction 4c: Cs_2CO_3

In a reaction flask, K_2Cl_4Pd (0.01 mmol, 0.5 mol%), a mixture of the 14 phosphine ligands (0.02 mmol) was added to the solvent mixture (10 mL). To the reaction, Cs_2CO_3 (4 mmol) was added, followed by the reactants, phenylboronic acid (2.4 mmol), 4-bromotoluene (2 mmol), and decane (2 mmol) as an internal standard. The reaction was heated to 80 °C. Sampling was done every 30 min for the first 4 hrs and then at 24 hrs again. The reaction was monitored by GC-FID. For the GC-FID samples, 100 μL were sampled and subjected to a silica column and then syringe filtered into a GC vial. It was diluted (1:200) with DCM.

2.7.1.5 Reaction 5c: K_2CO_3

In a reaction flask, K_2Cl_4Pd (0.01 mmol, 0.5 mol%), a mixture of the 14 phosphine ligands (0.02 mmol) was added to the solvent mixture (10 mL). To the reaction, K_2CO_3 (4 mmol) was added, followed by the reactants, phenylboronic acid (2.4 mmol), 4-bromotoluene (2 mmol), and decane (2 mmol) as an internal standard. The reaction was heated to 80 °C. Sampling was done every 30 min for the first 4 hrs and then at 24 hrs again. The reaction was monitored by GC-FID. For the GC-FID samples, 100 μL were sampled and subjected to a silica column and then syringe filtered into a GC vial. It was diluted (1:200) with DCM.

Reaction 5c gave the highest conversion according to the GC-FID results. Therefore, K_2CO_3 was identified as the optimal base.

2.7.2 Solvent deconvolution: Step 2

2.7.2.1 Reaction 6c: Solvents – Toluene, 1,4-dioxane and DMF

To a mixture of the three solvents (toluene, 1,4-dioxane and DMF, 10 mL) solid K_2Cl_4Pd (0.01 mmol, 0.5 mol%) and a mixture of the 14 phosphine ligands (0.02 mmol) were added. To the mixture, K_2CO_3 (4 mmol) was added, followed by the reactants, phenylboronic acid (2.4 mmol), 4-bromotoluene (2 mmol), and decane (2 mmol) as an internal standard. The reaction was heated to 80 °C. Sampling was done every 30 min for the first 4 hrs and then at 24 hrs again. The reaction was monitored by GC-FID. For the GC-FID samples, 100 μL were sampled and subjected to a silica column and then syringe filtered into a GC vial. It was diluted (1:200) with DCM.

2.7.2.2 Reaction 7c: Solvents – Ethanol, butanol and acetonitrile

To a mixture of the three solvents (ethanol, butanol and acetonitrile, 10 mL) solid K_2Cl_4Pd (0.01 mmol, 0.5 mol%) and a mixture of the 14 phosphine ligands (0.02 mmol) were added. To the mixture, K_2CO_3 (4 mmol) was added, followed by the reactants, phenylboronic acid (2.4 mmol), 4-bromotoluene (2 mmol), and decane (2 mmol) as an internal standard. The reaction was heated to 80 °C. Sampling was done every 30 min for the first 4 hrs and then at 24 hrs again. The reaction was monitored by GC-FID. For the GC-FID samples, 100 µL were sampled and subjected to a silica column and then syringe filtered into a GC vial. It was diluted (1:200) with DCM.

The GC-FID results indicated that reaction 7b was the best. The solvents in reaction 7b were further split en deconvoluted.

2.7.2.3 Reaction 8c: Ethanol

Solid K_2Cl_4Pd (0.01 mmol, 0.5 mol%) and a mixture of the 14 phosphine ligands (0.02 mmol) were added to ethanol (10 mL). To the mixture, K_2CO_3 (4 mmol) was added, followed by the reactants, phenylboronic acid (2.4 mmol), 4-bromotoluene (2 mmol), and decane (2 mmol) as an internal standard. The reaction was heated to 80 °C. Sampling was done every 30 min for the first 4 hrs and then at 24 hrs again. The reaction was monitored by GC-FID. For the GC-FID samples, 100 µL were sampled and subjected to a silica column and then syringe filtered into a GC vial. It was diluted (1:200) with DCM.

2.7.2.4 Reaction 9c: Butanol

Solid K_2Cl_4Pd (0.01 mmol, 0.5 mol%) and a mixture of the 14 phosphine ligands (0.02 mmol) were added to butanol (10 mL). To the mixture, K_2CO_3 (4 mmol) was added, followed by the reactants, phenylboronic acid (2.4 mmol), 4-bromotoluene (2 mmol), and decane (2 mmol) as an internal standard. The reaction was heated to 80 °C. Sampling was done every 30 min for the first 4 hrs and then at 24 hrs again. The reaction was monitored by GC-FID. For the GC-FID samples, 100 µL were sampled and subjected to a silica column and then syringe filtered into a GC vial. It was diluted (1:200) with DCM.

2.7.2.5 Reaction 10c: Acetonitrile

Solid K_2Cl_4Pd (0.01 mmol, 0.5 mol%) and a mixture of the 14 phosphine ligands (0.02 mmol) were added to acetonitrile (10 mL). To the mixture, K_2CO_3 (4 mmol) was added, followed by

the reactants, phenylboronic acid (2.4 mmol), 4-bromotoluene (2 mmol), and decane (2 mmol) as an internal standard. The reaction was heated to 80 °C. Sampling was done every 30 min for the first 4 hrs and then at 24 hrs again. The reaction was monitored by GC-FID. For the GC-FID samples, 100 μL were sampled and subjected to a silica column and then syringe filtered into a GC vial. It was diluted (1:200) with DCM.

According to the GC-FID results, reaction 8c gave the best results. Therefore, it was concluded that ethanol was the optimal solvent.

2.7.3 Phosphine ligand deconvolution: Step 3

A mixture of 14 phosphine ligands was used for the Suzuki reaction. The phosphine ligands under investigation were split-and-pooled into two reactions containing seven phosphine ligands each.

2.7.3.1 Reaction 11c: Phosphine ligands – L1, L2, L3, L4, L5, L7 and L8

To a mixture of solid K_2PdCl_4 (0.01 mmol, 0.5 mol%) and K_2CO_3 (4 mmol) in ethanol (10 mL), L1 (0.02 mmol), L2 (0.02 mmol), L3 (0.02 mmol), L4 (0.02 mmol), L5 (0.02 mmol), L7 (0.02 mmol) and L8 (0.02 mmol) were added. This was followed by the addition of the other reagents, phenylboronic acid (2.4 mmol), 4-bromotoluene (2 mmol), and decane (2 mmol) as an internal standard. The reaction was heated to 80 °C. Sampling was done every 30 min for the first 4 hrs and then at 24 hrs again. The reaction was monitored by GC-FID. For the GC-FID samples, 100 μL were sampled and subjected to a silica column and then syringe filtered into a GC vial. It was diluted (1:200) with DCM.

2.7.3.2 Reaction 12c: Phosphine ligands – L11, L12, L16, L17, L19, L20 and L21

To a mixture of solid K_2PdCl_4 (0.01 mmol, 0.5 mol%) and K_2CO_3 (4 mmol) in ethanol (10 mL), L11 (0.02 mmol), L12 (0.02 mmol), L16 (0.02 mmol), L17 (0.02 mmol), L19 (0.02 mmol), L20 (0.02 mmol) and L21 (0.02 mmol) were added. This was followed by the addition of the other reagents, phenylboronic acid (2.4 mmol), 4-bromotoluene (2 mmol), and decane (2 mmol) as an internal standard. The reaction was heated to 80 °C. Sampling was done every 30 min for the first 4 hrs and then at 24 hrs again. The reaction was monitored by GC-FID. For the GC-FID samples, 100 μL were sampled and subjected to a silica column and then syringe filtered into a GC vial. It was diluted (1:200) with DCM.

Reaction 12c gave the best conversion and was, therefore, further split into seven reactions containing a phosphine ligand in each.

2.7.3.3 Reaction 13c: Phosphine L11

To a mixture of solid K_2PdCl_4 (0.01 mmol, 0.5 mol%) and K_2CO_3 (4 mmol) in ethanol (10 mL), L11 (0.02 mmol) was added, followed by the addition of the other reagents, phenylboronic acid (2.4 mmol), 4-bromotoluene (2 mmol), and decane (2 mmol) as an internal standard. The reaction was heated to 80 °C. Sampling was done every 30 min for the first 4 hrs and then at 24 hrs again. The reaction was monitored by GC-FID. For the GC-FID samples, 100 µL were sampled and subjected to a silica column and then syringe filtered into a GC vial. It was diluted (1:200) with DCM.

2.7.3.4 Reaction 14c: Phosphine L12

To a mixture of solid K_2PdCl_4 (0.01 mmol, 0.5 mol%) and K_2CO_3 (4 mmol) in ethanol (10 mL), L12 (0.02 mmol) was added, followed by the addition of the other reagents, phenylboronic acid (2.4 mmol), 4-bromotoluene (2 mmol), and decane (2 mmol) as an internal standard. The reaction was heated to 80 °C. Sampling was done every 30 min for the first 4 hrs and then at 24 hrs again. The reaction was monitored by GC-FID. For the GC-FID samples, 100 µL were sampled and subjected to a silica column and then syringe filtered into a GC vial. It was diluted (1:200) with DCM.

2.7.3.5 Reaction 15c: Phosphine L16

To a mixture of solid K_2PdCl_4 (0.01 mmol, 0.5 mol%) and K_2CO_3 (4 mmol) in ethanol (10 mL), L16 (0.02 mmol) was added, followed by the addition of the other reagents, phenylboronic acid (2.4 mmol), 4-bromotoluene (2 mmol), and decane (2 mmol) as an internal standard. The reaction was heated to 80 °C. Sampling was done every 30 min for the first 4 hrs and then at 24 hrs again. The reaction was monitored by GC-FID. For the GC-FID samples, 100 µL were sampled and subjected to a silica column and then syringe filtered into a GC vial. It was diluted (1:200) with DCM.

2.7.3.6 Reaction 16c: Phosphine L17

To a mixture of solid K_2PdCl_4 (0.01 mmol, 0.5 mol%) and K_2CO_3 (4 mmol) in ethanol (10 mL), L17 (0.02 mmol) was added, followed by the addition of the other reagents, phenylboronic acid (2.4 mmol), 4-bromotoluene (2 mmol), and decane (2 mmol) as an internal

standard. The reaction was heated to 80 °C. Sampling was done every 30 min for the first 4 hrs and then at 24 hrs again. The reaction was monitored by GC-FID. For the GC-FID samples, 100 μL were sampled and subjected to a silica column and then syringe filtered into a GC vial. It was diluted (1:200) with DCM.

2.7.3.7 Reaction 17c: Phosphine L19

To a mixture of solid K_2PdCl_4 (0.01 mmol, 0.5 mol%) and K_2CO_3 (4 mmol) in ethanol (10 mL), L19 (0.02 mmol) was added, followed by the addition of the other reagents, phenylboronic acid (2.4 mmol), 4-bromotoluene (2 mmol), and decane (2 mmol) as an internal standard. The reaction was heated to 80 °C. Sampling was done every 30 min for the first 4 hrs and then at 24 hrs again. The reaction was monitored by GC-FID. For the GC-FID samples, 100 μL were sampled and subjected to a silica column and then syringe filtered into a GC vial. It was diluted (1:200) with DCM.

2.7.3.8 Reaction 18c: Phosphine L20

To a mixture of solid K_2PdCl_4 (0.01 mmol, 0.5 mol%) and K_2CO_3 (4 mmol) in ethanol (10 mL), L20 (0.02 mmol) was added, followed by the addition of the other reagents, phenylboronic acid (2.4 mmol), 4-bromotoluene (2 mmol), and decane (2 mmol) as an internal standard. The reaction was heated to 80 °C. Sampling was done every 30 min for the first 4 hrs and then at 24 hrs again. The reaction was monitored by GC-FID. For the GC-FID samples, 100 μL were sampled and subjected to a silica column and then syringe filtered into a GC vial. It was diluted (1:200) with DCM.

2.7.3.9 Reaction 19c: Phosphine L21

To a mixture of solid K_2PdCl_4 (0.01 mmol, 0.5 mol%) and K_2CO_3 (4 mmol) in ethanol (10 mL), L21 (0.02 mmol) was added, followed by the addition of the other reagents, phenylboronic acid (2.4 mmol), 4-bromotoluene (2 mmol), and decane (2 mmol) as an internal standard. The reaction was heated to 80 °C. Sampling was done every 30 min for the first 4 hrs and then at 24 hrs again. The reaction was monitored by GC-FID. For the GC-FID samples, 100 μL were sampled and subjected to a silica column and then syringe filtered into a GC vial. It was diluted (1:200) with DCM.

Reaction 15c and 16c gave conversion of 98% after 24 hrs. Reaction 16c (benzyldiphenylphosphine) was chosen as the best phosphine ligand, since it reached 80% in 1 hr, compared to reaction 15c, which only reached 15% in 1 hr.

2.8 Variation in the deconvolution approach to the Suzuki C-C coupling between phenylboronic acid and 4-bromotoluene.

2.8.1 Step 1: Base deconvolution

2.8.1.1 Reaction 1d: NaOH

In a reaction flask, K_2Cl_4Pd (0.01 mmol, 0.5 mol%), a mixture of the 14 phosphine ligands (0.02 mmol) was added to the solvent mixture (10 mL). To the reaction, NaOH (4 mmol) was added, followed by the reactants, phenylboronic acid (2.4 mmol), 4-bromotoluene (2 mmol), and decane (2 mmol) as an internal standard. The reaction was heated to 80 °C. Sampling was done every 60 min for the first 4 hrs and then at 24 hrs again. The reaction was monitored by GC-FID. For the GC-FID samples, 300 μL were sampled and subjected to a silica column and then syringe filtered into a GC vial. It was diluted (1:200) with DCM.

2.8.1.2 Reaction 2d: Na_2CO_3

In a reaction flask, K_2Cl_4Pd (0.01 mmol, 0.5 mol%), a mixture of the 14 phosphine ligands (0.02 mmol) was added to the solvent mixture (10 mL). To the reaction, Na_2CO_3 (4 mmol) was added, followed by the reactants, phenylboronic acid (2.4 mmol), 4-bromotoluene (2 mmol), and decane (2 mmol) as an internal standard. The reaction was heated to 80 °C. Sampling was done every 60 min for the first 4 hrs and then at 24 hrs again. The reaction was monitored by GC-FID. For the GC-FID samples, 300 μL were sampled and subjected to a silica column and then syringe filtered into a GC vial. It was diluted (1:200) with DCM.

2.8.1.3 Reaction 3d: NEt_3

In a reaction flask, K_2Cl_4Pd (0.01 mmol, 0.5 mol%), a mixture of the 14 phosphine ligands (0.02 mmol) was added to the solvent mixture (10 mL). To the reaction, NEt_3 (4 mmol) was added, followed by the reactants, phenylboronic acid (2.4 mmol), 4-bromotoluene (2 mmol), and decane (2 mmol) as an internal standard. The reaction was heated to 80 °C. Sampling was

done every 60 min for the first 4 hrs and then at 24 hrs again. The reaction was monitored by GC-FID. For the GC-FID samples, 300 μL were sampled and subjected to a silica column and then syringe filtered into a GC vial. It was diluted (1:200) with DCM.

2.8.1.4 Reaction 4d: K_2CO_3

In a reaction flask, K_2Cl_4Pd (0.01 mmol, 0.5 mol%), a mixture of the 14 phosphine ligands (0.02 mmol) was added to the solvent mixture (10 mL). To the reaction, K_2CO_3 (4 mmol) was added, followed by the reactants, phenylboronic acid (2.4 mmol), 4-bromotoluene (2 mmol), and decane (2 mmol) as an internal standard. The reaction was heated to 80 °C. Sampling was done every 60 min for the first 4 hrs and then at 24 hrs again. The reaction was monitored by GC-FID. For the GC-FID samples, 300 μL were sampled and subjected to a silica column and then syringe filtered into a GC vial. It was diluted (1:200) with DCM.

This reaction was performed in duplicate (reaction 4d_2)

2.8.1.5 Reaction 5d: KOH

In a reaction flask, K_2Cl_4Pd (0.01 mmol, 0.5 mol%), a mixture of the 14 phosphine ligands (0.02 mmol) was added to the solvent mixture (10 mL). To the reaction, KOH (4 mmol) was added, followed by the reactants, phenylboronic acid (2.4 mmol), 4-bromotoluene (2 mmol), and decane (2 mmol) as an internal standard. The reaction was heated to 80 °C. Sampling was done every 60 min for the first 4 hrs and then at 24 hrs again. The reaction was monitored by GC-FID. For the GC-FID samples, 300 μL were sampled and subjected to a silica column and then syringe filtered into a GC vial. It was diluted (1:200) with DCM.

2.8.1.6 Reaction 6d: Cs_2CO_3

In a reaction flask, K_2Cl_4Pd (0.01 mmol, 0.5 mol%), a mixture of the 14 phosphine ligands (0.02 mmol) was added to the solvent mixture (10 mL). To the reaction, Cs_2CO_3 (4 mmol) was added, followed by the reactants, phenylboronic acid (2.4 mmol), 4-bromotoluene (2 mmol), and decane (2 mmol) as an internal standard. The reaction was heated to 80 °C. Sampling was done every 60 min for the first 4 hrs and then at 24 hrs again. The reaction was monitored by GC-FID. For the GC-FID samples, 300 μL were sampled and subjected to a silica column and then syringe filtered into a GC vial. It was diluted (1:200) with DCM.

The reaction was performed in duplicate (reaction 6d_2)

Following the analysis of the results, K_2CO_3 was chosen as the best base and used in the subsequent deconvolution reactions.

2.8.2 Step 2: Solvent deconvolution

2.8.2.1 Reaction 7d: Ethanol

In a reaction flask, K_2Cl_4Pd (0.01 mmol, 0.5 mol%), a mixture of the 14 phosphine ligands (0.02 mmol) was added to ethanol (10 mL). To the reaction, K_2CO_3 (4 mmol) was added, followed by the reactants, phenylboronic acid (2.4 mmol), 4-bromotoluene (2 mmol), and decane (2 mmol) as an internal standard. The reaction was heated to 80 °C. Sampling was done every 60 min for the first 4 hrs and then at 24 hrs again. The reaction was monitored by GC-FID. For the GC-FID samples, 300 µL were sampled and subjected to a silica column and then syringe filtered into a GC vial. It was diluted (1:200) with DCM.

2.8.2.2 Reaction 8d: Butanol

In a reaction flask, K_2Cl_4Pd (0.01 mmol, 0.5 mol%), a mixture of the 14 phosphine ligands (0.02 mmol) was added to butanol (10 mL). To the reaction, K_2CO_3 (4 mmol) was added, followed by the reactants, phenylboronic acid (2.4 mmol), 4-bromotoluene (2 mmol), and decane (2 mmol) as an internal standard. The reaction was heated to 80 °C. Sampling was done every 60 min for the first 4 hrs and then at 24 hrs again. The reaction was monitored by GC-FID. For the GC-FID samples, 300 µL were sampled and subjected to a silica column and then syringe filtered into a GC vial. It was diluted (1:200) with DCM.

2.8.2.3 Reaction 9d: Acetonitrile

In a reaction flask, K_2Cl_4Pd (0.01 mmol, 0.5 mol%), a mixture of the 14 phosphine ligands (0.02 mmol) was added to acetonitrile (10 mL). To the reaction, K_2CO_3 (4 mmol) was added, followed by the reactants, phenylboronic acid (2.4 mmol), 4-bromotoluene (2 mmol), and decane (2 mmol) as an internal standard. The reaction was heated to 80 °C. Sampling was done every 60 min for the first 4 hrs and then at 24 hrs again. The reaction was monitored by GC-FID. For the GC-FID samples, 300 µL were sampled and subjected to a silica column and then syringe filtered into a GC vial. It was diluted (1:200) with DCM.

2.8.2.4 Reaction 10d: Toluene

In a reaction flask, K_2Cl_4Pd (0.01 mmol, 0.5 mol%), a mixture of the 14 phosphine ligands (0.02 mmol) was added to toluene (10 mL). To the reaction, K_2CO_3 (4 mmol) was added, followed by the reactants, phenylboronic acid (2.4 mmol), 4-bromotoluene (2 mmol), and decane (2 mmol) as an internal standard. The reaction was heated to 80 °C. Sampling was done every 60 min for the first 4 hrs and then at 24 hrs again. The reaction was monitored by GC-FID. For the GC-FID samples, 300 µL were sampled and subjected to a silica column and then syringe filtered into a GC vial. It was diluted (1:200) with DCM.

2.8.2.5 Reaction 11d: 1,4-Dioxane

In a reaction flask, K_2Cl_4Pd (0.01 mmol, 0.5 mol%), a mixture of the 14 phosphine ligands (0.02 mmol) was added to 1,4-dioxane (10 mL). To the reaction, K_2CO_3 (4 mmol) was added, followed by the reactants, phenylboronic acid (2.4 mmol), 4-bromotoluene (2 mmol), and decane (2 mmol) as an internal standard. The reaction was heated to 80 °C. Sampling was done every 60 min for the first 4 hrs and then at 24 hrs again. The reaction was monitored by GC-FID. For the GC-FID samples, 300 µL were sampled and subjected to a silica column and then syringe filtered into a GC vial. It was diluted (1:200) with DCM.

2.8.2.6 Reaction 12d: DMF

In a reaction flask, K_2Cl_4Pd (0.01 mmol, 0.5 mol%), a mixture of the 14 phosphine ligands (0.02 mmol) was added to DMF (10 mL). To the reaction, K_2CO_3 (4 mmol) was added, followed by the reactants, phenylboronic acid (2.4 mmol), 4-bromotoluene (2 mmol), and decane (2 mmol) as an internal standard. The reaction was heated to 80 °C. Sampling was done every 60 min for the first 4 hrs and then at 24 hrs again. The reaction was monitored by GC-FID. For the GC-FID samples, 300 µL were sampled and subjected to a silica column and then syringe filtered into a GC vial. It was diluted (1:200) with DCM.

From the results, ethanol was chosen as the best solvent and used as a solvent for the deconvolution of the phosphine ligands.

2.8.3 Step 3: Phosphine ligand deconvolution:

2.8.3.1 Reaction 13d: L11

In a reaction flask, K_2Cl_4Pd (0.01 mmol, 0.5 mol%) and ligand L11 (0.02 mmol) were added to ethanol (10 mL). To the reaction, K_2CO_3 (4 mmol) was added, followed by the reactants, phenylboronic acid (2.4 mmol), 4-bromotoluene (2 mmol), and decane (2 mmol) as an internal standard. The reaction was heated to 80 °C. Sampling was done every 60 min for the first 4 hrs and then at 24 hrs again. The reaction was monitored by GC-FID. For the GC-FID samples, 300 μL were sampled and subjected to a silica column and then syringe filtered into a GC vial. It was diluted (1:200) with DCM.

2.8.3.2 Reaction 14d: L12

In a reaction flask, K_2Cl_4Pd (0.01 mmol, 0.5 mol%) and ligand L12 (0.02 mmol) were added to ethanol (10 mL). To the reaction, K_2CO_3 (4 mmol) was added, followed by the reactants, phenylboronic acid (2.4 mmol), 4-bromotoluene (2 mmol), and decane (2 mmol) as an internal standard. The reaction was heated to 80 °C. Sampling was done every 60 min for the first 4 hrs and then at 24 hrs again. The reaction was monitored by GC-FID. For the GC-FID samples, 300 μL were sampled and subjected to a silica column and then syringe filtered into a GC vial. It was diluted (1:200) with DCM.

2.8.3.3 Reaction 15d: L16

In a reaction flask, K_2Cl_4Pd (0.01 mmol, 0.5 mol%) and ligand L16 (0.02 mmol) were added to ethanol (10 mL). To the reaction, K_2CO_3 (4 mmol) was added, followed by the reactants, phenylboronic acid (2.4 mmol), 4-bromotoluene (2 mmol), and decane (2 mmol) as an internal standard. The reaction was heated to 80 °C. Sampling was done every 60 min for the first 4 hrs and then at 24 hrs again. The reaction was monitored by GC-FID. For the GC-FID samples, 300 μL were sampled and subjected to a silica column and then syringe filtered into a GC vial. It was diluted (1:200) with DCM.

2.8.3.4 Reaction 16d: L17

In a reaction flask, K_2Cl_4Pd (0.01 mmol, 0.5 mol%) and ligand L17 (0.02 mmol) were added to ethanol (10 mL). To the reaction, K_2CO_3 (4 mmol) was added, followed by the reactants, phenylboronic acid (2.4 mmol), 4-bromotoluene (2 mmol), and decane (2 mmol) as an internal

standard. The reaction was heated to 80 °C. Sampling was done every 60 min for the first 4 hrs and then at 24 hrs again. The reaction was monitored by GC-FID. For the GC-FID samples, 300 µL were sampled and subjected to a silica column and then syringe filtered into a GC vial. It was diluted (1:200) with DCM.

2.8.3.5 Reaction 17d: L19

In a reaction flask, K_2Cl_4Pd (0.01 mmol, 0.5 mol%) and ligand L19 (0.02 mmol) were added to ethanol (10 mL). To the reaction, K_2CO_3 (4 mmol) was added, followed by the reactants, phenylboronic acid (2.4 mmol), 4-bromotoluene (2 mmol), and decane (2 mmol) as an internal standard. The reaction was heated to 80 °C. Sampling was done every 60 min for the first 4 hrs and then at 24 hrs again. The reaction was monitored by GC-FID. For the GC-FID samples, 300 µL were sampled and subjected to a silica column and then syringe filtered into a GC vial. It was diluted (1:200) with DCM.

2.8.3.6 Reaction 18d: L20

In a reaction flask, K_2Cl_4Pd (0.01 mmol, 0.5 mol%) and ligand L20 (0.02 mmol) was added to ethanol (10 mL). To the reaction, K_2CO_3 (4 mmol) was added, followed by the reactants, phenylboronic acid (2.4 mmol), 4-bromotoluene (2 mmol), and decane (2 mmol) as an internal standard. The reaction was heated to 80 °C. Sampling was done every 60 min for the first 4 hrs and then at 24 hrs again. The reaction was monitored by GC-FID. For the GC-FID samples, 300 µL were sampled and subjected to a silica column and then syringe filtered into a GC vial. It was diluted (1:200) with DCM.

2.8.3.7 Reaction 19d: L21

In a reaction flask, K_2Cl_4Pd (0.01 mmol, 0.5 mol%) and ligand L21 (0.02 mmol) were added to ethanol (10 mL). To the reaction, K_2CO_3 (4 mmol) was added, followed by the reactants, phenylboronic acid (2.4 mmol), 4-bromotoluene (2 mmol), and decane (2 mmol) as an internal standard. The reaction was heated to 80 °C. Sampling was done every 60 min for the first 4 hrs and then at 24 hrs again. The reaction was monitored by GC-FID. For the GC-FID samples, 300 µL were sampled and subjected to a silica column and then syringe filtered into a GC vial. It was diluted (1:200) with DCM.

2.8.3.8 Reaction 20d: L1

In a reaction flask, K_2Cl_4Pd (0.01 mmol, 0.5 mol%) and ligand L1 (0.02 mmol) were added to ethanol (10 mL). To the reaction, K_2CO_3 (4 mmol) was added, followed by the reactants, phenylboronic acid (2.4 mmol), 4-bromotoluene (2 mmol), and decane (2 mmol) as an internal standard. The reaction was heated to 80 °C. Sampling was done every 60 min for the first 4 hrs and then at 24 hrs again. The reaction was monitored by GC-FID. For the GC-FID samples, 300 μL were sampled and subjected to a silica column and then syringe filtered into a GC vial. It was diluted (1:200) with DCM.

2.8.3.9 Reaction 21d: L2

In a reaction flask, K_2Cl_4Pd (0.01 mmol, 0.5 mol%) and ligand L2 (0.02 mmol) were added to ethanol (10 mL). To the reaction, K_2CO_3 (4 mmol) was added, followed by the reactants, phenylboronic acid (2.4 mmol), 4-bromotoluene (2 mmol), and decane (2 mmol) as an internal standard. The reaction was heated to 80 °C. Sampling was done every 60 min for the first 4 hrs and then at 24 hrs again. The reaction was monitored by GC-FID. For the GC-FID samples, 300 μL were sampled and subjected to a silica column and then syringe filtered into a GC vial. It was diluted (1:200) with DCM.

2.8.3.10 Reaction 22d: L3

In a reaction flask, K_2Cl_4Pd (0.01 mmol, 0.5 mol%) and ligand L3 (0.02 mmol) were added to ethanol (10 mL). To the reaction, K_2CO_3 (4 mmol) was added, followed by the reactants, phenylboronic acid (2.4 mmol), 4-bromotoluene (2 mmol), and decane (2 mmol) as an internal standard. The reaction was heated to 80 °C. Sampling was done every 60 min for the first 4 hrs and then at 24 hrs again. The reaction was monitored by GC-FID. For the GC-FID samples, 300 μL were sampled and subjected to a silica column and then syringe filtered into a GC vial. It was diluted (1:200) with DCM.

2.8.3.11 Reaction 23d: L4

In a reaction flask, K_2Cl_4Pd (0.01 mmol, 0.5 mol%) and ligand L4 (0.02 mmol) were added to ethanol (10 mL). To the reaction, K_2CO_3 (4 mmol) was added, followed by the reactants, phenylboronic acid (2.4 mmol), 4-bromotoluene (2 mmol), and decane (2 mmol) as an internal standard. The reaction was heated to 80 °C. Sampling was done every 60 min for the first 4 hrs and then at 24 hrs again. The reaction was monitored by GC-FID. For the GC-FID samples,

300 µL were sampled and subjected to a silica column and then syringe filtered into a GC vial. It was diluted (1:200) with DCM.

2.8.3.12 Reaction 24d: L5

In a reaction flask, K_2Cl_4Pd (0.01 mmol, 0.5 mol%) and ligand L5 (0.02 mmol) was added to ethanol (10 mL). To the reaction, K_2CO_3 (4 mmol) was added, followed by the reactants, phenylboronic acid (2.4 mmol), 4-bromotoluene (2 mmol), and decane (2 mmol) as an internal standard. The reaction was heated to 80 °C. Sampling was done every 60 min for the first 4 hrs and then at 24 hrs again. The reaction was monitored by GC-FID. For the GC-FID samples, 300 µL were sampled and subjected to a silica column and then syringe filtered into a GC vial. It was diluted (1:200) with DCM.

2.8.3.13 Reaction 25d: L7

In a reaction flask, K_2Cl_4Pd (0.01 mmol, 0.5 mol%) and ligand L7 (0.02 mmol) were added to ethanol (10 mL). To the reaction, K_2CO_3 (4 mmol) was added, followed by the reactants, phenylboronic acid (2.4 mmol), 4-bromotoluene (2 mmol), and decane (2 mmol) as an internal standard. The reaction was heated to 80 °C. Sampling was done every 60 min for the first 4 hrs and then at 24 hrs again. The reaction was monitored by GC-FID. For the GC-FID samples, 300 µL were sampled and subjected to a silica column and then syringe filtered into a GC vial. It was diluted (1:200) with DCM.

2.8.3.14 Reaction 26d: L8

In a reaction flask, K_2Cl_4Pd (0.01 mmol, 0.5 mol%) and ligand L8 (0.02 mmol) were added to ethanol (10 mL). To the reaction, K_2CO_3 (4 mmol) was added, followed by the reactants, phenylboronic acid (2.4 mmol), 4-bromotoluene (2 mmol), and decane (2 mmol) as an internal standard. The reaction was heated to 80 °C. Sampling was done every 60 min for the first 4 hrs and then at 24 hrs again. The reaction was monitored by GC-FID. For the GC-FID samples, 300 µL were sampled and subjected to a silica column and then syringe filtered into a GC vial. It was diluted (1:200) with DCM.

None of the phosphine ligands was chosen as the best since all the reactions resulted in >95% conversion, however reaction 19d gave the fastest reaction.

2.9 Iodobenzene calibration curve

The conversions for the reaction between PhI and butyl acrylate was calculated based on the calibration of PhI (**Figure S2.1**). The % conversion was calculated from the initial PhI concentration and the PhI concentration at a specific time interval.

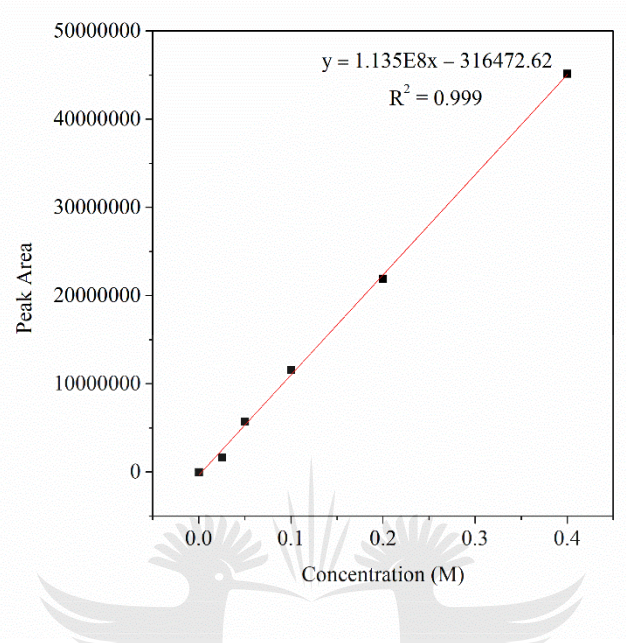

Figure S2.1: Calibration curve for iodobenzene for the determination of the conversions.

2.10 PhI reaction conversions

Table S2.2: Reaction numbers with the relative conversions for the PhI Heck reaction

Reaction number	Area of PhI at first product peak formation	Concentration of PhI calculated from the calibration curve	Conversion (%)
2a	1298226.5	0.014228057	92.9
3a	1675951.1	0.017556409	91.2
6a	1126621.5	0.012715945	93.6
10a	1001721.7	0.01161538	94.2
12a	1747366.7	0.018185693	90.9
16a	1409348.7	0.015207219	92.4

2.11 Bromobenzene calibration curve

The conversions for the reaction between PhBr and butyl acrylate for the Heck reaction was calculated using a calibration curve of PhBr (**Figure S2.2**). The % conversion was calculated from the initial PhBr concentration and the PhBr concentration at a time interval which gave the first product peak.

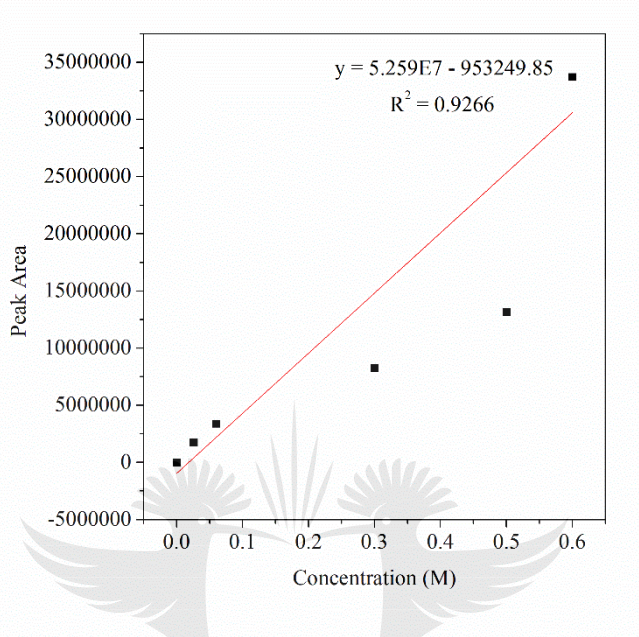

Figure S2.2: Calibration curve for PhBr.

2.12 PhBr reaction conversions

Table S2.3: Reaction numbers with the relative conversions for the PhBr Heck reaction

Reaction number	Area of PhBr at first product peak formation	Concentration of PhBr calculated from the calibration curve	Conversion (%)
2b	1281158	0.046044447	76.9
3b	1363778.9	0.047946139	76.0
6b	1261555.5	0.045593255	77.2
10b	1371044.6	0.048113374	75.9
12b	1210493.8	0.044417965	77.8
16b	1569918.6	0.052690871	73.7

2.13 Conversion for the deconvolution reactions of Suzuki cross-coupling between phenylboronic acid and 4-bromotoluene.

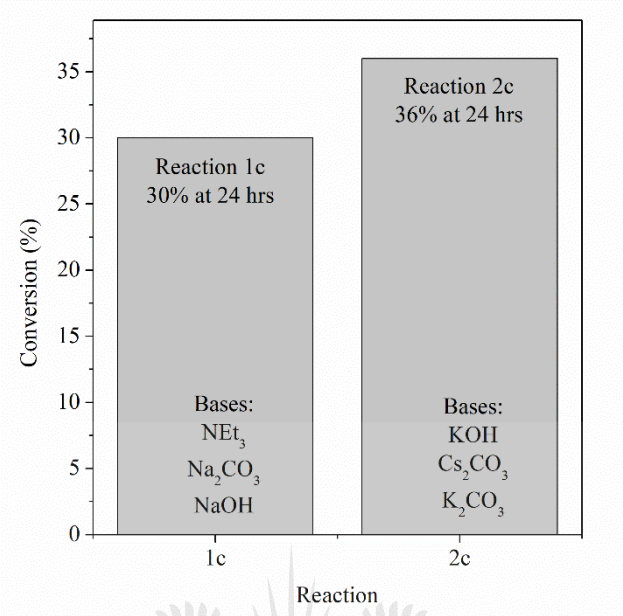

Figure S2.3: Conversions for reactions 1c and 2c at 24 hrs. Bases for reaction 1c was split-and-pooled to have NEt_3, Na_2CO_3 and NaOH in one reaction. Reaction 2c was split-and pooled to have KOH, Cs_2CO_3 and K_2CO_3 in the reaction. Reaction 1c gave approximately 30% conversion and reaction 2c at 36% conversion

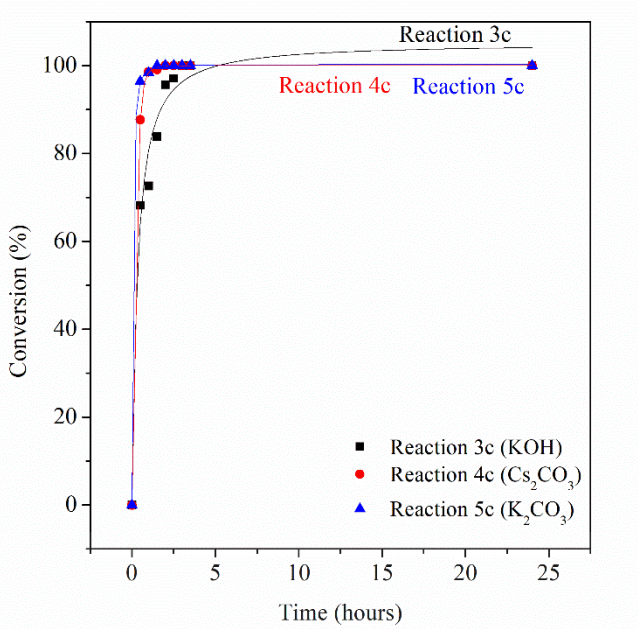

Figure S2.4: Conversions for reactions 3c, 4c and 5c over 24 hrs. Reaction 3c contained KOH, reaction 4c contained Cs_2CO_3 and reaction 5c contained K_2CO_3. All three reaction resulted in 100%. However, reaction 5c was the fastest, reaching 100% at 1.5 hrs.

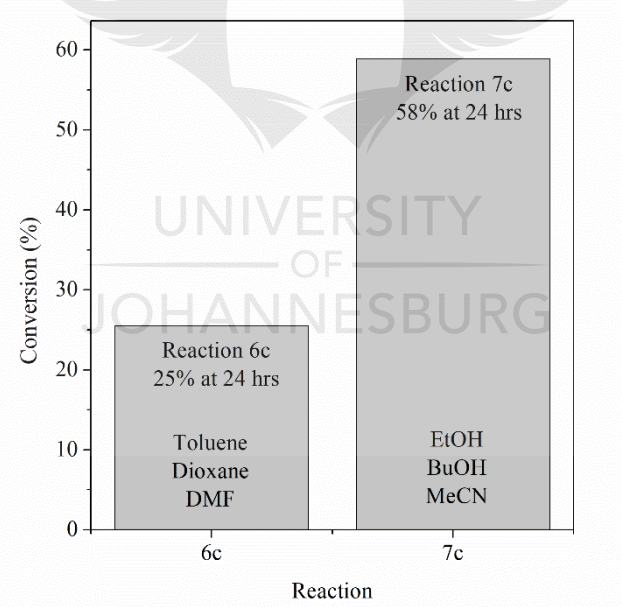

Figure S2.5: Conversions over time for reactions 6c and 7c. Reaction 6 c contained a mixture of toluene, 1,4-dioxane and DMF and reaction 7c contained ethanol, butanol and acetonitrile. Reaction 7c was identified as the best reaction since it gave a conversion of 59% at 24 hrs, compared to reaction 6c, which only gave a conversion of 25% at 24 hrs.

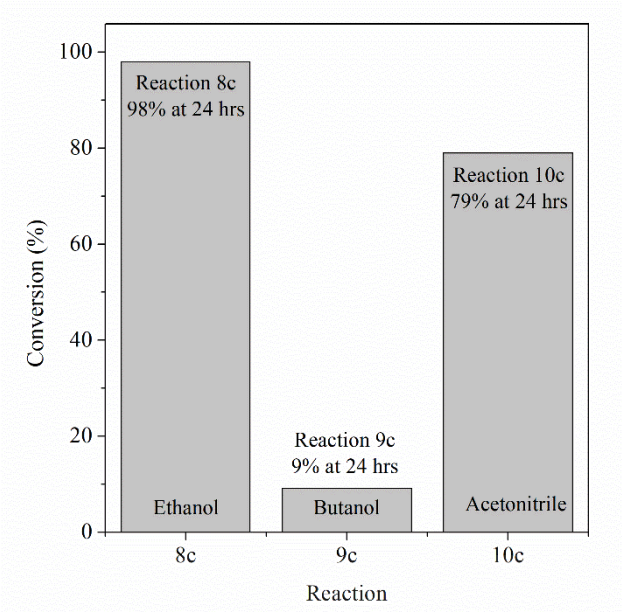

Figure S2.6: Conversions for reactions 8c, 9c and 10c at the 24 hr time interval. Reaction 8c, identified as the best reaction, had ethanol as the solvent and gave a conversion of 98%. Reaction 9c with butanol as the solvent gave a conversion of 9% and reaction 10c had acetonitrile as the solvent and gave a conversion of 79%.

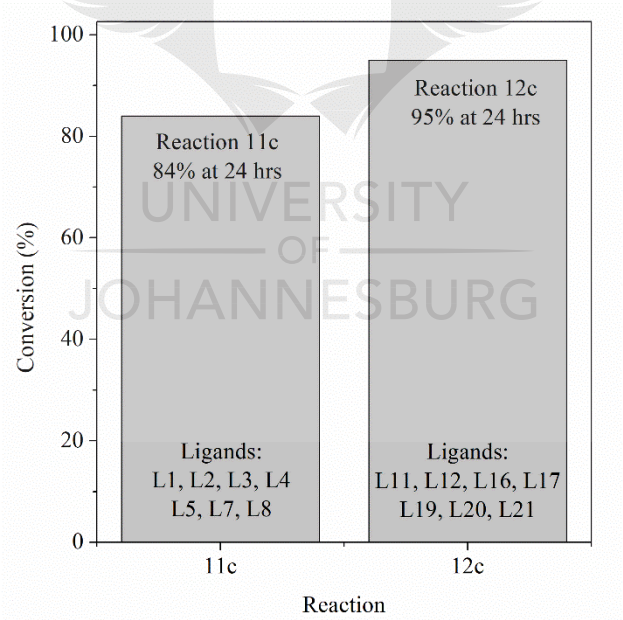

Figure S2.7: The 24 hrs conversions for reaction 11c and 12c. Reaction 11c contained a pooling of ligands L1, L2, L3, L4, L5, L7, and L8. Reaction 12c contained ligands L11, L12, L16, L17, L19, L20, and L21. Reaction 12c gave the best conversion (95%) in 24 hrs. This reaction was, therefore, further split and deconvoluted to find the best ligand.

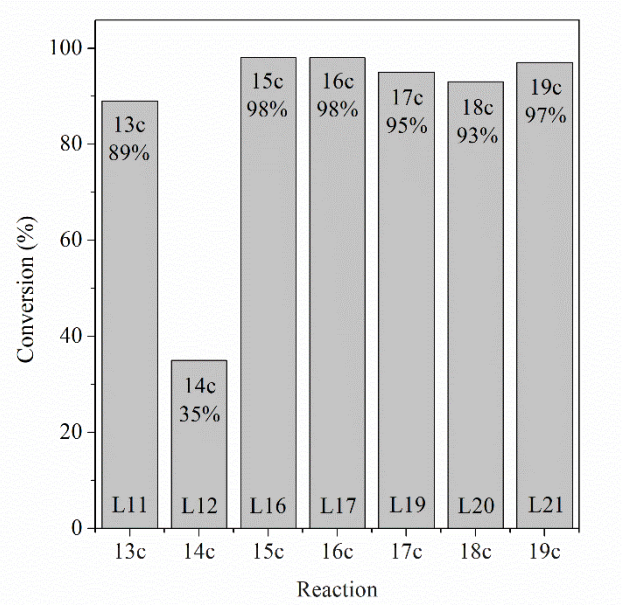

Figure S2.8: Conversions of reactions 13c, 14c, 15c, 16c, 17c, 18c and 19c for 24 hrs. Most of the reaction gave conversion >85%, except for reaction 14c, which gave a conversion of 35% for 24 hrs. The conversions for reaction 15c and 16c both reached 98% in 24 hrs. These reactions were individually compared to determine which one reached a higher conversion in a shorter time.

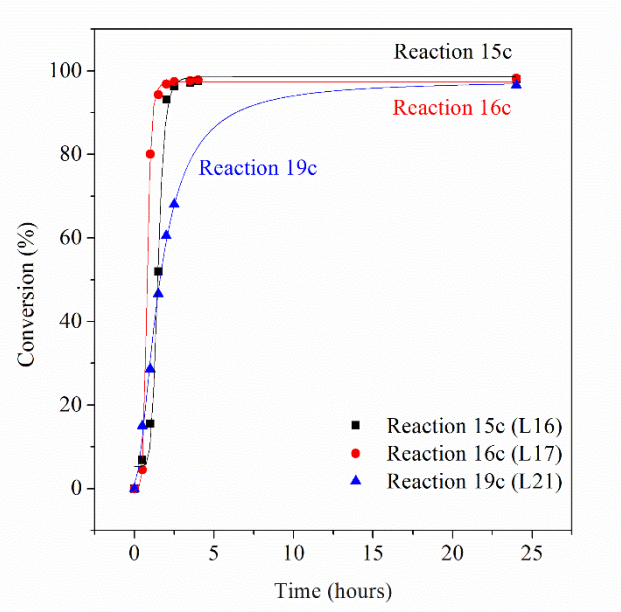

Figure S2.9: The conversions for reaction 15c, 16c and 19c were individually compared to determine which reaction gave a higher conversion in a shorter time. From the figure, it can be seen that reaction 16c gave an 80% conversion within 1 hr compared to 15c and 19c, which gave conversions of 15% and 28% within 1 hr. Therefore, it was concluded that L17 was the optimal phosphine ligand.

2.14 A variation in the deconvolution approach to the Suzuki cross-coupling reaction between phenylboronic acid and 4-bromotoluene

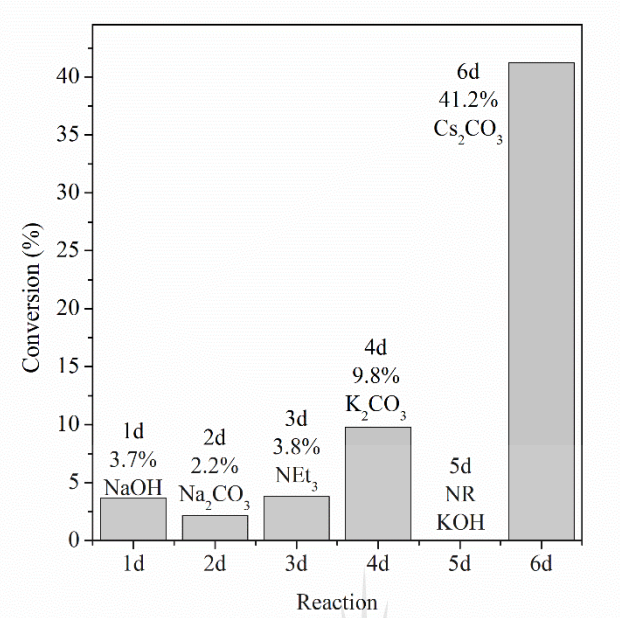

Figure S2.10: The conversions for reactions 1d – 6d, in the variation of the deconvolution approach of the Suzuki reaction. Reactions 1d – 6d contained NaOH, Na_2CO_3, NEt_3, K_2CO_3, KOH and Cs_2CO_3 bases in each reaction, respectively. The bases K_2CO_3 and Cs_2CO_3 gave the highest conversions for 24 hrs.

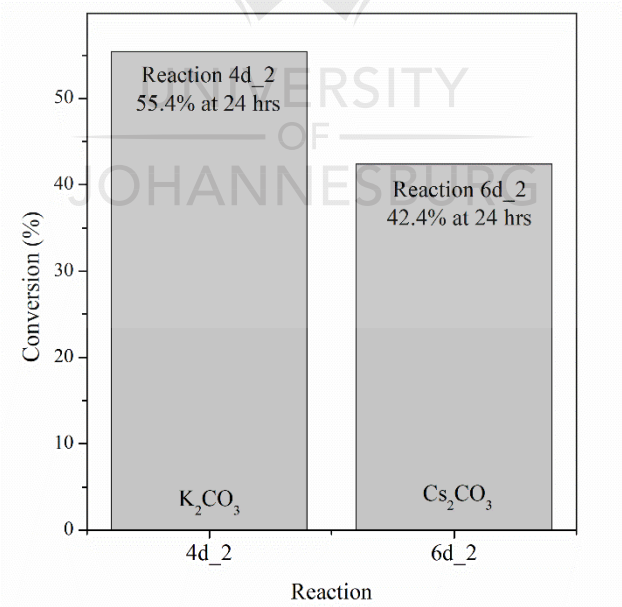

Figure S2.11: Second replicate experiment for the reactions containing K_2CO_3 and Cs_2CO_3 as bases. It was observed that the reactions containing these two bases gave similar results each time. Comparing these two experiments, it can be seen that K_2CO_3 gave a higher conversion at 24 hrs.

A t-test was conducted to determine if there is a significant difference between the conversions of these two bases. The pooled standard deviation and test statistic value was calculated as follows:

$$s_{pooled} = \frac{\sqrt{\sum_{i=1}^{N_1}(x_i - \bar{x}_1)^2 + \sum_{j=1}^{N_2}(x_j - \bar{x}_2)^2}}{N_1 + N_2 - N_t}$$

$$t = \frac{\bar{x}_1 - \bar{x}_2}{s_{pooled}\sqrt{\frac{N_1 + N_2}{N_1 N_2}}}$$

Where N_1 is the number of replicates in the first sample set (K_2CO_3) and N_2 the second sample set (Cs_2CO_3). N_t represent the total number of sample sets (2 in this case) The mean of the conversions for K_2CO_3 and Cs_2CO_3 is represented by $\bar{x}_1$ and $\bar{x}_2$, respectively. The conversion values of each replicated for K_2CO_3 and Cs_2CO_3 is represented by x_i and x_j, respectively.

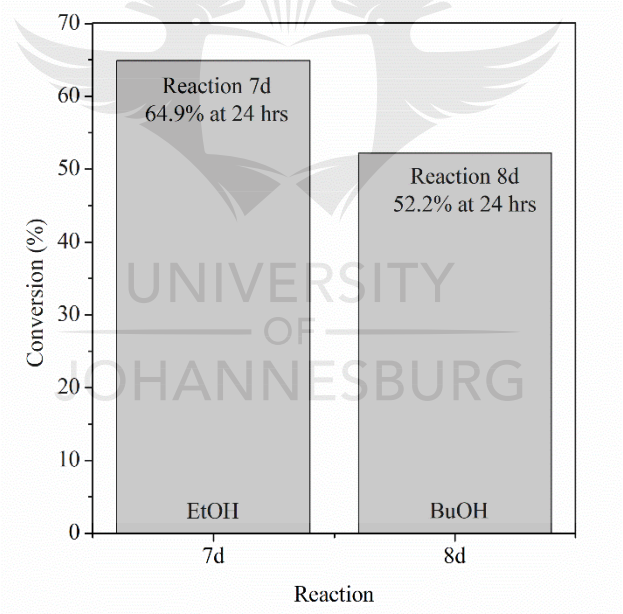

Figure S2.12: Conversions for reactions 7d and 8d at the 24 hrs. Reaction 7d, containing ethanol, was identified as the best reaction with a conversion of 64.9% at 24 hrs. Reaction 8d containing butanol as the solvent gave a conversion of 52.2%.

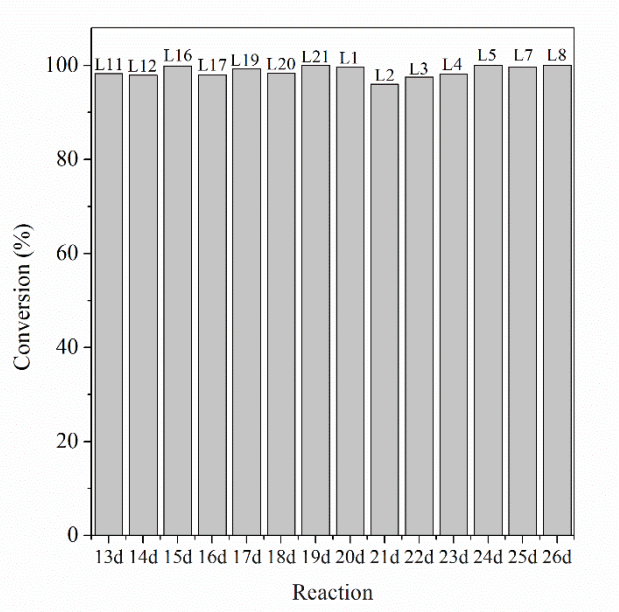

Figure S2.13: Conversions of reactions 13d – 26d for 24 hrs. All the reactions gave conversions >95%. No conclusion could be made as to which phosphine ligand resulted in the best reaction.

Chapter 3

Robotics-Assisted High-throughput Catalytic Investigation of PVP Nanoparticles in the Oxidation of Morin

Supplementary information

3.1 Concentration variation studies for Pd-and Au-PVP NPs

Table S3.1: The corresponding kobs and standard deviation (SD) obtained for the concentration studies of Pd-PVP NPs in the oxidation of morin.

Concentration in µM	**k_{obs}**	**SD**
5	0.0147	6.54796E-4
17.5	0.03279	6.49018E-4
35	0.0652	0.00327
47.5	0.08699	0.00822
60	0.10323	0.00803
72.5	0.10736	0.0108
85	0.11222	0.00467
97.5	0.10882	0.00803
110	0.09253	0.00572
122.5	0.09223	0.01578
135	0.09156	0.00552
150	0.09156	0.00552

Table S3.2: The corresponding kobs and standard deviation (SD) obtained for the concentration studies of Au-PVP NPs in the oxidation of morin.

Concentration in μM	**k_{obs}**	**SD**
5	0.00756	0.00202
17.5	0.0106	9.01716E-4
35	0.01149	0.00139
47.5	0.01442	0.00248
60	0.01804	0.00144
72.5	0.02047	0.00145
85	0.02277	0.00112
97.5	0.02511	5.67392E-4
110	0.02844	0.00151
135	0.03251	0.00232
150	0.0336	0.00223

3.2 Morin concentration variation studies

For the catalytic studies, the variation in the concentration of morin dye was included in determining the effect of the concentration on the k_{obs}. This was done at temperatures of 25 °C, 35 °C and 45 °C. The Opentrons liquid handling robot was used for pipetting the reagents into a 96-well plate. For this study, the concentration of both catalysts (Pd- and AuPVP NPs) was kept constant at 85 μM and 35 μM, respectively. The concentration of hydrogen peroxide was also kept constant at 0.45 mM.

The concentration was varied from 3.3 – 100 μM (12 concentrations), with four replicates included for both catalysts. Therefore, the Opentrons was set up to pipette 30 μL for the catalyst solution as well as the hydrogen peroxide solution. The water and morin solution was varied from 0 – 300 μL, as indicated in **Figure S3.1**.

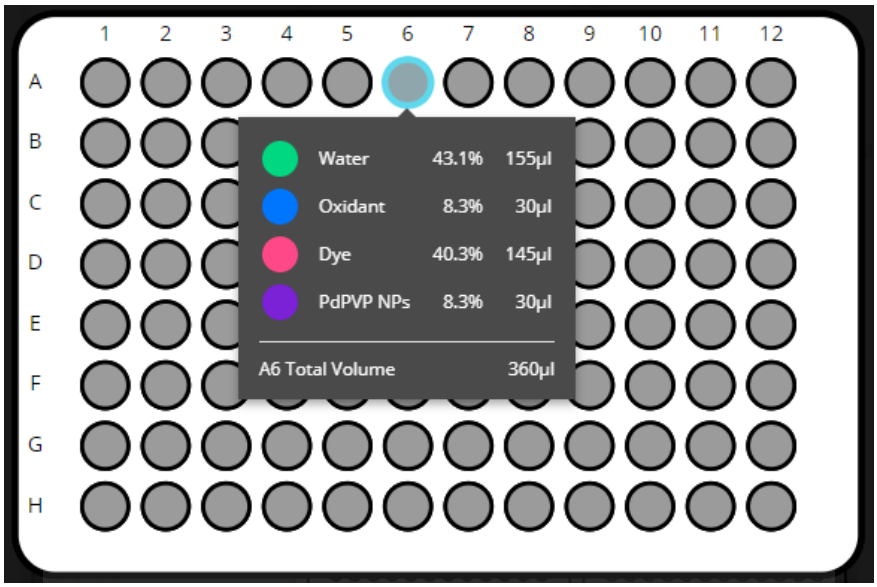

Figure S3.1: Final plate representation following the addition of all the reagents by the Opentrons for the morin concentration variation study. This figure shows the composition of well A6 as an example. This well contains 155 µL water, 30 µL oxidant or peroxide (0.45 mM), 30 µL of PdPVP NPs (35 µM) and 145 µL of morin dye (48.3 µM). For this plate, the concentrations (3.3 – 100 µM) and volume of the morin dye were increased from A1 – H1 to A12 – H12, in a range of 10 – 300 µL.

3.3 Hydrogen peroxide concentration variation

A similar study was conducted for the hydrogen peroxide. The concentration (12 concentrations) was varied over the 96-well plate, with four replicates of each catalyst. The morin and catalyst concentration was kept constant. For the PdPVP NPs, a concentration of 85 µM was used. For the AuPVP NPs and the morin dye, concentrations of 35 µM and 50 µM were used, respectively.

Therefore, the set up included a constant volume of 30 µL of the catalysts and morin solution, varying the volumes of the water and hydrogen peroxide solution from 0 – 300 µL as indicated in **Figure S3.2**.

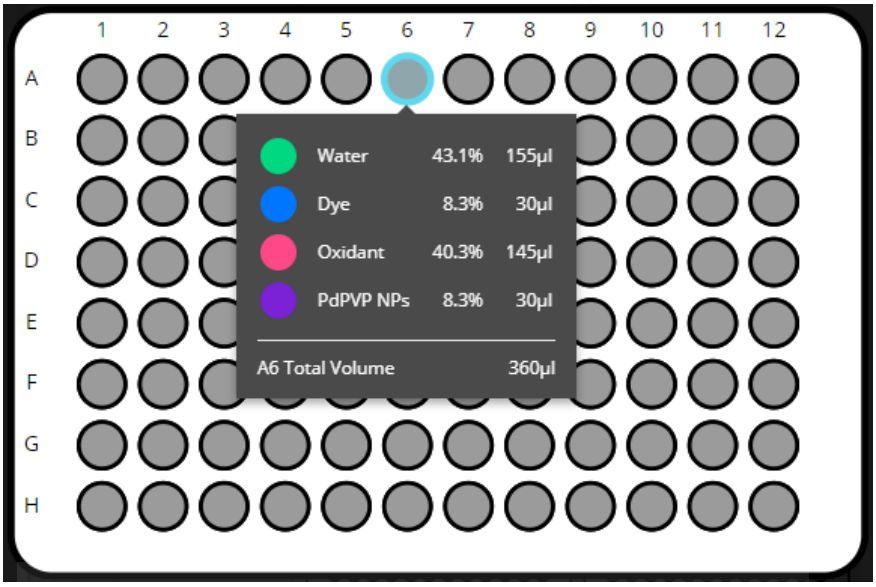

Figure S3.2: Final plate representation following the addition of all the reagents by the Opentrons for the peroxide concentration variation study. This figure shows the composition of well A6 as an example. This well contains 155 µL water, 30 µL morin solution (50 µM), 30 µL of PdPVP NPs (35 µM) and 145 µL of peroxide (9.67 mM). For this plate, the concentrations (0.67 – 20 mM) and volume of the peroxide were increased from A1 – H1 to A12 – H12, in a range of 10 – 300 µL.

3.4 Screening of mesoporous metal oxides for the oxidation of morin

Mesoporous metal oxide catalysts (8) were screened for the oxidation of morin. The concentration of each catalyst was varied from 0.0025 – 0.025 mg/mL. The rows A – H contained a concentration range of each catalyst (**Table S3.3**). A stock solution of each catalyst was prepared by weighing out approximately 0.005 g of each catalyst. The catalysts were dispersed in deionised water in an ultrasonic bath. The volume of the catalyst dispersion was increased from column 1 to 12 from 0 – 100 µL, in a 96-well plate (**Figure S3.3**). The concentration of morin was 150 µM, and that of hydrogen peroxide was 7.5 mM.

Table S3.3: The rows in the 96-well plate (A to H) representing the mesoporous metal oxide catalyst under investigation.

Row	Catalyst
A	TiO_2-MMO
B	ZrO_2-MMO
C	CeO_2-MMO
D	Co_3O_4-MMO
E	Fe_2O_3-MMO
F	NiO_2-MMO
G	ZnO_2-MMO
H	MnO_2-MMO

The catalysts were screened for their activity in the oxidation of morin. The decrease in absorbance of morin at λ 410 nm was monitored using a microplate reader. This was done for 2 hrs with a 2 min interval. However, not all of the catalysts were active towards the oxidation of morin. Preliminary results showed that the Zr-MMO, Co-MMO, Ni-MMO and Mn-MMO were active towards the oxidation of morin. A decrease in the absorbance was seen over a period of two hrs, as seen in

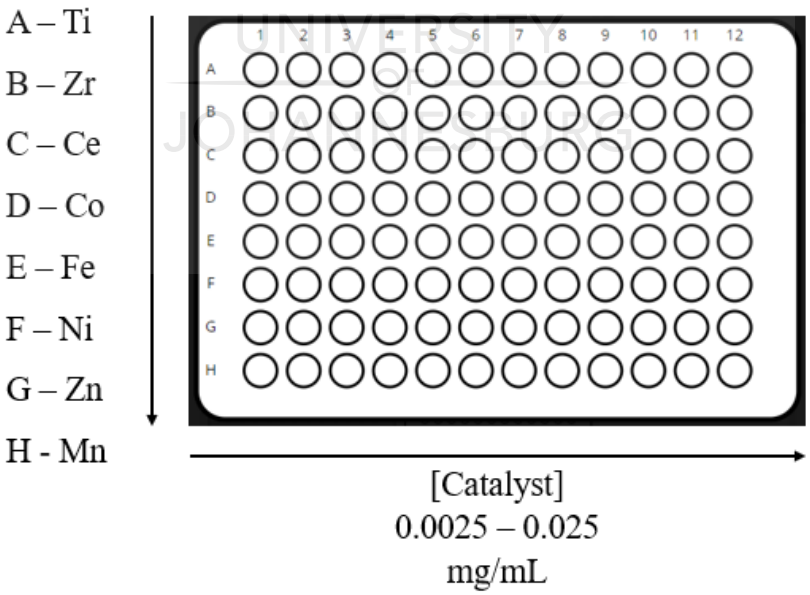

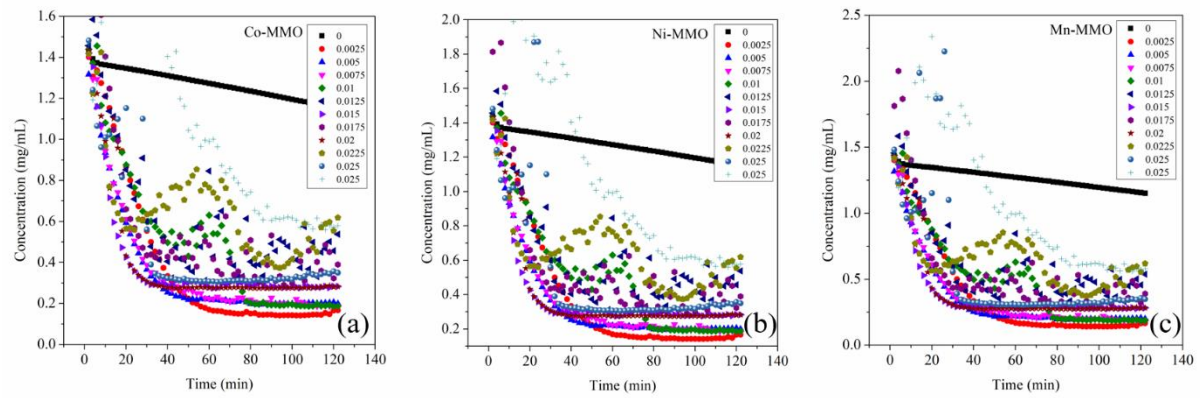

Figure S3.4.

Figure S3.3: The schematic representation of the 96-well plate used for the screening of 8 mesoporous metal oxide catalysts for the oxidation of morin. The catalysts were added to row A – H, using a concentration range of 0.0025 – 0.025 mg/mL which were increased from column 1 to 12.

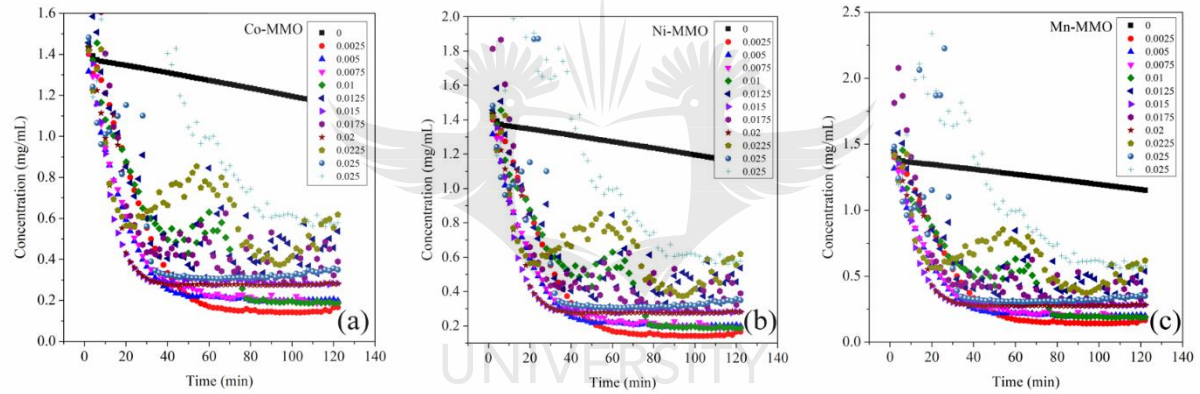

Figure S3.4: Decrease in absorbance of morin at λ410 nm in the presence of Co-MMO (a), Ni-MMO (b) and Mn-MMO (c) catalysts.

3.5 Synthesis of AuDEN in the 96-well plate

The synthesis of dendrimer encapsulated gold nanoparticles (AuDENs) in a 96-well plate was investigated. A 6.5 µM dendrimer (G6-OH terminated) solution was prepared from which 30 µL was added to a 96-well plate using six replicates. Using 6.5 µM for a stock solution, gives a final dendrimer NP concentration of 0.65 µM in 300 µL (total volume in the well after the addition of all reagents). A gold chloride solution was added to the dendrimer solution using a 55 mol excess of the Au. The plate was shaken in the microplate reader for 30 min to allow coordination of the Au to the dendrimer. The AuDEN was formed after the addition of sodium borohydride ($NaBH_4$). The AuDEN formation can be seen from the spectrum in **Figure S3.5**.

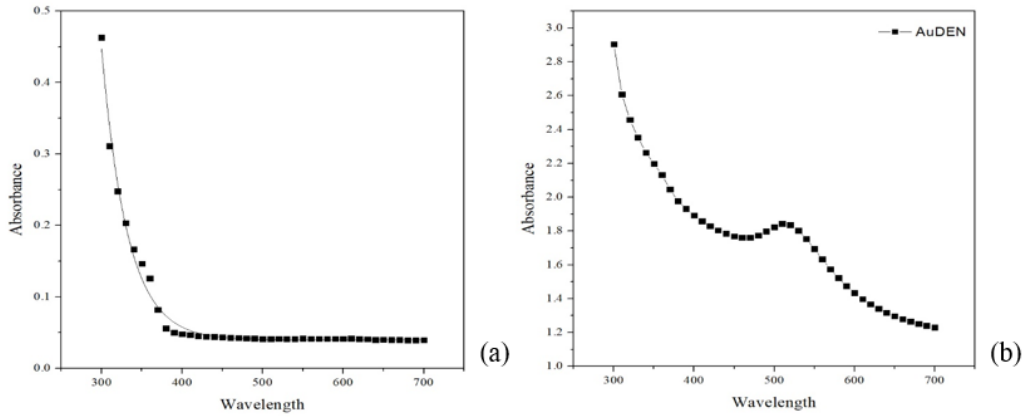

Figure S3.5: **(a)** Absorbance spectrum (λ 300 – 700 nm) for the G6-OH dendrimer before Au coordination. **(b)** Absorbance spectrum for the dendrimer encapsulated gold NP. A plasmon resonance peak can be seen at approximately λ 520 nm. This indicates the formed AuNPs

A solution of 4 nitrophenol (4-NP) was added to each well, to determine if the synthesised AuDEN would be able to reduce the 4-NP to 4-aminophenol. A slight decrease in the absorbance at λ 400 nm was seen over 1 hour (**Figure S3.6**). This study looks promising; however, more work is necessary to prove it.

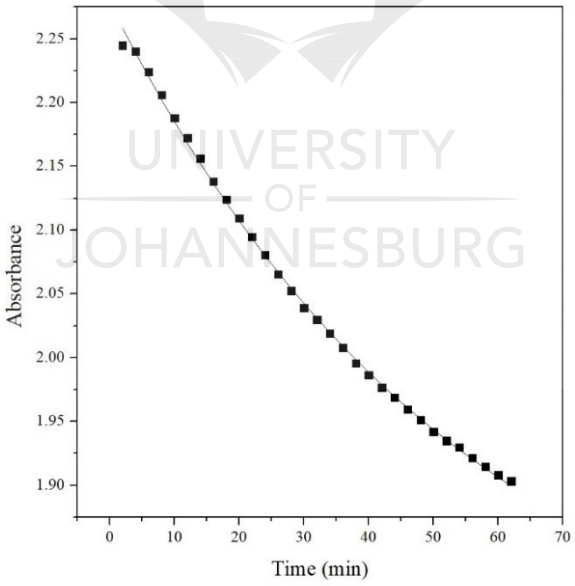

Figure S3.6: Decrease in the absorbance at λ 400 nm for the 4-NP dye over 1 hour. A slight decrease in the absorbance can be seen

Chapter 4

Robotic Catalysis: A High-throughput Method for Miniature Screening of Mesoporous Metal Oxides

Supplementary information

1. Introduction

High-throughput screening of catalysts entails the parallel synthesis and evaluation of the numerous catalysts. For the parallel synthesis of numerous mesoporous metal oxide heterogeneous catalysts, small droplets of the mesoporous metal oxide (MMO) formulation/s were deposited onto a suitable substrate to be calcined, which takes place at very high temperatures. The catalysts are then evaluated simultaneously for a specific reaction. In this study, the mesoporous metal oxide catalysts were evaluated for their activity in the oxidative degradation of morin dye. This was achieved by a plate reader, and the reaction was followed by the decrease in the absorbance of the morin dye.

The plate reader is a UV/Vis light spectrophotometer which reads the plate from the bottom. Therefore, the UV/Vis light is sent through the plate (or each well, when normally operated) from the bottom and the difference in the absorbance is then calculated by the amount of light absorbed by the reaction. It was, therefore, important to select an appropriate substrate for the synthesis of the mesoporous metal oxide catalyst so that the UV/visible light plate could still be used. Glass was chosen as the substrate since it was able to withstand the high calcination temperature and it is transparent to allow the UV/visible light through to monitor the oxidation of morin and to screen multiple catalysts at the same time.

Numerous catalysts (up to 96) had to be deposited and synthesised on the glass plate to show that mesoporous metal oxides can be synthesised in small amounts and be screened for a specific reaction using high-throughput screening and a customised 96-well catalyst plate. For the miniaturisation of the catalysts, very small amount of the mesoporous metal oxide formulations were deposited onto the glass plate for calcination, to obtain a small amount (μg) of the catalysts on one plate. To achieve this, an acoustic liquid handler was used to transfer small droplets (2.5 up to 5000 nL) of the mesoporous metal oxide formulation onto the glass

plate. The instrument used was a Labcyte, ECHO 550 acoustic liquid handler. It bombards formulation in a source plate with acoustic sound waves, which ultimately generates nano-droplets. These nano-droplets are projected upwards into (or onto) a destination plate (**Figure S4.1**). Conventionally, a microtiter well plate is used as the destination plate; however, we used a glass plate for formulation deposition

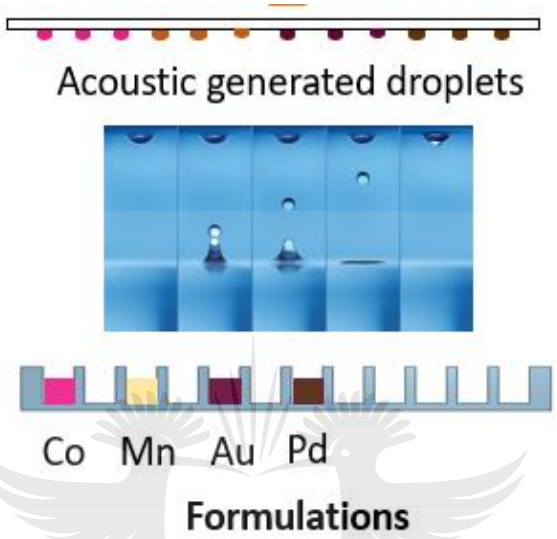

Figure S4.1: Illustration of the nano-droplet generation of the catalyst formulations used for this study, using the ECHO acoustic liquid handler. The formulation in the source plate (Co, Mn, Au and Pd formulations) is subjected to acoustic sound waves from the instrument, causing nano-droplets to be generated which is projected upwards to the destination plate (glass plate).

2. Solvent compatibility test

The use of the ECHO acoustic liquid handler has a few disadvantages. Only a few solvents are compatible with the Labcyte ECHO 550 liquid handler. This is due to the small amounts (2.5 nL) that the instrument transfers to the destination plate. Small droplets have a large surface to volume ratio. The higher the surface to volume ratio, the faster the droplet will evaporate. If low boiling point solvents (ethanol) are used as a transfer solvent, the droplets evaporate more readily. However, when using a high boiling point solvent, such as ethylene glycol, the chance of evaporation decreases. It was, therefore, important to test the droplets formed by the ECHO when the conventional mesoporous metal oxide formulation solvent (ethanol) was used. Initially, two solvents, ethanol and isopropanol, were used to synthesis cobalt formulations, and these formulations were tested on the ECHO liquid handler to determine the droplet size.

Both the formulations were placed in the source plate (384 well plate). The instrument was set to dispense 30 nL of each formulation onto a glass plate. The experiment using the ethanol formulation was unsuccessful as there was no transfer to the glass plate, due to evaporation of the ethanol. As soon as the droplet is deposited onto the glass plate, the ethanol evaporates almost immediately. Using the isopropanol formulation, a thin film of the formulation could be seen on the glass plate, however droplets were not evenly dispersed, and some droplets were splashed onto the plate. To obtain catalysts on the glass plate, neat droplets of the formulations are required to be transferred to the glass plate. Other solvent systems were, therefore, investigated.

A few solvent systems were tested, which included ethanol, methanol, ethylene glycol, ethylene glycol/ethanol and ethylene glycol/methanol. The MMO formulations were prepared using these solvents systems, and the formulation transfers were done onto the glass plate after which the droplets were examined.

With both the methanol and ethylene glycol solvent systems, it was seen that the surfactant did not completely dissolve. It was, therefore, not investigated further. Two different droplet volumes were also investigated, a small volume of 30 nL and a larger volume of 240 nL. The formulations were transferred onto the glass using the ECHO acoustic liquid handler. Droplet transfers and examination are listed in **Table S4.1**.

Table S4.1: Droplet transfer examination with different solvent systems. All the solvent systems were tested with a cobalt MMO formulation.

Solvent system	Amount transferred	Comment
Ethanol (with F127)	30 nL	Drops were not dispensed properly. The drops could almost not be seen.
Ethanol (with F127)	240 nL	Drops were not dispensed properly. The drops could almost not be seen.
Ethylene glycol	30 nL	The formulation was transferred onto the plate as neat round droplets.
Ethylene glycol	240 nL	The formulation was transferred onto the plate as neat round droplets.
Ethylene glycol (with F127)	30 nL	No transfer of droplets was seen.
Ethylene glycol (with F127)	240 nL	The formulation was transferred as droplets; however, some of the droplets were splashed onto the plate rather than being transferred as a neat droplet.
Ethylene glycol/methanol	30 nL	The formulation was transferred onto the plate as neat round droplets.
Ethylene glycol/methanol	240 nL	The formulation was transferred onto the plate as neat round droplets.
Ethylene glycol/methanol (with F127)	30 nL	The formulation was transferred onto the plate as neat round droplets.
Ethylene glycol/methanol (with F127)	240 nL	The formulation was transferred onto the plate as neat round droplets.
Ethylene glycol/ethanol (with F127)	30 nL	The formulation was transferred onto the plate as neat round droplets.
Ethylene glycol/ethanol (with F127)	240 nL	The formulation was transferred onto the plate as neat round droplets.

Based on these results, the ethylene glycol/ethanol solvent system in a 1:1 ratio was used in further experiments. Firstly, the F127 surfactant and metal salt is dissolved in the ethanol and stirred for approximately 10 min to ensure complete dissolution. After that, the ethylene glycol is added to the mixture, and it is further stirred for 2 hrs. The ethanol ensures that both the surfactant and metal salt are dissolved, and the ethylene glycol keeps the nano-droplets stable on the glass plate, preventing evaporation. Stable droplets can be seen in **Figure S4.2**.

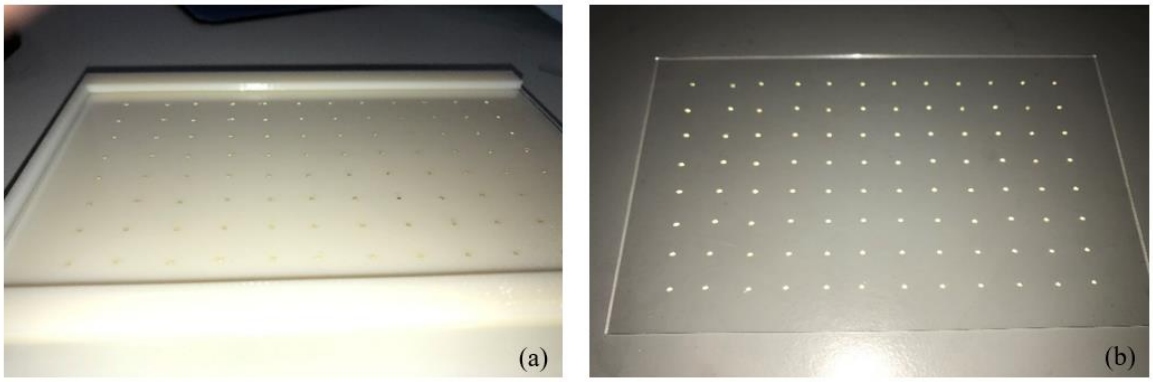

Figure S4.2: **(a)**The glass plate, in a 3D printed holder designed to hold the glass plate in the ECHO, containing 96 droplets on a mesoporous metal oxide formulation. **(b)**The volume of each droplet is 240 nL. The transferred droplets are neat and defined.

Using a different solvent system with a higher boiling point solvent, the heat treatments had to be adjusted slightly. The formulation was, therefore, aged at 80°C overnight, dried at 100°C for 6 hrs and calcined at 400°C for 4 hrs. Moreover, the addition of ethylene glycol to the formulation could alter the mesoporous structure. Characterisation of the bulk Co_3O_4-MMO catalyst is included to show that the presence of ethylene glycol does not affect the formation of the mesoporous metal oxides.

3. Characterisation of the bulk and miniature catalysts

3.1. Brunauer-Emmett-Teller analysis

Unfortunately, not enough sample could be obtained from the catalyst plate for BET analysis of the miniature catalyst. Therefore, only the bulk sample was analysed using BET (**Figure S4.3** and **Figure S4.4**).

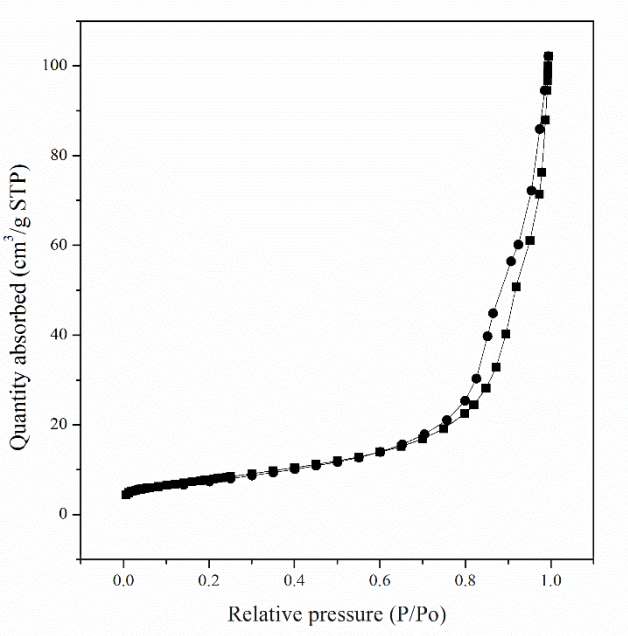

Figure S4.3: Nitrogen sorption results for Co_3O_4 MMO. The results show an IV hysteresis loop. The surface area obtained was 28.25 m^2/g.

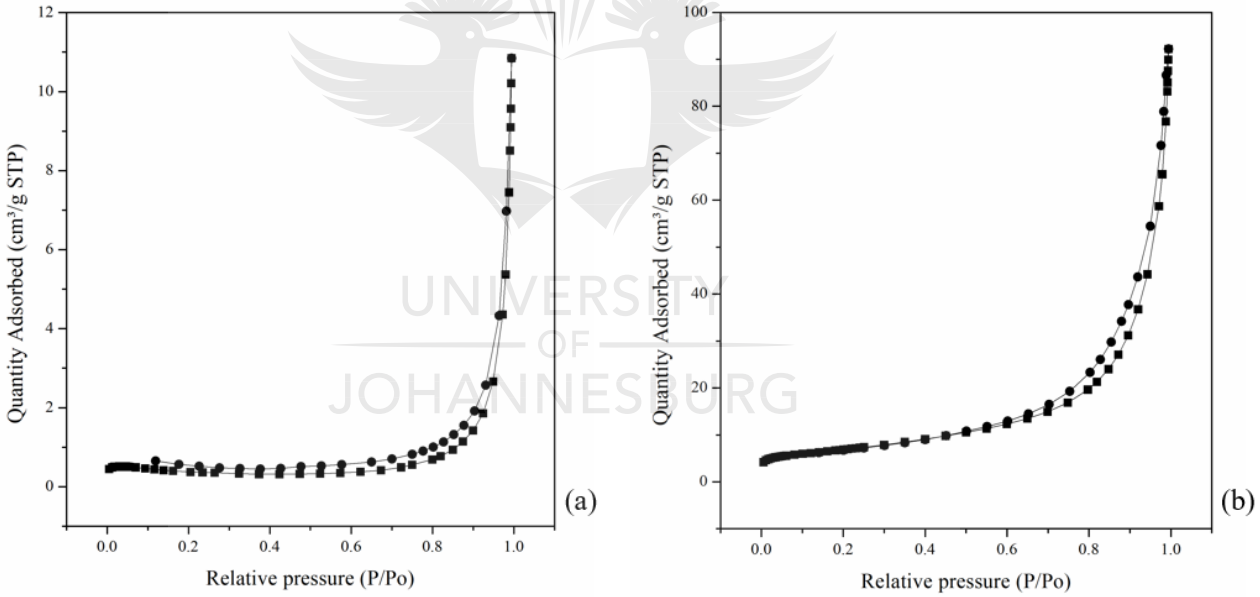

Figure S4.4: Nitrogen sorption results for **(a)** Au/Co_3O_4 MMO and **(b)** Pd/Co_3O_4 MMO. The results of both show IV hysteresis loops. Surface areas of **(a)** 24.35 and **(b)** 1.12 m^2/g for and respectively.

The surface areas of the Co_3O_4-MMO and the Au/Co_3O_4-MMO around 30 m^2/g is relatively good. The slight decrease in the surface area of the Au/Co_3O_4-MMO is an indication that the Au-PVP NPs occupies the pores in the Co_3O_4 material, decreasing the surface area slightly. Moreover, the Pd/Co_3O_4-MMO catalyst didn't give a good surface area, i.e. 1.12 m^2/g. This

might be due to Pd-PVP NPs agglomeration in the pores and on the surface of the Co_3O_4-MMO catalyst, decreasing the surface area tremendously.

3.2. Transmission electron microscopy (TEM)

The TEM imaging confirmed that the introduction of the ethylene glycol did not affect the synthesis of the mesoporous cobalt oxide. The mesoporous networks can be seen from **Figure S4.5**, and the particle size is approximately 20 nm.

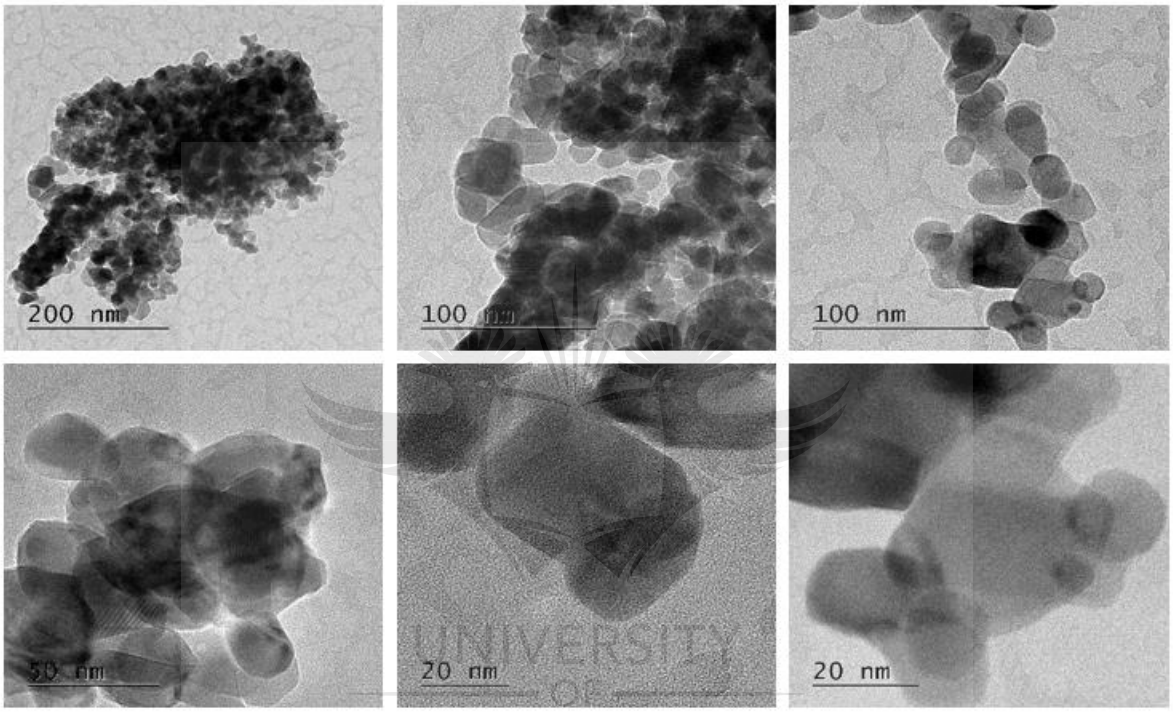

Figure S4.5: TEM imaging of the bulk Co_3O_4-MMO sample. The sample was dispersed in dH_2O using a sonicator bath and dispensed onto a copper grid. The particle size is approximately 20 nm, and the mesoporous networks can be seen.

3.3. Scanning Electron Microscopy imaging (SEM)

As mentioned above, to screen the catalyst using a high-throughput system, the catalyst should be available in very small amounts. Since miniature catalysts were synthesised on a glass plate, it had to be ensured that catalysts formed were indeed mesoporous metal oxide materials and that the morphology of the material was similar to the material synthesised using the conventional method. In conjunction with the TEM imaging of the bulk and miniature catalysts, the catalysts were analysed on the glass plate using SEM imaging.

For SEM (JEOL JSM-6610) characterisation of the miniature catalysts, the formulation was deposited onto an indium tin oxide (ITO) microscope slide. It was sputtered with gold to make the particles more conductive. For the bulk sample, the particles were suspended in methanol and deposited onto an ITO microscope slide and sputtered with gold. The morphology of the two samples cannot be compared using SEM imaging since this characterisation does not provide sufficient detail necessary to make conclusions. The SEM images are given in **Figure S4.6**.

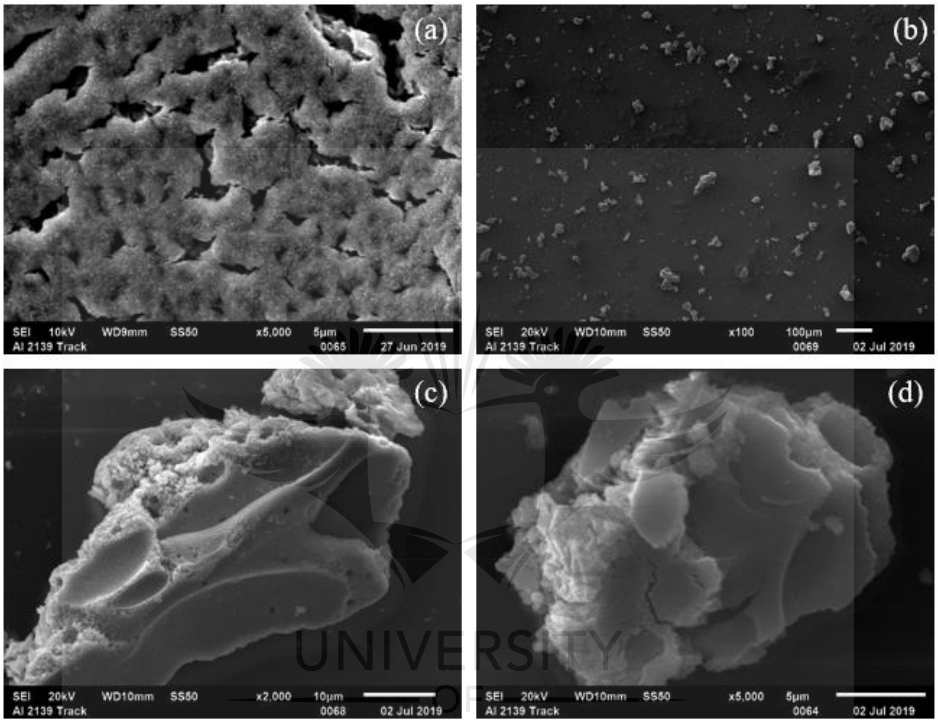

Figure S4.6: SEM imaging of the bulk **(a)** and **(c)**, and miniature **(b)** and **(d)** Co_3O_4-MMO catalyst on the indium-tin-oxide microscope coverslip. The coverslip represents the glass plate used for parallel synthesis of the catalyst.

From **Figure S4.6**, some detail of the morphology of the bulk and miniature samples can be seen. For example, **Figure S4.6 (c)** shows some porosity in the bulk sample; however, this technique didn't give enough detail about the internal structure of the material as with the TEM imaging. With TEM analysis, the mesoporous channels in the material can be seen. Even though the SEM imaging could not give as much detail as the TEM imaging, the morphology of both the bulk and miniature samples could be compared, and it can be concluded that the morphology is similar. Therefore, it can be said that the miniature Co_3O_4-MMO catalysts could

be synthesised on the glass plate with comparable morphology and properties as with the conventional method.

4. Dispensing catalyst formulation onto glass plates

The ECHO acoustic liquid handler accommodates original plastic microtiter well plates (96, 384 and 1536 wells). To create the catalyst plates, a glass plate had to be used for the catalyst formulation deposition and synthesis. The glass plate was not compatible with the ECHO liquid handler, and thus a customised plate had to be designed to hold the glass plate, which could also be used in the ECHO liquid handler. A CAD model was designed (using the Onshape CAD software) using the same dimensions as the original microtiter plates (**Figure S4.7**). The model was then 3D printed, and the glass plate was inserted into the model and used in the ECHO liquid handler. The catalyst formulations were then deposited onto the glass plate and not into a microtiter plate (as used with normal operation). This customised model made it possible to deposit numerous catalyst formulations onto the glass plate and form numerous different mesoporous metal oxide catalysts that were subjected to high-throughput screening for the oxidation of morin.

Figure S4.7: **(a)** CAD model for glass insert, designed using the Onshape CAD program. **(b)** A 3D printed model of the glass plate holder, with the glass plate, used for the deposition of mesoporous metal oxide formulations. The dimensions are given.

5. Siliconisation of the glass plate

It was noticed during the transfer of the formulations onto the glass plate, that the droplets weren't transferred as neat droplets. Some splashes were observed after the transfer. This might

be a problem since the cross-contamination of the well/catalyst areas might occur. The droplets are required to remain in the same position (the same well area) on the glass plate until calcination and the bottomless 96-well plate is positioned over each catalyst. It was concluded that the smooth surface of the glass plate causes the droplets to splash and migrate over the plate, cross-contaminating other well areas. This might be due to the hydrophilic surface of the glass plate. To overcome this issue, the glass plate was treated to give the surface a hydrophobic coating. Two different treatments were tested, an automobile glass treatment (Rain-X) and a silane compound. With these treatments, a hydrophobic surface was added to the glass plate surface.

Initially, Rain-X (rainx.com) was used as a treatment. This is a synthetic hydrophobic treatment for glass surfaces. This treatment causes water to bead and is most commonly used on automobile surfaces such as windscreens and sometimes on the wiper blades as well. Small and large droplets were tested on the glass plate after treatment with Rain-X. However, it was observed that the formulation didn't bead when larger droplets were used. The Rain-X treatment only worked when small droplets were transferred. When the droplet volume was increased, it spread to the neighbouring well area, as seen in **Figure S4.8 (b)**.

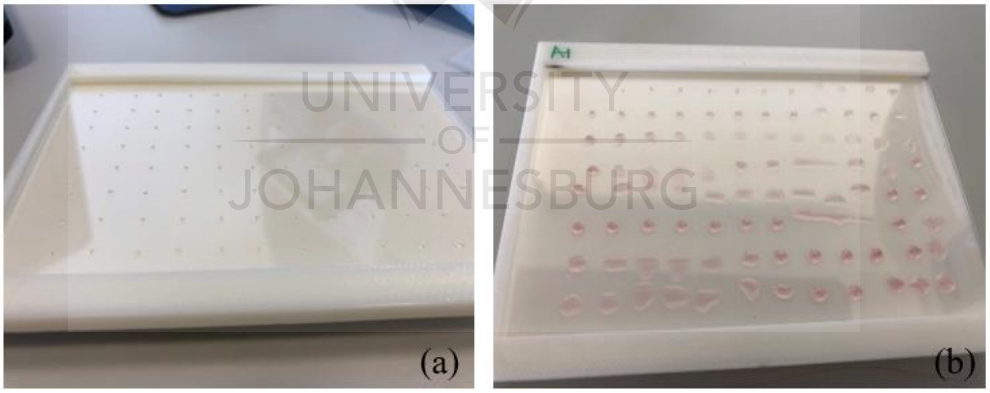

Figure S4.8: Hydrophobic treatment of glass plate using Rain-X. From **(a)**, it can be seen that this treatment works well when using small volumes. Unfortunately, when larger volumes are used (b) the droplets spread-out and cross-contaminated neighbouring well areas. A Co_3O_4 MMO formulation was used for both plates.

An alternative treatment was to siliconise the glass plate. This was done by the treatment of the glass plate with an organic compound, dimethyldichlorosilane. The compound dimethyldichlorosilane was dissolved in chloroform. The glass plate was submerged into the

solution for a few minutes. After that, it was left to dry overnight at room temperature and then dried in an oven at 80 °C for 2 hrs. The plates were then washed with a soapy solution and dried with a paper towel. This treatment is good for small and larger volumes, as depicted in **Figure S4.9**. All glass plates were siliconised before use.

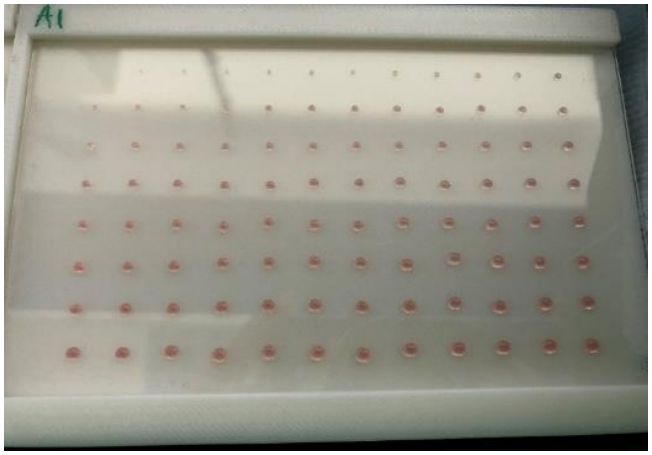

(b)

Figure S4.9: Siliconisation of the glass plate using dimethyldichlorosilane. This hydrophobic treatment is good for small and larger volumes. The Co formulation volume was increased from 30 nL to 5000 nL over the 96-well areas.

6. Formation of the mesoporous metal oxide catalysts on the glass plate

After the solvent system, droplet generation, and glass treatments were investigated, the catalysts plates could be prepared. The formulation/s were transferred onto the glass plate using the ECHO acoustic liquid handler, and the plate/s were placed into an oven for the heat treatment to form the MMO catalysts. The formulations on the plates were aged at 80°C overnight. Thereafter, it was dried at 150°C for 6 – 24 hrs. The catalysts were then calcined at 400°C for 4 hrs with a ramp in temperature of 1 – 2°C/min.

6.1. Static electric interference with catalyst on the glass plate

The synthesis of the MMO catalysts on a glass plate comes with some disadvantages. During the calcination of the formulations in the furnace, the glass plate is not covered. Therefore, after calcination, the catalysts are exposed to the surroundings of the furnace as well as the room environment when removed. Moreover, since the catalysts are formed on top of the glass plate as solids, and not in a cavity (such as a crucible or beaker as under normal circumstances), they are free to move around on the plate. Examples of this can be seen in **Figure S4.10**. This is a major problem since cross-contamination of neighbouring well areas may occur, and some catalysts may get misplaced and not represent the accurate amount of catalyst synthesised, once the 3D printed 96-well plate is placed over the catalysts.

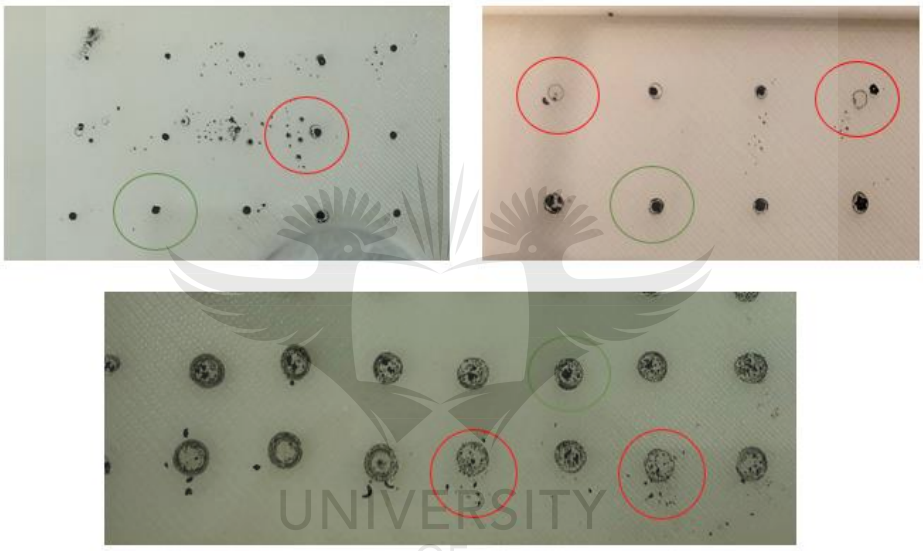

Figure S4.10: Representation of some of the MMO catalysts affected by the static electricity after removal of the catalyst plate from the oven. Static electricity might not be the only problem; it might simply be that the catalyst comes loose from the plate.

Moreover, static electricity/charge was one of the major issues to overcome. It was observed that the 3D printed 96-well plates attracted static electricity, and once placed over the catalysts on the glass plate, the static electricity causes the catalysts to come loose from the plate and stick to the wells of the 3D printed plate. To overcome this issue, the 3D printed plates were placed in an anti-static bag (**Figure S4.11**), before placement onto the glass. This was to reduce or minimise the static on the 3D printed plates, hence reducing the static on the catalyst, preventing movability of the catalyst on the glass plate. Unfortunately, these bags did not always prevent static charge on the 3D prints, and an alternative procedure was necessary.

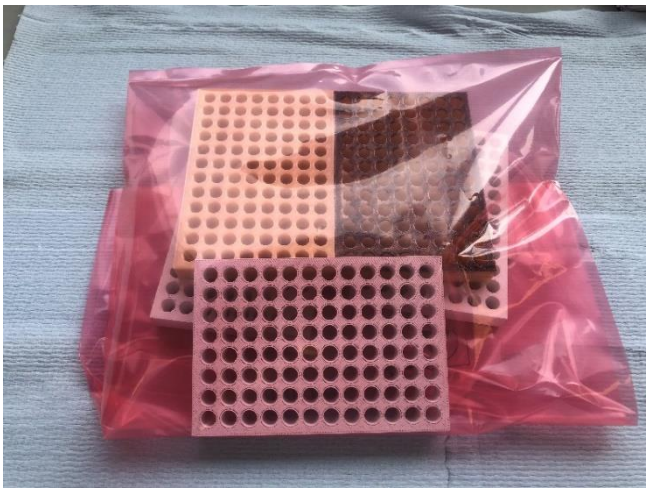

Figure S4.11: Anti-static bags containing the 3D printed 96-well plate before the 3D printed plates are placed onto the catalyst plates. These bags reduce static charge on the prints.

6.2 Aluminium block for catalyst calcination

An aluminium block (**Figure S4.12**) was designed to fit the glass plate containing the formulations, with a bottomless 96-well aluminium plate to fit over the formulation whilst calcining. This prevents the calcined catalysts from migrating to neighbouring wells area. Even though the catalysts may come loose from the plate, it remains in the correct well area until the 3D printed bottomless 96-well plate is placed over the catalyst. After calcination, the entire block could be moved to the glue dispensing robot to glue the 3D printed 96well plate to the glass plate containing the calcined catalysts.

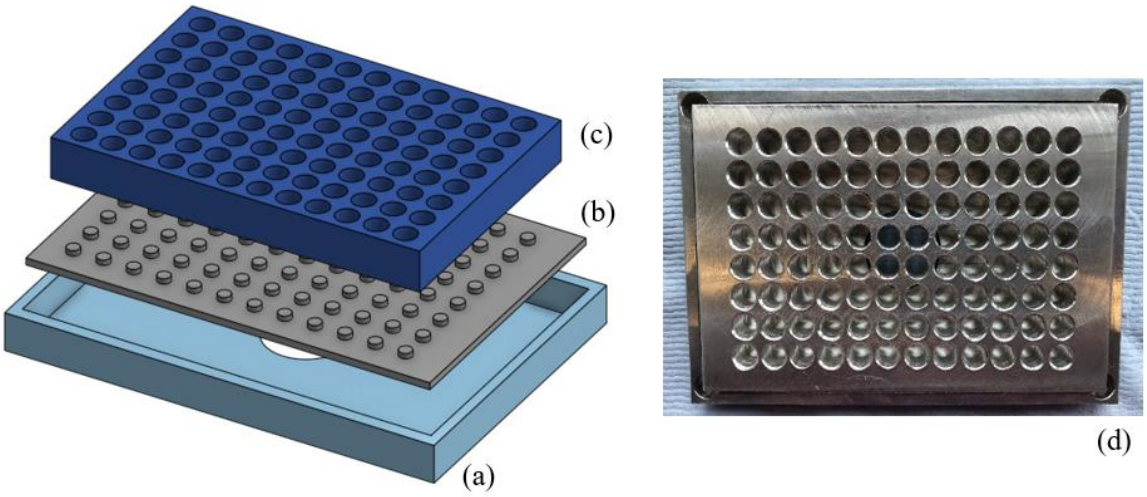

Figure S4.12: A 3D rendered image of the aluminium block for the catalyst formulation calcination on the glass plate, and to prevent catalyst migration over the plate. **(a)** The aluminium block to fit the glass plate with catalyst formulations. **(b)** The glass plate with dispensed catalyst formulations. **(c)** a bottomless 96-well aluminium plate to be placed over the catalyst formulations before calcination. This prevents the calcined catalysts from migrating to neighbouring well areas. The actual aluminium block **(d).**

7. Customised 96-well microtiter plate for catalyst evaluation

7.1. 3D printed bottomless 96-well plate

Following the synthesis of the catalyst plates, a reaction well for each catalyst had to be created to evaluate the catalyst simultaneously. A 3D printed bottomless 96 well plate was designed using the Onshape software (**Figure S4.13 (a)**) and 3D printed (**Figure S4.13 (b)**)to be placed over the catalysts onto the glass plate. This allows the individual catalysts to each be in a separate well.

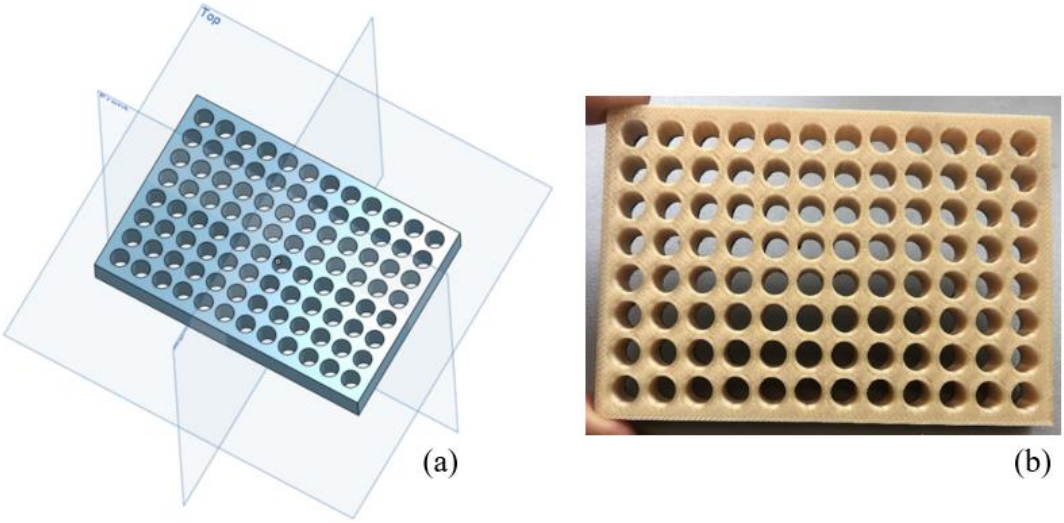

Figure S4.13: **(a)** CAD model of the bottomless 96-well plate to be fitted over the catalysts on the glass plate. **(b)** 3D printed bottomless 96-well plate. It was 3D printed using Ultem material. This material is chemically resistant.

One of the challenges of using a customised approach was to ensure a watertight seal between the 3D printed model and the glass plate. This prevents any leakages to and from neighbouring wells, preventing cross-contamination. Initially, an LCP (liquid crystal phase) sandwich set was used to fix the 3D printed 96-well plate onto the glass plate (**Figure S4.14**). This set includes the glass plate and a double-sided adhesive with 96 holes representing a 96-well plate. This set has the same dimensions as an original 96-well plate. The 3D printed plate was designed with the same dimension to fit exactly on top of the adhesive.

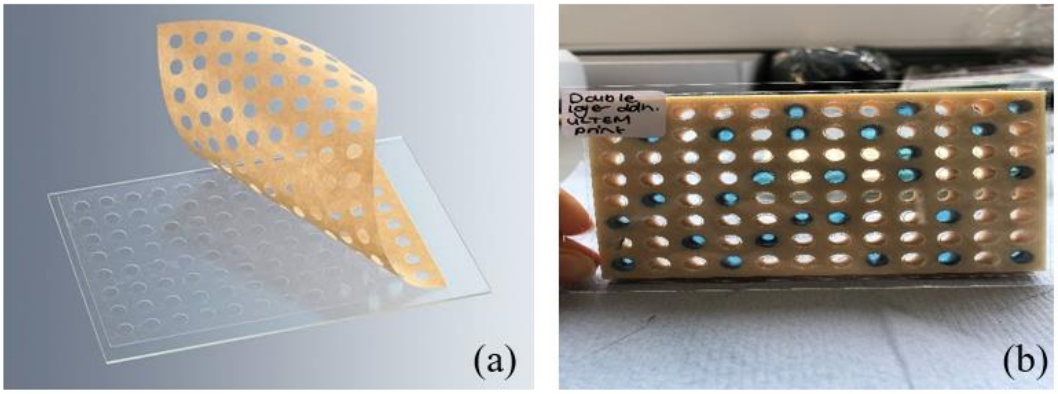

Figure S4.14: **(a)** Originally, the LCP sandwich set includes the glass plate for crystal deposition. However, it was used to deposit the catalyst formulations onto, and a double-sided 96-well adhesive to stick the 3D printed 96-well plate. **(b)** A 3D printed bottomless 96-well plate adhered to the glass plate using the LCP double-sided adhesive. The leak test was conducted using a blue food colouring solution in certain wells to determine leakage to neighbouring wells.

The system was tested for any leakage before continuing with further experiments. The double-sided adhesive was placed on top of the glass plate, followed by the 3D printed bottomless 96-well plate. After the adhesion, a blue food colouring solution was added to only a few wells, to investigate any leakage to neighbouring wells. No leakage occurred within the first 30 min; however, after a few hours, it was observed that the blue solution had leaked to neighbouring wells as well as out through the sides. Moreover, a double layer of the adhesive was tested; however, a watertight seal could not be achieved. Upon closer inspection, it was observed that the well holes of the adhesive weren't spaced out accurately as with the 3D printed plate. Therefore, when the 3D printed plate was placed on the top of the adhesive, some of the holes did not match, which caused leakages.

A watertight seal was achieved by applying a slow curing epoxy glue to the 3D print and sticking it to the glass plate. This was done by using a Nordson EFD Pro4 glue dispensing robot (**Figure S4.15**). The robot ensured that the same amount of glue is dispensed evenly between the holes, and when adhered to the plate creates a watertight seal. The glue is dispensed according to the 2D pattern (**Figure S4.16**) in the shape of the top view of 3D print. This allows the robot to precisely deposit the glue onto the 3D print, making this step reproducible every time a catalyst plate is created.

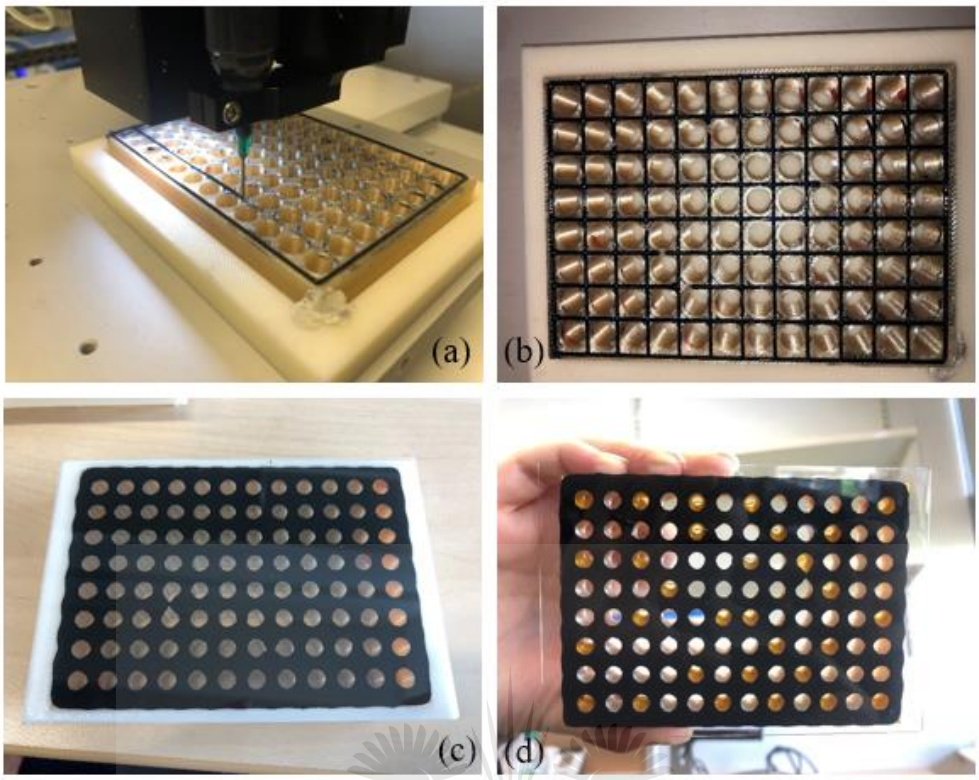

Figure S4.15: **(a)** The Nordson EFD Pro4 glue dispensing robot in action, dispensing a slow curing epoxy glue according to the 2D pattern designed in Onshape.com. **(b)** the pattern of glue on the bottomless 96-well 3D print. **(c)** The bottomless 96-well plate adhered to the glass plate seen from the bottom, to form the catalyst plate with 96 wells, each containing one specific catalyst. **(d)** A leak test was conducted for 24 hrs after the bottomless 96-well plate was stuck to the glass plate. No leaks were observed.

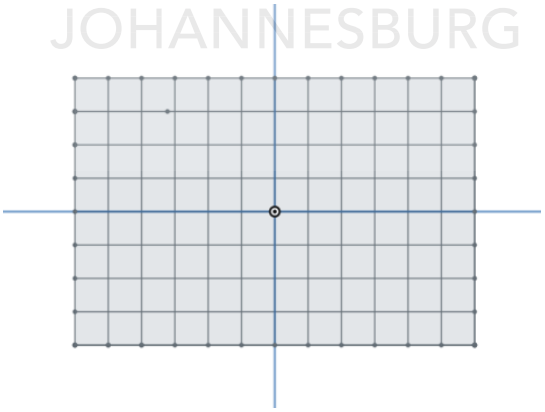

Figure S4.16: Glue pattern designed in Onshape and exported as a .dxf file. The software of the robot can read .dxf files and will dispense the glue accordingly. The glue was dispensed along each line which ran in between the holes on the customised 3D printed bottomless 96-well plate.

Each 3D printed 96-well plate had to be placed in the same position on the robot deck for the robot to dispense the glue accurately each time. Therefore, a 3D printed holder was designed and printed to fit into the dock of the robot (**Figure S4.17**). The plate is left to dry overnight to ensure that the epoxy glue is completely dry before the reagents are added to each well.

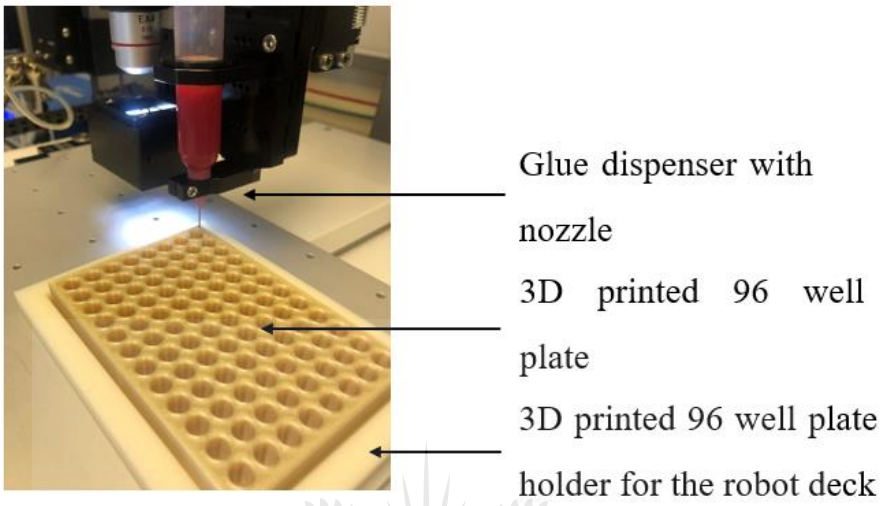

Figure S4.17: 3D printed 96-well plate holder with the 96-well plate inserted, on the robot deck. The robot has a nozzle for the glue dispensing.

8. Ultrasonication of the miniature catalysts in the plate

Conventional methods for MMO catalyst evaluation involves the grinding of the catalyst after calcination and the dispersion in the reaction using ultrasonication. If the catalyst is not dispersed properly, it lowers the surface area of the catalyst. This ultimately lowers the activity of the catalyst. With the synthesis of the miniature catalysts on the glass plate, it was not possible to grind the catalyst before use. Also, the catalysts could not be sonicated before the reaction. With the evaluation of the first catalyst plate, the k_{obs} values (rate of reaction) were lower than expected. It was concluded that the catalysts were too aggregated which lead to slower reaction rates. With the evaluation of the other catalyst plates, it was attempted to sonicate the plates before the oxidation reactions. A plate holder was designed, and 3D printed to be used in the sonicator bath to allow the bottom of the glass plate to touch the water in the sonicator bath (**Figure S4.18**).

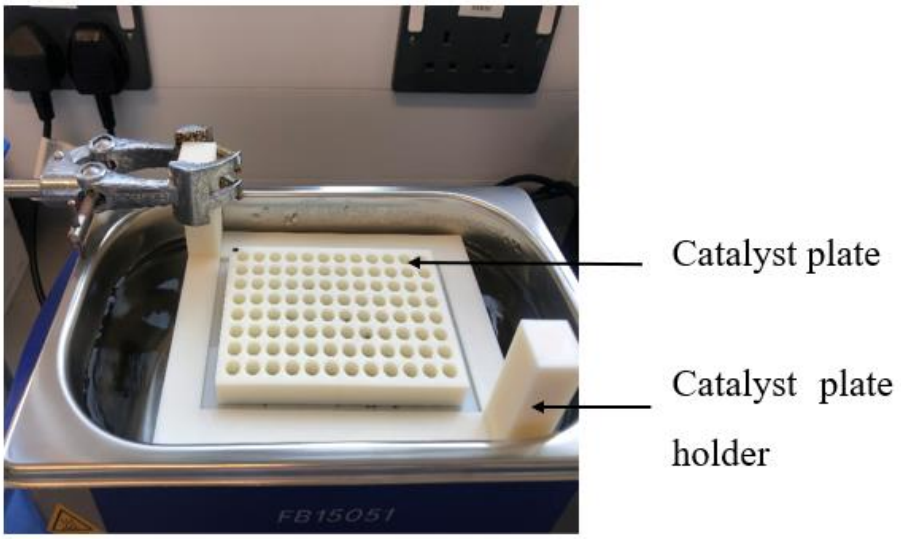

Figure S4.18: 3D printed catalyst plate holder to hold the catalyst plate over the water in the sonicator bath to disperse the catalysts in the reaction solution.

The catalyst plate was sonicated for approximately 2 min before running the reaction. A clear increase in the k_{obs} was observed for the catalyst plates that had been sonicated. However, during the sonication of the plate, it was observed that the middle wells were better sonicated compared to the perimeter wells. This could increase the k_{obs} of the catalysts in the middle wells.

9. Catalyst plate evaluation toward the oxidation of morin

Following the synthesis of catalyst plates, the catalysts were evaluated for the oxidation of morin using peroxide (H_2O_2) as an oxidant. Positive and negative controls were included with each plate, except for the Co_3O_4-MMO plate, where only a negative control was included. The positive control consisted of the bulk Co_3O_4-MMO catalyst with a concentration of 0.025 mg/mL of the catalyst in the final reaction. The stock solution used for the positive control was prepared by weighing out the required amount, followed by sonication. The negative control didn't contain any catalyst. Therefore, the first two columns (16 wells) of each plate was left empty for the controls

9.1 Opentrons

A pipetting robot, the Opentrons OT2, was used to add all the reagents to each well. This robot uses a multichannel pipette, making it possible to pipette the same volume to 8 wells

simultaneously. Initially, water (100 µL) was added to each well, followed by H_2O_2 (50 µL, 7.5 mM) and at the end, the morin dye (50 µL, 150 µM). The dye was made up in a 0.1 M carbonate buffer ($NaHCO_3$:$NaCO_3$) as illustrated in **Figure S4.19**.

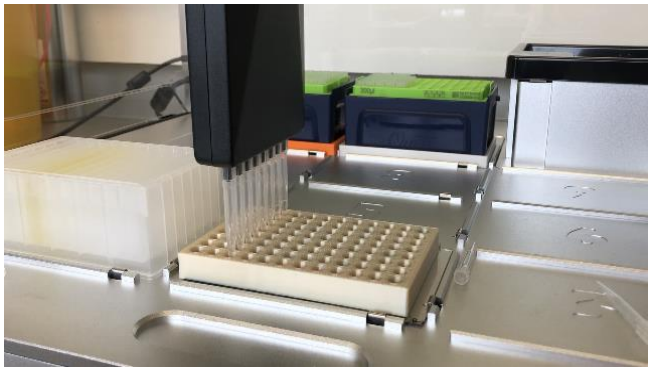

Figure S4.19: The Opentrons OT2 pipetting robot used to the transfer of the reagents of the oxidation of morin. The reagents included water (100 µL), followed by H_2O_2 (50 µL, 7.5 mM) and morin dye (50 µL, 150 µM).

The accuracy of the reaction is increased when using a pipetting robot by eliminating human error. The reagents are pipetted accurately into each well, ensuring that each reaction contained the same amount of reagents. This allows for better screening results.

9.2 Catalyst plate evaluation

9.2.1 Co_3O_4-MMO plate

The synthesis of the Co_3O_4-MMO plate and evaluation for the oxidation of morin was used as a proof of principle. Initially, very small amounts (30 nL) of the Co-MMO formulation was dispensed onto the glass, however, upon removal of the glass plate from the calcination oven, the small particles were highly affected by static and didn't remain on the glass plate. Therefore, when the plate was evaluated for the oxidation of morin, no activity was seen.

The volume (representing the mass of the catalyst) of the formulation was subsequently increased. A volume range of 2500 – 4990 nL was used, with the first volume being 2500 nL, followed by a volume increase of 30 nL for the consecutive 79 wells. Therefore, the concentration of the catalyst in the final reaction (200 µL) in each well is increased over the plate. From these volumes used, high k_{obs} values were expected; however, the k_{obs} obtained were much lower compared to the positive control. **Table S4.2** represents the 96-well plate and shows the respected k_{obs} values obtained for each catalyst (each of the wells). A green-yellow-

red colour scheme was applied to the data (k_{obs}) obtained for the entire 96-well plate. With this, it can be seen which wells gave the best results.

With conventional catalyst evaluation, the catalyst is dispersed in the reaction using sonication. Sonication ensures that all the particles are properly dispersed and that the entire surface area of each particle is available to the reagents to adsorb to. When the particles are not sonicated and dispersed, it decreases the surface area of the particles, decreasing the available active sites on the catalyst. The miniature catalysts in the customised catalyst plate were not sonicated. The particles were, therefore agglomerated together, which decreased the surface area, explaining why the rates are not as high as expected.

Unfortunately, only a negative control was included with the Co_3O_4-MMO plate. Even though the k_{obs} is not as high as expected, some of the catalysts did show activity, where the k_{obs} were higher than the negative control. It, therefore, shows that this system can be used for the parallel synthesis of mesoporous metal oxide oxidation catalysts, with the simultaneous evaluation of each catalyst for a specific reaction.

9.2.2. Co/Mn-MMO plate

This catalyst plate contained a combination of Co and Mn MMO catalysts, to give multicomponent Co/Mn catalysts. The Co-MMO volume was kept constant, and the Mn volume was varied over the 80 catalysts. A volume of 2500 nL of the Co-MMO formulation was used for each catalyst, and the Mn-MMO formulation was varied from 250 – 2225 nL. This was done to form multicomponent mesoporous metal oxides and to determine the effect of Mn on the activity of the catalysis. After the addition of water in the wells of the catalyst plate, the Co/Mn-MMO plate was sonicated to attempt dispersion of the catalysts in each well. From observation, it was seen that the middle wells were sonicated to a better extend, compared to the perimeter wells.

The k_{obs} for some of the catalysts were high compared to the positive control (bulk Co_3O_4-MMO catalyst). This might be due to the sonication that wasn't uniform across the plate, and that only the catalyst in the middle of the plate was sonicated and dispersed properly. This can be seen in **Table S4.5**. The k_{obs} obtained for the wells in the middle of the plate was higher compared to the perimeter wells. This corresponds to what was observed during sonication. However, despite the inconsistency in the k_{obs} obtained, it can still be seen that the addition of

Mn increases the k_{obs} of the catalysts. Therefore, a synergistic effect is achieved when multicomponent mesoporous metal oxide catalysts are used.

9.2.3. Au/Co_3O_4- and Pd/Co_3O_4-MMO plates

With these catalyst plates, the effect of gold - and palladium PVP stabilised nanoparticles (Au-PVP and Pd-PVP NP) supported onto Co_3O_4 MMO was investigated. Varying amounts of the metal PVP nanoparticle formulation were deposited with the cobalt MMO formulation. A constant volume of the cobalt formulation (2500 nL) was used, with a range of 200 nL to 2175 nL of a 0.3 M Pd-PVP and 0.05 M Au-PVP nanoparticle formulation. That, therefore, gave a Pd concentration ranging from approximately 1% - 13%, and 0.4% - 4% for the Au, over the 84 synthesised catalysts on the plate. Using these plates, the effect of the % Pd or Au can be determined, and the optimum concentration can be screened.

For the Au supported onto Co_3O_4-MMO a trend was seen with the increasing concentration of the AuNPs. It was seen that the k_{obs} increased as the loading of the Au increased over the plate. From **Table S4.3**, it can be seen that the k_{obs} values were higher for the bottom middle wells in the plate, compared to the perimeter wells. As mentioned above, this can be due to the inconsistent sonication of the plate.

Unfortunately, for the Pd supported onto Co_3O_4, no trend could be observed for the kobs and increasing %Pd loading. This may be due to the high concentration of the Pd-PVP NPs (0.3 M), used in small amounts to achieve low %Pd loading on such small volumes. Using a high concentration the Pd-PVP NPs solution, the particles have a tendency to agglomerate making the particles less effective for catalysis. This may be the reason for the lower k_{obs} values (lower compared to the Au/Co_3O_4-MMO kobs values) obtained for the Pd/Co_3O_4-MMO plate. Moreover, the same trend in the kobs values for the middle wells was seen with this plate. **Table S4.4**, shows clearly that the kobs values are higher to the middle wells compared to the perimeter wells. Again this due to the inconsistent sonication, where it was observed that the middle wells received better sonication.

Table S4.2: A representation of the 96-well catalyst Co_3O_4-MMO plate with the respective k_{obs} values obtained for each catalyst on the plate. A green-yellow-red colour scale was applied to the data, where the green colour represents the higher k_{obs} values, followed by yellow and red, which represents the lower k_{obs} values. Row 1 represents the negative control. Unfortunately, at this stage, a positive control was not included.

	1	2	3	4	5	6	7	8	9	10	11	12
A	0.01546	0.01546	0.01546	0.01546	0.01546	0.01546	0.01546	0.01546	0.01546	0.01546	0.01546	0.01546
B	0.01326	0.00836	0.00857	0.01559	0.01386	0.02016	0.01477	0.00686	0.01648	0.01649	0.0084	0.0106
C	0.014	0.01086	0.01193	0.01582	0.00868	0.00902	0.02078	0.00441	0.02047	0.01469	0.00587	0.00707
D	0.01711	0.01417	0.0151	0.01281	0.0117	0.01185	0.01597	0.02029	0.01958	0.02164	0.01432	0.00918
E	0.01568	0.01259	0.01011	0.01587	0.01262	0.01395	0.00892	0.03395	0.02173	0.02001	0.00458	0.00381
F	0.01344	0.01675	0.0163	0.01759	0.01642	0.02125	0.00665	0.00984	0.02254	0.02194	0.00897	0.00906
G	0.01662	0.01077	0.01878	0.0211	0.02272	0.01953	0.02071	0.01312	0.02864	0.01534	0.00214	0.01034
H	0.01799	0.00973	0.02119	0.02393	0.01864	0.02253	0.01757	0.00928	0.00751	0.00464	0.01097	0.00727

Table S4.3: A representation of the 96-well catalyst Au/Co_3O_4-MMO plate with the respective k_{obs} values obtained for each catalyst on the plate. A green-yellow-red colour scale was applied to the data, where the green colour represents the higher k_{obs} values, followed by yellow and red, which represents the lower k_{obs} values. Column 1 and 2 represents the negative and positive controls, respectively.

	1	2	3	4	5	6	7	8	9	10	11	12
A	0.0118475	0.0941175	0.017235	0.0436	0.01584	0.02843	0.02775	0.028555	0.01869	0.024775	0.02206	0.022955
B	0.0118475	0.0941175	0.02531	0.03273	0.0334	0.05035	0.037735	0.028905	0.03479	0.0314	0.024405	0.03258
C	0.0118475	0.0941175	0.03367	0.041845	0.04205	0.05103	0.04436	0.05248	0.04107	0.042735	0.040445	0.044705
D	0.0118475	0.0941175	0.039475	0.050685	0.0623	0.068905	0.073485	0.073365	0.065	0.06091	0.05022	0.03463
E	0.0118475	0.0941175	0.07567	0.048355	0.077485	0.075245	0.08171	0.11315	0.08306	0.06461	0.06349	0.03589
F	0.0118475	0.0941175	0.0861	0.110665	0.105115	0.12352	0.159785	0.13899	0.084455	0.06759	0.037125	0.05242
G	0.0118475	0.0941175	0.13925	0.10606	0.134855	0.20865	0.186105	0.14352	0.105825	0.08237	0.045535	0.05076
H	0.0118475	0.0941175	0.08889	0.077105	0.040845	0.099275	0.157525	0.151515	0.12477	0.073765	0.06208	0.086035

Table S4.4: A representation of the 96-well catalyst Pd/Co_3O_4-MMO plate with the respective k_{obs} values obtained for each catalyst on the plate. A green-yellow-red colour scale was applied to the data, where the green colour represents the higher k_{obs} values, followed by yellow and red, which represents the lower k_{obs} values. Column 1 and 2 represents the negative and positive controls, respectively.

	1	2	3	4	5	6	7	8	9	10	11	12
A	0.0118475	0.0941175	0.01009	0.011585	0.0111	0.009645	0.01008	0.011815	0.01088	0.00761	0.009465	0.01154
B	0.0118475	0.0941175	0.0096	0.01199	0.014685	0.01817	0.012495	0.011235	0.011145	0.01391	0.012965	0.01093
C	0.0118475	0.0941175	0.009385	0.015695	0.015435	0.01472	0.013375	0.01335	0.009465	0.011555	0.008505	0.01192
D	0.0118475	0.0941175	0.01483	0.01805	0.018135	0.034505	0.014855	0.020765	0.0186	0.01655	0.01694	0.011105
E	0.0118475	0.0941175	0.013345	0.024685	0.02036	0.02873	0.02177	0.02566	0.02112	0.01274	0.017215	0.0119
F	0.0118475	0.0941175	0.013585	0.021295	0.02949	0.01963	0.02284	0.013645	0.02372	0.017915	0.0101	0.01096
G	0.0118475	0.0941175	0.01753	0.01958	0.0363	0.03248	0.020415	0.01091	0.03086	0.029325	0.01667	0.017445
H	0.0118475	0.0941175	0.02245	0.021755	0.04049	0.02453	0.03129	0.025835	0.025645	0.01778	0.01808	0.017065

Table S4.5: A representation of the 96-well catalyst Co/Mn-MMO plate with the respective k_{obs} values obtained for each catalyst on the plate. A green-yellow-red colour scale was applied to the data, where the green colour represents the higher k_{obs} values, followed by yellow and red, which represents the lower k_{obs} values. Column 1 and 2 represents the negative and positive controls, respectively.

	1	2	3	4	5	6	7	8	9	10	11	12
A	0.0118475	0.0941175	0.012625	0.012325	0.011175	0.017405	0.010965	0.013345	0.00751	0.0117	0.027625	0.013025
B	0.0118475	0.0941175	0.023185	0.034055	0.236815	0.14967	0.02283	0.01817	0.00834	0.028185	0.01796	0.02105
C	0.0118475	0.0941175	0.045105	0.17353	0.045935	0.16143	0.127225	0.015955	0.030765	0.010635	0.005375	0.01429
D	0.0118475	0.0941175	0.06237	0.123635	0.16878	0.18386	0.14768	0.00869	0.011885	0.010455	0.008465	0.00691
E	0.0118475	0.0941175	0.106575	0.022395	0.075295	0.16611	0.04017	0.015005	0.014205	0.052075	0.04735	0.01288
F	0.0118475	0.0941175	0.04399	0.00955	0.030765	0.10319	0.01941	0.022335	0.048265	0.030015	0.01032	0.04932
G	0.0118475	0.0941175	0.01265	0.013755	0.01561	0.11525	0.018855	0.015095	0.010995	0.012675	0.021735	0.011965
H	0.0118475	0.0941175	0.03757	0.01296	0.03959	0.04825	0.022315	0.01964	0.07552	0.022455	0.02031	0.018115

10. Catalyst immobilisation on a glass plate

Some of the disadvantages of the synthesis of the MMO catalyst on a glass plate is that solid catalysts are formed which do not stick to the glass plate. Static charge influences how the catalysts are sometimes removed from the glass and cause it to stick to the 3D printed 96-well plate. This is a major problem since the results obtained might not be reproducible due to the loss of catalysts from the plate.

Immobilisation of the catalyst onto the glass plate would solve these problems by ensuring that the entire amount of catalyst is available to take part in the reaction. It was decided to treat the glass plate with a hydrophilic treatment to expose the hydroxyl (OH) groups of the glass. This will enable the formulation to react with the OH groups on the glass and subsequently be immobilised.

A piranha solution was used to etch the surface of the glass plate to expose the OH groups. A piranha solution is a mixture of concentrated sulfuric acid and hydrogen peroxide using ratios of 3:1 or 7:1. This solution is mostly used to treat glassware in the laboratory to remove trace amounts of organic residues from glass substrates. The preparation of this solution is very dangerous since the mixing of the sulfuric acid and hydrogen peroxide produces an extremely exothermic reaction which can cause the temperature to rise above 100 °C. The mixing of the two reagents produces a highly activated and oxidising peroxymonosulfuric acid (H_2SO_5) represented in **Figure S4.20**, which is sometimes also referred to as Caro's acid. This solution is very unstable and/or explosive depending on the conditions used to prepare it

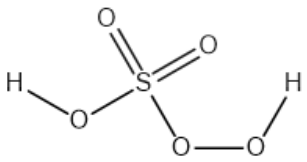

Figure S4.20: Peroxymonosulfuric acid also known as Caro's acid.

Caution was used with the preparation of this solution. The glass plate was inserted into the piranha solution and left for 15 min. It was removed and rinsed with deionised water, dried and ready to be used. A Co-MMO formulation was used to test the formulation transfer onto the piranha treated glass plate. From **Figure S4.21**, it can be seen that there is a difference in the droplet transfer onto the piranha treated and untreated glass plate. Since a highly hydrophilic layer is formed on the glass plate when treated with the piranha solution, the MMO formulation

doesn't bead, but rather spread out over the glass. No droplets were formed on the treated glass. This can be both an advantage and a disadvantage. The advantage is that the catalyst formed after calcination might be immobilised onto the glass; however, the disadvantage is cross-contamination between neighbouring well areas.

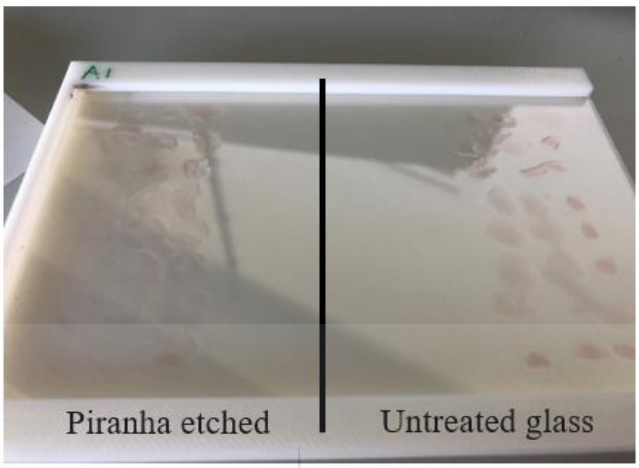

Figure S4.21: Formulation transfer onto the piranha etched glass plate as well as the untreated glass plate.

To evaluate the immobilised Co_3O_4-MMO catalysts for the oxidation of morin, boundaries had to be created on the glass plate before formulation transfer. Epoxy glue was used to create a pattern on the glass plate to separate the formulations from well to well The epoxy glue was burned off during the calcination step, which left the immobilised catalysts on the glass plate (**Figure S4.22**).

Figure S4.22: The immobilised Co_3O_4-MMO catalysts on the glass plate, after treatment of the glass plate with the piranha solution.

No loss of catalyst was seen from the plate after calcination. A 3D printed 96-well plate was glued to the glass plate after calcination, and the reaction was setup. Unfortunately, the 3D printed plate well didn't stick properly to the plate and came loose. It was concluded that due to the extreme hydrophilic surface of the treated glass plate, the epoxy glue was not able to adhere properly to the glass plate. This caused many leakages, and the reaction could not be processed. However, this is a method worth investigating, and in the future, more research will be done on this matter.

Chapter 5

The use of robotics and 3D printing in chemistry – An open-source approach

Supplementary information

1. Bill of Materials (BOM)

Table S5.1: Bill of materials for the EvoBot robot. This includes the hardware for the construction of the robot. The table shows the description of the parts with the quantity purchased, the distributor (and distributor part no) and the price.

Description	Quantity Purchased	Quantity required	Distributor or Manufacturer	Stock or Part no	Comments	Unit Price (R)	Total
Polylactic acid (PLA) 3D prinitng filament	1	1 kg	3D printing store		All parts were 3D printed using PLA	300	300
Z Stepper motors	2		3D printing store	MOT003	NEMA 17 x 40 mm, 1.8 deg/step	239	478
X Stepper motor	1		3D printing store	MOT001	NEMA 17 x 48 mm, 1.8 deg/step	269	269
Head PCB	3		JP Electronic control			373	1119
Arduino Mega	1		3D printing store			499	499
RAMPS 1.4 Controller board	1		3D printing store	RAM001		399	399
Stepper motor driver	2		3D printing store	STP002	DRV8825 with heat sink	99.95	199.9
Aluminium V-slot profile 20x20 mm	4		3D printing store	TSL011	Cut to 600 mm	74.25	297
Aluminium V-slot profile 20x20 mm	4		3D printing store	TSL011	Cut to 432 mm	49.5	198
Aluminium V-slot profile 20x20 mm	1		3D printing store	TSL011	Cut to 390 mm	49.5	49.5
Aluminium V-slot profile 20x20 mm	4		3D printing store	TSL011	Cut to 550 mm	74.25	297
Aluminium V-slot profile 20x40 mm	6		3D printing store	TSL012	Cut to 390 mm	79.5	477

Description	Quantity Purchased	Quantity required	Distributor or Manufacturer	Stock or Part no	Comments	Unit Price (R)	Total
Aluminium V-slot profile 20x40 mm	4		3D printing store	TSL012	Cut to 378 mm	79.5	318
Aluminium V-slot profile 20x40 mm	6		3D printing store	TSL012	Cut to 590 mm	119.25	715.5
V-slot wheel kit	45		3D printing store	VWH001	Solid, Delrin	44.1	1984.5
Spacers	90				3D printed with PLA	0	0
M5 bolts	100		Hardware			2.5	250
Pulley, GT2	3		3D printing store	PUL021	16 teeth for 6 mm belt, 5 mm bore	39.95	119.85
Timing Belt, GT2	2	1.5 m	3D printing store	BEL002	6 mm wide, 1 m long	49.95	99.9
Inside hidden bracket	40		3D printing store			14	560
T-Nuts	20	100	3D printing store	TNT002	20 series Turn T-nuts, M5 pack of 5	14.25	285
Polyethylene Flexible Conduit tubing	1	1 m	RS Components	429678	16 mm diameter, 1 m	103.91	103.91
Switch	3		RS Components	6820835	Sim roller lvr, SPDT, sldr tm, 10.1A	35.8	107.4
						Grand Total	**9126.46**

Table S5.2: Bill of materials for the syringe module. This includes the hardware for the construction of the robot. The table shows the description of the parts with the quantity purchased, the distributor (and distributor part no) and the price.

Description	Quantity Purchased	Quantity required	Distributor or Manufacturer	Stock or Part no	Comments	Unit Price (R)	Total
PLA Filament	1	1 kg	3D printing store			300	300
Syringe PCB	1		JP Electronics		A minimum of 25 PCB had to be purchased	23	575
Syringe PCB setup	1		JP Electronics			700	700
NEMA 8 Stepper Motor	1		Micro Robotics		NEMA 8, 1.8 N.cm, 1.8 deg/step, micro stepper motor	332.35	332.35
Linear Actuator	1		RS Components	4540990	N type, linear actuator, 28.1 N, 12 V dc	1681.63	1681.63
Pinion Gear	1		RS Components	5217477	Delrin spur gear, 1.0 module, 15 teeth	55.52	55.52
Gear rack	1	10 cm	RS Components	5217837	Module 1.0 Delrin gear rack, 2m long	1354.91	1354.91
Bearing Rail	1		RS Components	4485433	Drylin N linear bearing rail, 300 L x 17 Wmm	132.82	132.82
Bearing carriage	2		RS Components	4485405	Drylin N linear bearing carriage, 17 Wmm	50.24	100.48
Switch	5		RS Components	6821496	Switch, sim roller, micro load, solder term	17.754	88.77
Syringe	1				Disposable 5ml syringe taking from Laboratory	10	10
						Grand Total	**5331.48**

Table S5.3: Bill of materials for the head PCB. This includes the hardware for the construction of the robot. The table shows the description of the parts with the quantity purchased, the distributor (and distributor part no) and the price.

Description	Quantity Purchased	Quantity required	Supplied in multiples of	Distributor or Manufacturer	Stock or Part no	Comments	Unit Price (R)	Total
Battery connector	20	20	5	RS Components	8486774	2.00 mm pitch 4 circuit Battery connector	11.102	222.04
Expansor port	5	4	5	RS Components	403816	16-bit, I/O Expander, I2C, MCP23017-E/SO	22.488	112.44
Power connector	10	1	10	RS Components	7100396	Termi-Block header 2 way PCB straigth	3.139	31.39
PCB Header 2 way	1	1	10	RS Components	3885854	AMP MODU 2-economy PCB header 2W	29.6	29.6
Micromatch 6way female	5	1	5	RS Components	6805123	Connector, F-o-B, PCB, Micro-Match, 6 w top	4.972	24.86
Micromatch 8way female	5	1	5	RS Components	7455393	Connector, PCB female 8 way, Micro-Match	10.082	50.41
Generic resistor	10	4	10	RS Components	7077666	Carbon resistor, 0.25 W, 5% 1k	0.251	2.51
8 Way jumper cable	5	5	5	RS Components	5325360	1.27 mm pitch, 250 mm	24.646	123.23
Wire jumpers male to female	20	20		RS Components	7916454	10 pcs	64.42	1288.4
Plug	5	5	5	RS Components	7100422	Termi-Block Plug 2 way, 15-13 A WG	17.614	88.07
PVC Wire	1		100 m roll	RS Components	7482112	Black PVC equipment Wire 16/0.2 mm, 100 m	314.33	314.33
							Grand Total	**2287.28**

Table S5.4: Bill of materials for the syringe PCB. This includes the hardware for the construction of the robot. The table shows the description of the parts with the quantity purchased, the distributor (and distributor part no) and the price.

Description	Quantity Purchased	Quantity required	Value	Voltage	Supplied in multiples of	Distributor or Manufacturer	Stock or Part no	Comments	Unit Price (R)	Total
L6470H Stepper driver	2	2				RS Components	8289898	dSPIN Microstep motor driver SPI HTSSOP	140.83	281.66
Header SMT connector	3	3				RS Components	7656499	2.54 mm	15.62	46.86
Capacitor 10nF	50	6	10nF	50 V	50	RS Components	4646672	0805 X7R ceramic capacitor, 10 nF, 50 V	0.531	26.55
Capacitor 100nF	25	3	100nF	50 V	25	RS Components	2644416	0805 X7R ceramic capacitor, 100 nF, 50 V	0.714	17.85
Capacitor 220nF	50	2	220nF	50 V dc	50	RS Components	7235051	Ceramic SMT capacitor 220nF 50 V dc	2.608	130.4
Eletrolitic capacitor 100uF	25	2	100uF	25 V	25	RS Components	7395572	Al Cap WX series SMT 100 uF, 25 V	2.279	56.975
Small signal diode	20	2		85 V	20	RS Components	5444534	Small signal diode,BAV99 0.125A 85V	0.445	8.9
Voltage regulator	25	1		5 V	25	RS Components	6869379	LDO regulator 5V, 1.3 A, SOT223	3.263	81.575
Resistor 1K	2	2	1K			RS Components	1754165	Resistor Aluminium Housed 75 W, 5%, 1K	171.87	343.74

Description	Quantity Purchased	Quantity required	Value	Voltage	Supplied in multiples of	Distributor or Manufacturer	Stock or Part no	Comments	Unit Price (R)	Total
PCB assembly with extra parts						JP electronics				701
									Grand Total	**1695.51**